DEVELOPMENT OF A POWER CONDITIONER FOR A PMSG-BASED WIND ENERGY SYSTEM INTEGRATED INTO A WEAK GRID

By: Akrama Khan

Thesis submitted to the Department of Electrical Engineering, University of Cape Town, in complete fulfilment of the requirements for the degree of Doctor of Philosophy

August 2020

Declaration

This dissertation is submitted to the Department of Electrical Engineering, University of Cape Town, in complete fulfilment of the requirements for the degree of Doctor of Philosophy. It has not been submitted before for any degree or examination at this or any other university. The author confirms that this thesis is based on his own work, both in concept and execution. A portion of this work has been published in a peer reviewed international conference and also accepted to be published in an international journal.

"I know the meaning of plagiarism and declare that all the work in the document, save for that which is properly acknowledged, is my own."

Signed by candidate

Akrama Khan

Aug 06, 2020

Acknowledgments

Countless thanks to Almighty Allah, the creator of this universe. His will and blessings enabled me to complete this thesis successfully. All respects for the last Holy Prophet Muhammad (P.B.U.H) who forever is a touch of knowledge and kindness for humanity.

This thesis is dedicated to my dearest parents who always prayed for my success and betterment. I am also thankful to my siblings for their kind nature and encouragement.

It is a privilege and pleasure to express my sincere gratitude to my respected supervisor, Prof M. A. Khan for his scholarly guidance, keen interest and encouraging attitude which was a real source of inspiration for me during the tenure of my studies.

Special thanks to my co-supervisor Prof. Michel Malengret. His kind supervision and expert ideas kept me on track towards completion of the project. I am also grateful for the technical assistance received from Mr. Chris Wozniak who was patient and helpful when things did not go as planned with the experimental setup.

Thanks to all my fellow members of the AMES research group for all the time they set aside to help me.

Sincere thanks to my wife Ahlam who showed her understanding and patience throughout this period. Finally, bundle of thanks to my beloved daughters Hamnah and Farwah for being the continuous source of joy in my life.

Abstract

With the growing use of non-linear loads and due to their ever changing nature, electricity networks experience power imbalance continually. These non-linear asymmetrical loads draw distorted unbalanced currents and voltages at the point of common coupling (PCC) which propagate into the distribution network. Power quality has therefore become an important issue, which has resulted in the development of numerous control strategies and other interventions to maintain the integrity of the electric network.

Recent advancements in power electronics have provided new ways to optimize power systems by regulating the active power transfer. These developments lead to opportunities for renewable energy systems to harness energy and at the same time inject optimized currents into the network by means of distributed units. An emerging problem with most such units is that they are located far from the PCC and are usually designed for the small linear loads. Moreover, the problem is exacerbated during overload conditions when the voltage level drops below the allowed minimum level due to the high network impedance which characterizes a weak grid.

This thesis aims to study similar scenarios where a permanent magnet synchronous generator (PMSG) based wind energy conversion system (WECS) is integrated into a weak AC grid. The system comprises of a machine-side (MSC) and a grid-side (GSC) converter, which provides available ancillary services and is envisaged to augment existing power quality conditioners such as STATCOM devices.

To represent a weak grid, a Thevenin equivalent model of the electric network is considered with unbalanced loads. The main objective of this project is to transform the traditional converter topology into a versatile system that can perform as a power conditioner. In particular, it monitors a distribution line, sense changes in the load, detects faults and redistributes the currents to ensure maximized power transfer into the network.

The system under consideration possesses the capability of independent injection of active and reactive currents within the defined limits. Since the system under consideration is integrated

into a weak grid, the perceived load is always considered to be unbalanced. Under the specified condition, if a fault occurs at one or two phases, unbalanced voltages are observed at the PCC.

Two scenarios are created to perform the case study. Firstly, a no-fault case is considered with symmetrical voltages at the PCC. To ensure maximum power transfer into the network with least losses, a set of currents is injected according to the optimal current injection technique. Secondly, asymmetrical faults are considered at the PCC and currents are injected according to the coordinated sequence current injection technique. This technique defines a new current injection limit which not only improves the power transfer but also enhances the power factor. Furthermore, the peak magnitude of the three phase currents is also kept within the rated current limit.

For both scenarios described above, the MSC regulates the DC link voltage so as to limit the active power coming from the generator according to the grid condition. The GSC however performs two important functions. It implements small active/reactive power perturbations for the impedance estimation, and once the impedances are determined, magnitudes of the required currents are calculated and injected based on the proposed techniques.

Validation of the analysis is done experimentally on a 3.3kW PMSG connected to a programmable regenerative power supply which emulates a weak grid. The MSC and GSC utilized in this project are conventional two-level converters which are controlled by means of a FPGA based controller.

Contents

List of Tables

List of Figures

Nomenclature

CPP	Conventional Power Plants
DAQ	Data Acquisition
DFIG	Doubly Fed Induction Generator
DFT	Discrete Fourier Transform
DGs	Distributed Generation Sources
DLG	Double Line to Ground
DSP	Digital Signal Processor
DVR	Dynamic Voltage Restorer
ENSTO-E	European Network for Transmission System Operators for Electricity
ESR	Equivalent Series Resistance
ESS	Energy Storage System
FACTS	Flexible AC Transmission Systems
FFT	Fast Fourier Transform
FOC	Field Oriented Control
FRT	Fault Ride Through
FPGA	Field Programmable Gate Array
GSC	Grid Side Converter
HVRT	High Voltage Ride Through
IM	Induction Machine
IPPs	Independent Power Producers
LOS	Loss of Synchronism
LVRT	Low Voltage Ride Through
MSC	Machine Side Converter
MV	Medium Voltage
MPPT	Maximum Power Point Tracking
NI	National Instruments
OPF	Optimal Power Flow
OCF	Optimal Current Flow
PCC	Point of Common Coupling
PI	Proportional Integral
PLL	Phase Locked Loop
PSO	Particle Swarm Optimisation
PMSG	Permanent Magnet Synchronous Generator
RCI	Reactive Current Injection
SCIG	Squirrel Cage Induction Generator
SCR	Short Circuit Ratio
SLG	Single Line to Ground
STATCOM	Static Synchronous Compensator
SVPWM	Space Vector Pulse Width Modulation
TSR	Tip Speed Ratio

VSC	Voltage Source Converter
WECS	Wind Energy Conversion System
WPPs	Wind Power Plants
WRIG	Wound Rotor Induction Generator
WT	Wind Turbine
ZVRT	Zero Voltage Ride Through

List of Symbols

P	active power
Q	reactive Power
dV	change in voltage w.r.t time
dP	change in active power w.r.t time
dQ	change in reactive w.r.t time
pf	power factor
X/R	ratio of Impedance and resistance
S_{sc}	short circuit power
P_s	rated source power
Z_{th}	Thevenin impedance
V_{th}	Thevenin voltage
I_{th}	Thevenin current
I_{mag}	current magnitude
I_d	active current
I_q	reactive current
I_{rated}	rated current
E_k	kinetic energy
ρ	air density
A	area swept by the blades
v	wind velocity
$C_{p,Betz}$	wind turbine power coefficient
β	pitch angle
λ	tip speed ratio
R	turbine blade radius
$\omega_{turbine}$	turbine speed
v_{wind}	wind velocity
K_p	maximum power coefficient
λ_{dq}	*dq-axis* flux linkage
V_{dq}	*dq-axis* voltages
I_{dq}	*dq-axis* currents
L_{dq}	*dq-axis* inductances
R_{dq}	*dq-axis* resistances
T_e	electromagnetic torque
PQ_{grid}	active and reactive power components at the grid
P_{opt}	maximum captured wind energy
R_s	stator resistance
$K_c(f)$	core loss constant
$P_{turbine}$	power generated from the turbine
$P_{rotational}$	rotational losses
P_{cu}	copper losses

$P_{rotational}$	rotational losses
P_{shaft}	power dissipated at the shaft
P_{conv}	power loss in the converters
$P_{conduct.}$	conduction losses in the converters
P_{sw}	switching losses in the converters
P_{cap}	DC link capacitor losses
$I_{chrg.}$	capacitor charging current
I_{disc}	capacitor discharging current
P_{filter}	power loss across the filter
$V_{a\beta}$	stationary reference frame voltages
V_g	grid voltage
θ_g	phase angle w.r.t grid
$I_{a\beta}$	stationary reference frame currents
ΔV_d	resultant change in d-axis voltage
ΔV_q	resultant change in q-axis voltage
Z_g	grid impedance
$Vth_n{}'$	weighted Thevenin voltage
$I_a{}'$	weighted optimal current
$V_{ref}{}'$	weighted reference voltage
P_W	active power from wind
P_L	active power at load
Z_t^+	positive sequence transfer impedance
V_{SLG}^+	positive sequence voltage during SLG fault
V_{DLG}^+	positive sequence voltage during DLG fault
$V_{\Delta WPP}^+$	boosted positive sequence voltage by the WPP
θ_I	current angle w.r.t voltage
θ_Z	impedance angle w.r.t current
I_{limit}	current transfer limit
V_f	fault voltage
$V_{dq,conv}^{+-}$	positive and negative sequence voltages at GSC
$V_{dq,grid}^{+-}$	positive and negative sequence voltages at PCC
P_{limit}	limited active power
u	unbalance factor

Chapter 1
Introduction

In recent years, wind power generation is featured as one of the fastest growing industries in renewable energy sector. With the increased penetration of wind power systems, it is mandatory to discuss the possible design challenges. When installing a wind power plant, grid strength is one of the most important design considerations. In addition, power quality reduction in terms of losses and stability of the systems when connected to weak AC grids are also major concerns in wind farm planning. In this chapter, basic components of an electric network and its characteristics are described. Integration of distributed generation units into the network and power quality requirements are also addressed. More specifically, connection of wind power plants with weak AC grids in relation to the grid codes during faults are highlighted. This chapter also covers objectives, guiding questions, scope, contribution and organisation of the thesis. Furthermore, detailed reasoning behind the project is given, which will develop the basis for problem recognition and solution in the following chapters of the thesis.

1.1 Background

An electric power network consists of three fundamental elements: the generating unit, the transmission system and the distribution system. The transmission system operates as a connecting link between the generating unit and the distribution system. It comprises high voltage systems containing transmission lines and transformers. On the other hand, a distribution system refers to lower voltages, radial lines and transformers based on the utility loads. Fig. 1.1 illustrates the main components of an electrical power network.

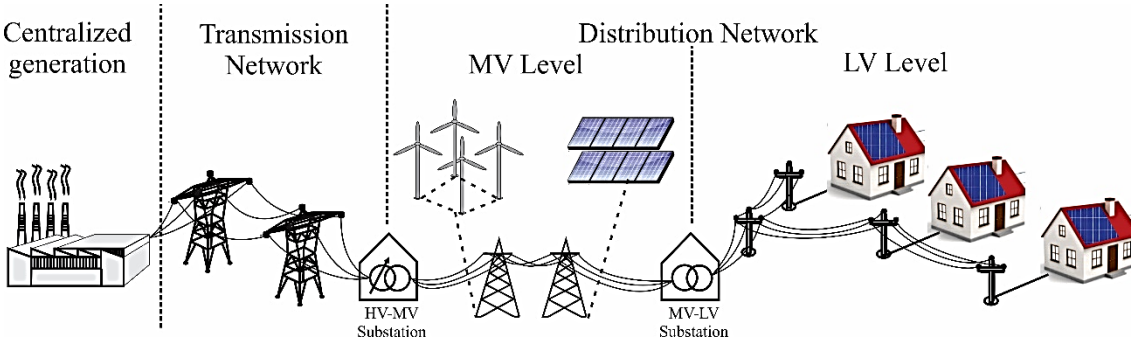

Figure 1.1: Main Components of an Electric Power Network [1]

The basic purpose of an electrical network is to interconnect the power sources and the load centres, so that the generated power can be transferred to the required destination with reliability and efficiency [2].

It has been observed that the transmission systems are getting burdened with the increased integration of modern load equipment. Furthermore, it has become difficult to operate with such loads optimally, hence giving rise to reliability and efficiency issues. Considering the load equipment is electronically controlled, it is sensitive to all kinds of power distortions. The power distortions have a deteriorating impact on the equipment, leading to higher production cost and reduced efficiency. Additionally, the power converters used as part of this equipment produce current harmonics which increase the overall current distortions in a system [3].

Customers connected to an electrical network are no longer regarded only as consumers, considering they can also generate and sell power via a deregulated system. Recently, the number of installed distributed generation sources (DGs) has increased. However, connecting a new DG to the network must meet certain power quality requirements which assures security of the system during power quality distortions. In order to comply with the power quality criteria, it is necessary to operate the transmission system in a stable and a protected way. To achieve this, the existing utilities and independent power producers (IPPs) are needed to stay committed and dispatch optimally [4].

Over the past few years, wind energy has become popular and competitive among all other conventional energy sources. An immense amount of research related to wind energy production has been conducted and has resulted in massive technological advancements. For instance the turbine design, generators, power converters and control algorithms have evolved significantly. From the electrical engineering perspective, power converters and generators are the two major components in a wind energy conversion system (WECS) [5]-[8].

Wind power generation has also been prevailing enormously compared to the other conventional energy sources. To ensure quality power transfer with maintained grid stability, utility requirements are fulfilled based on certain rules which are referred to as grid codes. These codes have also been updated over time depending on different prerequisites [9]-[10]. With reference to wind energy systems, the main points in a grid code include active and reactive power control for frequency and voltage regulation. It also deals with the power quality, harmonic oscillations, flickers, system security and fault ride through (FRT) compliances.

Wind turbine producers and wind farm operators have faced several problems while integrating wind farms into weak AC grids. For a weak AC grid with high X/R ratio, the primary goal is to maximise the active power transfer to the desired destination. However, due to lack of transmission capabilities and varying load characteristics, it is considered as a major inability of weak AC grids. Variation in load characteristics might also cause severe faults which could force the wind power plant to violate grid code requirements and even demand higher reactive power. Grid connection is usually the most important factor when it comes to wind farm planning. For selecting a point of common coupling (PCC), voltage level alone does not provide enough information. Therefore, grid strength is considered to be the deciding parameter which is numerically expressed as the value of short circuit ratio (SCR) or X/R ratio at a particular point. Grid strength has a direct relation with the network quality. The stronger the grid, the lesser the voltage change will be at the PCC. However, in case of a weak grid, regulation of active and reactive power impacts the voltage greatly [11]. From voltage stability perspective, a typical P-V curve is illustrated in Fig. 1.2 with respect to two X/R ratios '*2*' and '*10*'. It shows voltage variation slope at a point on the network when active power is demanded by the loads. To plot the curve,

load reactive power is kept constant as the load active power increases. It can be seen that in case of a weak grid, the voltage drops rapidly with the increase in load demand.

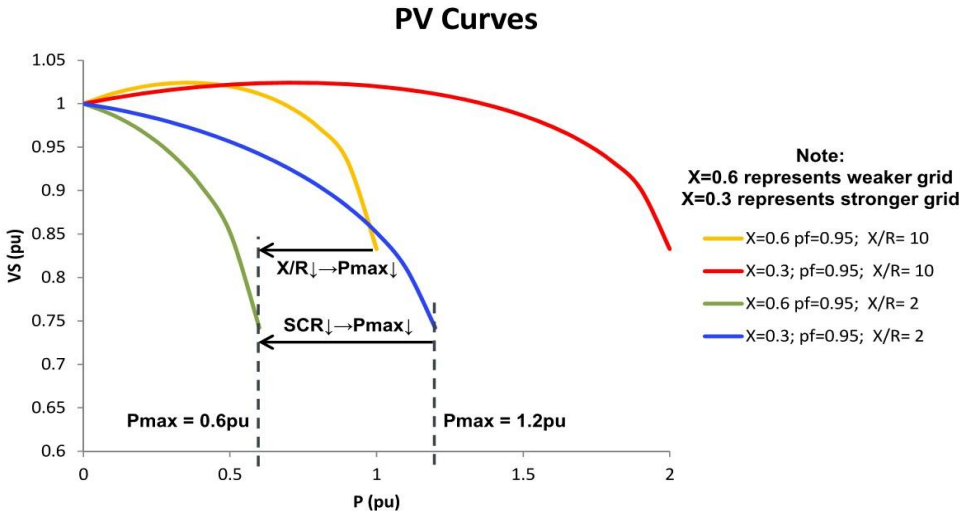

Figure 1.2: Voltage Variation dV due to dP [12]

Similarly, a V-Q curve is employed to demonstrate the reactive power margins of an AC grid in Fig. 1.3. The curves provide information about the stiffness of the grid based on the slope. For a strong grid, the curve has a low slope whereas high slope is for weak grids. The V-Q curves also assist in determining the amount of reactive power needed to achieve the required voltage level. Weak AC grids and wind farm connections are explained in chapter-2.

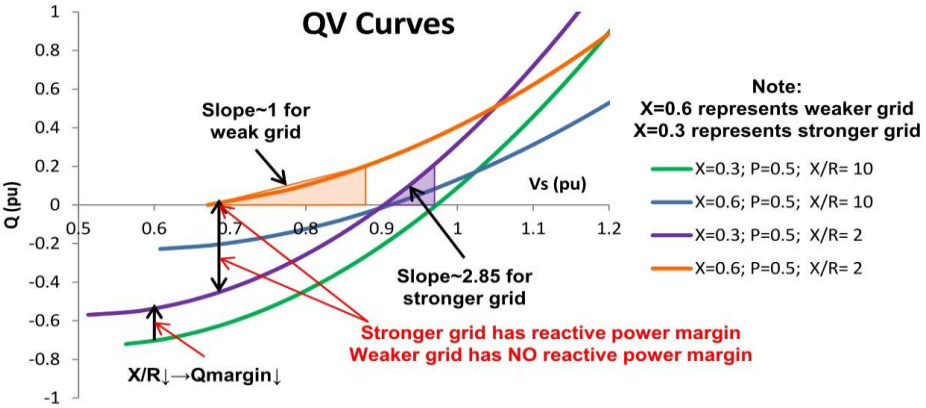

Figure 1.3: Voltage Variation dV due to dQ [12]

1.2 Reliability and Stability Considerations

The integration of wind energy systems into a weak AC grid can cause multiple issues related to reliability, stability and security of the power network. Furthermore, frequency deviations also occur which create transient conditions at the PCC. These issues can be overcome by selecting appropriate wind turbines and efficient control techniques.

Since the quality of a wind resource is an important factor, wind power plants are generally located in remote areas with high wind potential. These remote areas are usually less populated where the grids are usually considered as weak grids. Therefore, overall strength of the grid go hand in hand with the stability of the wind power plants (WPPs). For successful operation of a power system, the system stability particularly relies on voltage, frequency and angle stability. The major problem in weak AC grids is the unreliability of connection, especially when a sudden large disturbance occurs, leading to voltage and frequency offsets which eventually require a disconnection [13]. Hence, proper measures must be taken to deal with such instabilities.

For an improved wind farm connection, the control of a WECS can be subdivided into two control sections i.e turbine-control and grid-control. The turbine-control usually deals with the voltage and frequency control of the generator to ensure maximum power transfer. The grid-control majorly provides reactive power support for voltage compensation and limits the active power transfer during fault ride through conditions. By successfully implementing these controls, stable operations can be achieved from a WECS connected to weak AC grids [14].

1.3 Control System Response to Grid Faults

Grid faults can be classified into two categories, symmetrical (all three phases) and asymmetrical (single or double line-to-line/ground) faults. Furthermore, a short circuit can also lead to both fault types. During symmetrical and asymmetrical faults, positive sequence voltage decreases whereas negative sequence voltage appears in case of asymmetrical faults only. Usually, a fault occurs for a certain amount of time until the faulted part is cleared or disconnected from the network. The disconnection can be done easily through relays or circuit-breakers. However, it is

sometimes preferred to not disconnect immediately and wait for the equipment to restore (within few seconds). If a system recovers from a fault back to normal then it is usually with the assistance of a strong supervisory control system running at the back-end.

The reduced positive sequence voltage during a fault can lead the generating units (rotational machines) towards angle and frequency instabilities which also depend on the pre-fault power level, recovery period and strength of the grid [15]. On the grid side, connected loads also get affected during low voltage dips. The effect of low grid voltage can be reduced by compensating for the dip with the help of reactive power injection. Thus, stability can be improved by boosting the grid voltage back to the nominal value during a fault condition.

During asymmetrical faults, negative sequence voltage arises in the grid whereas positive sequence voltage does not drop to a severe level. The risk of instability in asymmetrical faults is comparatively lower than the symmetrical faults. However, with the rise of negative sequence voltages, over-voltages occur on the non-faulted phases. It further causes oscillations in the power system components such as generators and power converters. The problems created by asymmetrical faults are discussed in chapter-6. As a general rule of thumb, the impact of asymmetrical faults can be reduced by boosting the positive sequence voltage and attenuating the negative sequence voltage to zero.

According to recent grid codes for grid-connected wind turbines, ride through operation should always be implemented during grid fault conditions. The fault ride through (FRT) covers a broad fault-voltage range, covering zero voltage ride through (ZRVT), low voltage ride through (LVRT) and high voltage ride through (HVRT). Among all other grid codes, FRT is always a major concern for wind turbines producers and operators. After the fault is removed, when the grid voltage retains the nominal value, the power system's components experience transients. Therefore, it is necessary that the wind energy systems stay connected during a fault and properly restore when the fault is clear. In summary, the stability can be achieved by following the points mentioned below:

- During a fault, wind turbines must stay connected and balance the power after fault is cleared.

- During a symmetrical fault when positive sequence voltage drops down only positive sequence current should be injected to ensure maximum active power transfer into the weak AC grid.
- During an asymmetrical fault, positive and negative sequence currents must be injected to compensate for both phase and magnitude offsets.
- Seeing that the grid codes are not defined for any specific asymmetrical fault, reactive currents must be injected according to the agreement between the operator and supplier.
- During a fault period, only limited active power shall be permissible to implement the FRT.

1.4 Problem Statement

According to modern international grid codes, it is an important requirement for grid connected WECS' that the power converters must be able to regulate ±0.5% of the controlled voltage by injecting reactive power without requesting support from any external hardware/components, such as static synchronous compensator (STATCOM) or flexible AC transmission systems (FACTS) [16].

Considering that the weak AC grids are usually located in remote areas, type-4 (PMSG based) wind turbine configuration could be a useful topology to be installed there at MV level. Therefore, considering such a system with no external hardware support during unstable grid voltage conditions, the available conventional power converters must be utilized in such a way to inject the currents optimally. The optimal current injection should reduce the losses and achieve maximized power transfer into the grid to stabilize the voltage. Additionally, the control system must be robust enough to estimate the dynamic parameters of the network, detect the type of a fault and deal with it according to the defined current transfer limits.

1.5 Aim and Objectives

The study performed in this thesis relates to the efficient use of power converters in a PMSG based WECS integrated into a weak AC grid. The aim is to distribute optimal currents in order to optimize the power transfer during symmetrical and asymmetrical grid voltage conditions.

Considering the abovementioned aim as a case study, the main objectives to be achieved are set as:

- Develop technical understanding about a weak AC grid and investigate its characterization methods.
- Review different configurations of WECS and their connection problems with the weak AC grids.
- Study popular international grid codes and stability challenges for the integration of WECS into AC grids during fault conditions.
- Examine the parameters and the control model of a PMSG.
- Survey techniques for optimal power/current flow and control modes for the grid connection of a wind turbine.
- Investigate methods for sensing the unbalanced voltage conditions and estimating the dynamic parameters of a power network accurately.
- Develop algorithms which compute optimal reference currents required during symmetrical and asymmetrical voltages.
- Implement the complete system experimentally in the laboratory by combining the individual components and analyse the amount of power transferred to the point of common coupling (PCC).

1.6 Research Questions

The following research questions provided guidelines through the validation process of the optimal current injection techniques discussed in this thesis:

- Does any single solution for optimum power/current flow exist?
- What techniques are suitable to perform estimation of the dynamic parameters of a grid and how accurate are these?
- In case of a PMSG integrated into the grid, what would be the configuration of converters and what actions could be performed?
- Is an extra shunt converter always necessary to perform the voltage compensation?

- How a grid side converter can estimate the grid parameters and inject the optimal currents during balanced and unbalanced conditions?
- How the active and reactive power limits are defined for a grid fault to implement FRT?

1.7 Scope of the thesis

As mentioned in the objectives, the behaviour of a PMSG based WECS integrated into a weak AC grid is investigated during symmetrical and asymmetrical voltage conditions. Two current calculation algorithms are proposed and implemented for both voltage conditions. Control models of the machine side converter (MSC) and the grid side converter (GSC) are developed and implemented by using the PI controllers. During symmetrical voltages, positive sequence active current components are adjusted optimally to yield maximum output power.

It is to be noted here that the symmetrical 'faults' in particular are not discussed in this thesis because these have been studied in the past repeatedly and only appear 5% on an actual network compared to the asymmetrical faults [17].

Asymmetrical faults on the other hand, have not been studied extensively when it comes to weak grid conditions. During asymmetrical grid voltages, both positive and negative sequence currents are injected to implement FRT under the given circumstances.

Numerical analysis is performed based on Thevenin equivalent of the network where the time variant load impedances are considered. If the loads are considered as distributed network elements, then each line having an independent source would require different amount of currents based on the load nature.

Since a weak AC grid is under discussion, the wind turbine is considered to be located in a remote area connected to medium voltage level utility. For the lab-setup, a downscaled (3.3kW) WECS and a weak AC grid are emulated to perform the experimental investigations. The types of asymmetrical faults considered in the thesis are single-line to ground (SLG) and double-line to ground (DLG) faults which occur commonly in a transmission system.

1.8 Contribution of the Thesis

In this thesis, per phase control model of the PQ variation technique is proposed for the grid impedance measurement. Based on that, two modified current calculation techniques are implemented to optimize the power transfer of a PMSG-based WECS integrated into a weak AC grid during symmetrical and asymmetrical grid voltage conditions.

During symmetrical grid voltages, the first technique derives a generalised algorithm for calculating optimal currents for a Thevenin equivalent network which assures minimum distribution losses. The technique is validated on a real time grid-tied PMSG based WECS. Simplified calculations are applied by evaluating the system in a weighted domain where currents and voltages are weighted with respect to the line resistances of the network. This technique allows the system to inspect the distribution line, detect changes in the load and redistribute the optimal currents to achieve maximized power transfer into the network.

During asymmetrical faults, the second technique calculates and allows injection of the coordinated currents based on impedance of the Thevenin equivalent network. It does not only define the new active/reactive current transfer limits but also enhances the power factor of the system during a fault. It limits the incoming active power from the generator and implements FRT by regulating the DC link voltage with the help of MSC. The GSC on the other hand, injects coordinated currents at the same angle as that of the estimated impedance but within the defined current transfer limits.

The power optimization solution is provided by exploring, identifying and improving the existing features of the GSCs. Moreover, awareness is provided about the general power theory related to real power systems and the reactive current injection requirements. In addition to investigating the weak grid's pertinent issues, this thesis also discusses GSCs active and reactive current transfer limits under the given conditions.

1.9 Organization of the Thesis

The organization of the thesis is as follows:

Chapter 1: Introduction, presents background of an electric network and its fundamental components. It discusses the impact of integration of modern non-linear loads into the network in terms of reliability and efficiency. It also reviews the integration of distributed generation systems and the related power quality requirements. In particular, a wind energy conversion system and its utilization during grid fault events is explained. Motivation behind the project is clarified which states the precise reasons of the research being conducted. Objectives of the project are also defined which will be achieved with the help of research questions. The chapter also includes overall scope and scientific contribution of the project.

Chapter 2: Integration of Wind Farms into Weak AC grids, provides detailed information on weak AC grids and their characteristics. Different wind turbine configurations and wind farm connections are described thoroughly. The factors affecting the selection of PCC for wind farm integration are explained. Two widely-used international grid codes are highlighted along with their compliances for both symmetrical and asymmetrical faults. Stability challenges of the WPPs connected to weak AC grids, the FRT techniques, their capability and implementation are also part of this chapter.

Chapter 3: Permanent Magnet Synchronous Generator based Wind Energy System, explores wind turbines basic concepts. A permanent magnet synchronous generator (PMSG) based WECS together with the control models of machine and grid side converters are analysed. The generator parameters, total power generation and associated power losses of the system are investigated.

Chapter 4: Grid Impedance Estimation, reviews conventional and modern impedance estimation techniques. The PQ variation technique is discussed in the chapter and a mathematical analysis is employed to evaluate its performance. A modified approach is then

proposed and implemented with respect to a grid-tied inverter. Experimental investigations are also performed to estimate decoupled load impedance on each phase.

Chapter 5: Optimal Current Injection during Balanced/Symmetrical Grid Voltages, starts with a review on the optimal power flow, its definition and characterization as reported by different authors in the past. Followed by the definition, a historical background of optimal power flow methods is discussed. Classical methods along with the recent techniques are summarized. According to general power theory, the definition of apparent power is also reviewed and a unique definition of apparent power is proposed with the help of optimal current calculation method. The vector representation and the optimal supply currents are determined for the WECS under consideration connected to the Thevenin equivalent of a weak AC grid. At the end, numerical and experimentation validations of the abovementioned method are presented in comparison with the conventional methods during symmetrical grid voltage conditions.

Chapter 6: Coordinated Current Injection during Unbalanced/Asymmetrical Grid Voltages, highlights the causes and problems during asymmetrical grid voltage conditions. A case study is performed in this chapter by implementing asymmetrical faults on a type-4 WECS integrated into a weak AC grid. The information from the estimated dynamic parameters of the network is utilized to implement current transfer limits, and coordinated currents are injected to support LVRT. Dual sequence current injection is applied to reduce the negative sequence oscillations in the system. Experimental validation of the analysis is also presented in the chapter.

Chapter 7: Conclusion, summarizes the thesis and outlines the conclusions from the research work. It also presents suggestions for future extension of the project.

1.10 References

[1] https://ca.audubon.org/conservation/energy-storage-and-electricity-grid [Accessed Online: Dec 2016]
[2] B. Mahdad, T. Bouktir, and K. Srairi, “Strategy of Location and Control of FACTS Devices for Enhancing Power Quality,” *IEEE Mediterranean Electrotechnical Conference*, pp. 1068–1072, 2006.
[3] T. Duong, Y. Jiangang, and V. Truong, “A new method for secured optimal power flow under normal and network contingencies via optimal location of TCSC,” *Int. J. Electr. Power Energy Syst.*, vol. 52, no. 1, pp. 68–80, 2013.
[4] F. Iov, A. D. Hansen, P. Sørensen, and N. A. Cutululis, “Mapping of grid faults and grid codes,” DTU Library 2007.

[5] M. Mohseni and S. M. Islam, “Review of international grid codes for wind power integration: Diversity, technology and a case for global standard,” *Renew. Sustain. Energy Rev.*, vol. 16, no. 6, pp. 3876–3890, 2012.
[6] V. Yaramasu, B. Wu, P. C. Sen, S. Kouro and M. Narimani, "High-power wind energy conversion systems: State-of-the-art and emerging technologies," in Proceedings of the IEEE, vol. 103, no. 5, pp. 740-788, May 2015.
[7] I. Erlich, F. Shewarega, C. Feltes, F. W. Koch and J. Fortmann, "Offshore Wind Power Generation Technologies," in Proceedings of the IEEE, vol. 101, no. 4, pp. 891-905, April 2013.
[8] F. Blaabjerg and K. Ma, "Wind Energy Systems," in Proceedings of the IEEE, vol. 105, no. 11, pp. 2116-2131, Nov. 2017.
[9] M. Altin, Ö. Göksu, R. Teodorescu, P. Rodriguez, B. B. Jensen, and L. Helle, “Overview of recent grid codes for wind power integration,” *Proceedings of the International Conference on Optimisation of Electrical and Electronic Equipment, OPTIM*, pp. 1152–1160, 2010.
[10] Clausen and Niels-erik, “Planning and Development of Wind Farms : Environmental impact and grid connection Wind Energy,” 2013.
[11] A. Adib, B. Mirafzal, X. Wang and F. Blaabjerg, "On Stability of Voltage Source Inverters in Weak Grids," in IEEE Access, vol. 6, pp. 4427-4439, 2018.
[12] https://www.coursehero.com/file/24910402/18-Antonio-Martinezpdf/ [Accessed Online: June 2017]
[13] R. Castel, “Connection of offshore wind farms to the grid in Europe and Brittany,” MSc Dissertation, Royal Institute of Technology, Sweden, 2010.
[14] Q. Salem and I. Altawil, “Stability Study of Grid Connected to Multiple Speed Wind Farms with and without FACTS Integration*,” Int. J. Electron. Electr. Eng., vol. 2, no. 3, pp. 168–174*, 2014.
[15] M. M. Shabestary and Y. A. I. Mohamed, "Advanced Voltage Support and Active Power Flow Control in Grid-Connected Converters Under Unbalanced Conditions," in IEEE Transactions on Power Electronics, vol. 33, no. 2, pp. 1855-1864, Feb. 2018.
[16] A. Ellis, R. Nelson, E. Von Engeln, R. Walling, “Review of Existing Reactive Power Requirements for Variable Generation” *IEEE Power and Energy Society General Meeting*, 2012.
[17] J. Mohammadi, S. Afsharnia, S. Vaez-Zadeh and S. Farhangi, "Improved fault ride through strategy for doubly fed induction generator based wind turbines under both symmetrical and asymmetrical grid faults," in IET Renewable Power Generation, vol. 10, no. 8, pp. 1114-1122, 2016.

Chapter 2
Integration of Wind Farms into Weak AC Grids

2.1 Introduction

Over the past few years, wind power generation has attained popularity due its renewable nature and decrease in cost per kWh compared to other conventional energy sources. To extract wind energy more efficiently and reliably, many configurations of the wind turbines have been introduced. The design of wind farms and selection of wind turbine generators must consider the strength of an AC grid to which it needs to be connected. Most of the wind energy turbines are located in remote areas which are typically far from the bulk energy consumption centre. In other words, these wind turbines need to be designed to operate adequately with weak AC grids. This chapter outlines the background of wind energy systems and their integration into weak AC grids. The technical challenges, design considerations and turbine configurations are studied. Integration methods and control parameters are reviewed according to international grid codes. Stability issues of integration of wind turbines during fault conditions and methods to improve the fault ride through, are also discussed.

2.2 Weak AC Grids

The term 'weak grid' can be defined as a grid which is susceptible to a sudden change in the operating conditions. It may also be characterized as a grid where voltage fluctuations arise with any major changes in the conditions or whenever the designed load exceeds its limits. On the other hand, a strong grid does not allow these changes to overcome the grid stability as it offers robust capability to counter any fluctuations and maintain the balanced grid conditions [1]. With reference to wind farms, grid strength at a specified point is determined by its line impedance

and the kinetic energy stored in the connected generator. Another useful representation is the short circuit ratio (SCR) which is the ratio between short circuit power (S_{sc}) and the rated source power (P_s) at the point of common coupling (PCC) [2]. It is noteworthy that SCR does not indicate the healthiness of an entire network, instead it measures the strength at one specified point only. This means that a network with multiple generators would have different SCR values at each connection point [3]. If the grid is assumed to be modelled as an equivalent Thévenin circuit, comprising a single Thevenin voltage V_{th} and Thevenin impedance Z_{th}, then, the SCR at the PCC can then be expressed as [4]:

$$SCR = \frac{S_{sc}}{P_s} = \frac{V_{PCC}{}^2}{Z_{th} P_s} \tag{2.1}$$

Where, S_{SC} is the short circuit power and P_S is the wind turbine power delivered by the turbine to the PCC. Medium voltage (MV) AC grids with SCR value below '*5*' are usually considered to be weak grids [5]-[6]. According to the German VDN grid code [7], a strong grid is implied as the one where the S_{SC} should remain greater than six times the nominal active power before and after the fault is cleared. In Danish grid code [8], a grid with SCR value above *10* is considered strong. However, in other parts of the world, with increasing number of installations of renewables, the SCR value can go even lower than *2*. A grid is considered weak when [9]-[13]:

- a high-impedance line is connected to a strong network and expanded with long lines with overall low $S_{SC.}$
- a network is overloaded with renewable energy sources replacing conventional power plants (CPP), resulting in lower $S_{SC.}$
- a wind power plant (WPP) is connected far from the centre of power generation through long distance lines and the bus has low $S_{SC.}$
- a WPP with high internal impedance is connected and as a result S_{SC} decreases even further.

Weak grids possess low SCR, high impedance and poor reactive power support [14] which means that SCR value is inversely proportional to the inductive impedance of a bus. Today, the tendency of a low SCR grid connection has become more of an important consideration when it comes to

integrating WPPs into AC grids. Therefore, SCR can also be characterized as a grid's capacity to retain its voltage level during any load or source dynamic event at the PCC.

2.3 Wind Energy Conversion Systems (WECS) and Weak AC Grids

The two major components of a WECS are the generator and the power converter. Both can be utilized in multiple combinations to achieve wide variety of different WECS configurations [15]-[17].

2.3.1 Type-1 Fixed Speed (SCIG) Configuration

The oldest wind turbine technology used is a squirrel cage induction generator (SCIG) based WECS. In type-1 configuration, the generator is usually integrated into the network with the aid of a soft starting device and a transformer as shown in Fig. 2.1 [18]. Its speed can only vary within 1% of the synchronous speed of the corresponding wind speed and hence called fixed speed configuration of WECS. Since it is directly connected to the grid without a converter, it requires a gear box to match the speed of the rotor to that of the wind turbine, which makes it a simple, robust and inexpensive technology. However, it offers a very limited control ability for the reactive power drawn from the grid. Also, it gets mechanically stressed under severe fault conditions at the grid and requires additional shunt-connected converters such as STATCOMs to comply with the grid code [19]. Despite all the above mentioned shortcomings, this configuration has been used over the years and is still functional in different parts of the world.

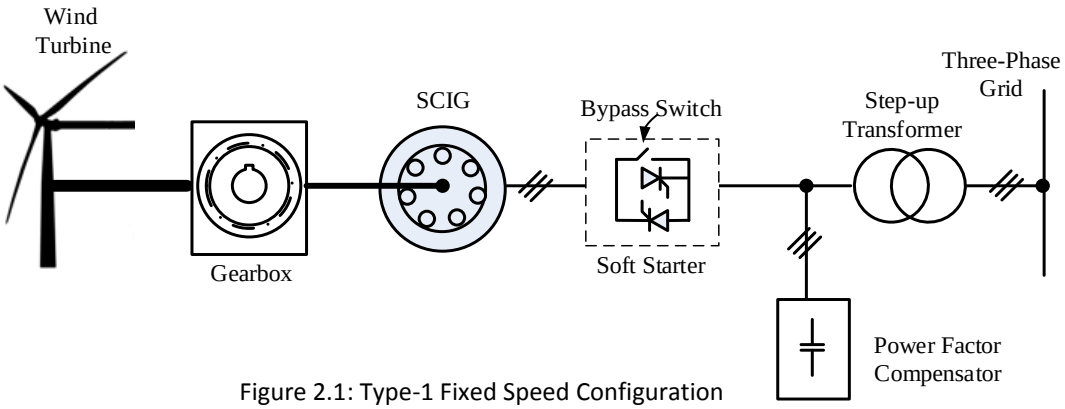

Figure 2.1: Type-1 Fixed Speed Configuration

2.3.2 Type-2 Semi-Variable Speed (WRIG) Configuration

The variable speed operation of the wind turbines is the most popular feature of WECS technology, which assists in enhanced energy capture from the wind and lowers the mechanical stress on the components during high wind gusts. It also cut down on the upkeep requirements and hence expands the life span of gearbox and bearings.

The type-2 configuration uses a wound rotor induction generator (WRIG) with a partially rated (10%) converter (no slip power recovery) as shown in Fig.2.2:

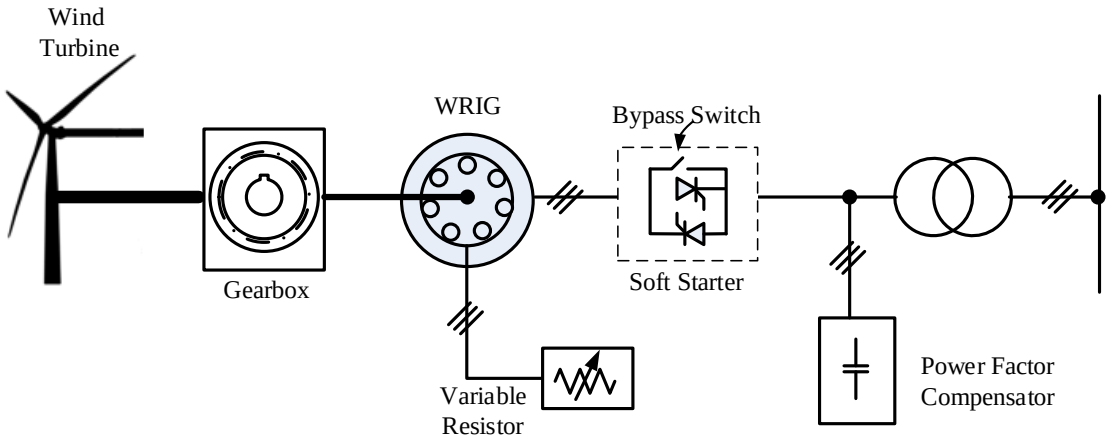

Figure 2.2: Type-2 Semi-Variable Speed Configuration

The changing rotor resistance influences the torque-speed relationship of the generator and hence variable speed can be achieved. The rotor resistance is changed with the help of partially rated converter and a ±10% speed variation can be implemented. With variable speed, more power can be extracted from the wind but at the same time more energy losses can also occur on the rotor resistance.

2.3.3 Type-3 Semi-Variable Speed (DFIG) Configuration

With the doubly fed induction generator (DFIG) configuration, the slip power is transferred to the PCC by means of stator and rotor windings. The slip power of DFIG is up to 30% of the rated power, therefore a partially rated converter is employed for the rotor side control. It also uses a gearbox and does not always need a soft starter [20]. As shown in Fig. 2.3, with the use of power

converters, the energy can be controlled in both directions. This configuration allows high speed wind capture and improved overall wind conversion efficiency. Due to the use of a partially scaled power converter, it offers limited fault ride through (FRT) capability. Furthermore, the inclusion of gear box increases the overall size and cost of the turbine as well as the requirement of routined maintenance of the slip rings and brushes. These wind turbines are usually employed in areas where easy access is available for regular maintenance.

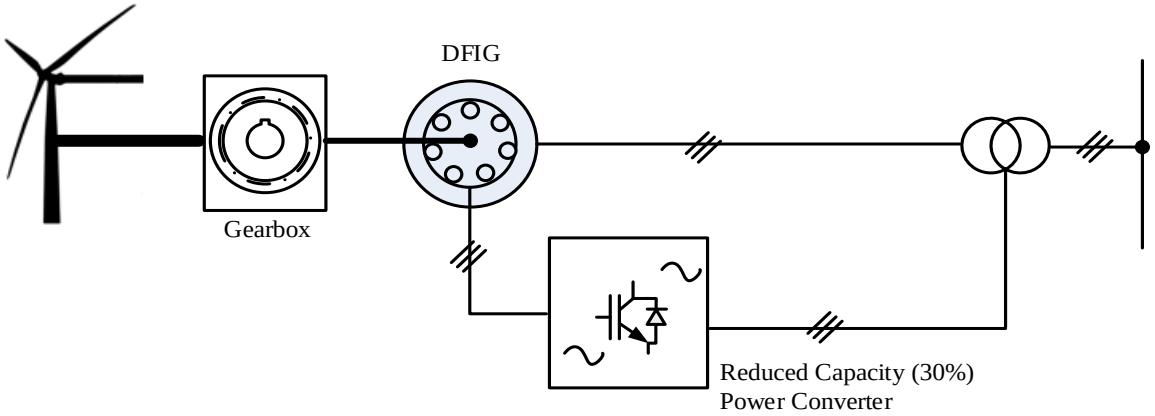

Figure 2.3: Type-3 Semi-Variable Speed Configuration

2.3.4 Type-4 Full-Variable Speed (PMSG) Configuration

In type-4 WECS, performance can be improved by using full scale power converters (100%). Full-scale converters allow the system to operate at full speed range and stay decoupled from the grid. Considering that the converter rating is the same as that of the generator, with the increase in its sizes, the power losses, cost and overall complexity of the system also increases. The most common configuration is shown in Fig. 2.4, where a PMSG is connected to the grid through back-to-back converters. The full-scale power converters help the system to implement reactive power compensation along with the smooth grid connection. PMSG based turbines also offer efficient wind energy conversion compared to other WECS [21]-[22]. The slip ring brushes and gearbox can be avoided due to high number of pole pairs. This configuration also offers best FRT without using any other ancillary support.

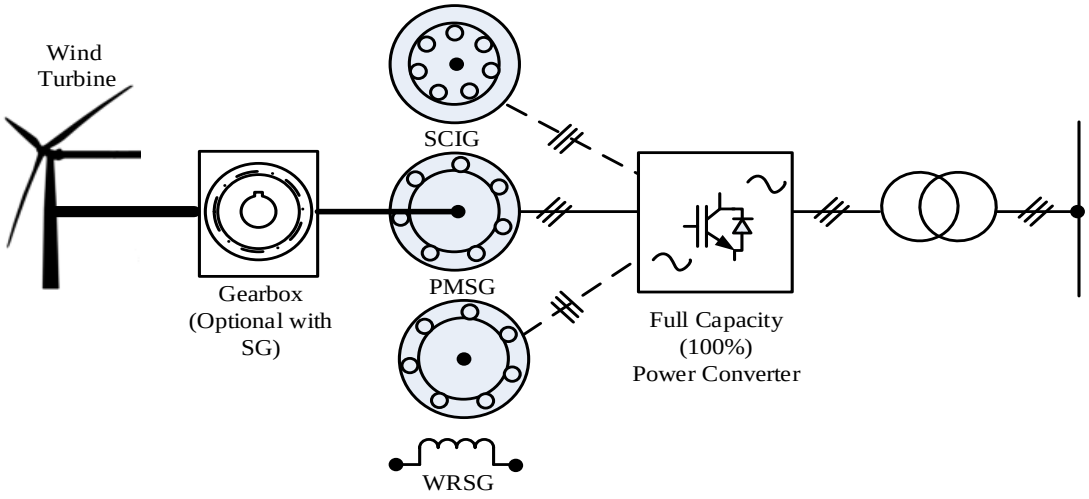

Figure 2.4: Type-4 Full-Variable Speed Configuration

Weak AC grids cast a considerable impact on the performance of wind turbines, especially during fault conditions on the grid side. Therefore, it is important to consider this impact when designing or selecting a wind turbine system. Fixed speed turbines cannot compensate for the large voltage variations and power fluctuations without having any external support [23]-[24]. Variable speed turbines are capable of operating under different wind situations and extract maximum power by implementing maximum power point technique (MPPT). MPPT is usually applied when the wind speed is less than the rated speed of the generator. In case of high wind speed, pitch control is employed to limit the flow of excessive power into the grid. Weak AC grids are more susceptible to grid faults which are usually in the form of voltage variations. In case of a deep voltage dip at the PCC, there will always be less power demand and to limit it, pitch control is a common solution. Power converters also allow the WECS to regulate the active/reactive powers to and from the weak AC grid which assists in improving the stability of the wind turbines [25]. This thesis contains study on the type-4 wind turbine and its integration with a weak AC grid. It also discusses optimal power regulation under symmetrical and asymmetrical grid voltage conditions.

2.4 Connection of Wind Farms with Weak AC Grids

Since the quality of a wind resource is an important factor, wind power plants are generally located in remote areas with high wind potential. Furthermore, these remote areas are less populated where the grid does not always have to be strong [26]. A weak grid connected to a

wind farm acts as a power supply system which absorbs the wind energy depending on its capacity and not on operating limits of the generator [27]. The main factors affecting the selection of a PCC for wind farm integration are SCR, X/R ratio, interaction of voltage source converters (VSCs) and gain of the controllers. These factors have a direct impact on the stability and must be considered carefully during wind farm design.

2.4.1 Short Circuit Ratio (SCR)

The SCR serves as the capability of an AC grid to allow the maximum amount of active power without effecting its stability. When selecting a PCC, the SCR is used to assess the grid strength. A PCC with low SCR value offers decreased voltage stability with the injection of both active and reactive powers [28]. With respect to wind farm connection, a grid with low SCR also limits the transfer of active power unless reactive power is provided through an external source or by increasing the converter power rating [29]. Fig 2.5 illustrates the relation between the PQ capabilities of the wind turbine generator into the AC grid. It can be seen that at SCR=1.1, it is not possible to transfer the rated active power if reactive power support is not provided.

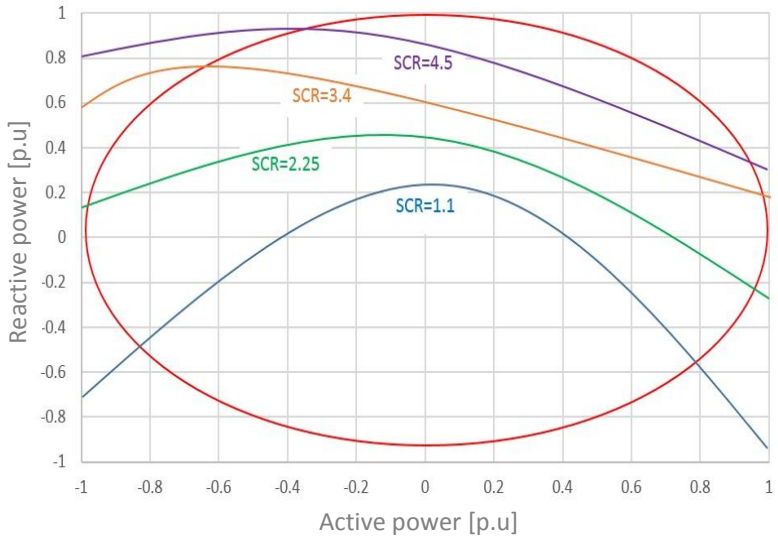

Figure 2.5: PQ Graph for different SCR Values

A low SCR also leads to poor voltage regulation due to large voltage deviations, especially in the case of large wind farms. To deal with voltage instabilities, voltage source converters (VSCs) are connected to the weak AC grids. VSCs are robust and can implement vector control to quickly

track the voltage references with the help of controllers [30]. By using VSCs, one important issue that usually arises is the DC-link voltage instability. DC-link voltage variations are usually linked with the performance of the phase-locked loop (PLL). In case of low SCR AC grid, if a severe voltage fault occurs, the system might lose its synchronism with the fundamental frequency after the fault is cleared. This phenomenon is called loss of synchronism (LOS) [31]. To overcome such situations, controller gains of the PLL need to be calculated carefully. Fast voltage and angle recovery with unstable controller gains will make it difficult for the PLL to track the AC voltage accurately, which may force the grid side control towards instability. Transient stability is another important feature of the wind farm modelling when connected to a weak AC grid. If a high voltage dip occurs at the PCC, wind farms are required to offer low voltage ride through (LVRT) and support the grid by injecting reactive power [32]. However, due to low SCR, wind farms offer a very limited capacity to maintain the stability.

2.4.2 X/R Ratio

The X/R ratio is another design criterion for wind farms. It is the ratio between reactance and resistance of a grid impedance. For an AC grid with certain SCR at the PCC, there might be voltage fluctuations due to varying X/R values. This shows that the occurring voltage variations are a function of active/reactive power flow and the grid impedance, represented as X/R ratio. High X/R ratio of the grid impedance possess high reactance and can be called an inductive grid, where grid voltages readily go beyond the stable region in case of a fault [33]. High X/R ratio is also sensitive to the flow of active power and limits its flow, whereas smaller X/R (resistive grid) ratio offers maximum transfer of active power. However, the more the transfer of active power through a resistive grid, the higher are the grid losses. Therefore, a reactive power support is required to regulate the AC grid within stable limits [34]. For more insight about the maximum active power transfer limit, a case is considered where SCR=1 with X/R ratios varied between *1-100* and is shown in Fig. 2.6.

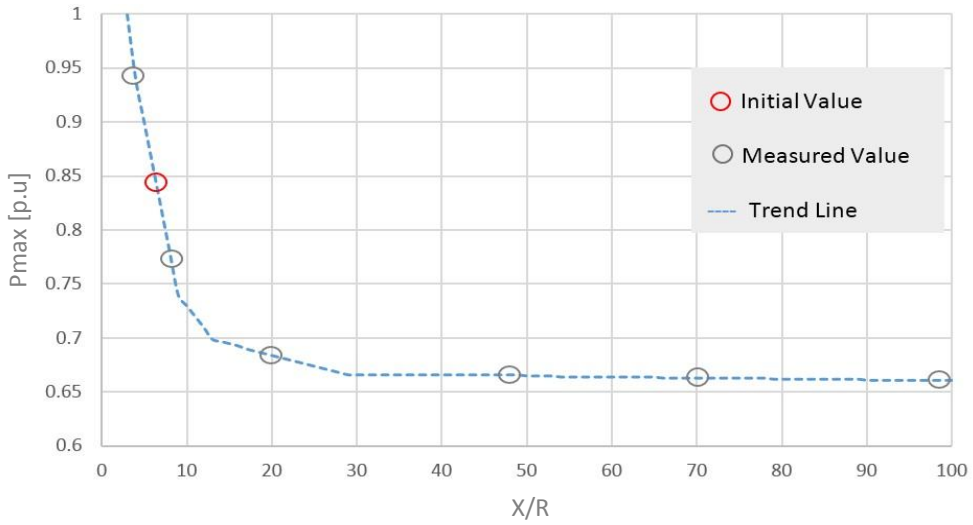

Figure 2.6: Maximum Transferable Power w.r.t X/R Ratio

From Fig. 2.6, it can be seen that the smaller the X/R ratio, the higher the maximum transferable active power is. However, it also results in more power losses with high P_{loss} slope as shown in Fig. 2.7. Thus, increasing the resistance to reduce the overall X/R ratio is not a feasible solution and therefore extra measures are needed to be taken to implement the voltage stability in case of a grid fault.

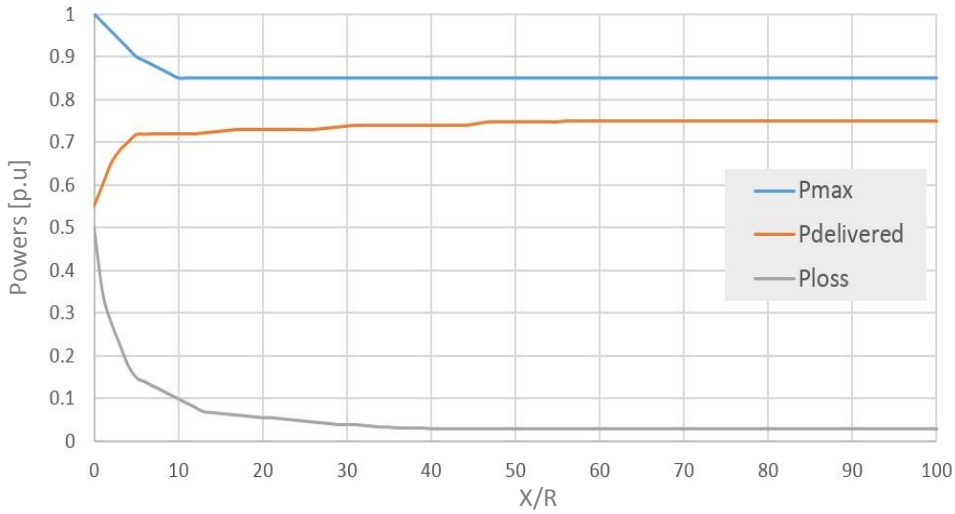

Figure 2.7: Power curves vs X/R Ratios

The X/R ratio can pose a great influence on the power quality of a wind farm. With reference to a weak grid, X/R ratio of *1.3-2.8* is considered suitable for wind farm integration [35].

2.4.3 Interaction between the VSCs and the AC Grids

Interaction of VSCs with a weak AC grid is another important technical consideration when modelling a wind farm. The vector control technique has become a conventional strategy over the years to control the VCSs. With vector current control technique, there are usually two control loops, inner and outer. The performance of inner loop predominantly depends on the outer loop interface, PLL behaviour and the controller parameters.

2.4.3.1 PLL Behaviour

With reference to grid interaction with the VSCs, grid voltage and phase angle are the variables which need to be monitored at all the times. To synchronize any generating system with the grid, multiple control schemes are devised. The control scheme tracks the angle information and achieves synchronization between the AC grid and the converter voltages. This strategy is based on phase locked loop (PLL) principle. The PLL scheme has evolved over the years to be used under different grid situations. It offers fast and accurate synchronization based on the implemented control technique. The classic PLL detects the angle and frequency within the same control loop. This could lead to delays in synchronisation and eventually the system would become unstable. To avoid this, efficient techniques are required for the detection of voltage and frequency variations during unstable grid voltage conditions [36]-[37]. PLL control is usually designed for fast synchronisation. However, in case of a weak AC grid, this could deteriorate the stability. On the other hand, slow performance of PLL could result in achieving better stability and increased power transfer [38]. However, this can also impact the dynamics of the control and can cause large phase angle deviations between the PLL and the PCC voltage.

2.4.3.2 Controller Parameters

The conventional control scheme which has been widely used in industries is vector control strategy and is based on its PI controller gain values. For better control dynamics and to reduce the steady state error, proportional and integral gain values are required to be calculated. Systems with different designs are modelled for distinctive controller gain values. Since weak AC grids are usually considered unstable, they require coordinated control. The gain values have a

significant impact on the overall performance of the system. For integration of wind farms with a weak AC grid, reduced PLL gains are suggested [39]-[40]. However, high gain values are being employed recently to apply voltage control for fast power ramp and stable active power output [41]. The control system must be designed to support stable operation under every AC grid situation. The integration between VSCs and AC grids depends largely on the grid strength. For instance, the current control loop of a converter can get destabilised due to high grid impedance and hence produce resonance in the system [42].

2.5 Grid Code Requirements

In this section grid code requirements are discussed in relation to wind turbine integration with weak AC grids. The two most well-known grid codes— German VDN and ENSTO-E— are reviewed in terms of their standards. The German VDN is a well-established code and has been followed in different parts of the world. European network for transmission system operators for electricity (ENSTO-E) has recently designed a grid code which is prevalent in most of the European countries [7][43].

Considering the grid code compliance under fault conditions. Both grid codes have introduced FRT requirements. According to German VDN, the wind power producers (WPPs) are expected to stay connected even if the grid voltage drops down to zero as shown in Fig. 2.8(a). At that point, reactive current injection (RCI) is required in proportion with the change in grid voltage. With reference to Fig. 2.8 (b), the gain margin is set between 0-10 with the default value of *2* i.e for each percent drop in the voltage, double the percent of reactive current should be injected. Therefore, when the grid voltage drops below 50%, 1pu reactive current needs to be injected. Meanwhile, limitation on active current is also applied to make sure that the total current magnitude does not exceed the rated value. The FRT code requirement is usually defined for the PCC of a WPP, whereas RCI is provisioned at the turbine output to support different WPP stability solutions.

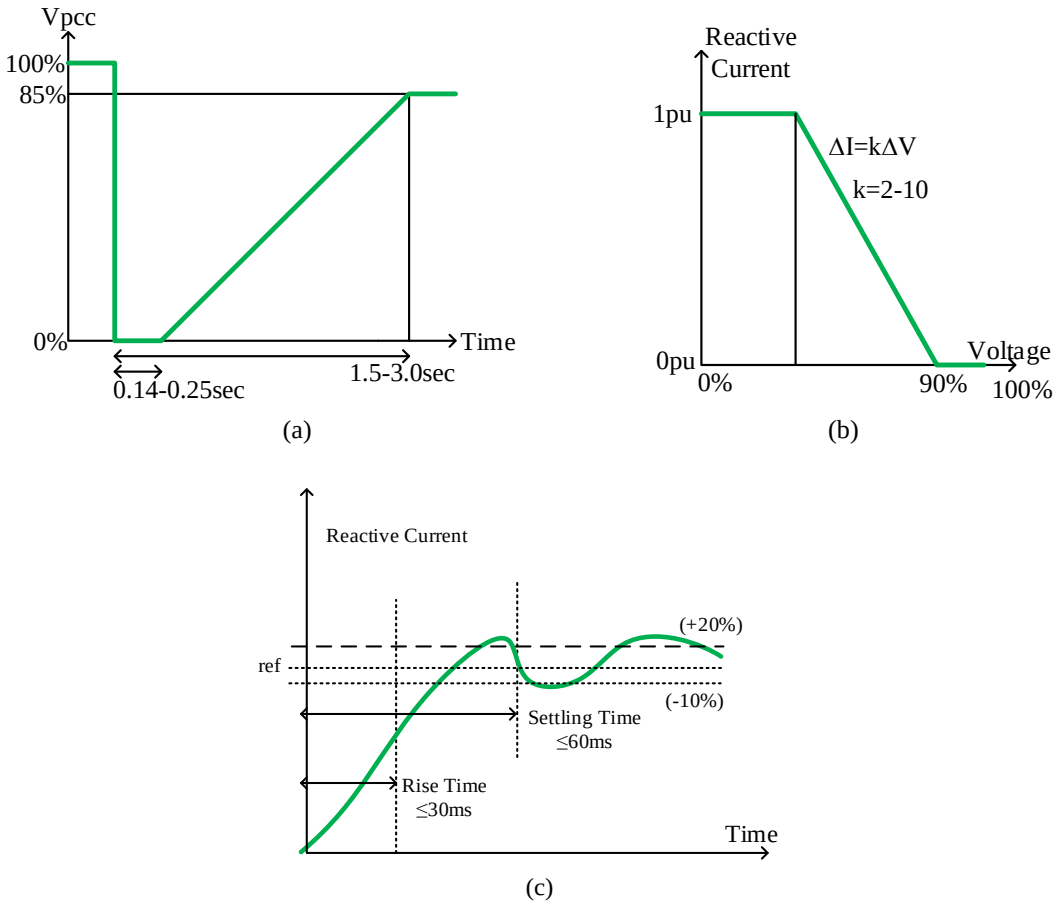

Figure 2.8: German Grid Code Requirements (a) FRT, (b) RCI , (c) RCI Step Response Requirements [7]

During post-fault recovery period, RCI is required to be continued for 500ms and at the same time active power ramp-up will be 10-20% of the nominal value. Hence German VDN requires the WPPs to carry out proportional voltage control scheme at the PCC and behaves similarly to conventional power plants (CPP).

Fault requirements of ENSTO-E are similar to German VDN with a few differences. For example, as shown in Fig 2.9, the ENSTO-E requires the WPP to stay connected to the grid even if the voltage drops down to zero. Furthermore, with respect to step response of RCI it is stated that the WPP or a single WT should be able to provide 2/3 of additional reactive current for the time period specified by the transmission system operator (TSO). This time period should not be less than 10ms and the additional reactive current should be injected with an accuracy of 10% [43].

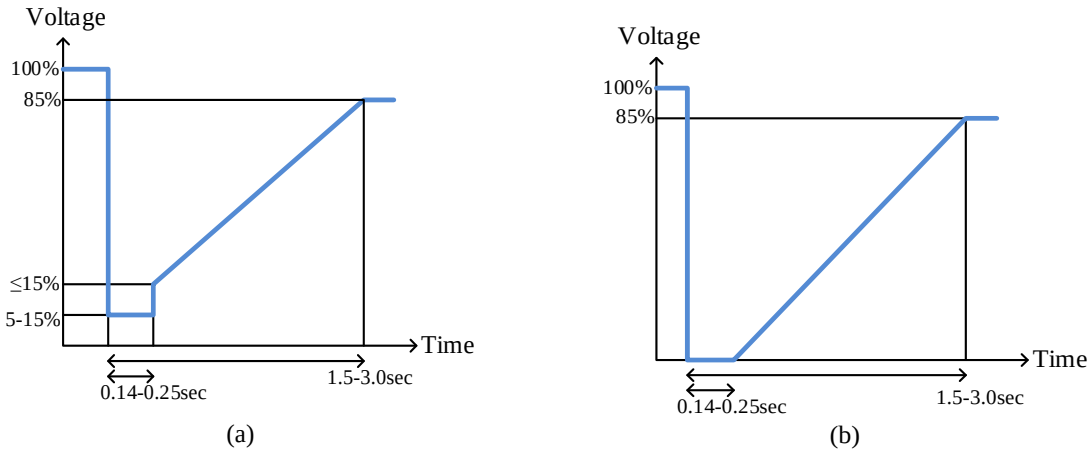

Figure 2.9: ENSTO-E Grid Code FRT Requirements (a) <110kV (b) >110kV [43]

In relation to the asymmetrical faults, not much explanation is provided in VDN on how to calculate the required reactive current. However, 40% of the maximum rated current is allowed to be injected [7]. In ENSTO-E the amount of required reactive current is decided between the TSO and the supplier.

From the two grid codes, it can be stated that the asymmetrical faults are not considered exclusively because of its less severity and less impact on the power system stability [44]. However, the asymmetrical faults do occur frequently. From the stats given in [45] symmetrical faults only appear 5%, compared to asymmetrical faults i.e in the form single line to ground fault 70%, line-to-line fault 15% and double line to ground fault 10%.

In summary, the abovementioned grid codes require the WPP to stay connected during voltage faults irrespective of the nature of fault. For both symmetrical and asymmetrical severe voltage faults, the WPP is required to inject positive sequence reactive current in proportion to the voltage deviation.

Similarly, weak AC grid terminology is also very much prevalent in the society but not discussed specifically in any of the grid codes. In this thesis, weak AC grid is discussed as a case study to address the power distribution issues in the rural areas where small wind turbines are connected. Both symmetrical and asymmetrical grid voltage conditions are considered, and optimal current injection is employed to ensure maximum power transfer into the network.

2.6 Stability Challenges in WPP Integrated to Weak AC Grids

Stability of the WPPs connected to weak AC grids depends on the overall strength of the grid. Most of the grid codes are regulated for the transient situations in the network. For instance, during FRT the WPP needs to stay connected to the AC grid and ensure minimum power losses. The FRT technique provides AC grid support by regulating the voltage and frequency operating ranges. If a WPP is connected to a weak AC grid, there might be chances of disconnection and power loss which can lead to system instability. In this case, a robust control technique is required to implement FRT and provide support for pre and post fault scenarios. The technical challenges which can occur during transient conditions and their stability solutions are discussed below:

2.6.1 Implementation of FRT Techniques

FRT is the ability of a WPP to sustain any fault situation on the grid side. It is also required to improve the WPPs performance during and after the grid fault is cleared. To implement FRT, reactive power is needed to be injected to support the grid voltage. The control is implemented either with the help of existing power converters of the WECS or an additional shunt connected device.

2.6.1.1 FRT with Power Converters

Full power converters are usually preferred to provide FRT support. These converters are programmed to perform coordinated power injection, based on the coordination of active and reactive powers so that the current magnitude I_{mag} remains within the maximum rated limits. For a grid with low X/R ratio, more of active current I_d is injected to support the active power, whereas for high X/R ratio reactive current I_q is prioritised to keep the coordination. The maximum coordinated current magnitude can be expressed as [46]:

$$I_{\mathrm{mag}} = \sqrt{I_d^2 + I_q^2} < I_{rated} \tag{2.2}$$

For different wind turbine systems, multiple control techniques have been devised and implemented by shifting the roles between the attached back-to-back converters. The grid side converter (GSC) usually handles the power injection into the grid. The DC link voltage regulation

could be performed by both machine side converter (MSC) or the GSC. To limit the active power transfer from the WPP to the AC grid during fault, DC link voltage regulation is usually achieved with the help of MSC [31]. At the same time, MSC can also be used to regulate the operation of the wind generator and achieve MPPT. The performance of the converters is detailed further in the section 2.6.2.

2.6.1.2 FRT with External Devices

It must be noted that to achieve FRT, higher reactive current injection is needed. This requirement particularly becomes serious in case of a weak AC grid, where dV/dQ sensitivity is high. It is also known that the full-scale converters have limited current capabilities confined within their ratings. For that reason, supplementary support is sometimes required for higher current injection. Furthermore, this support is not only needed for higher current injection but also required to handle the surplus power generated from the wind turbine [47]. To realise this, the most common practices are discussed below:

- Crowbar resistor and DC chopper

To control the surplus power in a type-3 WECS, a crowbar resistor is used. Once a fault is detected, the crowbar gets activated and the surplus power dissipates through it [48]. During the procedure the MSC remains blocked and the rotor windings of the DFIG are short circuited with the help of the resistor. The value of the resistance is selected to make sure that the fault current reduces to the nominal value. For improved dynamic response, the crowbar is switched-in using a controlled switch which could be an IGBT or a thyristor. Another possible application is to use a DC chopper in conjunction with the crowbar which also helps reducing the surplus energy in the DC link.

The DC chopper is usually employed in a type-4 WECS due to its fast dynamics and low initial cost. The concept has been evolved into electromagnetic braking system. The braking resistor is connected across the DC link capacitor with the help of an electric switch. It is designed according to the power rating of the WECS and depends on the heat dissipation capability of the resistor and the switch. Due to high power dissipation, this technique is considered less efficient [49].

- Pitch angle control

A simple approach to deal with the surplus energy for type-3 and type-4 wind turbines is by reducing the power capture from the wind. Whenever a voltage dip is detected at the grid side, pitch angle control gets activated to increase the pitch angle of the blades. With the increased pitch angle, the reference active power for the power converter will be reduced in proportion to the wind speed [50][46]. Due to large moment of inertia of the generator rotor, the overall dynamic response of the pitch control becomes very slow and struggles to comply with the grid codes.

- Energy storage system

The excessive wind energy can also be reserved in energy storage systems (ESSs), which usually consist of individual electric, mechanical and electromechanical systems or their combination based on the design considerations [51]. After the fault is cleared, the stored energy could be sent to the utility grid. The ESS is mostly based on an independently controlled power converter system and for that reason, the response time is much faster than the pitch control. The ESS is also sensitive to severe faults and usually requires a high storage capacity; resulting in increased overall cost of the system [52]. At MW power lever, the initial cost for ESS is very high and it must be designed optimally to be used during normal operating mode as well. For the grid code compliance and for less capital investment, another old strategy explained in [53] can also be used where inertia is being stored in the rotating blades to avoid the cost and complexity associated with the hardware.

- Reactive power compensator

For wind energy systems, ancillary services are also provided with the help of shunt-connected systems. These systems are used to improve the FRT capability and mitigate voltage fluctuations resulting from wind variations and load changes [54]. Reactive power compensators can also be classified as flexible AC transmission system (FACTS). FACTS devices can provide complete dynamic control over the transmission line impedance, magnitude and phase angle of the grid voltage. Static synchronous compensator (STATCOM) is the most famous among all the FACTS

devices. STATCOMs are used to enhance power stability by controlling the voltage transients and rotor speed of the wind turbine [54]. Capacitor banks are sometimes also attached to the STATCOMs to form an inexpensive compensation system for WECS connected to weak AC grids [56]. STATCOMs in combination with GSC provide coordinated reactive power support. The full-scale GSC provides most of the reactive power during the fault and the STATCOM is only activated when extra reactive current is required. This combination helps in reducing the size and cost of the STATCOM [57].

Dynamic voltage restorer (DVR) is another self-commuted reactive power compensator from the FACTS family. It is also used to provide enhanced FRT support for variable speed wind turbines with full-scale converters. A DVR consists of a three phase converter with an energy storage system (ESS) connected in series with the AC grid through a transformer. The purpose of the transformer is to isolate the DVR from the AC grid and regulate the voltage at the required level. During a fault condition, the DVR gets activated and injects synchronized voltage to compensate for the voltage dips by utilizing power from the ESS. [58]. However, a DVR is not recommended for deep voltage sags because unlike conventional transformer, a specific design is required for the connecting transformer to avoid saturation and inrush currents [59].

2.6.2 FRT capability of WPPs

As discussed in section 2.3 the most conventional wind turbine technologies are: SCIG, DFIG and PMSG. The SCIG connects directly to the AC grid and consumes reactive power during a fault. The unbalance created due to the difference between mechanical power coming from the wind and electrical power from the AC grid will help the rotor of the generator to accelerate. These generators suffer even more if connected to weak AC grids. To maintain power stability, more reactive power will be absorbed by the generator on the cost of voltage restoration. To restore the voltage, the generator will continue to accelerate more and this whole process will lead to further voltage instabilities. Eventually the wind generators are required to get disconnected during such events [60]-[62].

In DFIGs, the main drawback is the direct connection of its stator to the AC grid. Because of this, the converters are designed according to the slip power i.e 25-30% of the generator rated power

and result in deficit of reactive power support. Another shortcoming is its sensitivity to high current flow during a fault condition. The high current will flow through the stator and due to the magnetic coupling between stator and rotor, the rotor would also have high current, causing problems in the rotor windings and the converter control. DFIGs also lack control capability over unbalanced active power flow during faults, resulting in overvoltage at the DC link [63].

A PMSG offers better FRT capability compared to DFIGs because it consists of a full-scale converter system and operates independently from the AC grid. The conventional way of connecting a PMSG to an AC grid is through a set of back-to-back converters (MSC and GSC) along with the transformer and a filter. Where, the MSC implements the MPPT control, the GSC helps in regulating the DC link voltage and overall power injection. By considering the PMSG is completely decoupled from the AC grid. During a low voltage dip, the active power coming from the generator will continue with the same magnitude and leaves less margin for the GSC to handle the surplus power. Due to the imbalance between the power extracted and power transferred, an overvoltage will occur at the DC link. To deal with it, new control techniques have been introduced. In these new techniques, either the design of the control algorithm is improved, or the roles of converters are exchanged. To limit the active power transfer during grid fault and for improved FRT capability, DC link voltage regulation can be achieved with the help of MSC [31]. In this thesis, same topology is employed for the compliance of grid codes during FRT.

2.7 Conclusion

This chapter discusses the concept of a weak AC grid in comparison with a strong AC grid. Integration of wind farms into the weak AC grids and their design considerations are highlighted based on the strength of the grid. Some well-known wind energy conversion systems are reviewed and categorized with respect to the nature of the generator. Basic components of the wind energy systems are discussed and the control parameters are explained. Grid code requirements during fault ride through conditions are examined. Several techniques which are utilized to improve the connection and their related challenges are presented to enhance the transient stability of the wind farms connected to weak AC grids. Fault conditions are defined for the wind power plants and methods are discussed to deal with the help of power converters and

other external devices. Most of the literature has focused on the stability methods employed by using DFIG and PMSG based systems for normal (strong) AC grids. However, more study needs to be done when it comes to integrating wind energy systems into weak AC grids, dealing with fault conditions and their effects on stability as well as transmission losses.

2.8 References

[1] S. Hari, S. Islam, and C. V. Nayar, "Power Quality Simulation of a Variable Speed Wind Generator Connected to a Weak Grid," *Proc. Int. Conf. Harmon. Qual. Power, ICHQP*, vol. 3, pp. 988–993, 2000.

[2] N.-E. Clausen, "Planning and development of wind farms: Environmental impact and grid connection" *DTU Wind Energy, 2013.*

[3] A. Gavrilovic, AC/DC System strength as indicated by short circuit ratios, in Int. Conference on AC and DC Power Transmission, London, UK, 1991.

[4] D. Wu, G. Li, M. Javadi, A. Malyscheff, M. Hong, J. Jiang " Assessing Impact of Renewable Energy Integration on System Strength Using Site-Dependent Short Circuit Ratio" IEEE Transactions on Sustainable Energy, vol 9, pp 1072-1080, July 2018.

[5] A. Khan, M. A. Khan, P. S. Barendse "Effects of Load Variation on a Weak Grid under Unbalanced Voltage Conditions", *IEEE International Conference on Electric Machines (ICEM) 2014.*

[6] N. P. W. Strachan and D. Jovcic, "Stability of a variable-speed permanent magnet wind generator with weak AC grids," *IEEE Trans. Power Deliv.*, vol. 25, no. 4, pp. 2779–2788, 2010.

[7] Transmission Code 2007. Networks and System Rules of the German Transmission System operators, VDN-e.v. beim VDEW, www.vdn-berlin.de, August 2007.

[8] Energinet.dk, "Technical regulation 3.2.5 for wind power plants with a power output greater than 11 kW," Accessed online: http://energinet.dk/, 2010.

[9] X. Zhang, C. Liu, R. Ma, H. Bai, F. Gechter, F. Gao, "Instability of Grid Connected Converter under Weak Ac Grid Conditions" IEEE Transportation Electrification Conference and Expo (ITEC), USA, June 2019.

[10] M. Davari, Y. Rady, I. Mohamed "Robust Vector Control of a very Weak Grid Connected Voltage Source Converter considering the Phase Locked Loop Dynamics" IEEE Transactions on Power Electronics, vol 32, pp 977-994, Feb 2017.

[11] J. Khazaei, M. Beza, M. Bongiorno "Impedance Analysis of Modular Multi-Level Converters Connected to Weak AC Grids" IEEE Transactions on Power Systems, vol 33, pp 4015-4025, July 2018.

[12] L. Huang, H. Xin, H. Yang, Z. Wang, H. Xie "Interconnecting very Weak AC Systems by Multiterminal VSC-HVDC Links with a Unified Virtual Synchronous Control" IEEE Journal of Emerging and Selected Topics in Power Electronics, vol 6, pp 1041-1053, Sep 2018.

[13] X. Wang, J. Yao, J. Pei, P. Sun, H. Zhang, R. Liu "Analysis and Damping Control of Small Signal Oscillations for VSC Connected to Weak AC Grid during LVRT" IEEE Transactions on Energy Conversions, vol 34, pp 1667-1676, Sep 2019.

[14] S. Yongsug, V. Tijeras, T. A. Lipo, "Control scheme in hybrid synchronous stationary frame for PWM AC/DC converter under generalized unbalanced operating conditions," *IEEE Transactions on Industry Applications*, vol 42, no. 3, pp.825-835, June 2006.

[15] F. Blaabjerg, Z. Chen, and S. Kjaer, ''Power electronics as efficient interface in dispersed power generation systems,'' IEEE Trans. Power Electron., vol. 19, no. 5, pp. 1184–1194, Sep. 2004.

[16] European Commision, 2013 JRC Wind Status Report: Technology, Market and Economic Aspects of Wind Energy in Europe, Aug. 2014. [Online]

[17] R. L. Iglesias, R. L. Arantegui, and M. A. Alonso, ''Power electronics evolution in wind turbinesVA market-based analysis,'' J. Renew. Sustain. Energy Rev., vol. 15, no. 9, pp. 4982–4993, 2011.

[18] Y. Duan and R. Harley, ''Present and future trends in wind turbine generator designs,'' in Proc. IEEE Symp. Power Electron. Mach. Wind Appl. (PEMWA), Lincoln, NE, USA, Jun. 2009, pp. 1–6.

[19] M. Hossain, H. Pota, V. Ugrinovskii, and R. Ramos, ‘‘Simultaneous STATCOM and pitch angle control for improved LVRT capability of fixed-speed wind turbines,’’ IEEE Trans. Sustain. Energy, vol. 1, no. 3, pp. 142–151, Oct. 2010.
[20] L. Xu and P. Cartwright, ‘‘Direct active and reactive power control of DFIG for wind energy generation,’’ IEEE Trans. Energy Convers., vol. 21, no. 3, pp. 750–758, Sep. 2006.
[21] K. Tan and S. Islam, ‘‘Optimum control strategies in energy conversion of PMSG wind turbine system without mechanical sensors,’’ IEEE Trans. Energy Convers., vol. 19, no. 2, pp. 392–399, Jun. 2004.
[22] Q. Wang and L. Chang, ‘‘An intelligent maximum power extraction algorithm for inverter-based variable speed wind turbine systems,’’ IEEE Trans. Power Electron., vol. 19, no. 5, pp. 1242–1249, Sep. 2004.
[23] T. Ackermann, *Wind Power in Power Systems*. John Wiley & Sons, 2005.
[24] P. Lipnicki and T. M. Stanciu, “Reactive power control for Wind Power Plant with STATCOM,” MSc Dissertation, Aalborg University, Denmark, 2010.
[25] O. Anaya-Lara, N. Jenkins, J. Ekanayake, P. Cartwright, and M. Hughes, *Wind energy generation : modelling and control*. John Wiley & Sons, 2009.
[26] Y. Li, L. Fan and Z. Miao, "Stability Control for Wind in Weak Grids," in IEEE Transactions on Sustainable Energy, vol. 10, no. 4, pp. 2094-2103, Oct. 2019.
[27] P. Mitra, L. Zhang and L. Harnefors, "Offshore Wind Integration to a Weak Grid by VSC-HVDC Links Using Power-Synchronization Control: A Case Study," in IEEE Transactions on Power Delivery, vol. 29, no. 1, pp. 453-461, Feb. 2014.
[28] S. Barghi, M. A. Golkar, and A. Hajizadeh, “Effect of distribution system specifications on voltage stability in presence of wind distributed generation,” *16th Conf. Electr. Power Distrib. Networks*, no. 2, pp. 1–6, 2011.
[29] O. Gomis-Bellmunt, F. Hassan, C. Barker, and A. Egea-Alvarez, “Capability curves of a VSC-HVDC connected to a weak AC grid considering stability and power limits,” *11th IET Int. Conf. AC DC Power Transm.*, 2015.
[30] M. Hong, H. Xin, W. Liu, Q. Xu, and D. Gan, “Critical Short Circuit Ratio Analysis on DFIG Wind Farm with Vector Power Control and Synchronized Control,” *J. Electr. Eng. Technol.*, vol. 11, no. 2, pp. 320–328, 2016.
[31] Ö. Göksu, R. Teodorescu, C. L. Bak, F. Iov, and P. C. Kjær, “Instability of wind turbine converters during current injection to low voltage grid faults and PLL frequency based stability solution,” in *IEEE Transactions on Power Systems*, vol. 29, no. 4, pp. 1683–1691, 2014.
[32] M. Molinas, D. Moltoni, G. Fascendini, J. A. Suul, R. Faranda, and T. Undeland, “Investigation on the role of power electronic controlled constant power loads for voltage support in distributed AC systems,” *IEEE Annu. Power Electron. Spec. Conf.*, 2008.
[33] G. Joos and C. Abbey, “Voltage stability in weak connection wind farms,” in *IEEE Power Engineering Society General Meeting*, pp. 610–615, 2005.
[34] S. Abulanwar, W. Hu, F. Iov, and Z. Chen, “Characterization and assessment of voltage and power constraints of DFIG WT connected to a weak network,” *PES Gen. Meet. Conf. Expo. IEEE*, 2014.
[35] S. Lundberg, “Electrical limiting Factors for Wind Energy Installations,” *Int. J. Renew. Energy Eng.*, vol. 3, no. 2, pp. 305–310, 2000.
[36] M. Karimi Ghartemani, S. A. Khajehoddin, P. K. Jain, and A. Bakhshai, “Problems of startup and phase jumps in PLL systems,” *IEEE Trans. Power Electron.*, vol. 27, no. 4, pp. 1830–1838, 2012.
[37] N. Jaalam, N. A. Rahim, A. H. A. Bakar, C. Tan, and A. M. A. Haidar, “A comprehensive review of synchronization methods for grid-connected converters of renewable energy source,” *Renew. Sustain. Energy Rev.*, vol. 59, pp. 1471–1481, 2016.
[38] P. Zhou, Y. Xiaoming, H. Jiabing, and H. Yunhui, “Stability of DC-link voltage as affected by phase locked loop in VSC when attached to weak grid,” *IEEE Power Energy Soc. Gen. Meet.*, 2014.
[39] M. J. Korytowski, “Effects of the Phase Locked Loop on the Stability of a Voltage source converter in a weak grid environment,” PhD Dissertation, University of Pittsburgh, 2014.
[40] H. Ding, S. Fan, J. Z. Zhou, Y. Zhang, and A. M. Gole, “Parametric analysis of the stability of VSC-HVDC converters,” *AC DC Power Transm. 11th IET Int. Conf.*, 2015.
[41] G. Kalcon, G. Adam, O. Anaya-Lara, S. Lo, and K. Uhlen, “Small - Signal Stability Analysis of Multi - Terminal VSC - Based DC Transmission Systems,” *IEEE Trans. Power Syst.*, vol. 27, no. 4, pp. 1818–1830, 2012.
[42] B. Wen, D. Dong, D. Boroyevich, R. Burgos, and Z. Y. Shen, “Impedance-Based Analysis of Grid-Synchronization Stability for Three-Phase Paralleled Converters,” *IEEE Trans. Power Electron.*, vol. 31, no. 1, pp. 26–38, 2016.

[43] European network for transmission system operators for electricity: “ENTSO-E network code for requirements for grid connection applicable to all generators”, 26 June 2012.
[44] V. O. Zambrano, E. B. Makram, and R. G. Harley, "Transient response of synchronous and asynchronous machines to asymmetrical faults in an unbalanced network," *Electric Power Systems Research*, vol. 14, no. 2, pp. 155-166, 1988.
[45] J. Mohammadi, S. Afsharnia, S. Vaez-Zadeh and S. Farhangi, "Improved fault ride through strategy for doubly fed induction generator based wind turbines under both symmetrical and asymmetrical grid faults," in IET Renewable Power Generation, vol. 10, no. 8, pp. 1114-1122, 9 2016.
[46] E. Muljadi et al., Short Circuit Current Contribution for Different Wind Turbine Generator Types, IEEE Power & Energy Society General Meeting, Minneapolis, Minnesota, July 25-29, 2010.
[47] M. Nasiri and R. Mohammadi, “Peak current limitation for grid side inverter by limited active power in PMSG based wind turbines during different grid faults”, *IEEE Trans. Sus. Energy*, vol. 8, no. 1, Jan 2017.
[48] Z. Chen, J. Guerrero, and F. Blaabjerg, ‘‘A review of the state of the art of power electronics for wind turbines,’’ IEEE Trans. Power Electron., vol. 24, no. 8, pp. 1859–1875, Aug. 2009.
[49] J. Conroy and R. Watson, ‘‘Low-voltage ride-through of a full converter wind turbine with permanent magnet generator,’’IET Renew. Power Gener., vol. 1, no. 3, pp. 182–189, Sep. 2007.
[50] X. Tang, M. Yin, C. Shen, Y. Xu, Z. Y. Dong and Y. Zou, "Active Power Control of Wind Turbine Generators via Coordinated Rotor Speed and Pitch Angle Regulation," in IEEE Transactions on Sustainable Energy, vol. 10, no. 2, pp. 822-832, April 2019.
[51] F. Blaabjerg and K. Ma, ‘‘Future on power electronics for wind turbine systems,’’ IEEE J. Emerg. Sel. Topics Power Electron., vol. 1, no. 3, pp. 139–152, Sep. 2013.
[52] J. Shi, W. Lee and X. Liu, "Generation Scheduling Optimization of Wind-Energy Storage System Based on Wind Power Output Fluctuation Features," in IEEE Transactions on Industry Applications, vol. 54, no. 1, pp. 10-17, Jan.-Feb. 2018.
[53] P.-K. Keung, P. Li, H. Banakar, and B. T. Ooi, ‘‘Kinetic energy of wind-turbine generators for system frequency support,’’ IEEE Trans. Power Syst., vol. 24, no. 1, pp. 279–287, Feb. 2009.
[54] M. F. Farias, P. E. Battaiotto, and M. G. Cendoya, “Wind Farm to Weak-Grid Connection using UPQC custom power device,” *IEEE Int. Conf. Ind. Technol.*, pp. 1745–1750, 2010.
[55] H. Gaztañaga, I. Etxeberria-Otadui, D. Ocnasu, and S. Bacha, “Real-time analysis of the transient response Improvement of fixed-speed wind farms by using a reduced-scale STATCOM prototype,” *IEEE Trans. Power Syst.*, vol. 22, no. 2, pp. 658–666, 2007.
[56] B. Pokharel and W. Gao, “Mitigation of Disturbances in DFIG-based Wind Farm Connected to Weak Distribution System Using STATCOM,” in *North American Power Symposium (NAPS),IEEE*, 2010, pp. 1–7.
[57] T. H. Nguyen, D.-C. Lee, T. L. Van, and J.-H. Kang, “Coordinated Control of Reactive Power between STATCOMs and Wind Farms for PCC Voltage Regulation,” *J. Power Electron.*, vol. 13, no. 5, pp. 909–918, 2013.
[58] M. N. Eskander and S. I. Amer, “Mitigation of voltage dips and swells in grid-connected wind energy conversion systems,” *IETE J. Res.*, vol. 57, no. 6, pp. 515–524, 2011.
[59] C. Wessels, F. Gebhardt, and F. W. Fuchs, “Fault ride-through of a DFIG wind turbine using a dynamic voltage restorer during symmetrical and asymmetrical grid faults,” *IEEE Trans. Power Electron.*, vol. 26, no. 3, pp. 807–815, 2011.
[60] D. H. Nguyen and M. Negnevitsky, “A review of fault ride through strategies for different wind turbine systems,” *Proc. 20th Australas. Univ. Power Eng. Conf. (AUPEC), IEEE*, pp. 1–5, 2010.
[61] R. Amalorpavaraj, P. Kaliannan, S. Padmanaban, U. Subramaniam "Improved Fault Ride Through Capability in DFIG based Wind Turbines using Dynamic Voltage Restorer with Combined Feed-Forward and Feed-Back Control" IEEE Access, vol 5, pp 20494-20503, Sep 2017.
[62] P. Hunag, M. Moursi, S. Hasen " Novel Fault Ride-Through Scheme and Control Strategy for Doubly Fed Induction Generator-based Wind Turbine" IEEE Transactions on Energy Conversion, vol 30, pp 635-645, June 2015.
[63] B. Ambati, P. Kanjiya, V. Khadkikar " A Low Component Count Series Voltage Compensation Scheme for DFIG WTs to Enhance Fault Ride Through Capability" IEEE Transactions on Energy Conversion, vol 30, pp 208-217, March 2015.

Chapter 3
Permanent Magnet Synchronous Generator based Wind Energy System

3.1 Introduction

The basic procedures which are followed to determine the amount of energy extracted and converted by a wind energy conversion system (WECS) are discussed in this chapter. A detailed study on permanent magnet synchronous generator (PMSG) based WECS is presented in addition to the control models for machine and grid side converters. Furthermore, an analysis is performed to anticipate the amount of power transferred from the turbine to the grid along with the associated losses incurred by the system.

3.2 Wind Turbines Basics

This section discusses the basic concepts of a wind turbine. Power extracted from the wind in conjunction with the tip speed ratio (TSR) and maximum power point tracking (MPPT) is also investigated.

3.2.1 Wind Power

The power extracted from the wind is based on three major factors:

i. Wind speed
ii. Turbine characteristics
iii. Shaft Speed

The total power from the wind can be derived from the concept of kinetic energy (E_k) being produced from the moving air mass.

$$E_k = \frac{1}{2} m v^2 \tag{3.1}$$

This energy can also be represented as power (*P)* extracted from the wind with respect to the time (*t)*.

$$P = \frac{E_k}{t} \tag{3.2}$$

By combining the above expressions, the total power can be formulated as:

$$P_{tot} = \frac{1}{2} \rho A v^3 \tag{3.3}$$

Where ρ =air density, *A*=area swept by the blades and *v*= wind velocity.

The kinetic energy from the moving air is transferred into mechanical energy. The complete transfer of energy from the moving air is not possible. As a result, Betz quantified an expression and according to that, only 59% of energy can be absorbed from the moving air mass [1].

$$P_{Betz} = \frac{1}{2} \rho A v^3 . C_{p,Betz} \tag{3.4}$$

Where $C_{p,Betz}=0.59$, is the wind turbine power coefficient.

3.2.2 Power Coefficient and Tip Speed Ratio (TSR)

The power coefficient C_p, is the ratio between the actual power extracted and the maximum power that could be harnessed from the wind. It is expressed as:

$$C_p = \frac{P_{turbine}}{P_{Betz}} \tag{3.5}$$

The value of C_p is a function of wind speed, turbine speed and the pitch angle. The pitch angle is referred to as an angle at which the turbine blades are aligned in or out of the wind. For small scale wind turbines, pitch angle β is assumed to stay constant and does not affect the C_p .The tip speed ratio λ is the ratio between wind speed and the speed of the turbine.

$$\lambda = \frac{R.\omega_{turbine}}{v_{wind}} \tag{3.6}$$

Where R=turbine blade radius, $\omega_{turbine}$= rotating speed of the blades and v_{wind}=wind velocity.

The relationship between Cp and λ used in this thesis is presented in Fig. 3.1:

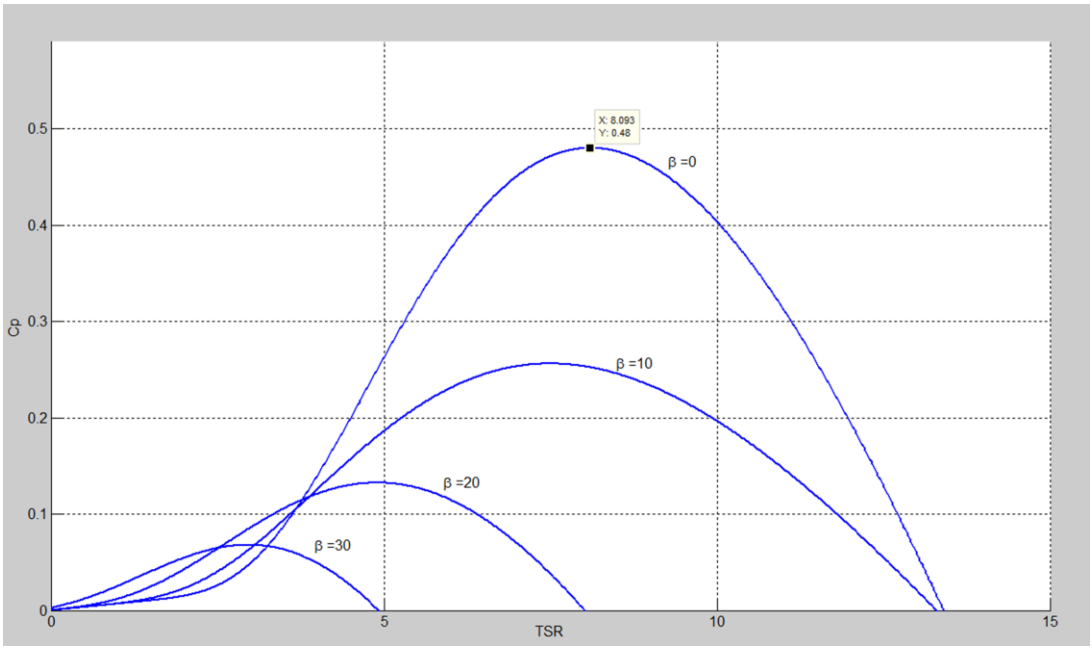

Figure 3.1: Power Coefficient vs Tip Speed Ratio

3.2.3 Maximum Power Point Tracking (MPPT)

To extract maximum power, the operating speed of the variable-speed turbines should be adjusted according to the wind speed. With the help of wind speed sensors, the operating speed of the turbine is estimated and then control scheme is applied to trace the wind speed profile. This type of tracking requires complete information about the wind turbine characteristics and its power vs speed curves at varying wind speeds and pitch angles. In this thesis, a fixed pitch wind turbine is considered and each wind speed will have its own individual power vs speed curve. From equation (3.4), C_p is the only controllable parameter. In Fig.3.2, the power-speed curves are presented which show the maximum power points at given speeds.

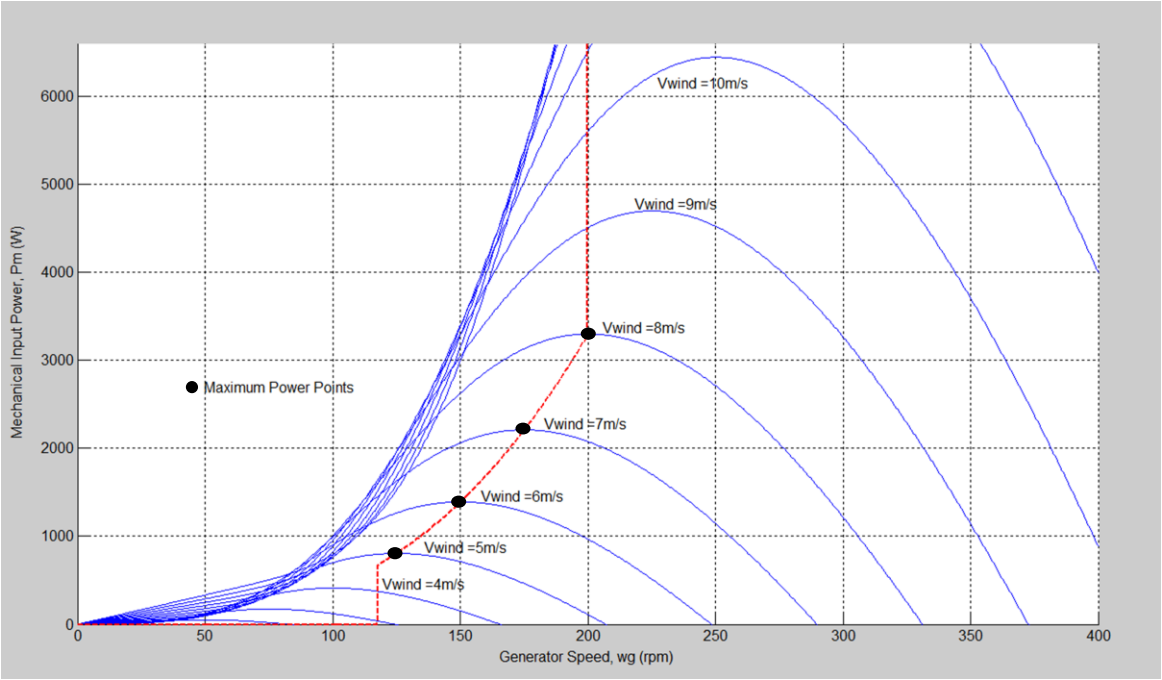

Figure 3.2: Power-Speed Curve

Besides power-speed curve, there are two other methods to implement MPPT for wind turbines. However, in this thesis the wind turbine is studied according to power-speed curve. With respect to power-speed curve, the generator speed needs to be maintained at all the times to harness maximum wind energy [2]. From the curves shown in Fig. 3.2 the maximum power coefficient K_p can be formulated as:

$$P_{\max} = K_p \omega^3 \tag{3.7}$$

3.3 Machine-Side Modelling and Control

The WECS studied in this thesis comprises a wind turbine emulator and a grid-tied PMSG with back-to-back converters. A 3.3kW surface mounted PMSG is considered for the experimental investigation. The generator is controlled during both symmetrical and asymmetrical grid voltage conditions. Since this thesis is more focused on the grid-side control and provides solution for enhanced power delivery into the grid, the machine-side control is simplified by considering the turbine to operate at a constant speed (200rpm) throughout the experiments. Although the

speed is set to remain fixed, the control structure discussed in section 3.4 for the grid-side converter (GSC) can still offer MPPT for varying wind speeds. However, it has not been employed because of not being part of the case study. On the other hand, the machine/generator side converter (MSC) is used to regulate the DC link voltage by controlling the speed of the generator.

In case of deep voltage sags, the MSC will utilize the available mechanical energy and increase the speed of the generator to regulate the DC link voltage and limit the active power injection. The speed and position of the generator will be monitored using an encoder. The phase and magnitude information of the voltages and currents will be determined using transducers. All the converted electrical signals from the physical quantities will be sent to the National Instruments PXI controller to perform the experimental analysis. Fig. 3.3 illustrates an overview of the machine-side control structure to be implemented in this thesis.

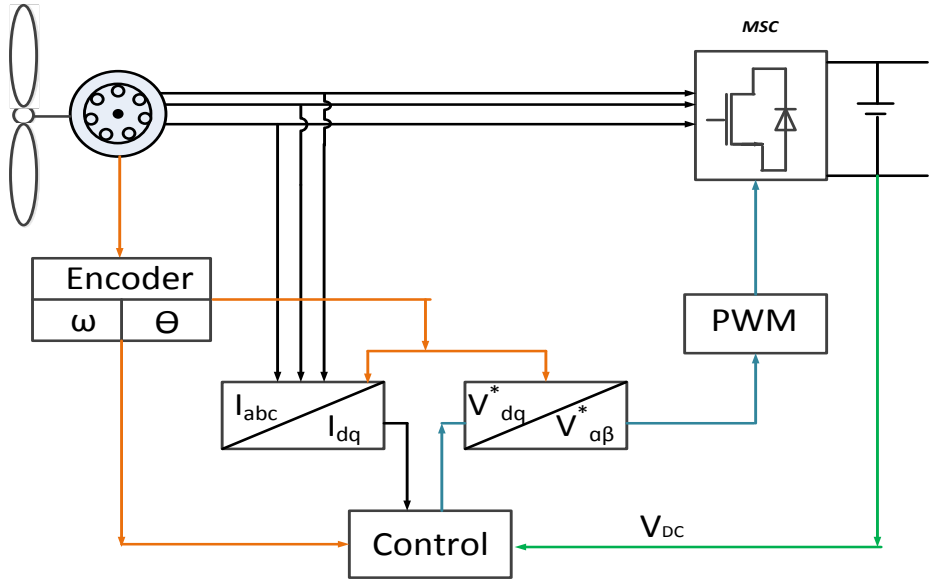

Figure 3.3: Machine-side Control Overview

3.3.1 DQ model of the Machine-Side

Variable speed wind turbines require dynamic control techniques under varying wind conditions. From reference frame theory, the synchronous reference frame consists of *d* (real) and *q* (imaginary) axis. These axis represent electrical space-phasor quantities and assist in

implementing field oriented control (FOC). The equivalent circuit of the PMSG in *dq* domain is shown as:

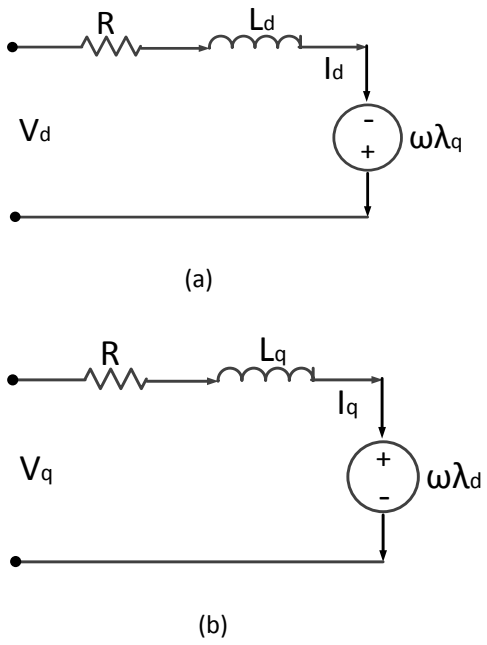

Figure 3.4: (a) *d*-axis Generator Model, (b) *q*-axis Generator Model

From Fig. 3.4, the total *dq* flux linkage of the machine is given as:

$$\lambda_q = L_q i_q \tag{3.8}$$

$$\lambda_d = L_d i_d + \lambda_{pm} \tag{3.9}$$

The two induced voltages in *dq*-axis coils are rotational and transformer emfs. The transformer emfs are induced due to the rate of change of flux linkage in the coil with respect to the *dq* axis and are represented as:

$$d-axis: \frac{d\lambda_d}{dt} \tag{3.10}$$

$$q-axis: \frac{d\lambda_q}{dt} \tag{3.11}$$

The rotational emfs are induced due to the movement between fluxes in the machine and stator windings. The emfs are expressed below for both *dq* axis. Where, ω is the machine rotational speed.

$$d-axis: -\omega\lambda_q \tag{3.12}$$

$$q-axis: \omega\lambda_d \tag{3.13}$$

Equations (3.12) and (3.13) introduce cross coupling in the *dq* voltage expressions and are presented as:

$$v_d = Ri_d + \frac{d}{dt}\lambda_d - \omega\lambda_q \tag{3.14}$$

$$v_q = Ri_q + \frac{d}{dt}\lambda_q + \omega\lambda_d \tag{3.15}$$

To remove the cross coupling, (3.12) and (3.13) are subtracted respectively from the *dq* voltages. As a result, both voltage expressions are considered decoupled from each other. By using (3.8) and (3.9), the abovementioned voltage expressions can also be written as:

$$v_d = Ri_d + L_d\frac{di_d}{dt} - \omega L_d i_q \tag{3.16}$$

$$v_q = Ri_q + L_q\frac{di_q}{dt} + \omega L_d i_d + \omega\lambda_{pm} \tag{3.17}$$

For surface mounted PMSG, L_d=L_q. The electromagnetic torque in (3.18) can be further simplified in (3.19) as:

$$T_e = \frac{3}{2}p[\lambda_{pm}i_q + (L_d - L_q)i_d i_q] \tag{3.18}$$

$$T_e = \frac{3}{2}p[\lambda_{pm}i_q] \tag{3.19}$$

3.3.2 Control of the Machine-Side

The MSC control consists of two control loops. The inner loop controls the current, whereas the outer loop is for the speed control. The inner control loop controls the magnitude of the direct current and mostly adjusted independently based on the control technique. However, the outer control loop regulates the reference value of the quadrature current and the applied torque. The most famous control method for PMSGs is the maximum torque per ampere method. From

equation (3.19), it is obvious that the direct current component does not affect the produced torque and therefore it is set to be equal to zero. This will assist in minimising the total stator current and incur reduced resistive losses. The transfer functions for both control loops are illustrated in Appendix-A.

As mentioned above, the power converter contains two cascaded control loops. In the conventional control method for PMSG based WECS, the MSC implements the MPPT and the DC link voltage regulation is performed by the GSC. However, in [3] a new technique is introduced to support fault ride through (FRT), where the DC link voltage is controlled by the MSC and the GSC is used to implement the MPPT when needed. With this method, whenever a voltage dip is detected, the DC link voltage continues to regulate at the nominal value by limiting the power generation from the PMSG [4]-[5]. Because the incoming power is controlled by the MSC, the GSC will act as a STATCOM and can independently inject active/reactive currents according to the grid codes. This technique is similar to de-loading approach introduced in [6], where mechanical part of the wind turbine acts as an energy storage by increasing the rotational speed. However, due to non-linear relationship between the DC link voltage and the incoming power, a feedback linearization technique is introduced in [7] to reduce the DC link voltage overshoots. By adopting this technique, the external device needed to support FRT can be avoided, hence making it less expensive but more computer intensive. The PI control structure implemented in this thesis is adapted from a new and improved method shown in Fig.3.5 [8]. The *d*-axis current component is set to zero and the *q*-axis current component in the outer loop regulates the DC link voltage. As mentioned earlier that the power generated from turbine is controlled by the grid side converter, it will act as a dynamic current limiter to reduce the *d*-axis current during a grid fault and hence the PMSG power can be controlled. Furthermore, the *q*-axis current component provides reactive power support according to the given grid codes. In this technique, per unit *d* and *q* voltages are compared with the reference values and the resulting error value is used to generate the PWM for the converter to compensate for the potential difference. The main advantage of this new technique is that it offers the best regulation of the generated active power as soon as a grid fault is detected [10].

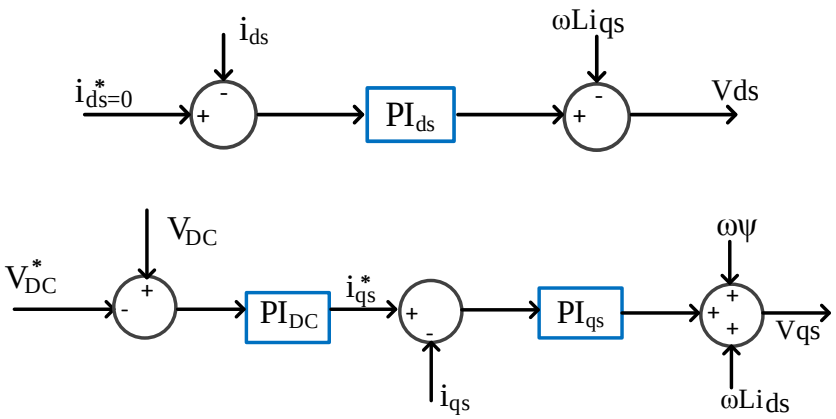

Figure 3.5: Machine-side PI Control Structure

3.4 Grid-Side Modelling and Control

The grid-side includes a full-scale converter integrated into the grid through an LC filter. The converter is envisaged to invert the DC-link voltage into three-phase AC voltage synchronised with the grid. Selection of the filter and its components is also critical for reducing harmonics in the grid currents. The space vector pulse width modulation scheme (SVPWM) will be employed for better utilization of the DC link voltage with reduced current harmonics. In this thesis, the grid-side control will operate in two modes depending on grid voltage conditions:

(a) Symmetrical grid voltages (b) Asymmetrical grid voltages.

During symmetrical grid voltages, the converter will inject the currents by adopting the basic voltage oriented control. The control will be employed for each phase depending on the dynamic load condition and the source voltage magnitude. It will also monitor the system's steady state and based on that, decoupled currents would be injected to avoid any transients.

During asymmetrical voltages, the converter will inject coordinated powers according to power factor control mode, which aims to regulate the reactive power and limit the active power being transferred from the wind turbine. For a weak AC grid with low X/R ratio, more of active current I_d is injected to support the active power, whereas for high X/R ratio, reactive current I_q is prioritised to keep the coordination. The maximum coordinated current magnitude can be expressed as:

$$I_{mag} = \sqrt{I_d^2 + I_q^2} \leq I_{rated} \tag{3.20}$$

The control will detect the nature off the fault and inject active/reactive currents based on the line impedance (Z=R+jX) values. Furthermore, it will maintain the coordination of active and reactive powers by keeping the current magnitude I_{mag} within the maximum rated limits. A single-line diagram along with the phasor diagram representing active and reactive powers injected from the converter are shown in the Fig.3.6.

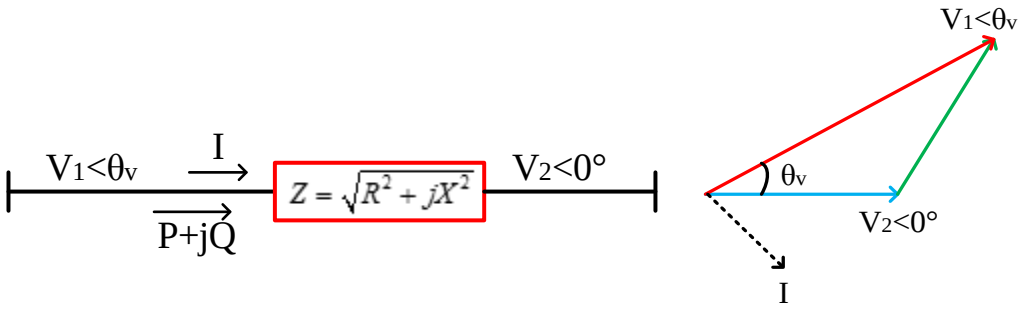

Figure 3.6: Single Phase Equivalent Power Flow and Phasor Diagram

From the power flow characteristics, active and reactive power equations with respect to load impedance are given as [11]:

$$P = \frac{V_1 V_2 X}{Z^2}\sin\theta_v + \frac{V_1^2 R}{Z^2} - \frac{V_1 V_2 R\cos\theta_v}{Z^2} \tag{3.21}$$

$$Q = \frac{V_1^2 X}{Z^2} - \frac{V_1 V_2 X\cos\theta_v}{Z^2} - \frac{V_1 V_2 R\sin\theta_v}{Z^2} \tag{3.22}$$

Hence, the current angle characteristics can be expressed as:

$$I_d = \frac{P}{V_1} = \frac{V_2 X}{Z^2}\sin\theta_v + \frac{V_1 R}{Z^2} - \frac{V_2 R\cos\theta_v}{Z^2} \tag{3.23}$$

$$I_q = \frac{Q}{V_1} = \frac{V_1 X}{Z^2} - \frac{V_2 X\cos\theta_v}{Z^2} - \frac{V_2 R\sin\theta_v}{Z^2} \tag{3.24}$$

With reference to Fig.3.6 above, if a very deep voltage sag appears on the grid-side, then V_2 will almost approach zero. To achieve maximum stability at this point the ratio between active and reactive currents can be obtained as:

$$V_2 = 0 \;\Rightarrow\; I_d = \frac{V_1 R}{Z^2} \text{ and } I_q = \frac{V_1 X}{Z^2} \;\Rightarrow\; \frac{I_d}{I_q} = \frac{R}{X} \tag{3.25}$$

The equation (3.25) is derived specifically for symmetrical grid faults where the grid voltage drops down to 10% of the rated voltage [12]. However, the same expression is employed in this thesis for asymmetrical grid faults to achieve maximum power delivery. The details are discussed and implemented in chapter-6. An overview of the grid-side control is illustrated in Fig.3.7.

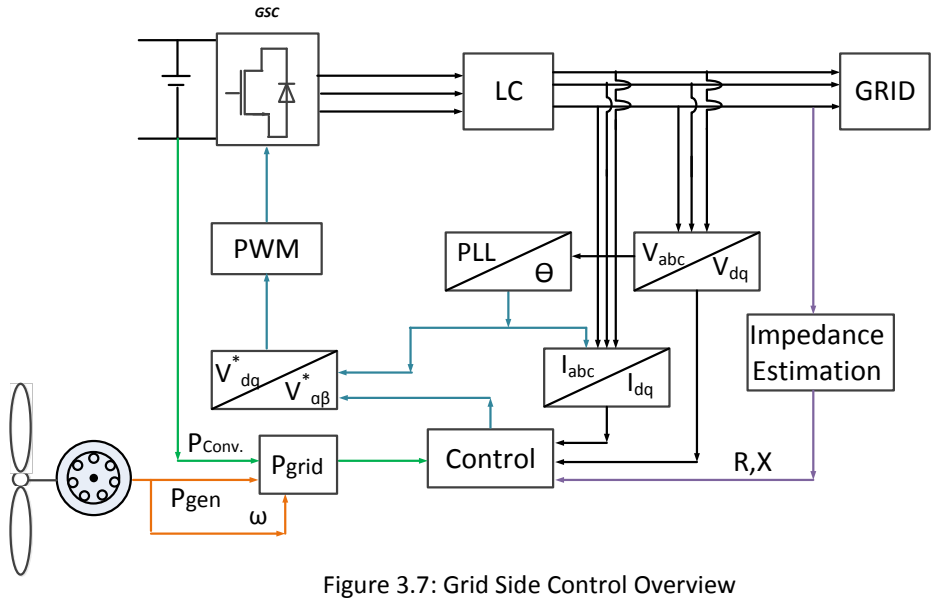

Figure 3.7: Grid Side Control Overview

3.4.1 DQ Model of the Grid-Side

Similar to the generator control, the grid-side model also needs to be understood in order to implement the control of the complete WECS. As mentioned in the section above, the GSC will act independently as a STATCOM for active and reactive current injections. This could be achieved by having a decoupled control on *dq*-axis current components. The converter and grid-side voltage equations are given as:

$$V_{d,grid} = R_T I_d + L_T \frac{dI_d}{dt} + V_{d,conv.} - \omega L_T I_q \tag{3.26}$$

$$V_{q,grid} = R_T I_q + L_T \frac{dI_q}{dt} + V_{q,conv.} - \omega L_T I_d \tag{3.27}$$

Where, R_T = parasitic resistance of the filter components, L_T = inductance of the LC filter and ω=angular frequency.

The active and reactive power components absorbed by the grid are expressed as:

$$P_{grid} = \frac{3}{2} V_d I_d \tag{3.28}$$

$$Q_{grid} = \frac{3}{2} V_q I_q \tag{3.29}$$

For asymmetrical faults, dual sequence current injection method will be adopted. The voltage expressions transformed from (3.26) and (3.27) for positive and negative sequences are given as [8]:

$$V_{dq,conv}{}^{+} = R_T I_{dq}^{+} + L_T \frac{dI_{dq}^{+}}{dt} + j\omega L_T I_{dq}^{+} + V_{dq,grid}^{+} \tag{3.30}$$

$$V_{dq,conv}{}^{-} = R_T I_{dq}^{-} + L_T \frac{dI_{dq}^{-}}{dt} - j\omega L_T I_{dq}^{-} + V_{dq,grid}^{-} \tag{3.31}$$

The detailed grid-side control modelling for asymmetrical faults is discussed in chapter-6.

3.4.2 Control of the Grid-Side

A coordinated control approach is applied with the GSC. In this thesis, a weak grid with unbalanced loading is considered and enhanced power delivery solution is implemented with the help of optimal current injection methods. The methods depend on the dynamic parameters of the grid and for that reason, the GSC will operate as a governing part and perform two important functions. Firstly, it will implement grid impedance estimation. Secondly, the currents will be injected based on the grid impedance values and the voltage conditions. The current injection schemes are discussed for both symmetrical and asymmetrical grid voltage conditions and implemented in chapters-5 and 6 respectively. The grid-side control is illustrated in Fig.3.8.

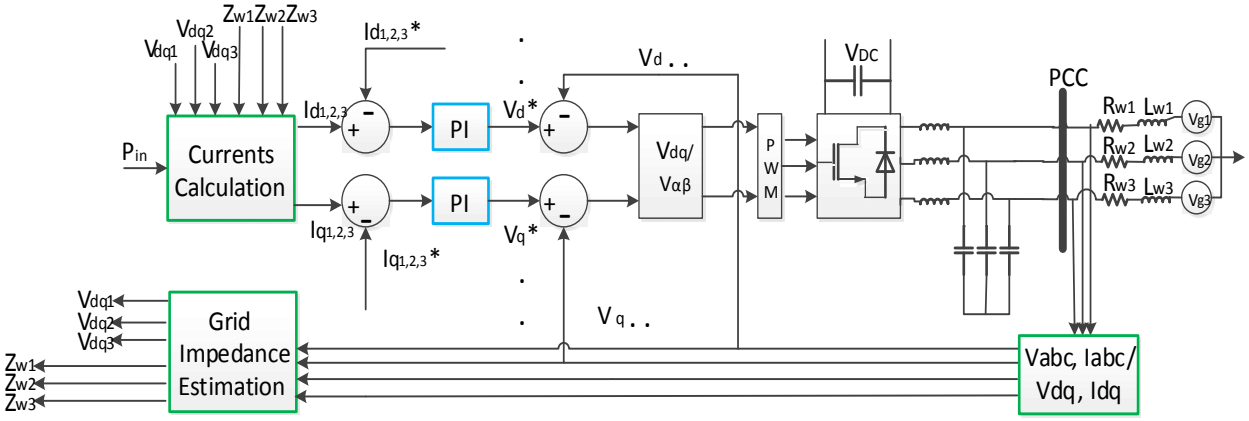

Figure 3.8: Grid Side Control Structure

As mentioned earlier, the GSC will operate as a supervisory component and according to Fig. 3.9, its performance will be analysed under two grid voltage conditions.

1- During balanced/symmetrical grid voltages (0.9pu ≤V_g≤1.1pu)
2- During unbalanced/asymmetrical grid voltages. (V_g<0.9pu)

Due to dual mode operation, the GSC will require an instruction from the outer control loop to decide the function sequence. For the first case (0.9pu ≤V_g≤1.1pu), with reference to Fig. 3.9 the GSC will implement the MPPT. By following the power-speed curve from Fig. 3.2, the maximum captured wind energy P_{opt} will be transmitted to the grid. Once P_{grid} is obtained, optimal current injection will be implemented which is discussed in chapter-5. Similarly for the second case (V_g<0.9pu) when reactive power is required, the GSC control will switch from the MPPT mode to the fault recovery mode and will redistribute the currents according to the coordinated current injection technique discussed in chapter-6.

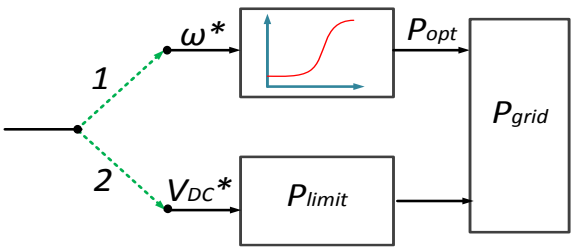

Figure 3.9: Control Mode Selection

3.5 Machine Parameters and Power Production

In this section, the theoretical performance and expected power production of the WECS being considered in this thesis is analysed. The power analysis is based on the functions of speed and loading, which include stator winding impedance, mechanical losses and flux characteristics associated with the generator. Ideal tracking of speed is considered for the analysis, hence maximum power extraction is expected. The applicable machine parameters are given in Table 3.1 and by incorporating these, a complete power loss analysis of the system is carried out analytically based on the expressions for calculating mechanical and electrical losses.

Table 3.1. Generator Parameters

Stator resistance, R_s	*0.76Ω*
d-axis stator inductance, L_d	*6.5mH*
q-axis stator inductance, L_q	*6.5mH*
PM excitation, λ_{pm}	*0.74Wb*
Core loss constant, $K_c(f)$	$K_c(f) = 0.0134\omega^2 + 1.585\omega$
Rotational losses, $P_{rotational}$	$P_{rotational}(\omega) = 0.0331\omega^2 + 13.75\omega - 23.5W$

3.5.1 Projected Power Transfer from Turbine to the Grid

The power generated from the turbine $P_{turbine}$ gets dissipated in the form of electrical and mechanical losses before reaching the grid. The resultant power which gets transferred to the grid can be mathematically expressed as:

$$P_{grid} = P_{gen} - P_{conv} - P_{filter} \tag{3.32}$$

The expected generator output power can be calculated by subtracting the predicted copper losses, frictional losses and the electromagnetic torque produced at the shaft from the power stored in the turbine.

$$P_{gen} = P_{turbine} - P_{cu} - P_{rotational} - P_{shaft} \tag{3.33}$$

- $P_{turbine:}$

From equation (3.4) the shaft /turbine power extracted from the wind can be given as:

$$P_{turbine} = \frac{1}{2}\rho A v^3 . C_p \tag{3.34}$$

From equation (3.6), the given wind speed is:

$$v_{wind} = \frac{R.w_{turbine}}{\lambda_{opt}} \tag{3.35}$$

By utilising the v_{wind}, $P_{turbine}$ can be written as:

$$P_{turbine} = \left[\frac{1}{2}\rho A C_p \frac{R^3}{\lambda_{opt}^3}\right]\omega^3 \tag{3.36}$$

$$P_{turbine} = \left[\frac{1}{2}\rho C_p \Pi \frac{R^5}{\lambda_{opt}^3}\right]\omega^3 \tag{3.37}$$

From Fig 3.1 and 3.2, it is assumed that the turbine operates at ideal TSR (λ_{opt}) and maximum power coefficient (C_p). Therefore, the optimal values are considered, where C_p=0.48 and λ_{opt}=8 at generator speed (ω_g) of 200rpm (20.93m/s). Now if the dry air density (ρ) is considered to be 1.20kg/m^3 and radius of the turbine (R) is 2.96m. Then the calculated $P_{turbine}$=*3665.86W*.

- $P_{cu:}$

The copper losses are the function of total stator current, provided in the relationship below:

$$P_{cu} = 3R_s(I_{ds}^2 + I_{qs}^2) \tag{3.38}$$

From Table 3.1, R_s=0.76Ω and during normal operational condition the *dq*-axis stator currents are I_{ds}=4.45A and I_{qs}=0.1A. Hence the calculated copper losses would be P_{cu}=*46.2W*. By minimising

the direct current component, the copper losses can also be reduced. However, it does not curtail the other losses in the machine.

- $P_{rotatinoal:}$

By assuming that the core losses stay constant under loaded condition. A derived polynomial given in Table 3.1 is used to calculate the rotational losses of the machine. The expression complies with the machine theory only when a speed higher than 4.2m/s is considered. At 20.93m/s (200rpm) the rotational losses are calculated to be 278.6W.

- $P_{shaft:}$

By incorporating speed and power values, the ideal torque required to maintain the speed is given in (3.40). The total electromagnetic torque is the difference between the torque produced at the shaft and the frictional torque experienced by the machine. Furthermore, the power dissipated at the shaft is a function of the electromagnetic torque developed and the speed attained.

$$P_{shaft} = T_{em}.\omega_{shaft} \tag{3.39}$$

Where,
$$T_{em} = \frac{3}{2} p\left[\lambda_{pm} i_q + (L_d - L_q) i_d i_q \right] \tag{3.40}$$

For a surface mounted permanent magnet machine, $L_d=L_q$, electromagnetic torque can be expressed as:

$$T_{em} = \frac{3}{2} p \lambda_{pm} i_q \tag{3.41}$$

Hence, for a 15 pole-pair machine at the shaft speed of 20.93m/s, the $P_{shaft}=34.84W$. From equation (3.33), the P_{gen} can be calculated as:

$$P_{gen}= 3665.86W – 46.2W - 278.6W - 34.84W = 3306.22W$$

- $P_{conv:}$

The power loss in the converters majorly include DC link capacitor losses, switching losses, conduction losses and the parasitic losses inside the connected filter. In this thesis two back-to-back two-level converters are used for the hardware setup. The power loss equation for the converters is expressed as:

$$P_{conv.} = P_{cap} + 2(3P_{conduct.} + 3P_{sw}) \tag{3.42}$$

The per-phase conduction and switching losses of the rated two-level converters calculated from the analysis performed in [13]-[15], are given as: $P_{conduct.} = 16.4W$ and $P_{sw} = 33.7W$.

The DC link capacitor losses can be determined by considering the rms value of current across the capacitor. The capacitor current has a charging and discharging component which can be expressed as [16]:

$$I_{rms} = \sqrt{I_{chrg.}^2 + I_{disc.}^2} \tag{3.43}$$

Where, $I_{chrg.}$ is the charging current and $I_{disc.}$ is the discharging current. If the values of the charging and discharging currents are known, their square root can be multiplied by the estimated equivalent series resistance (ESR) values of the capacitor to give the power dissipated across the DC link capacitors.

$$P_{cap} = ESR.I_{rms}^2 \tag{3.44}$$

Typical ESR values for different capacitors size are given in the Table 3.2 below.

Table 3.2. Typical Values of Equivalent Series Resistance [16]

Type	*22µF*	*100µF*	*470µF*	*1000µF*	*4700µF*
Standard Aluminium and Ceramic	1 to 5.4Ω	0.3 to 1.2Ω	0.1 to 0.24Ω	0.02 to 0.12Ω	0.01 to 0.23Ω

The capacitors used in this project for the DC link are *4x4700uF*, maximum ESR value is considered and the total loss per capacitor is shown in Table 3.3. This can give the best approximation of the

power dissipation, however more detailed analysis could also be performed by incorporating temperature and material profiles.

Table 3.3. DC Link Loss Calculation

I_{chrg}	I_{disc}	I_{rms}	ESR(Ω)	Loss/Capacitor	Total Loss(W)
3.16	2.69	4.15	0.23	3.96	3.96×4=15.84

An LC filter is used in this project. The passive damping resistor was set to be 1/3 of the capacitor impedance at the resonant frequency [17]-[19], and its value is approximated to be 0.3Ω. Hence the power dissipated across the filter is:

$$P_{filter} = I_{rated}^2 .R = 6.12W \tag{3.45}$$

By putting the values of P_{gen} , P_{filter} and P_{conv} in equation (3.32), the approximated power that reaches the grid at the PCC is, $\boldsymbol{P_{grid}}$ **or** $\boldsymbol{P_{PCC} = 2980W}$.

It is to be noted that several assumptions have been made before getting to this result. Mechanical losses related to the coupling between the prime mover (induction machine) and the generator were not included in the analysis. The impact of the temperature on the machine parameters has also been omitted. The basic aim of this section is to develop understanding about the power losses happening inside the system components. After calculating the approximated power transferred to the PCC, this value is used as a feedback for the control to perform optimal current injection for maximized power transfer into the given weak AC grid.

3.6 Conclusion

In this chapter basic concepts of the wind turbine parameters have been discussed. Conversion of wind power into electrical power and associated power losses are reviewed. Primary expressions for wind power, power coefficient, tip speed ratio and maximum power point tracking are derived. Additionally, *dq* control models are investigated for both grid and machine side converters. Dual sequence vector control is implemented for the grid-side during asymmetrical voltage conditions. Furthermore, actual machine parameters are considered and a

power loss analysis is conducted to predict the power delivered by the converters. The analysis was presented to illustrate the amount of power lost during generation in the form of rotation, conduction, heating, switching and copper losses.

3.7 References

[1] Gijs A.M. van Kuik. The Lanchester–Betz–Joukowsky Limit [Accessed Online 2007] https://onlinelibrary.wiley.com/doi/pdf/10.1002/we.218

[2] Subbaraya Yuvarajan, Lingling Fan Xin Wang, "MPPT Control for a PMSG-Based Grid-Tied Wind Generation System," in *North American Power Symposium (NAPS)*, pp. 1 – 7, 2010.

[3] Michalke G, Hansen AD, Hartkopf T. Control strategy of a variable speed wind turbine with multi-pole permanent magnet synchronous generator. *EWEC, Milano,* p.1–8, *2007*.

[4] Hansen AD, Michalke G. Modelling and control of variable-speed multi-pole permanent magnet synchronous generator wind turbine, *Wind Energy* 2008.

[5] Hansen AD, Michalke G. Multi-pole permanent magnet synchronous generator wind turbines' grid support capability in uninterrupted operation during grid faults. *IET Renew Power Gener* 2009.

[6] Anaya-Lara O, Jenkis N, Ekanayake J, Cartwright P, Hughes M. Wind energy generation: *modelling and control. John Wiley & Sons*, Ltd; 2009.

[7] Kim KH, Jeung YC, Lee DC, Kim HG "LVRT scheme of PMSG wind power systems based on feedback linearization", *IEEE Trans Power Electron* 2012.

[8] M. Nasiri and R. Mohammadi, "Peak Current Limitation for Grid Side Inverter by Limited Active Power in PMSG Based Wind Turbines During Different Grid Faults", *IEEE Trans. Sus. Energy*, vol. 8, no. 1, Jan 2017.

[9] M. Nasiri, J. Milimonfared, S.H. Fathi "A Review of Low-Voltage Ride –through Enhancement Methods for Permanent Magnet Synchrnous Generator Based Wind Turbines" *Elsevier RSER* 2015.

[10] M. F. Moussa, A. helal, Y. Gaber H. A. Youssef. "Unity Power Factor Control of Permanent Magnet Motor Drive System". http://papers.aast.edu/staffpdf/5695_45_119_UPF%20control%20of%20PMSM.pdf

[11] I. Erlich, F. Shewarega, S. Engelhardt, J. Kretschmann, J. Fortmann, and F. Koch," Effect of Wind Turbine Output Current during Faults on Grid Voltage and the Transient Stability of Wind Parks," *IEEE Power & Energy Society GeneralMeeting,* pp.1-8, 26-30 July 2009.

[12] X. Dong, H. Sun, C. Wang Z. Yun, Y. Wang P. Zhao "Power Flow Analysis Considering Automatic Generation control for multi Area Interconnection Power Networks" IEEE Transactions on Industry Applications, vol 53, pp 5200-5208, Dec 2017.

[13] Uwe Drofenik and Johann W. Kolar "A General Scheme for Calculating Switching and Conduction-Losses of Power Semiconductors in Numerical Circuit Simulations of Power Electronic Systems" IPEC, Niigata, Japan, 2005.

[14] J.W.Kolar, H. ERTL and F.C. Zach "Influence Of the Modulation Method on the Conduction and Switching Losses of a PWM Converter System" International Conference on Industry Applications Society, Annual Meeting, 1990.

[15] SKM 145GB123D & SK75MLI066T datasheets. http:// www.semikron.com/skcompub/en/igbt_modules-81.html [Accessed online: 2013]

[16] M. Ikonen, O. Laakkonen, M. Kettunen "Two-Level and Three-Level Converter Comparison In Wind Power Application" , http://www.elkraft.ntnu.no/smola2005/Topics/15.pdf [Accessed Online: 2015]

[17] N Lan Xiao, Zhilei Yao, Chunying Gong, Xing Wei, "Design of LCL Filter for Wind Power Inverter," in *World Non-Grid-Connected Wind Power and Energy Conference (WNWEC)*, 2010.

[18] D.V. Shwetha, S. Rao "Design and Simulation of LCL filter in Wind Energy Conversion System" IEEE International Conference on Automatic Control and Intelligent systems, Malaysia 2018.

[19] G. Gohil, L. Bede, R. Teodorescu, T. Kerekes, F. Blaabjerg " Line Filter Design of Parallel Interleaved VSCs for High-Power Wind Energy Conversion Systems" IEEE Transactions on Power Electronics, vol 30, pp 6775-6790, Dec 2015.

.

Chapter 4
Grid Impedance Estimation

4.1 Introduction

Multiple grid contingency applications depend on the grid impedance which has to be known in advance. This could be required to assist optimal power distribution by considering the grid impedance as Thevenin impedance seen from an arbitrary node [1]-[3]. To implement optimal power distribution, optimal current calculation and injection is required. The optimal current regulation techniques discussed in this thesis are based on complete information of pre-determined value of the Thevenin impedance. Once extracted, these values are fed-back to the controller to make necessary changes in terms of currents requirement. This chapter encompasses a review on conventional and recent impedance estimation techniques. A modified version of the PQ power variation technique is proposed because of its simple implementation and relevance with the theme of the research conducted in this thesis. This is also one of the major contributions of this thesis as discussed in section 1.8. To emulate an impedance model, an experimental setup is employed. Power variations are applied to estimate the impedances and compared with the actual values to validate the analysis.

4.2 Impedance Estimation Techniques

Usually grid impedance estimation is performed by two classified methods, i.e passive and active methods [4]. Passive method is based on acquiring and monitoring the signals which are already available in the system. The distortions in the signals which are to be monitored are mostly not large enough to be measured accurately, therefore it is hard to estimate the exact value of the impedance. With active method, disturbance is created deliberately at the PCC and the impedance is estimated depending on the response from the grid to that disturbance [5]-[9]. The

most common disturbances generated by the active method are summarized into three categories:

- *Current Transient:*

A current pulse is injected into the system to measure the resultant voltage transient. In this method high quality analogue-to-digital data acquisition devices are required to perform numerical measurements dynamically and reduce the associated noise in the signals.

- *Inter-Harmonics:*

Non-characteristic sub-harmonics are injected at the PCC to predict the grid impedance at a particular frequency. Discrete Fourier transform is applied to perform the analysis on the captured data points.

- *Power Variations:*

Similar to the current transient method, active and reactive components of the currents are perturbed to produce power variations. The amplitude of the power variations are recorded to perform the grid impedance calculation.

Due to repeated injection of the disturbances, active methods are also prone to high signal to noise ratio and total harmonic distortion. Furthermore, with having a very small detection zone, the accuracy of the acquired information also gets reduced under variable frequency conditions. The period of time during which the grid impedance is estimated is another consideration when implementing the active methods and as a result can be sub-categorized into two groups:

- *Online Method:*

This method is based on runtime grid impedance estimation. The injection of disturbance, acquisition of data and calculations are made at the same time the system is being executed. The inverter operates according to the changing operating conditions which also assist in improving the overall stability.

- *Offline Method:*

With offline method, the system operates in two phases. In the first phase, data is acquired and processed for the calculations and in the second phase estimated grid impedance values are used as functions for the control of the system.

4.3 Research Review of the Techniques

In this section a brief review is done on the conventional techniques available to estimate the impedance of the network. In [10], phasor measurement units (PMUs) are utilized to determine the impedance matrix based on synchronous voltages and currents for a multi-source multi-load grid. The information acquired is then used in a recursive least square algorithm. The authors have reduced the complexity of the algorithm but a large number of calculations are required to be performed concurrently at a high rate to improve the correctness. The authors have also introduced a forgetting factor to reduce the dependence on the past values of the acquired data for efficient impedance estimation. Since the algorithm does not inject any disturbance in the grid and the parameters are estimated using synchronous measurements of currents and voltages, specialized hardware is required at each node in the grid. The active methods usually lack synchronization between the grid nodes and introduce instability into the network and hence could not be implemented in conjunction with the discussed algorithm.

In [11], a method is proposed to measure the impedance by introducing resonance in the LCL filter connected between the inverter and the grid. The filter can be evoked in three different ways:

- By increasing the proportional gain of the current controller.
- By adding extra poles or zeros in the control design to push the response of the controller out of stability region.
- By varying the modulation index of the PWM.

This method is generally based on the natural resonance of the LCL filter which is susceptible to the change in the grid impedance. Therefore, the LCL filter needs to be properly damped to avoid unwanted instabilities. The precise instability is introduced by exploiting the frequency

characteristics and fast Fourier transform (FFT) is implemented for data analysis. The only disadvantage with this technique is that the implementation of FFT can overload the digital signal processor (DSP) for recursive measurements.

In [12], another technique is implemented. A digital processor is used to process the inter-harmonic disturbance with the help of delicate sensors. The digital processor contains discrete Fourier transform (DFT) modules to extract the inter-harmonic current response. One possible limitation of this method is to have knowledge of the initial grid impedance. For that, feed-forward voltage coefficients can be used to obtain the impedance values. The authors have also proposed another technique where weighted coefficients of the sensed filter currents are employed to suppress the resonant peak from 3rd order to 1st order harmonics without using any passive damping. This technique provides adaptive approach for the grid tied inverters to maintain stability especially for weak grids.

It has been noted that among active methods, the current injection is more beneficial compared to the voltage injection. With the current injection, the controller's response does not get affected by the system's parameters. The output filter and the grid impedance do not affect the rise time of the current unlike in voltage injection. Hence with the current injection scheme, tuning of the controllers is easy and response time can also be enhanced.

In [13], the grid impedance estimation is based on moving window DFT calculation. Because the running sum approach to calculate the DFT overloads the DSP, the moving window technique reduces the time required for the calculations. Furthermore, by repeated estimations and averaged results, it guarantees accuracy and reduced total harmonic distortion. The estimation is given as a ratio between the DFT of the voltage response and the injected current at the inter-harmonic frequency. Moreover, the previously estimated value of the impedance should be multiplied by the grid frequency and divided by the inter-harmonic frequency. For improved measurement, the inter-harmonic frequency is tried to be kept close to the grid frequency.

Another method for the impedance estimation is active and reactive power variation for a single phase system [14]. With this method, the grid impedance is determined by producing variation in the active and reactive powers. The variation happens by injecting current references in a synchronous reference frame. Two working points are considered which are created at the point

of disturbance and before the disturbance is created. The resultant change in the synchronous voltage is also measured to calculate the impedance values. During this method, the impedance is considered to be linear and the grid voltage will also stay constant.

This method was first introduced for multiphase circuits in [15]-[18] and was known as "Generalized Theory of the Instantaneous Reactive Power in Three Phase Circuits", which is also called "P-Q Theory". Since the case study of this thesis is to inject optimal currents for maximum power transfer, the P (active) Q (reactive) power variation technique is selected. With PQ variation technique, no separate injection of signal is required to create a disturbance; hence total harmonic distortion does not shoot abruptly. Furthermore, it is computationally less intensive and does not require advanced analogue-to-digital data acquisition devices, thereby consuming less processing (DSP/FPGA) memory. The experimental hardware considered for this thesis consists of a distributed unbalanced weak grid, where each line would have different impedances. The forthcoming sections will discuss the theory to estimate the individual line impedances of a multiphase system [14]-[18].

4.4 PQ Variation Technique

After discussing the conventional methods for grid impedance measurement and their implementation on multiphase and poly-phase systems. The PQ theory defined in [15]-[18] is illustrated in the sections below and an analysis is performed to evaluate its performance.

4.4.1 General Requirements for the PQ Variation Technique

To implement the PQ variation method, it must be made sure that the voltage and current values are acquired in synchronous reference frame. The synchronous reference frame rotates at the grid frequency and has the same voltage as that of the grid voltage. Whereas, the stationary reference frame demands the calculation of both amplitude and phase for correct phasor representation. The transformation from the stationary reference ($\alpha\beta$-axis) frame to rotating reference (dq-axis) frame is called Park's Transformation. According to the theory presented in [15]-[18], it must be noticed that the $-q$ axis is considered instead of q axis in Park's

transformation. Furthermore, all other variables are referred to the grid voltage (V_g). If grid voltage and the grid current are considered to be in the same phase, then the *d*-axis component should have a constant value and *q*-axis component is considered to be an error value. In stationary reference frame, the grid voltage can be represented as:

$$\begin{aligned} V_\alpha &= V_g \cos(\omega t + \theta_g) \\ V_\beta &= V_g \sin(\omega t + \theta_g) \end{aligned} \tag{4.1}$$

The magnitude of the grid voltage would be:

$$V_g = \sqrt{V_\alpha{}^2 + V_\beta{}^2} \tag{4.2}$$

And the phase angle can be calculated as:

$$\theta_g = \tan^{-1} \frac{V_\beta}{V_\alpha} \tag{4.3}$$

Now by considering $\theta_g=\theta$, V_d will become equal to V_g and V_q=0. The Park's transformation is:

$$\begin{bmatrix} V_d \\ V_q \end{bmatrix} = \begin{bmatrix} \cos\theta & \sin\theta \\ -\sin\theta & \cos\theta \end{bmatrix} \begin{bmatrix} V_\alpha \\ V_\beta \end{bmatrix} = \begin{bmatrix} \cos\theta & \sin\theta \\ -\sin\theta & \cos\theta \end{bmatrix} \begin{bmatrix} V_g \cos(\omega t + \theta_g) \\ V_g \sin(\omega t + \theta_g) \end{bmatrix} = \begin{bmatrix} V_g \cos(\theta_g - \theta) \\ V_g \sin(\theta_g - \theta) \end{bmatrix} \tag{4.4}$$

Similarly, the *dq*-axis current components can be written as,

$$\begin{bmatrix} I_d \\ I_q \end{bmatrix} = \begin{bmatrix} \cos\theta & \sin\theta \\ -\sin\theta & \cos\theta \end{bmatrix} \begin{bmatrix} I_\alpha \\ I_\beta \end{bmatrix} = \begin{bmatrix} \cos\theta & \sin\theta \\ -\sin\theta & \cos\theta \end{bmatrix} \begin{bmatrix} I_g \cos(\omega t + \theta_g) \\ I_g \sin(\omega t + \theta_g) \end{bmatrix} = \begin{bmatrix} I_g \cos(\theta_g - \theta) \\ I_g \sin(\theta_g - \theta) \end{bmatrix} \tag{4.5}$$

If the reference currents in the stationary reference frame are

$$\begin{aligned} I_\alpha^* &= \frac{2[(V_\alpha . P) + (V_\beta . Q)]}{V_{\alpha\beta}^2} \\ I_\beta^* &= \frac{2[(V_\beta . P) + (V_\alpha . Q)]}{V_{\alpha\beta}^2} \end{aligned} \tag{4.6}$$

Then, by substituting equations (4.1) in (4.4) and (4.6) would give the expressions for I_d and I_q. From equations (4.7) and (4.8), the relationship of I_d and I_q with active and reactive powers can be seen as:

$$I_d = I_\alpha^* \cos\theta + I_\beta^* \sin\theta$$

$$I_d = \frac{2}{V_g}\left[P\cos\theta + Q\sin\theta\right]\cos\theta + \left[P\sin\theta + Q\cos\theta\right]\sin\theta$$

$$I_d = \frac{2}{V_g}\left[P(\cos\theta)^2 + P(\sin\theta)^2\right] + \left[Q\sin\theta\cos\theta + Q\cos\theta\sin\theta\right] = \frac{2P}{V_g} \quad (4.7)$$

Since *–q*-axis is considered, -v_q and *–*i_q will be used to give I_q,

$$I_q = -\frac{2}{V_g}\left[P\cos\theta + Q\sin\theta\right]\sin\theta + \left[P\sin\theta - Q\cos\theta\right]\cos\theta = -\frac{2Q}{V_g} \quad (4.8)$$

4.4.2 Approach to the Technique w.r.t. a Grid-tied Inverter

From the analysis done in [14]-[18], it is shown that decoupled injection of active and reactive currents can be made possible by orthogonal projections of the current vectors for both poly and multi-phase systems. For example, a grid side converter is shown in Fig. 4.1 which is being connected to a three wire Thevenin model of a distributed network. The presented Thevenin model is composed of grid impedances (Z_1, Z_2, Z_3) with their individual AC voltage supplies (V_{th1}, V_{th2}, V_{th3}). The reason why each phase is treated individually is because of the ease of implementation of the poly-phase measurement scheme. The control detail is already given in section 3.4.2.

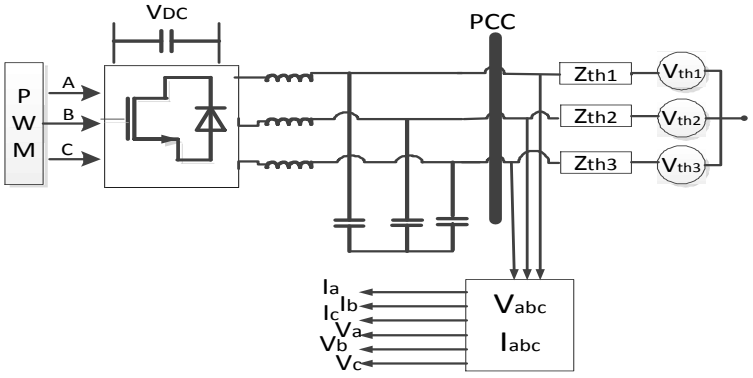

Figure 4.1: Grid Side Converter Integrated into Network's Thevenin model

During ideal operating conditions with no grid faults, all power generated from the converter is absorbed by the grid with zero reactive power component. For this case, appropriate current

references will be applied for each line to produce active/reactive power variations. These variations will affect the voltages at the PCC and the resultant change in the voltages is recorded to implement the impedance measurements. The PQ variation method is based on Clark and Park's transformations. The former is used to convert the three phase voltage/current signals into two phase signals with same magnitude but 90° phase shifted in a stationary reference frame. The latter is used for orthogonal projection of voltage/current vectors on a rotating axis with same angular frequency of the grid voltage/current. The reference values of the currents would impact the active/reactive power differently. The active current component I_d will maintain the amplitude and the reactive current component I_q deals with the phase. To understand these concepts, basic principles of power theory are revisited below.

The complex power with active and reactive components can be represented as:

$$S = V.I\angle(\theta_V - \theta_I)$$

$$= V.I\,\mathrm{Cos}(\theta_V - \theta_I) + jV.I\,\mathrm{Sin}(\theta_V - \theta_I) = P + jQ \tag{4.9}$$

Where,

$$P = \mathrm{Re}(S) = VI\cos(\theta_V - \theta_I) = VI\cos\theta$$
$$Q = \mathrm{Im}(S) = VI\sin(\theta_V - \theta_I) = VI\sin\theta \tag{4.10}$$

V and I are the rms values. The active and reactive powers from equation (4.10) can be decomposed in dq-axis components as:

$$P = \frac{1}{2}(V_d.I_d + V_q.I_q) \tag{4.11}$$

$$Q = \frac{1}{2}(V_q.I_d - V_d.I_q) \tag{4.12}$$

The expressions above show the dependence of active and reactive powers on dq-axis current components.

4.4.3 Implementation and Analysis of the Technique

With reference to the PCC shown in Fig. 4.1, a SCR value will be calculated to measure the strength of the grid. Since the system under consideration is going to be connected to a weak grid with low SCR value and unequal impedances, the impedance estimation will be implemented

by perturbing the current in each wire individually. The idea is to change the grid current reference in order to disturb the grid active and reactive powers and then measure the impedance by calculating the voltage variations with respect to reference values at the PCC. The PQ variation method can be implemented in both stationary and rotating reference frames. In rotational reference frame the resultant current references would be I_d^* and I_q^*. These currents are perturbed to perform a PQ variation which produces two voltage (ΔV_d and ΔV_q) operating points with respect to the initial grid voltages shown in Fig. 4.2. It is assumed that the grid impedance (Z_g) would always stay constant while measuring ΔV_d and ΔV_q [19]. Moreover, the system should also retain its steady state after the disturbance is applied.

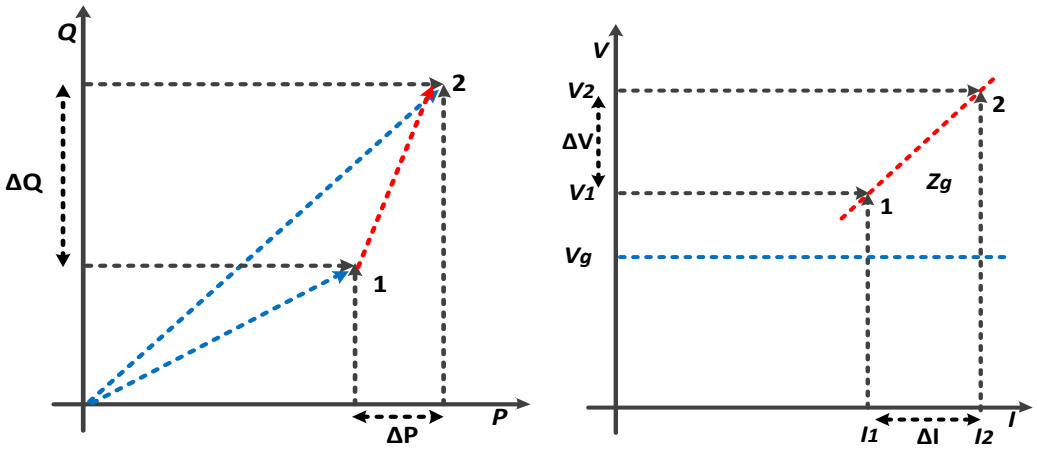

Figure 4.2: Power and Voltage Variations

Single phase active and reactive powers in rotational reference frame are given in equations (4.11) and (4.12). To produce power variations, reference currents in *dq*-axis are presented as (4.13) and (4.14).

$$I_d^* = \frac{2[(V_q.Q)+(V_d.P)]}{V_d^2+V_q^2} \tag{4.13}$$

$$I_q^* = \frac{2[(V_q.P)+(V_d.Q)]}{V_d^2+V_q^2} \tag{4.14}$$

The voltage equations at the PCC from Fig. 4.1 can be derived from [20] and are presented in (4.15) and (4.16), where R_{th} and L_{th} are the Thevenin resistance and inductance. It can be seen that both *dq* currents have a direct impact on the voltage of the other axis. That means if *dq* current changes, it will bring change to all of the *dq* voltage vectors regardless of the axis.

$$V_d = R_{th1} I_d - \omega L_{th1} I_q + V_{gd} \tag{4.15}$$

$$V_q = R_{th1} I_q - \omega L_{th1} I_d + V_{gq} \tag{4.16}$$

By considering that the grid inductance does not saturate, the current references in rotating reference frame are perturbed and the resultant voltage expressions at the two operating points are:

$$V_1 = V_{d1} + jV_{q1} \tag{4.17}$$

$$V_2 = V_{d2} + jV_{q2} \tag{4.18}$$

From (4.15) and (4.16), the above expressions can be represented as:

$$V_1 = (R_{th1} I_{d1} - \omega L_{th1} I_{q1} + V_{gd}) + j(R_{th1} I_{q1} + \omega L_{th1} I_{d1} + V_{gq}) \tag{4.19}$$

$$V_2 = (R_{th1} I_{d2} - \omega L_{th1} I_{q2} + V_{gd}) + j(R_{th1} I_{q2} + \omega L_{th1} I_{d2} + V_{gq}) \tag{4.20}$$

Since it is assumed that the grid voltage stays constant during the measurements, V_{gd} and V_{gq} can be omitted from the final expressions to compute the voltage variation. Hence V_1 and V_2 can be expressed as:

$$V_1 = R_{th1} I_{d1} - \omega L_{th1} I_{q1} + jR_{th1} I_{q1} + j\omega L_{th1} I_{d1} \tag{4.21}$$

$$V_2 = R_{th1} I_{d2} - \omega L_{th1} I_{q2} + jR_{th1} I_{q2} + \omega L_{th1} I_{d2} \tag{4.22}$$

The voltage change at the PCC between the two operating points will be:

$$\Delta V_{PCC} = V_1 - V_2 = \Delta V = \Delta V_d + j\Delta V_q \tag{4.23}$$

If, $$V_1 - V_2 = (R_{th1}\Delta I_d - \omega L_{th1}\Delta I_q) + j(R_{th1}\Delta I_q + \omega L_{th1}\Delta I_d) \tag{4.24}$$

Then, the final voltage variation expressions in *dq*-axis would be:

$$\Delta V_d = R_{th1}\Delta I_d - \omega L_{th1}\Delta I_q \tag{4.25}$$

$$\Delta V_q = R_{th1}\Delta I_q + \omega L_{th1}\Delta I_d \tag{4.26}$$

From (4.11) and (4.12), it can be seen that there is cross- coupling between *d* and *q* axis currents. Any change in the currents will affect the magnitude as well as the direction of voltage components of the other axis. To remove this coupling, the reference currents will be injected in such a way that only I_d^* should be perturbed when measuring R_{th} and in the case of L_{th} measurement, only I_q^* is perturbed. i.e when, $\Delta I_d = 0$, $\Delta I_q \neq 0$ and vice versa. In [5] it has been verified that ΔV_q causes sensing error during phase locked loop (PLL) measurement, so only ΔV_d will be considered for impedance estimation. After applying the above mentioned conditions in (4.25) and (4.26), R_{th1} and L_{th1} can be expressed as:

$$R_{th1} = \frac{\Delta V_d.\Delta I_d + \Delta V_q.\Delta I_q}{\Delta I_d^2 + \Delta I_q^2}, \quad L_{th1} = \frac{\Delta V_q.\Delta I_d - \Delta V_d.\Delta I_q}{[\Delta I_d^2 + \Delta I_q^2].\omega} \tag{4.27}$$

Hence, $$Z_{th1} = R_{th1} + j\omega L_{th1} \tag{4.28}$$

Likewise, the complete process can be repeated for Z_{th2} and Z_{th3} measurements. It is also necessary that the measurements should be taken when the system retains its balance after a power disturbance. Furthermore, it is better to acquire the reference values at the start of the perturbation because V_g usually takes longer to get settled down at its nominal value.

4.5 Experimental Setup and Results

In the previous sections, different impedance estimation techniques have been reviewed and one is chosen to be implemented. The analysis performed in the previous section is based on two assumptions:

i. The grid impedance stays constant during the estimation phase.
ii. The grid side voltage does not change in terms of its amplitude, phase and frequency over the measurement period.

If a non-linear impedance is considered, a reactive power transient would be seen whenever there is a change in the grid parameters (R_g, L_g, V_g). Therefore, by monitoring the reactive power transient, changes could be detected in the grid parameters.

4.5.1 Modified PQ Variation Technique

According to the standard PQ variation technique, the impedance estimation is performed for fixed duration of time intervals and takes into account if the system is in a steady state or not. So, the main objective of the modified technique is to detect if the steady state has been achieved by the system. To bring this adaptability in the system, a method needs to be followed which confirms decoupled perturbations without generating any transients. Therefore, with the modified technique, impedance estimation will be performed for each phase individually. To implement this, active power must be disturbed in a way so that reactive power is not affected. Unlike the slow power ramp (averaged) variation method [21], the technique implemented in this chapter will not only reduce the transients but will also enhance the dynamic response of the system. The control block diagram is shown in Fig. 4.3.

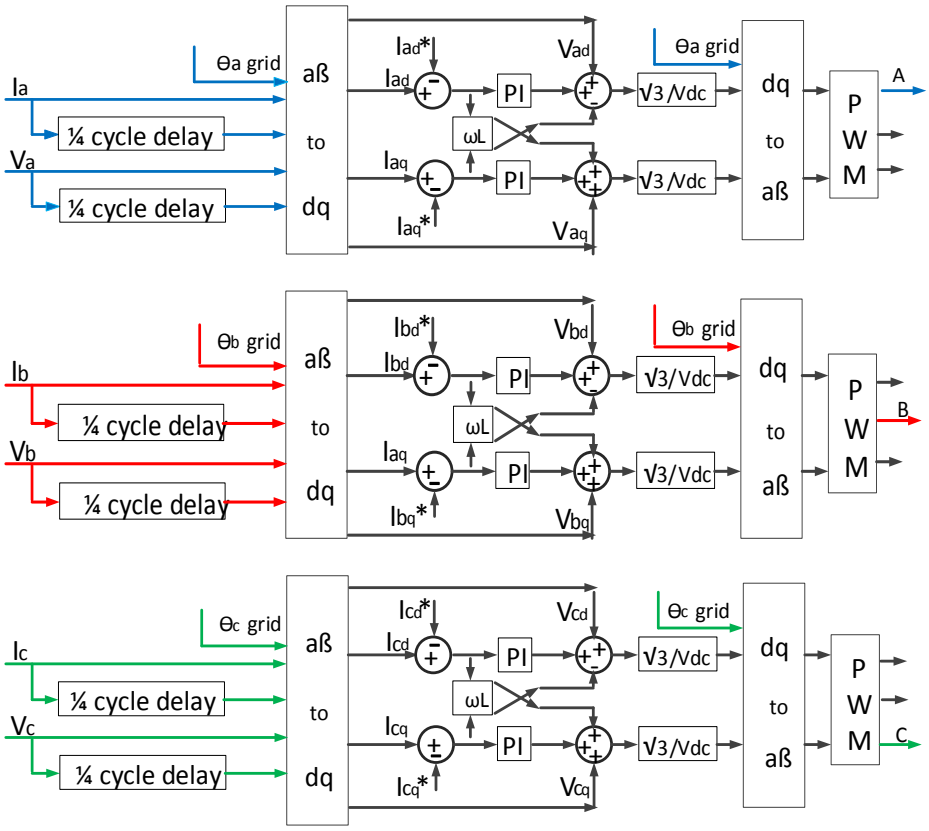

Figure 4.3: Grid Side Control for Impedance Measurement and Per Phase Reference Current Injection

To implement impedance estimation for each line, a factious phase is generated from a single phase quantity to create a two-phase system. These two phase signals will be orthogonal to each other and emulate Clarke's transformed signals, α and β [22]-[24]. Park's transformation is then applied to these signals to get the DC values for the PI controller and implement synchronous reference frame based control. The fictitious orthogonal signal (β) is created by introducing a 90° phase shift or a delay of ¼ cycle on the line phase with respect to the real phase (α). It is numerically represented as:

$$\left.\begin{aligned} X_\alpha &= X\sin\omega t \\ X_\beta &= X\sin(\omega t - 90) \end{aligned}\right\} \tag{4.29}$$

Or,

$$X_{\beta} = X_{\alpha(k-n)} \ , \ n = \frac{1}{4}\left(\frac{T}{T_s}\right) \tag{4.30}$$

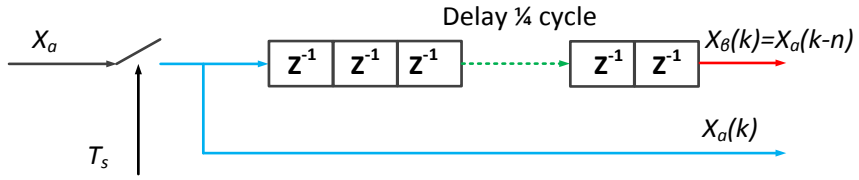

Figure 4.4: Quarter Cycle Delayed Real and Imaginary Phases

Where, *X* is the amplitude of a single phase current or voltage, *k* is the sample number, *T* is the fundamental period and T_s is the sample period. Real time voltage and current signals are extracted and each signal is delayed by a quarter-cycle to attain values in the *αβ* stationery reference frame. The abovementioned expressions are also illustrated as a Labview code in Fig. B.1 of Appendix-B. A single phase stationary reference model of the grid side converter along with the LC filter is shown in Fig. 4.5, where $V_{\alpha\beta}$ represents constant voltage supply and $u_{\alpha\beta}$ represents dependant voltage source.

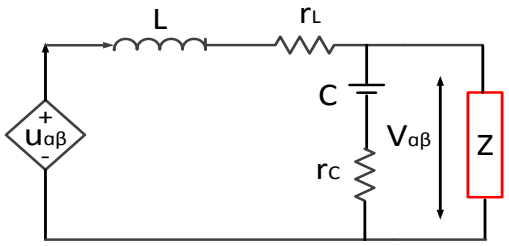

Figure 4.5: Stationary Reference Frame Single Phase Model

It is difficult to estimate the impedance in the stationary reference frame because both amplitude and phases should be measured to calculate the correct phasor subtraction. Therefore, signals are transformed into *dq* rotating reference frame where the reference frame rotates at the grid frequency with same phase as that of the grid voltages. Since *dq* transformation will be applied on each phase individually, the single phase *dq* model of the grid side converter can be developed as:

$$\begin{bmatrix} X_d \\ X_q \end{bmatrix} = T \begin{bmatrix} X_\alpha \\ X_\beta \end{bmatrix} \tag{4.31}$$

Where *T* is the transformation matrix,

$$\left.\begin{aligned} T &= \begin{bmatrix} \cos\omega t & \sin\omega t \\ -\sin\omega t & \cos\omega t \end{bmatrix} \\ T^{-1} &= \begin{bmatrix} \cos\omega t & -\sin\omega t \\ \sin\omega t & \cos\omega t \end{bmatrix} \end{aligned}\right\} \tag{4.32}$$

The capacitor voltage and inductor current can be expressed in rotating reference frame as:

Capacitor voltage:

$$\frac{d}{dt}\left(T^{-1}\begin{bmatrix} u_d \\ u_q \end{bmatrix}\right) = T^{-1}\begin{bmatrix} I_d \\ I_q \end{bmatrix}\left(\frac{1}{C(1+r_C/Z)}\right) - T^{-1}\begin{bmatrix} V_d \\ V_q \end{bmatrix}\left(\frac{1}{ZC(1+r_C/Z)}\right) \tag{4.33}$$

Inductor Current:

$$\frac{d}{dt}\left(T^{-1}\begin{bmatrix} I_d \\ I_q \end{bmatrix}\right) = T^{-1}\begin{bmatrix} u_d \\ u_q \end{bmatrix}\frac{1}{L} - T^{-1}\begin{bmatrix} I_d \\ I_q \end{bmatrix}\left(\frac{r_L}{L} + \frac{r_C}{1+r_C/Z}\right) - T^{-1}\begin{bmatrix} V_d \\ V_q \end{bmatrix}\left(\frac{1}{L} - \frac{r_C}{L(1+r_C/Z)}\right) \tag{4.34}$$

If,

$$\frac{d}{dt}T^{-1} = \begin{bmatrix} -\omega\sin\omega t & -\omega\cos\omega t \\ \omega\cos\omega t & -\omega\sin\omega t \end{bmatrix} \tag{4.35}$$

Then

$$T\frac{d}{dt}T^{-1} = \omega\begin{bmatrix} -\cos\omega t\sin\omega t + \sin\omega t\cos\omega t & -(\cos\omega t)^2 - (\sin\omega t)^2 \\ (\sin\omega t)^2 + (\cos\omega t)^2 & -\cos\omega t\sin\omega t + \sin\omega t\cos\omega t \end{bmatrix} \tag{4.36}$$

$$T\frac{d}{dt}T^{-1} = \omega\begin{bmatrix} 0 & -1 \\ 1 & 0 \end{bmatrix} = \begin{bmatrix} 0 & -\omega \\ \omega & 0 \end{bmatrix} \tag{4.37}$$

Inserting equation (4.37) into (4.33) and (4.34), would give:

$$\frac{d}{dt}\begin{bmatrix} u_d \\ u_q \end{bmatrix} = \begin{bmatrix} I_d \\ I_q \end{bmatrix}\left(\frac{1}{C(1+r_C/Z)}\right) + \begin{bmatrix} 0 & -\omega \\ \omega & 0 \end{bmatrix}\begin{bmatrix} V_d \\ V_q \end{bmatrix} - \begin{bmatrix} V_d \\ V_q \end{bmatrix}\left(\frac{r_C}{CZ(1+r_C/Z)}\right) \tag{4.38}$$

$$\frac{d}{dt}\begin{bmatrix} I_d \\ I_q \end{bmatrix} = \begin{bmatrix} u_d \\ u_q \end{bmatrix}\frac{1}{L} + \begin{bmatrix} 0 & -\omega \\ \omega & 0 \end{bmatrix}\begin{bmatrix} I_d \\ I_q \end{bmatrix} - \begin{bmatrix} I_d \\ I_q \end{bmatrix}\left(\frac{r_L}{L} + \frac{r_C}{L(1+r_C/Z)}\right) - \begin{bmatrix} V_d \\ V_q \end{bmatrix}\left(\frac{1}{L} - \frac{r_C}{LZ(1+r_C/Z)}\right) \tag{4.39}$$

By further simplifying and neglecting the parasitic resistances r_L and r_C, the cross coupling terms between the *dq* components can be formulated as:

$$\frac{d}{dt}\begin{bmatrix} V_d \\ V_q \end{bmatrix} = \frac{1}{C}\begin{bmatrix} I_d \\ I_q \end{bmatrix} + \begin{bmatrix} 0 & -\omega \\ \omega & 0 \end{bmatrix}\begin{bmatrix} V_d \\ V_q \end{bmatrix} \tag{4.40}$$

$$\frac{d}{dt}\begin{bmatrix} I_d \\ I_q \end{bmatrix} = \frac{1}{L}\begin{bmatrix} u_d \\ u_q \end{bmatrix} + \begin{bmatrix} 0 & -\omega \\ \omega & 0 \end{bmatrix}\begin{bmatrix} I_d \\ I_q \end{bmatrix} - \frac{1}{L}\begin{bmatrix} V_d \\ V_q \end{bmatrix} \tag{4.41}$$

Equations (4.40) and (4.41) can be represented in Fig. 4.6 below:

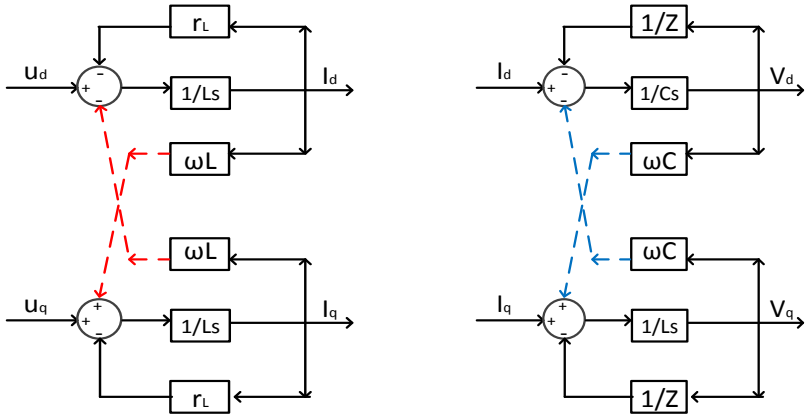

Figure 4.6: GSC and the Filter coupling components: (a) Inductor Currents, (b) Capacitor Voltages

Since the input voltage is the capacitor voltage and the output current is the filter (inductor) current. The capacitor voltages are ignored for the final *dq* decoupling model implemented in this thesis. Fig. B.2 in Appendix-B illustrates the Labview code for the decoupling of current components. The control technique shown above helps in gaining access to each phase individually. It is quite useful in case of unbalanced grid voltages because each phase voltage is used as an individual feedback signal and single phase PLLs are implemented to extract the angle information. I_d* and I_q* values are then perturbed accordingly to perform impedance measurement on each phase.

The complete hardware structure considered for this thesis consists of two parts. The left half contains a turbine emulator and a PMSG connected to the machine side converter (MSC). The right half comprises of a grid side converter (GSC) connected to a Thevenin model of a weak grid through an LC filter. A block diagram of the complete setup is shown in Fig. 4.7 below.

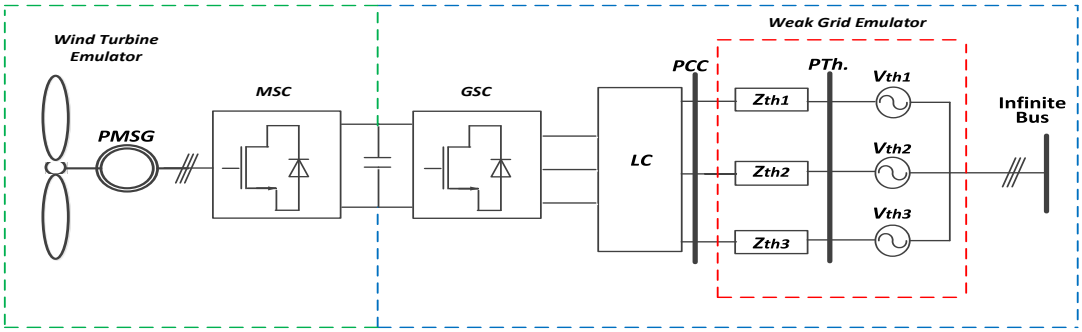

Figure 4.7: Complete System Block Diagram

4.5.2 The Impedance Estimation

To validate the analysis and to implement it in a more realistic way, a three phase programmable AC supply with negligible line impedance is used to emulate the weak grid condition. However, for correct impedance measurement and to increase the weak grid effect, an extra set of unbalanced impedances with high X/R values is connected. With reference to Fig. 4.8, it can be seen that the output impedance of the power supply emulating the weak grid is balanced and its value is very low i.e $2m\Omega$ and $2\mu H$. Therefore, a separate set of unbalanced impedances with comparatively higher reactance values is connected in series with each line, to act as Thevenin impedances. The impedance values are selected (Z_{th1}=2.62Ω, Z_{th2}=1.05Ω, Z_{th3}=1.38Ω) in order to give higher X/R (X_1/R_1=> 3.84, X_2/R_2=> 3.22, X_3/R_3=>3.85) ratios with approximated SCR value of '*3*' to emulate a weak grid scenario.

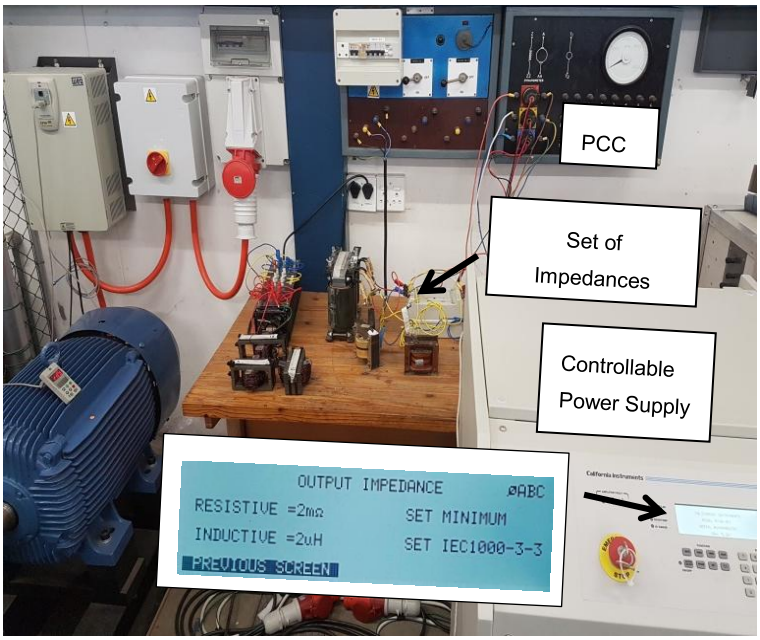

Figure 4.8: Weak Grid Emulator: Impedance Setup and the Controllable Power Supply

The parameters of the experimental setup are given below:

- Nominal active power P per phase: 990W
- Nominal reactive power Q per phase: 0Var
- Active power step ΔP : 50% of P
- Reactive power step ΔQ: is equal to ΔP

To calculate the impedance of the system under consideration, an automated disturbance is created on both I_d and I_q with the help of control structure shown in Fig. 4.3. At initial state, the rated currents are I_d =4.4A and I_q=0. It is to be noted that each line's impedance should be considered constant during its estimation period. Subsequently the I_d* and I_q* reference values are perturbed in such a way that ΔI_d and ΔI_q are adjusted to be 2.2A to implement the resultant power variations (ΔP and ΔQ).

It is also to be noted that the accuracy of estimation depends on the amount of power variation and the time interval ΔT it is being applied for. With the injection of disturbance, both resistance and inductance could get affected by a non-negligible value. Therefore, the points of work should not be too near. The accuracy of the estimation increases with the delay between the estimation points, and for that, 15 seconds are allocated for each perturbation.

To understand the impedance estimation routine, a flowchart is illustrated in Fig. 4.9. A current step is introduced to create the disturbance on each phase so that the voltage variation and the impedance can be measured. For individual phase measurements, the step current injections and the measurements take 15sec each and the transition time between the phases is set to be 40sec. In this thesis, the automated method of injection of disturbances and calculation of impedances completes within 270sec. The time duration of the complete procedure could also be improved; however, it is out of scope of the current research and can be considered as a separate topic for research in future.

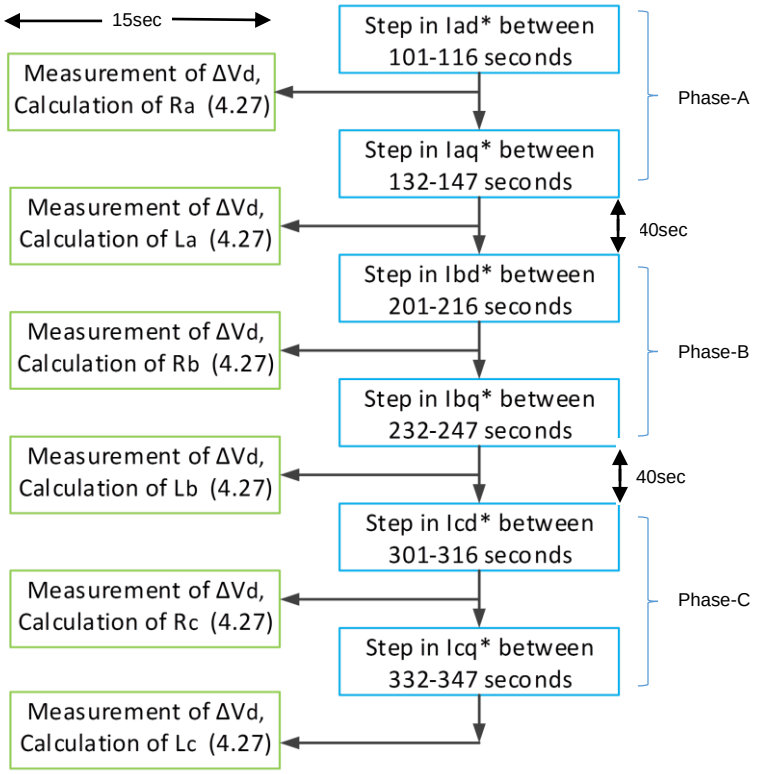

Figure 4.9: Impedance Estimation Procedure

For further explanation, Fig. 4.10-4.12 can be considered. In Fig. 4.10, the *d*-axis current I_{ad}* is perturbed between *101-116* seconds, likewise the *q*-axis current I_{aq}* is changed between *132-147* seconds for the impedance measurement on phase-*A*. Similarly, in Fig. 4.11, the estimation period for phase-*B* is between *201-247* seconds and for phase-*C*, it is shown between *301-347* seconds in Fig. 4.12. The ΔI_d and ΔI_q are adjusted to be 2.2A and resulting voltage

variations at the PCC are also shown in Fig. 4.10-4.12. The ΔV_d values are then applied to equation (4.27) for both resistive and inductive values estimation.

With the injection of disturbance, the estimated values of the impedance components usually fluctuate from their mean values. Since the focus of this thesis is to investigate the calculation and injection of the optimal currents, not much consideration has been given to the filter design and its components. The calculation process only starts when the synchronous voltages and currents have been sampled and during this, the impedance components start to stabilise just close to second point of work. Thus, the sampling point is also important because it decides if the estimated value is close or not to the actual value.

Like other impedance components, the power variation also impacts the DC link voltage. This means that the system components should be allowed to get back to their previous state while the estimation is being made. It is important that once the system attains its steady state after the first disturbance, no reactive power oscillation should be introduced before restarting a new estimation. If this condition is not met, the next estimation will lead to lower accuracy, the capacitor value also plays an important role, especially when the power variation takes long to reach its steady state after a perturbation. Mostly, the DC link capacitors are designed according to the system rating and the reactive power requirement. However, selecting the minimum value capacitance could increase the dynamic response of the system at the cost of unwanted reactive power oscillations. Consequently, a good design approach needs to be adopted to achieve a decent time response with reduced reactive power transients. As mentioned above, Fig. 4.10-4.12 (a) present the perturbed current references to implement power variations on the phases A, B & C. In Fig. 4.10-4.12 (c), the DC link voltage response is illustrated and small voltage transients can be seen when reactive current is injected. Fig. 4.10-4.12 (d) depict the resultant *d*-axis voltage variations at two points for each perturbation. Whereas, Fig. 4.10-4.12 (e) & (f) are the zoomed-in screenshots of the voltage variations for the measurement of resistances and inductances respectively.

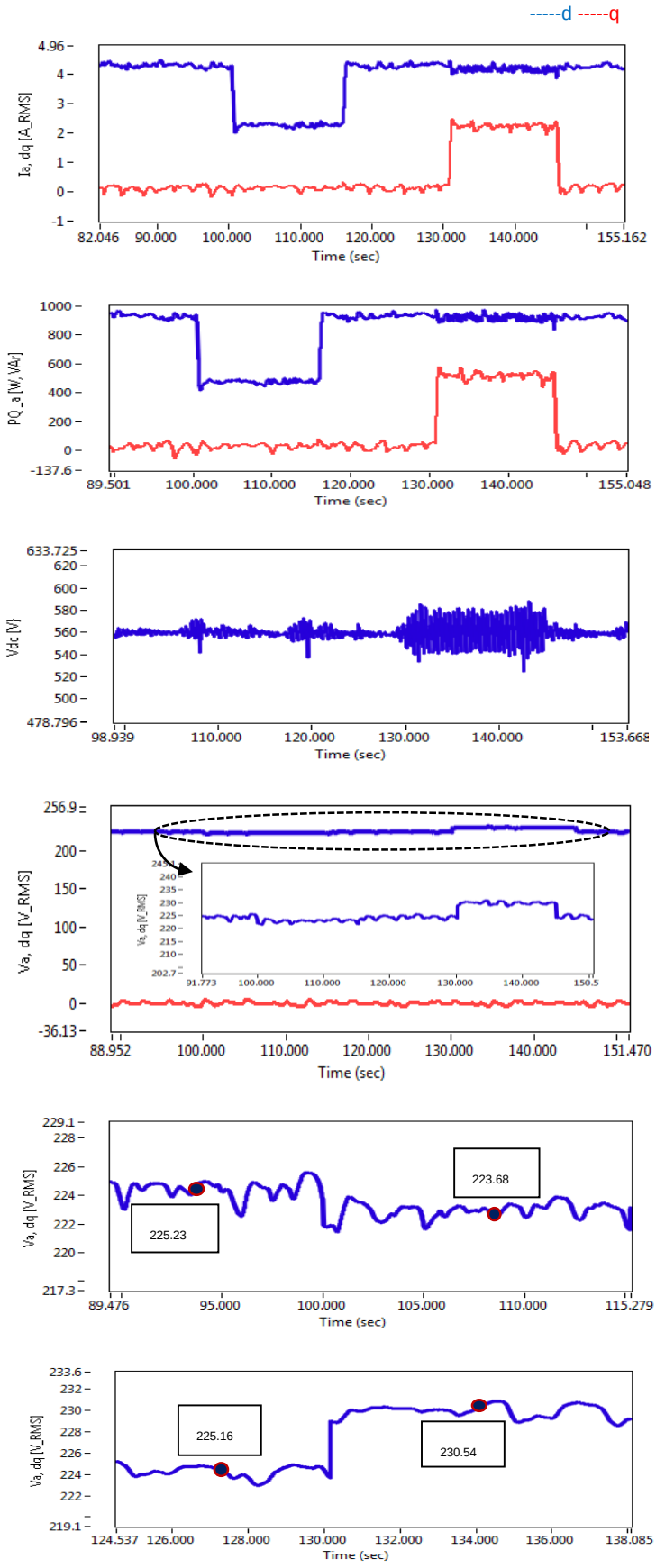

Figure 4.10: Phase A: (a) Current perturbations, (b) Power perturbations, (c) DC link Voltage Variation, (d) Voltage perturbations, (e) ΔV_d (zoomed-in) for resistance measurement, (f) ΔV_d (zoomed-in) for inductance measurement

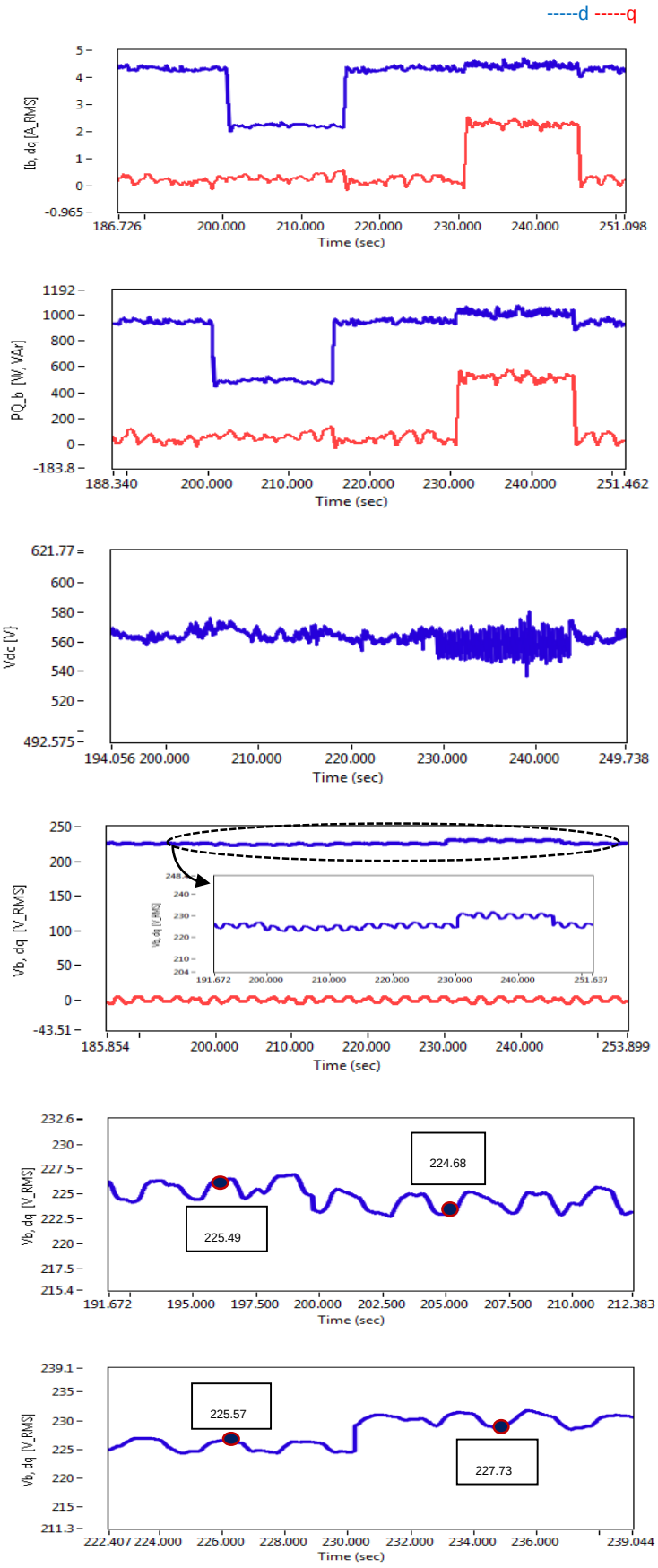

Figure 4.11: Phase B: (a) Current perturbations, (b) Power perturbations, (c) DC link Voltage Variation, (d) Voltage perturbations, (e) ΔV_d (zoomed-in) for resistance measurement, (f) ΔV_d (zoomed-in) for inductance measurement

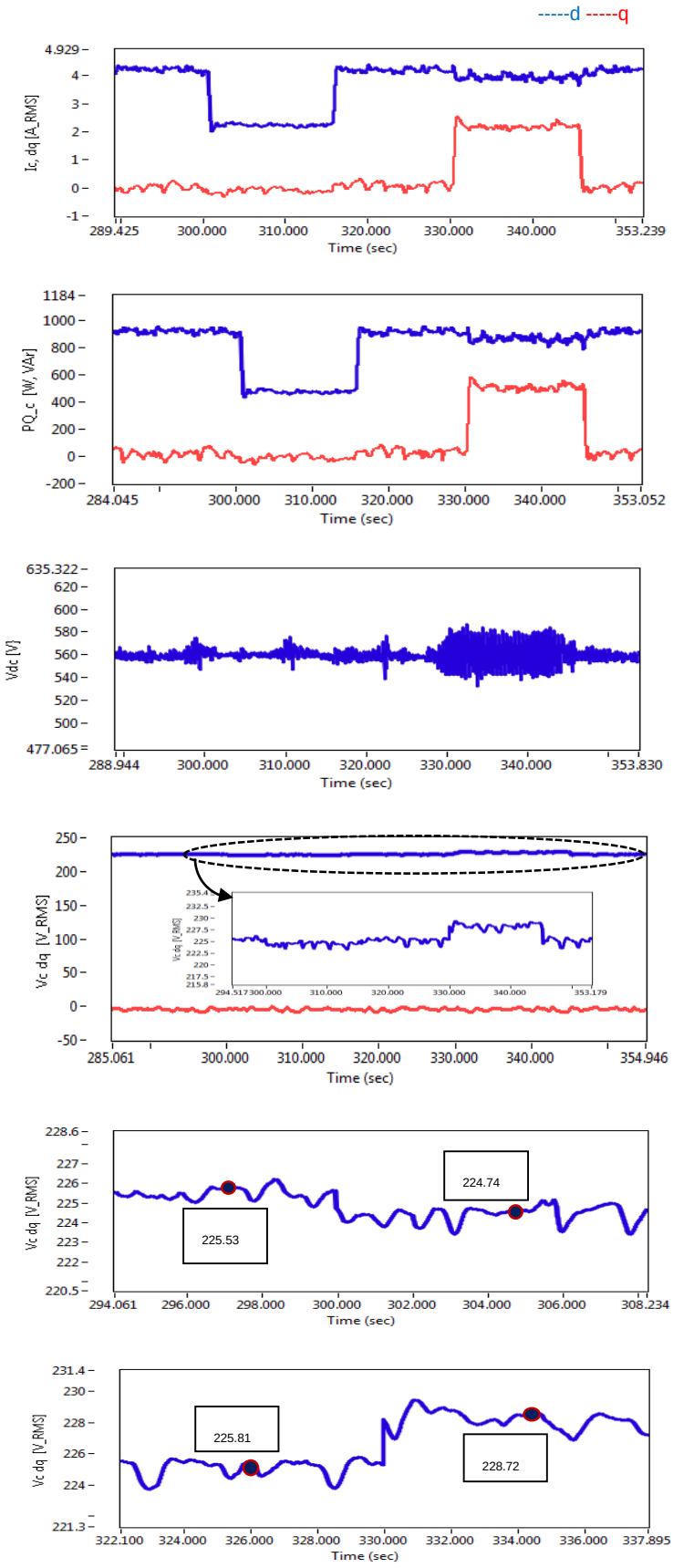

Figure 4.12: Phase C: (a) Current perturbations, (b) Power perturbations, (c) DC link Voltage Variation, (d) Voltage perturbations, (e) ΔV_d (zoomed-in) for resistance measurement, (f) ΔV_d (zoomed-in) for inductance measurement

The data points shown in Fig. 4.10-4.12 (e) & (f) are the two operating voltage points. These values can be read easily with the help of data point locator onto the interfacing software window. Once extracted, these values are applied in equation (4.27) to measure the resistance and inductance on each phase. The comparison between the actual and estimated values is summarized in Table 4.1 and the estimation error is shown to be less than 10% for resistance measurements and less than 4% for inductance measurements. The percentage accuracy of the smaller component values is reduced and this could be considered as one limitation of the discussed technique. However, considering the case study and the hardware limitations in the lab (discussed in chapter-7), this technique is still applied in this thesis.

Table 4.1. Comparison between the Actual and Estimated Values of the Grid Impedance

Parameters	**$R_{th1}\Omega$**			**L_{th1} (mH)**			**$Z_{th1}\Omega$**
Description	**Actual Value**	**Estimated Value**	**% Error**	**Actual Value**	**Estimated Value**	**% Error**	**Actual Value**
Values	0.66	0.70	6.06	8.10	7.78	3.95	2.62
Parameters	**$R_{th2}\Omega$**			**L_{th2} (mH)**			**$Z_{th2}\Omega$**
Description	**Actual Value**	**Estimated Value**	**% Error**	**Actual Value**	**Estimated Value**	**% Error**	**Actual Value**
Values	0.31	0.34	9.67	3.20	3.12	2.50	1.05
Parameters	**$R_{th3}\Omega$**			**L_{th3} (mH)**			**$Z_{th2}\Omega$**
Description	**Actual Value**	**Estimated Value**	**% Error**	**Actual Value**	**Estimated Value**	**% Error**	**Actual Value**
Values	0.35	0.37	5.71	4.30	4.21	2.09	1.38

4.6 Conclusion

This chapter shows why grid impedance estimation is an important factor to be known in advance, especially when designing a control system. Conventional and the recently introduced techniques on grid impedance estimation are reviewed. The PQ variation technique is chosen and its per phase implementation is proposed. Single phase transformation model of a three phase system is illustrated in *dq* rotating reference frame. Experimental investigation is done on a set of known impedances to validate the scheme and the designed control. Furthermore, to compute the percentage calculation error of the proposed technique, a comparison is shown between actual and estimated values of the impedances.

4.7 References

[1] M Malengret, T.C Gaunt CT "General theory of average power for multi-phase systems with distortion, unbalance and direct current components. *Electric. Power Systems Research, j.epsr.* (Vol. 84, pp 224-230) 2011.

[2] Johannsson H., Assesments of Power Systems, WO 2012/163979 A2: *International Application Published Under The Patent Coorperation Treaty (PCT),* 2011.

[3] Pinzon, C., Method and device for assessing the stability of an electric power transmission network *, EP 1211 775 A1 : European Patent Office,* 2000.

[4] *Adrain V.*Timbusm Pedro Rodriguez, Remus Teodorescu, Mihai Ciobotaru. *Line Impedance Estimation using Active and Reactive Power Variations.* 2007.

[5] Je-Hee Cho, Ki-Young Choi, Yong-Wook Kim, Rae Young Kim "A novel P-Q variations method using a decoupled injection of reference currents for a precise estimation of grid impedance", *IEEE Energy Conversion Congress and Exposition (ECCE), 2014.*

[6] L. Asiminoaei, R. Teodorescu, F. Blaabjerg, and U. Borup, "A new method of on-line grid impedance estimation for PV inverters," in *Proc.of APEC'04*, vol. 3, pp. 1527–1533, 2004.

[7] M. Ciobotaru, R. Teodorescu, P. Rodriguez, A. Timbus and F. Blaabjerg, "Online grid impedance estimation for single-phase gridconnected systems using P-Q variations," *Proc. of PESC'07, pp. 2306-2312, Jun. 2007.*

[8] Georgakis, D.; Papathanassiou, S.; Hatziargyriou, N.; Engler, A.; Hardt, C., "Operation of a prototype microgrid system based on micro-sources quipped with fast-acting power electronics interfaces," *Power Electronics Specialists Conference, 2004. PESC 04. 2004 IEEE 35th Annual, vol.4, pp. 2521- 2526.*

[9] Sumner, M.; Palethorpe, B.; Thomas, D.; Zanchetta, P.; Di Piazza, M.C., "Estimation of power supply harmonic impedance using a controlled voltage disturbance," *IEEE 32nd Annual Power Electronics Specialists Conference, 2001.PESC. 2001, vol.2, pp. 522-527.*

[10] Jing Yang, Tongwen Chen, Min Wu. *Online Impedance Matrix Estimation of interconnected Power Systems, 2009.*

[11] Marco Liserre, Frede Blaabjerg, Remus Teodorescu. *Grid impedance detection via excitation of LCL-filter resonance.* 2005.

[12] Guoqiao Shen, Jun Zhang, Xiao Li, Chengrui Du, Dehong Xu. *Current control optimization for grid-tied inverters with grid impedance estimation.* 2010.

[13] Roberto Petrella, Alessandro Revelant, Piero Stocco. *Advances on inter-harmonic variable frequency injection-based grid-impedance estimation methods suitable for PV inverters.*2009.

[14] Mihai Ciobotaru, Remus Teodorescu, Pedro Rodriguez, Adrian Timbus, Frede Blaabjerg. *Online grid impedance estimation for single-phase grid-connected systems using PQ variations.* 2007.

[15] H. Akagi, Y. Kanazawa, and A. Nabae. *Generalized theory of the instantaneous reactive power in three-phase circuits*, Proc. Int. Power Electron. Conf. (JIEE IPEC), pp.1375 - 1386, 1983.

[16] X.Q. Guo X. Zhang B.C. Wang et al. "Asymmetrical grid fault ride-through strategy of three-phase grid-connected inverter considering network impedance impact in low-voltage grid" *IEEE Trans. Power Electron. vol. 29 no. 3 pp. 1064-1068* 2014.

[17] A. Ghanem, M. Rashed, M. Sumner, M. A. Elsayes and I. I. I. Mansy, "Grid impedance estimation for islanding detection and adaptive control of converters," in *IET Power Electronics, vol. 10, no. 11, pp. 1279-1288, 9 9* 2017.

[18] H. Akagi, S. Ogasawara. *The theory of instantaneous power in three-phase four-wire systems: a comprehensive approach.* 1999.

[19] Adrian. V. Timbus, Pedro Rodriguez, Remus Teodorescu, Mihai Ciobotaru "Line Impedance Estimation Using Active and Reactive Power Variations" *IEEE Power Electronics Specialists Conference, PESC 2017.*

[20] V.Blasko and V.Kaura "A new mathematical model and control of a three phase AC-DC voltage source converter" *IEEE Trans. Power Electronics, vol.12, no.1, pp. 116-123, Jan. 1997.*

[21] *P. L. Carotenuto "*Grid impedance estimation in PV grid-connected systems through PQ variation methods A Simulink-based approach," Universitat Politecnica de Catalunya, MSc Thesis 2011.

[22] B. Crowhurst, E. El-Saadany, L. El Chaar and L. Lamont, "Single-phase grid-tie inverter control using DQ transform for active and reactive load power compensation", *IEEE International Conference on Power and Energy (PECon), pp. 489-494,* 2010.

[23] G. Franceschini, E. Lorenzani, C. Tassoni and A. Bellini, "Synchronous reference frame grid current control for single-phase photovoltaic converters", *IEEE Annual Meeting on Industry Applications Society (IAS'08), pp. 1-7,* 2008,

[24] N. A. Ninad, L. A. C. Lopes and A. Rufer, "A vector controlled single-phase voltage source inverter with enhanced dynamic response", *IEEE International Symposium on Industrial Electronics (ISIE),* 2010.

Chapter 5
Optimal Current Injection during Balanced/Symmetrical Grid Voltages

5.1 Introduction

With the progress in technology, it is becoming easier and cheaper to harness energy from different sources and introduce it into the grid at various distributed points. This energy is not only injected into the grid to supply the local loads at the PCC but can also provide power to other points on the network, where power is also required for consumption. The conventional method of power injection was that the current remains in phase with voltage angle. This can be done with the aid of power converters by controlling the phase-angle of the currents in each wire. However, this is not the most efficient method of power transfer in case of a weak grid [1].

If a Thevenin model of a weak distributed power network is considered, characteristics of impedance as well as voltage on a line becomes time dependent and changes with any variation in the connected load. As a result, each line would require different magnitudes of current depending on the nature of the load [2]. Multiple techniques have been devised to meet these conditions where standard definitions of power quality are adopted [3]-[5]. These techniques are particular cases of the general power theory with balanced current flow and equal load impedances. However, the research conducted in [6] and [7] reviews the existing power theories for multiphase systems with unbalanced line voltages and loads. Moreover, it also derives a generalized algorithm for calculating instantaneous and average powers for Thevenin equivalent networks with minimum distribution losses. The theory presented in [6] and [7] is further extended and published as a patent [8].

The objective of this chapter is to expand the research presented in [6]-[9] and validate it on a real time PMSG based WECS connected to a weak AC grid. The main aim is to utilize the existing back-to-back converters topology as an intelligent system that can inspect a MV distribution line, detect changes in the network parameters and redistribute the optimal currents so as to introduce the available active power into a network with minimal losses.

Considering that the PMSG based WECSs in remote areas, do not always have shunt connected reactive power support. The discussed technique in this chapter which also covers the main contribution of this thesis, redistributes the currents so as to maximize the active power transfer. This could make it more suitable for small scale wind turbines where limited ancillary support is available to assist the grid during unbalance. However, its applications can be extended to large scale wind turbines as well [8].

5.2 Literature Review on Optimal Power Flow

The definition of optimal power flow has evolved significantly over the past few years. In the beginning it was characterized as the minimization of amount of power required by the generators to reduce the amount of fuel consumed by the generators used for electricity generation [10]-[13]. This had a direct impact on the cost of power generation, thereby the focus was only on the economic optimisation of power. Subsequently cheap fuel was used by the generating units, however transmission losses appeared to be another problem. Hence, optimal power started to be defined as a function of cost of fuel and transmission losses [14]. Later on multiple definitions were developed based on optimization functions where each individual function performed iteratively until an optimum solution was found.

Initially the idea of transmission losses was not included as a function of incremental cost. In [15] it was explained how the power network was made up of several generating units with their own cost functions. It was further shown that the fuel cost functions were also based on the function of load' voltages. This method was improved in later researches and partial derivative was included with respect to the power generation units. The partial derivative became part of the loss reduction formula which applied number of assumptions to get to the approximated results

instead of an exact solution. Number of simplifications were then applied to the definitions by using phase voltages instead of scalar quantities and rate of change of fuel cost was also set equal to zero. Eventually, a set of non-algebraic equations were developed which is now called the famous Newton-Raphson method.

With respect to power optimization, combination of active and reactive powers were started to be applied to enhance the voltage profiles with reduced real power losses on a transmission line [16]. After dealing with the transmission losses and cost functions, the location also joined in as an additional functional. By reducing the transmission losses and having the power generated at an optimal location where it is being required by the loads, also assisted in increasing the overall efficiency.

In [17], optimised reactive power distribution is discussed. It is mentioned that the linear reactive power optimization regulates the system voltage and reduces the real power losses. According to that, the optimization could be achieved by varying the transformer taps, generator voltages and the shunt capacitors.

An approach discussed in [18] builds up optimal power system parameters. The technique determines the power system loss sensitivity by defining the steady state stability functions. Similarly, another technique uses the sensitivity of the system as 'Method of Box' to reduce the voltage deviations and the system losses [19].

Another factor which is today's concern is the carbon free energy emission. Therefore, the focus on green energy has also become an important factor for power optimization [20]. It has also been part of the past research, for instance in [15] theories were developed for the reduced costs of different fuels and their impact on the environment was studied based on their individual cost functions.

The focus of the power optimization was then redirected in Grigby's therory. According to the theory, a system hierarchy was developed and based on that optimal power was defined. For instance, the reliability was ranked higher than the economic value of the system. Which means, as soon as the system becomes stable, the focus will shift to the economic optimization [21].

The definition of optimization completely changes in case of micro-grid applications. For instance in case of a PV-system, the focus remains on maximum power output with least incurred losses. This assists in least aging of batteries and better cost management of the grid. The best way to implement this is to apply limit to the peak power exchange between the grid and the customer which is called peak load shaving. Peak load shaving also offers advantages such as by limiting the number of peak power generation units, efficiency of the system increases and due to less number of units it also allows less carbon emission. Consequently, the definition of power optimization depends whether if you are a system operator or a small de-regulated generating unit operator [22].

Another explanation given in [23] discusses two functions, one for power system transmission losses and the other for load balancing of the system. Both functions were set to be different even though they were dependant on the same variables such as reactive and active powers. Reactive power in the abovementioned case does not really impact the fuel cost of generation units. However, it weakens the system's equipment by requiring large amount of power than the rated power [24]. That means the reactive power has a direct influence on the cost of the system, which needs to be optimised and kept within the limits to avoid size constraints of the systems.

Moreover, self-healing methods of the grids are also discussed in [25]. The described techniques not only assist in power optimization but also protect the network during power outages. Where the necessary variables communicate with the system operator at each node and necessary computations are made before performing any action. The pre-computations are usually required to detect if any changes occur in the network. The addition of degeneration units must be known to the central control of the power station so that the power can be transferred optimally to the point where it is required. This back and forth communication is an application of smart grids, where each node can communicate with the central control unit and performed actions are pre-calculated. The objective of smart grids is to provide freedom to the operators to monitor the grid in real time and predict the changes. This assists the operators to make decisions wisely and enhance the grid stability and reliability by providing simple optimal power flow solutions [26].

With the increase of non-linear devices such as electronically switched loads, unbalanced loads, data processing equipment as well as industrial power rectifiers and inverters, power supply quality has become a serious concern. These devices cause harmonic currents to flow in the system and result in damaging the equipment [27]. Therefore, in recent literature [21] the definition of power optimization has been broadened from safety and reliability to economic supply. The new deeper definition of economic supply is based on the cost of damage occurred due to non-linear devices, hence it also adds to the overall cost function of the system. Since power system quality impacts the performance and life of the equipment. Multiple methods have been developed to improve the network quality by rectifying the distorted signal into a DC signal and invert it again for a cleaner output [28].

5.3 Literature Review on Optimal Power Flow Methods

From the aforementioned discussion, each optimal power flow (OPF) definition can be implemented according to its own particular method. These methods consist of a set of mathematical equations which could be both linear and non-linear. For instance in [29] the OPF solution is classified as:

a) Minimization of total generation cost
b) Minimization of system's active power losses
c) Multi-objective function (both a and b)

Depending on the classes mentioned above, solutions are provided which linearize the first and second order derivatives of the object functions to formulate their own search directions. To implement an OPF solution, the most important characteristic is its computation time. If a technique takes longer to perform the actions compared to the dynamic changes happening in the network then the technique is considered to be useless. The section below discusses a few famous OPF techniques.

5.3.1 Newton Method

The method was first defined in [30] and later on improved in [29]. According to the method, approximated voltage is calculated to develop series of complex power equations based on the changes happening in the network. The voltages are approximated by Gaussian elimination and back-substation methods which transform the complex power solution into voltage angle and magnitude values. Eventually the transformation made is checked again to confirm if a correct solution is found.

The method explained in [30] does not consume a lot of computational memory however reduction methods can still be applied to optimise the memory utilisation. Its algorithm is shown in Fig. 5.1 below. It is further mentioned that the method does not have an ability to communicate with the negative transfer impedance such as in the case of three winding transformers.

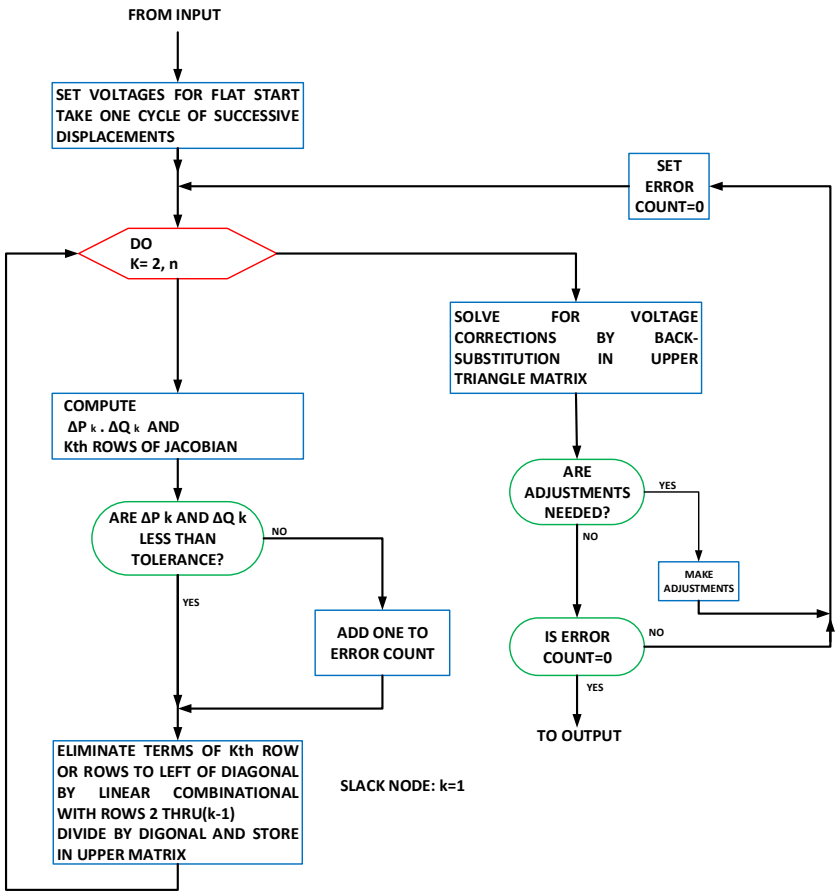

Figure 5.1: Flow-chart of the Newton Method Algorithm [30]

To simplify this method, another technique is formulated in [31] which reduces the size of the matrix and thereby minimises the memory usage. The research conducted in [31] also claims that to achieve ultimate optimization, every possibility should be considered as an option at each node on the network. However, considering the complexity of the network, it is not always possible to monitor each node individually. It further discusses three methods for optimal power approximation of the network. According to the first method, each node must be ranked according the number of branches connected to the node and at the same time ignoring the elimination steps. This is simple to implement and quick to execute. The second method is based on the elimination process, where nodes with least number of connected branches are omitted. The last method is the most complicated and least used, where the node creates new equivalent branches at each step and it is applied by performing calculations at every possible step for each node.

5.3.2 Gradient and Lagrangian Method

The gradient method described in [32] follows almost the same method explained above, however it measures the behaviour at each system's change, e.g. transformer tap settings, change in nodal voltages, load variation etc. The idea is to apply gradient on the function and then control variables are changed to locate the negative gradient which gives values in descending order. When the negative gradient value approaches zero, it implies no change in the control variables hence considered to be as an optimum point. An example of gradient method algorithm is given in Fig. 5.2.

In [33] Lagrangian multipliers are introduced to perform economic analysis of active and reactive power generation. These are used to describe the dynamics of the system and then gradient is applied to find the optimum solution. This technique assists in estimating the line loads and node voltages before any changes happen in the generating system. This information is further used to perform loss reduction on the transmission lines. Another technique is explained in [34] which is applied along with the gradient method. It derives two computational methods where sensitivity relationship between the control variables is determined to work out the optimal solution.

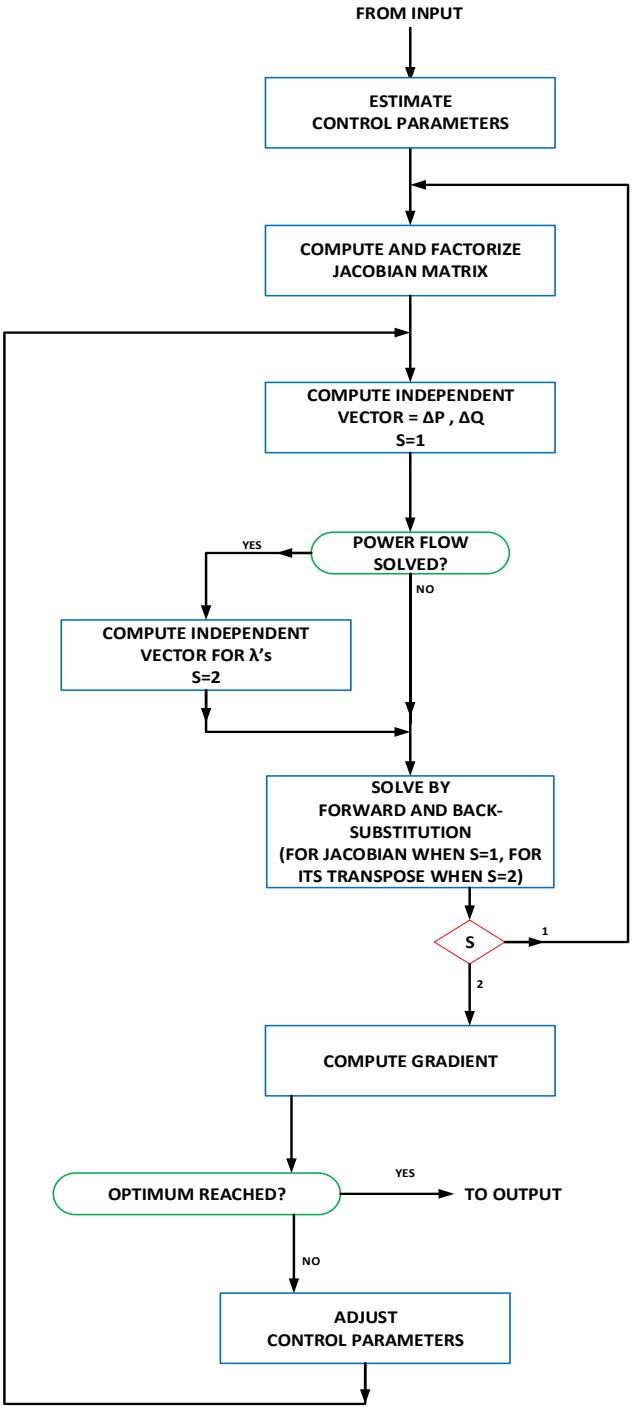

Figure 5.2: Flow-chart of the Gradient Method Algorithm [32]

It is further mentioned in [32] that the gradient method only works if linearity of the system equations is kept intact. In case where additional changes are applied in the network, these

equations can be transformed from first order to second order, however it will increase the computation time.

5.3.3 Modified Interior Point Method

The interior point method is considered to be the most efficient technique [35]. The cost functions involved in this method can be written in terms of quadratic equations. Due to its flexibility, the equations could extend to second order functions by using Taylor's expansion without curtailing any limit error. Furthermore, the Hessian product is also a constant value for higher order functions. This technique can be explained in number of steps, first it measures the grid voltage and converts it into rectangular coordinates. Then, it selects a node as a starting point and implements the Newton method. After that, Newton direction is determined which assists in computing the updated step length changes. If the step length is close to zero, it will be considered as an optimum solution otherwise the whole method is repeated again.

In [29], it has been mentioned that this is the most implemented technique of today because it depends on the real time control variables and not on the preordained values of the network functions. Furthermore, this technique also does not require a feasible starting point to converge [36]. According to [37], it is indeed an acceptable technique however only provides generalized approximations of the optimal solution.

5.3.4 Phase Shifting Method

Flexible AC transmission systems (FACTS) have emerged as a recently developed modern way to enhance the overall performance of a system based on the reactive power injection. It comprises of capacitor banks, phase shifters and unified power flow controllers to manipulate the characteristics of a grid to meet certain requirements. With the modern advancements in power electronics, the availability of FACTS devices have become easier to be integrated to the system as a supplementary equipment. These are utilised in a system to enhance the overall performance by increasing the stability margins and reducing the transmission power losses.

Implementation of OPF using phase shifting method also increases the security of a network. For instance it can locate the presence of capacitor or inductor banks in a network to be utilised at a point where power compensation is required [29]. Furthermore, reduction of active power is also a big concern when integrating the FACTS devices because increase in reactive power may decrease the active power which might be required by the grid [38].

5.3.5 Particle Swarm Optimization Method

Particle swarm optimisation (PSO) method has an advantage over the Gradient method because it can locate both local and global minimum values for optimal solutions. It further offers a benefit of not being dependant on the starting variables and can perform optimally with limited information [39]-[41]. The theme of this method is inspired from the particles analogy floating through the space and looking for direction and speed. When two particles come across each other they communicate and share information about the optimal locations and hence arrive at the new best [29].

5.3.6 Smart Grids

Smart grids offer the features of future power grids. In smart grids, each node can communicate with the central processing unit and based on the retrieved information functions are performed [42]. With the transfer of active information, the security as well as the power flow in a network can be optimized. The central control functions gain control on each node and assign tasks according to the requirement. Smarts grids are undoubtedly faster and offer best OPF solutions. However, their performance rely on the advanced technologies which are still needed to be implemented in most parts of the world [43]. A brief comparison is shown between the conventional and the smart grids in Table 5.1.

Table 5.1. Comparison between Conventional and Smart Grids [42].

Conventional Grids	Smart Grids
Electromechanical	Digital
One-Way Communication	Two-Way Communication
Centralised Generation	Distributed Generation
Hierarchical	Network
Few Sensors	Sensors Throughout
Blind	Self-Monitoring
Manual Restoration	Self-Healing
Failures and Blackouts	Adaptive and Islanding
Manual Check/Test	Remote Check/Test
Limited Control	Pervasive Control

All the aforementioned techniques are formulated to calculate the total generation cost and the power losses at transmission level. In this thesis, the above mentioned optimal control variables which are used to calculate the power losses are scaled down from transmission to distribution level. Hence, the power losses at distribution level can be minimized by gaining control over the active/reactive current components and then redistributing them optimally into the network to achieve optimal current flow (OCF).

This thesis focuses on OCF solution in a wind energy system because the OPF is highly constrained with large dimensional nonlinear optimization problem, which is normally difficult to solve for large sized practical power systems. Furthermore, the OPF inflicts more cost to the power generation and maintenance of power balance at transmission level. Whereas, OCF tends to

remove all the components contributing to the power loss at distribution level and can be called a subset of OPF.

In case of OCF, there are definite controllable variables, which are adjusted to achieve the objective functions. These functions comprise of gird impedance estimation and calculation of coordinated optimal currents to ensure maximum power transfer into the grid. Furthermore, overall power losses are kept low at each node of the system.

5.4 Literature Review on Definition of Apparent Power

With an increase in non-linear devices and loads into the power network, inaccuracies of particular power theories have become a significant matter. From past twenty years researchers have been proposing multiple definitions of apparent power based on the problems and their suggested solutions. In [44], the author has addressed the issues faced when defining apparent power conversion from single phase to three phase system under asymmetrical conditions. In [45], a concept of physical interpretation of apparent power has been discussed given that various authors consider different reference points when measuring voltages which leads to dubious results. It is further mentioned that all non-sinusoidal power theories will have no significance until and unless apparent power has a physical meaning. However, the abovementioned statement is countered in [46], where it is said that the ambiguous apparent power also exists in three phase sinusoidal systems.

The research conducted in [47], proposes a definition based on four conditions for an m-wire system with unequal wire resistances but balanced loading. An example is demonstrated in [48] to show the ineffectiveness of the definitions for the unbalanced systems during fault conditions. The RMS current can be decomposed into active and reactive currents. The reactive current can be further decomposed to orthogonal components which could be utilised for useful applications such as reactive power compensation.

A new variable is defined in [49] which converts the theory of instantaneous power into RMS domain represented as a collective admittance and two components of reactive power. First the reactive current is split into two components in instantaneous domain. Then, the conversion is

applied which gives three current components in RMS domain; i.e. one active and two reactive components. Another concept is introduced in [50] which is based on the early definition of apparent power in a three-phase system. It is stated as "the maximum power that can be delivered by a voltage source at a particular instant whilst the total line losses are kept constant." The defined apparent power in a three-phase system carries same physical value equal to the product of RMS voltage and current in a single-phase system.

To explain that, a three-phase system is considered and the loads are replaced by balanced resistive loads so as to keep the line losses equal. The power delivered to the system would be $P=R\ (I_1^2+ I_2^2+ I_3^2)$ with an apparent power, $S=3VI =(V_1^2+ V_2^2+ V_3^2)^{1/2}. (I_1^2+ I_2^2+ I_3^2)^{1/2}$. In linear algebra this can also be represented as the product of magnitude of two vectors $S = \|V\|.\|I\|$. This definition was later on majorly used for non-sinusoidal systems.

A theory is presented in [51] for the linear non-sinusoidal single-phase systems. According to the theory, it is claimed that the analysis done in frequency domain offers better physical interpretation of the power modules and improves the power factor. In [52], the idea is extended and single-phase decomposition theory is applied on a three-phase system with symmetrical voltages. The author explains physical meaning of the scattered currents which are the result of varying conductance of the load with respect to frequency. This idea however does not satisfy the requirement in case of a non-linear load because it requires elimination of frequency component from the load admittance. The theory is supposed to be implementable for both symmetrical voltages and loads and does not extend for asymmetrical voltages or unbalanced loads.

Another interesting research paper stated that, there is no such case where the active power exceeds the apparent power [53]. In [54] a more generalised power theory is presented in RMS domain for m-number of wires with any resistance to compute optimal currents to be transmitted for maximum power transfer. The author further explains that the virtual star point is not always the reference point. This analysis is only applicable to sinusoidal quantities and the calculated apparent power contains a product of voltage and current dependant factors which are referred to a selected reference point. According to the author, the reference point is defined

where the sum of the weighted RMS voltages is equal to zero. However, throughout the analysis the reference point was kept fixed, which is not applicable in case of asymmetrical waveforms. Some other authors have also considered systems with unbalanced resistances based on Lagrange multipliers applied in RMS domain but did not consider the impact of a time dependant reference point. Consequently, no results could be extended for the calculation of apparent power in the instantaneous domain [55]. The research conducted in [56] eventually concludes that the apparent power cannot have a single definition to deal with the varying power system properties and be simultaneously useful during fault conditions.

It can be summarized that to formulate a general power theory a unique definition of apparent power must be proposed which removes all the ambiguities and provides clear information about the power factor and the active/reactive power components. It must also make sure that the proposed unique definition should be able to deal with the systems containing m-number of phases, variable wire resistances, with or without the neutral wire and unbalanced loads under all kinds of fault conditions.

5.5 Optimal Current Calculation Method

In [57], concept of minimization of the reactive current is discussed where the reactive power component is proposed to be compensated without energy storage at the compensator. In [6], an alternate technique is discussed where the reactive power component is compensated with the aid of an active compensator when energy storage is available. This work is continued with the objective of reactive power compensation where optimal currents are distributed in an m-wire system. According to that, the system is evaluated in a weighted domain, where voltages are weighted with respect to the resistance on the wires. Similarly the general power theory has been extended and modified in [7], where a weighted null reference point is created for the apparent power measurements.

The method discussed in this chapter is inspired from the same theory presented in [6]-[7], and is adopted for the calculation of optimal currents to ensure maximum active power transfer during symmetrical grid voltage conditions on a weak AC grid. It is to be noted that analysis

performed below is based on the predetermined values of Thevenin resistance and voltage of each wire in an m-wire network.

5.5.1 Vector Representation

A three wire system is considered as a Thevenin equivalent of a distributed power network where Thevenin resistances are expressed as Rth_1, Rth_2 and Rth_3. The system is illustrated in Fig. 5.3, where each line is supplied with an independent voltage source being referenced to a weighted null point. The weighted line voltages and currents can be represented in terms of phasors as, $I' = I_1, I_2, I_3$ and $Vth' = Vth_1, Vth_2, Vth_3$.

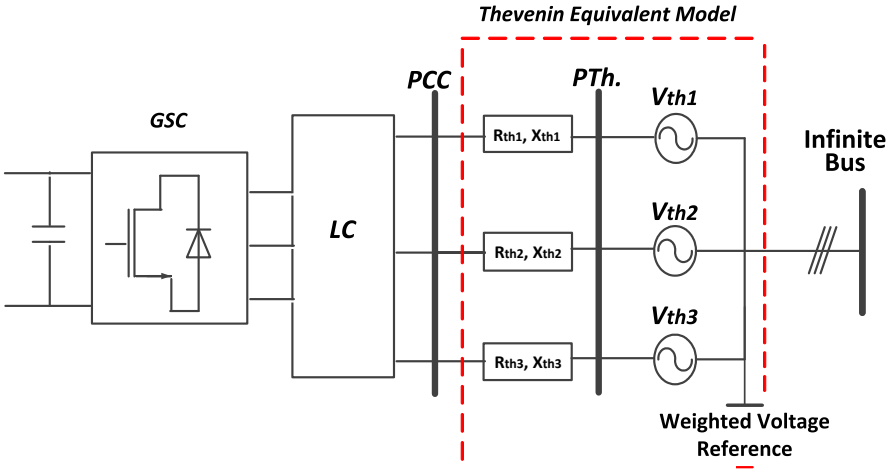

Figure 5.3: Grid-side Block Diagram

The instantaneous power transferred to the load can be expressed below in (5.1), where $Vth'.I'$ is the dot product of the vectors.

$$P_{th} = \sum_{n=1}^{m} V_{th,n}.I_n = V_{th}^{'}.I^{'} \tag{5.1}$$

The system under consideration comprises a PMSG based WECS integrated into a weak AC grid with no shunt connected reactive power support. With minimal reactive power support and considering balanced voltage condition, only active current components will be transferred into the system and the line losses can be given as:

$$P_{loss} = \sum_{n=1}^{m} I_n^2 . R_{th,n} \tag{5.2}$$

Let us consider for an m-wire system, the weighted current vectors can be represented as:

$$I' = \{I_1 . \sqrt{R_{th,1}}, I_2 . \sqrt{R_{th,2}}, \ldots\ldots, I_3 . \sqrt{R_{th,3}}\} = I . R_{th}^{1/2} \tag{5.3}$$

Where $R_{th}^{1/2}$ is a diagonal matrix representing the square root of line resistances:

$$R_{th}^{1/2} = \begin{bmatrix} \sqrt{R_{th,1}} & 0 & 0 & 0 \\ 0 & \sqrt{R_{th,2}} & 0 & 0 \\ \ldots & \ldots & \ldots & 0 \\ 0 & 0 & \ldots & \sqrt{R_{th,m}} \end{bmatrix} \tag{5.4}$$

From (5.3), if I' is considered to be as a resistance weighted vector then the power loss can be expressed as:

$$P_{loss} = I' . I' = \left\| I' \right\|^2 \tag{5.5}$$

And in case where only active current component is present, the minimum power loss can be represented as:

$$P_{loss} = I_a' . I_a' = \left\| I_a' \right\|^2 \tag{5.6}$$

The I_a' will be considered as an optimal current for minimal line losses represented as a weighted vector. Once weighted current is calculated, it can be converted to real physical value as:

$$I_a = I_a' \, R_{th}^{-1/2} \tag{5.7}$$

5.5.2 Vector Solution and Optimal Supply Current

The expression (5.7) is derived in context with the Kirchhoff's current law and the law of voltage conservation. If the vectors I' and V_{th}' are defined in an m-dimensional subspace S'^2 then the solution vector I_a' must also reside there. By applying the vector properties, if I' is projected onto the subspace S'^2, then the optimal vector I_a' can also be found out. Two orthogonal weighted

voltage vectors V_1' and V_2' are required to obtain the projected current vector I_a' as shown in Fig. 5.4.

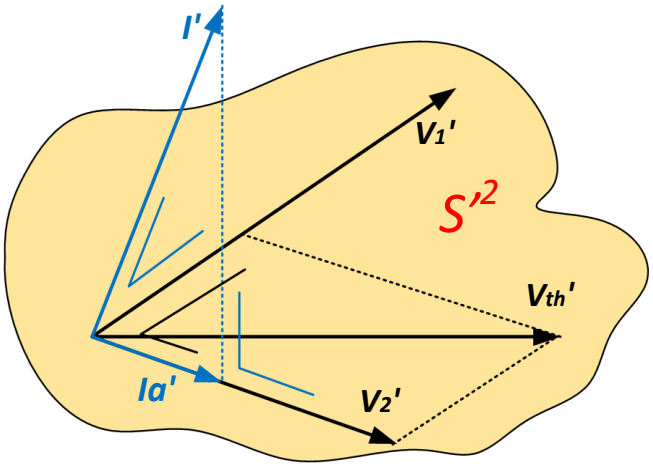

Figure 5.4: Projection of I' onto V_2'

First, vector V_1' is selected orthogonal to I'. To simplify the calculations V_1' is considered equal to a unity vector $1'$. The second vector V_2' which is not orthogonal, can be found out by subtracting the projection of V_{th}' onto V_1' from V_{th}', and is expressed as [56]:

$$V_2' = V_{th}' - Proj.of V_{th}' onto V_1'$$

$$V_2' = V_{th}' - \left(\frac{V_{th}' . V_1'}{\|V_1'\|^2} \right) V_1' \tag{5.8}$$

By substituting $V_1'=1'$, in the above expression,

$$V_2' = V_{th}' - \left(\frac{V_{th}' . 1'}{\|1'\|^2} \right) 1' \tag{5.9}$$

Or

$$V_2' = V_{th}' - V_{ref} . 1' \tag{5.10}$$

It must be noted that the V_{ref} also takes into account the Thevenin resistance and as a result the abovementioned expression can be written as:

$$V_2' = \left(V_{th} - V_{ref}\right).R_{th}^{-1/2} \tag{5.11}$$

Where,

$$V_{ref} = \frac{\sum_{n=1}^{m}(V_{th,n} / R_{th,n})}{\sum_{n=1}^{m}(1/R_{th,n})} \tag{5.12}$$

The weighted Thevenin voltages (Vth_n) are adjusted at every instant with reference to the null point and can be expressed as:

$$\begin{aligned} Vth_n = \{&V_{PCC,1} - I_{rated,1}Z_{th,1}, V_{PCC,2} - I_{rated,2}Z_{th,2}, \\ &\ldots\ldots, V_{PCC,m} - I_{rated,m}Z_{th,m}\} \end{aligned} \tag{5.13}$$

Hence V_2' can also be given as:

$$V_2' = V_{ref}.R_{th}^{-1/2} \tag{5.14}$$

For optimal current solution, I_a' can be expressed as:

$$I_a' = Proj._{of}\ I'ontoS'^2 = Proj._{of}\ I'ontoV_1' + Proj._{of}\ I'ontoV_2' \tag{5.15}$$

Since I' and V_1' are orthogonal, the projection of I' onto V_1' will be a zero vector:

$$\therefore I_a' = Proj._{of}\ I'ontoV_2' = \left(\frac{I'.V_2'}{\|V_2'\|^2}\right)V_2' \tag{5.16}$$

From (5.7) and (5.12), I_a' can be formulated as:

$$I_a' = \left(\frac{I.R_{th}^{1/2}\left(V_{th} - V_{ref}\right)R_{th}^{-1/2}}{\|V_2'\|^2}\right)V_2' \tag{5.17}$$

$$I_a' = \left(\frac{I.V_{th} - I.V_{ref}}{\|V_2'\|^2}\right)V_2' \tag{5.18}$$

Since $I.V_{ref} = 0$ and $I.V_{th}$=P_{th}, the optimal weighted current vector I_a' is:

$$I_a' = \left(\frac{P_{th}}{\|V_2'\|^2} \right) V_2' \tag{5.19}$$

Keeping in mind the unbalanced loading, $P_{th}/\| V_2'\|^2$ can be considered equal to a constant 'k_A'. Hence, based on (5.7), I_a can be expressed as:

$$I_a = k_A . V_2' . R_{th}^{-1/2} \tag{5.20}$$

5.5.3 Current Calculation for the System under Consideration

According to the proposed technique, the amount of power lost in an '*m*' number of wires system is directly proportional to the Thevenin resistance of each wire. That is why the system is looked in a weighted domain, where voltages are weighted with respect to the resistances. With reference to Fig. 5.3, optimal current I_a (I_{opt}) required for each wire is determined by following the steps below:

1- The weighted Thevenin voltages for '*m*' number of wires at PTh will be calculated by subtracting the voltage drop across the Thevenin impedances, from the voltages at the PCC:

$$\begin{aligned} V_{PTh} = \{ & V_{PCC,1} - I_{rated,1} Z_{th,1}, V_{PCC,2} - I_{rated,2} Z_{th,2}, \\ & ....., V_{PCC,m} - I_{rated,m} Z_{th,m} \} \end{aligned} \tag{5.21}$$

2- In the next step, the calculated Thevenin voltages will be referenced to PTh side weighted null point reference. The idea of null point is presented for an unbalanced grid where the voltages at the point of consumption (PTh) do not add to zero. Therefore, to satisfy KVL, voltages need to be calculated at every cycle (with time-variant X, R values) [6]. Hence, V_{ref} is the average resistance weighted voltage between the reference points PCC and PTh. The expression for calculating reference voltage in a three wire system is given below:

$$V_{ref} = \sum_{m=1}^{3} (V_{PTh,m} / R_{th,m}) / \sum_{m=1}^{3} (1 / R_{th,m}) \tag{5.22}$$

3- The V_{ref} is further weighted below in (5.23) as an *m*-dimensional vector which depicts resistance corrected weighted vector value from the weighted null point.

$$V_{ref}{}' = \left(\frac{V_{ref}}{\sqrt{R_{th,1}}}, \frac{V_{ref}}{\sqrt{R_{th,2}}}, ..., \frac{V_{ref}}{\sqrt{R_{th,m}}} \right) \tag{5.23}$$

4- The optimal power P_{opt} is calculated in (5.25) which needs to be transferred to the load at PTh. Where, P_{in} is the power at PCC coming from the source. Absolute sum of the weighted reference voltage is given as:

$$\left\| V_{ref}{}' \right\|^2 = \left(V_{ref}{}'_1 \right)^2 + \left(V_{ref}{}'_2 \right)^2 + \left(V_{ref}{}'_3 \right)^2 \tag{5.24}$$

$$P_{opt} = \frac{-\left\| V_{ref}{}' \right\|^2 \pm \sqrt{\left\| V_{ref}{}' \right\|^4 + 4P_{in} \left\| V_{ref}{}' \right\|^2}}{2} \tag{5.25}$$

Note that the above expression has two solutions for P_{opt}. One is the power exported and the other is the power imported. The lesser of the two is the power imported and the greater one is the power exported.

5- In the final step, a constant k_A is formulated which helps in acquiring the optimal currents to be redistributed in the wires.

$$\mathrm{k}_A = \frac{P_{opt}}{\left\| V_{ref}{}' \right\|^2} \tag{5.26}$$

$$i_{opt} = \left(\frac{\mathrm{k}_A \mathrm{v}_{ref}{}'_1}{\sqrt{R_{th,1}}}, \frac{\mathrm{k}_A \mathrm{v}_{ref}{}'_2}{\sqrt{R_{th,2}}}, \frac{\mathrm{k}_A \mathrm{v}_{ref}{}'_3}{\sqrt{R_{th,3}}} \right) \tag{5.27}$$

The PMSG considered for the experimental setup has a rated output power of 3.3kW. The total power (P_{in}) that reaches the PCC after considering the power losses at the DC link and the converters is approximated to be 2.98kW. From Table 4.1, the line resistances are R_{th1}=0.66Ω, R_{th2}=0.31Ω, R_{th3}=0.35Ω, with balanced V_{PCC}=225V and the rated current of the generator is I_{rated}=4.4A. In Table 5.2 below, optimal currents are calculated for the hardware setup under consideration confirming maximum power transfer at PTh. with least incurred losses.

Table 5.2. Optimal Current Calculation

P_{in} (2.98kW)	Wire 1	Wire 2	Wire 3
R_{th} (Ω)	0.66	0.31	0.35
V_{PCC} (V_{RMS})	225	225	225
I_{rated}(A_{RMS})	4.4		
V_{Th}((V)	222.08	223.63	223.45
V_{ref} (V)	223.257		
V_{ref}' (V)	274.81	400.98	377.37
||V_{ref}'||^2	378716.94		
P_{opt} (W)	2956.91		
k_A	0.008		
i_{opt} (A_{RMS})	2.64	5.62	4.98

The calculated optimal currents (I_{opt}) from the table above are certainly the best combination. Any other values would either give more line losses or less resultant power transfer [6]-[8].

5.5.4 Numerical Validation and Comparison

To support the claim that the derived currents are optimal, a simple comparison is done between the currents calculated using the aforementioned technique and the general power theory.

From the general power theory, current on each line can be calculated as:

$$Iout_i = \frac{-Vth_i + \sqrt{Vth_i^2 - 4Pin_i Zth_i}}{2Zth_i} \qquad \{for\ i=1\ to\ m\} \tag{5.28}$$

Different permutations of the line currents from (5.28) can be used in (5.29) to calculate the maximum transferable power on each line at PTh.

$$P_{PTh_i} = Vth_i Iout_i \tag{5.29}$$

The calculated power values from the permutation method were found to be very close to the values found using the optimal current calculation technique. However, the permutation method can also give unrealistic values by not following the $(P_{out}<P_{in})$ limit and sometimes gives higher values of the total output power than the rated input power. For example in Table 5.3, eight sets of line currents are considered. By injecting these currents the total extractable power and the associated losses are shown accordingly. From the first two sets *1* and *2*, the yielded transferred output power is more than that of the set *5* which is obtained from the Table 5.2. However, the power losses in these two sets are also higher when compared to the values from the set *5*. Furthermore, the sets *3* and *4* transfer less output powers which are not desirable in this case, whereas the sets *6* and *7* transfer higher output powers than the rated input power (2.98kW) and are not realistic. On the other hand, the set *8* contains all three rated balanced currents; it still produces less output power with higher losses. Compared to the set *8,* set *5* offers higher power delivery with 10% reduction in the overall losses. Thereby confirms the most optimal set of currents is the set *5*, where the total calculated transferrable power is *2957.10W*.

Table 5.3 Transferred Power at Pth v/s Line Currents

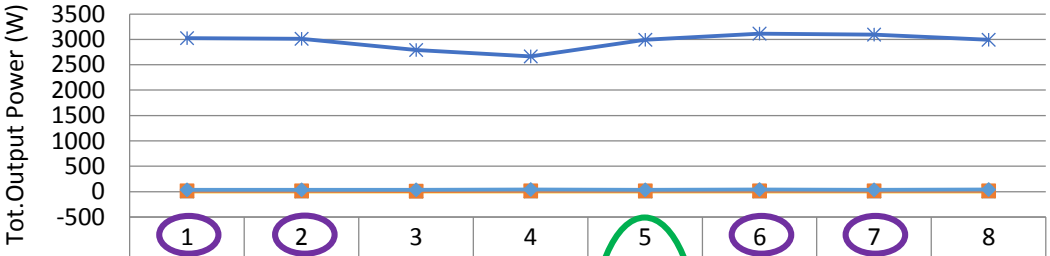

	1	2	3	4	5	6	7	8
Output Power (W)	2983.4	2976.5	2761.1	2625.7	2957.1	3076.0	3058.5	2951.1
Total Line Losses (W)	24.4	24.6	20.2	25.2	23.1	24.9	23.8	25.7
Line 1 Current (A)	3.64	3.84	2.83	3.93	2.64	2.81	2.68	4.41
Line 2 Current (A)	4.85	4.98	5.03	4.85	5.62	5.82	5.66	4.41
Line 3 Current (A)	4.88	4.52	4.51	4.68	4.98	5.15	5.12	4.41

Un-realistic values: output power + line losses > input power

5.5.5 Experimental Validation and Comparison

The results shown in Table 5.3 could be made even more noticeable in comparison with the balanced current injection, if the magnitudes and degree of unbalance between the line resistances were higher.

Since the system under consideration is a weak AC grid with high X/R ratios, the line resistor values were set to be smaller than the reactance values. Therefore, higher resistor values could not be added into the system to demonstrate the noteworthy benefits of the technique experimentally. For that reason, Z values were considered from Table 4.1 with the magnitudes given as, Z_{th1}=2.62Ω, Z_{th2}=1.05Ω, Z_{th3}=1.38Ω. Another reason of using Z instead of R was the hardware limitation, and due to that the values of R were difficult to obtain with acceptable accuracy, whilst the X values were easier to obtain more accurately. A table is given below to calculate the optimal currents by considering line impedance magnitudes of a three wire network.

Table 5.4. Optimal Current Calculation for |Z|

P_{in} (2.98kW)	Wire 1	Wire 2	Wire 3
Z_{th} (Ω)	2.62	1.05	1.38
V_{PCC} (V_{RMS})	225	225	225
I_{rated}(A_{RMS})	4.4		
$V_{Th(}$ (V)	213.43	220.36	216.47
V_{ref} (V)	217.849		
V_{ref}' (V)	134.58	212.59	156.81
$\|\|V_{ref}'\|\|^2$	87902.081		
P_{opt} (W)	2885.30		
k_A	0.032		
i_{opt} (A_{RMS})	2.7	6.8	4.0

A lab test bench shown in Fig. 5.5 is used to demonstrate the current injection for the considered reactive load. A 30kW de-rated induction machine is used as a prime mover for a 3.3kW surface mounted PMSG. Since the converters are connected in series without having any shunt ancillary support and the load information was also unknown at the point of design. The converters are decided to be chosen slightly higher than the generator rating ($1.5*P_{gen}$) to support higher currents. The reason why high rated currents might be required is because the grid is considered to be a Thevenin equivalent model of a distributed network where each line would have an independent source and likely to have unequal connected loads.

Figure 5.5: Lab Experimental Setup

In Fig. 5.6, detailed blocks of the hardware setup are illustrated. An induction machine (IM) as a prime mover is coupled with the PMSG. A control panel is shown which consists of a National Instruments-PXI FPGA controller, two-level back-to-back converters, data acquisition boards, protection circuitry and an *LC* filter. A set of additional impedance is also shown connected at the PCC. **A video link of the complete lab setup is given in Appendix-C**.

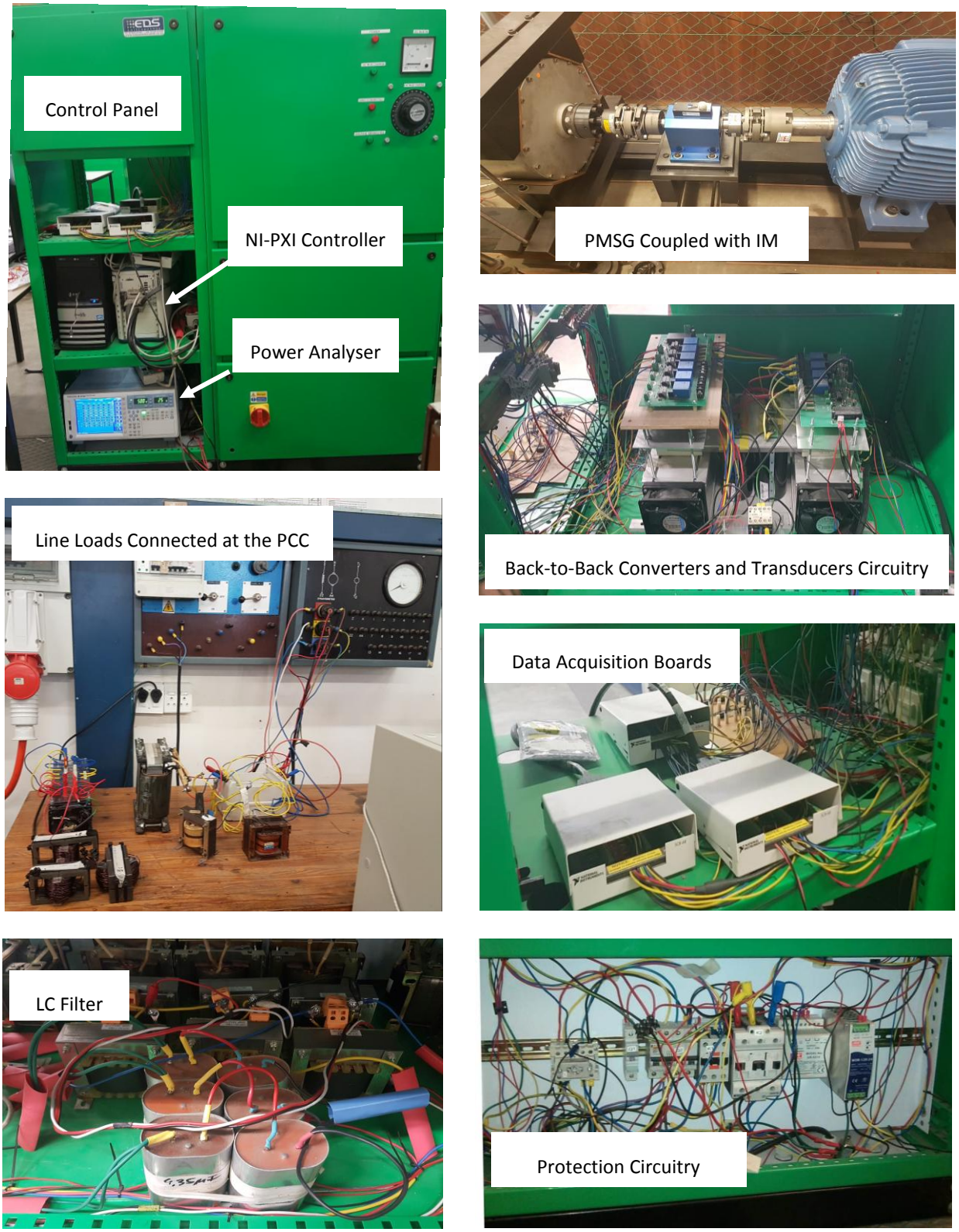

Figure 5.6: Lab Experimental Setup Detail

To validate the effectiveness of the abovementioned technique, a comparison is performed with the help of two cases discussed below. The analysis is performed considering balanced grid voltages, therefore reactive power would not be required and maximum active power is transferred with least distribution losses.

5.5.5.1 Case-1

In this case, balanced rated currents (I_{rated}=4.4A) are injected considering Z_1=2.62Ω, Z_2=1.05Ω and Z_3=1.38Ω with balanced V_{grid}=225V. The three phase grid voltage and the injected current magnitudes are illustrated in Fig. 5.7.

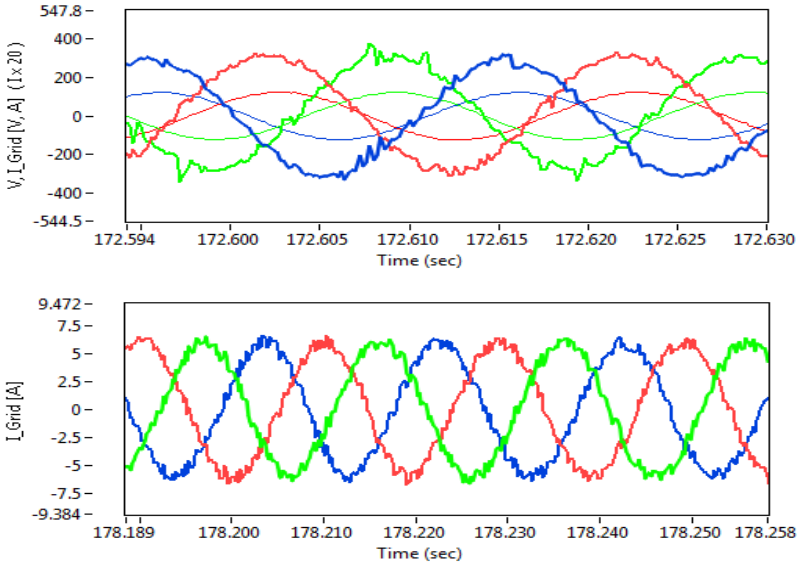

Figure 5.7: (a) Three-phase Grid Voltage and Injected Currents x20, (b) Three Phase Injected Currents Magnitude

The *d*-axis current components of the RMS values of phases A, B and C are presented in Fig. 5.8(a), (b) & (c). The yielded output power at PTh is also shown in Fig. 5.8(d) which is approximately equal to ***2870W***.

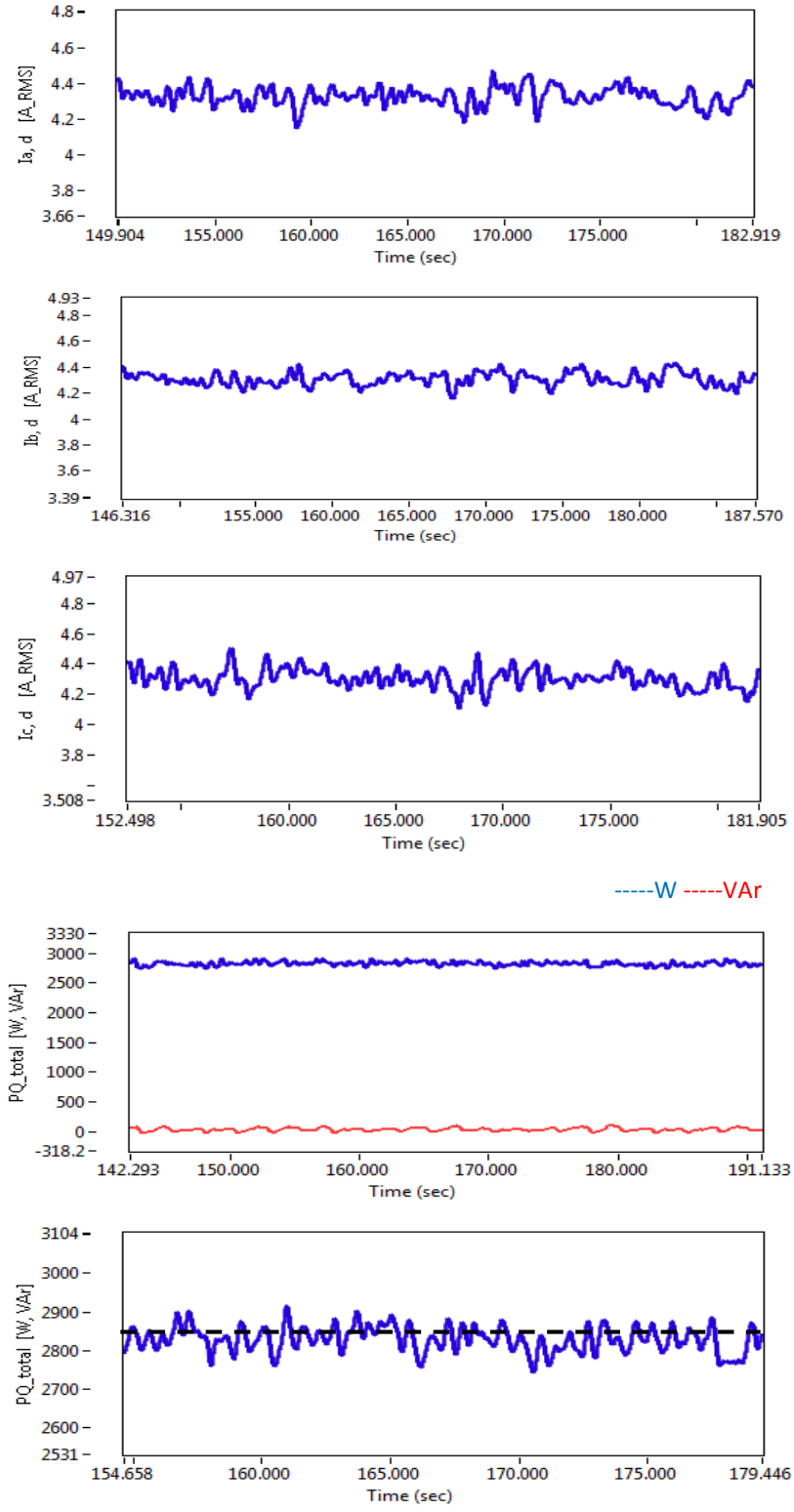

Figure 5.8: (a) Phase-A, d-axis Current Component, (b) Phase-B, d-axis Current Component, (c) Phase-C, d-axis Current Component, (d) Active and Reactive Powers at PTh, (e) Active Power at PTh (zoomed-in)

5.5.5.2 Case-2

In this case, the calculated optimal currents from Table 5.4 are injected considering the same conditions as of the case-1. According to the technique, the Thevenin voltages are referenced to a point where P_{PTh} is absorbed and performs useful work. The Thevenin equivalent model under consideration is supposed to have unbalanced loads as distributed elements, consequently each line would require different magnitude of currents. The three phase calculated current magnitudes in proportion with the grid voltages are illustrated in Fig.5.9 (a) & (b).

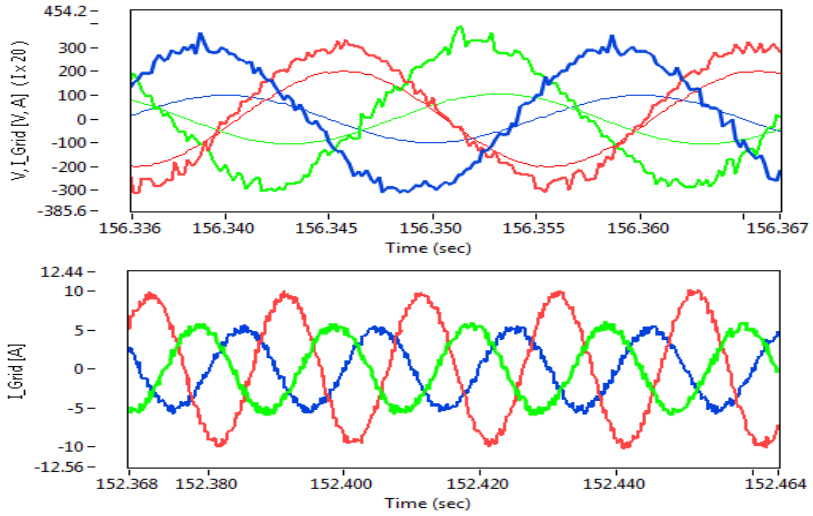

Figure 5.9: (a) Three-phase Grid Voltage and Injected Currents x20, (b) Three Phase Injected Currents Magnitude

The *d*-axis current components of the RMS values of phases A, B and C and the extracted output power at PTh are shown in Fig. 5.10. From Fig. 5.10, it is clearly depicted that the calculated currents using optimal current technique were injected and the transferred power is approximated to be ***2890W,*** which has 13.6% reduction in losses compared to the case-1. This value is almost equal to P_{opt} calculated in Table 5.4, and is certainly the most extractable power with least possible losses under the given conditions.

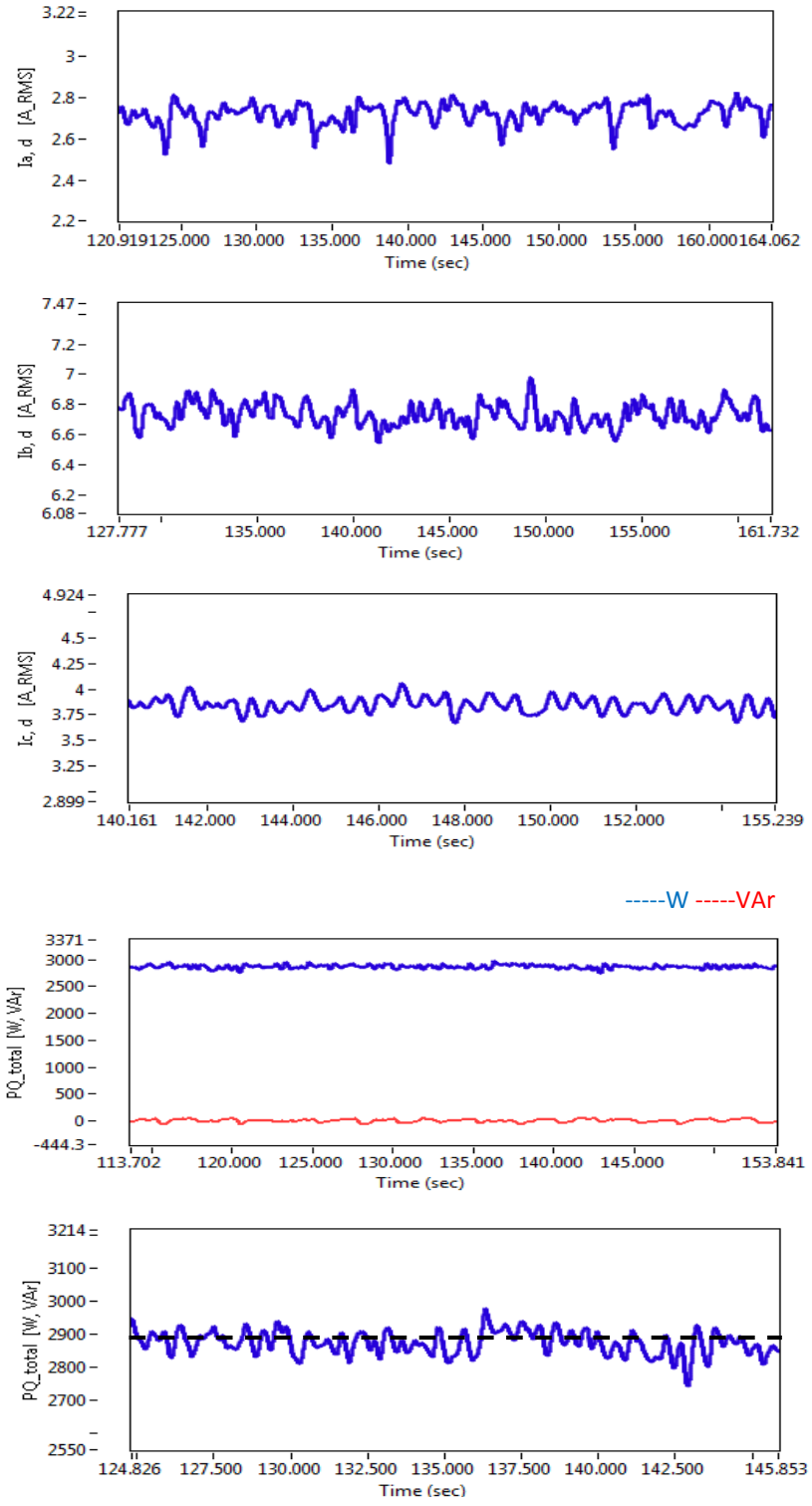

Figure 5.10: (a) Phase-A, *d*-axis Current Component, (b) Phase-B, *d*-axis Current Component, (c) Phase-C, *d*-axis Current Component, (d) Active and Reactive Powers at PTh, (e) Active Power at PTh (zoomed-in)

As mentioned earlier, the proposed technique performs lucratively in proportion to the degree of unbalance of the loads. The more the line impedance magnitude is unbalanced, the more noticeable the power transfer would be. To elaborate it, examples are given in Table 5.5 where balanced and optimal currents are injected into the network considering three sets of line impedances. It is shown that the loss reduction and power extraction is optimal in case of high impedance unbalance [8].

Table 5.5 Performance Comparison between Case 1 and 2

	Grid Condition (P_{in}=2.98kW, V_{grid}=225V)	**Transferred Power and the Calculated Losses with Balanced Current Injection (Case-1)**	**Transferred Power and Calculated Losses with Optimal Current Injection (Case-2)**	**Percentage Reduction in Losses**
Impedance Under Consideration	Z_1=2.62Ω, Z_2=1.05Ω, Z_3=1.38Ω	P_{PTh}=2.870kW Losses=**110W**	P_{PTh}=2.885kW Losses=**95W**	13.6%
High Impedance Unbalance	Z_1=0.62Ω, Z_2=1.05Ω, Z_3=2.38Ω	P_{PTh}=2.890kW Losses=**90W**	P_{PTh}=2.919kW Losses=**60W**	33.3%
Approximately Equal Impedances	Z_1=1.22Ω, Z_2=1.05Ω, Z_3=1.38Ω	P_{PTh}=2.917kW Losses=**63W**	P_{PTh}=2.918kW Losses=**62W**	1.5%

5.6 Power Stability Study

The power system stability can be classified into three major categories:

i. Voltage Stability
ii. Angle Stability
iii. Frequency Stability

This thesis is focused on the optimization of power magnitudes to support the system during voltage disturbances at the PCC. Multiple studies have already been performed to analyse the voltage stability for the AC grids with different strength levels. Usually, P-V and Q-V curves provide comparisons between the characteristics of weak and strong AC grids. A weak AC grid allows large voltage variations and limits the stable operation capabilities due to high impedance values. A weak AC grid with low short circuit (SCR) value sometimes also demands a separate energy source which can assist in achieving stable voltage limits at the PCC. Voltage stability is defined as the capability of a system to maintain stable voltage within the defined limits in the presence of disturbances occurring at the PCC. Depending on the type of disturbance the voltage stability can be classified as [59]-[60]:

- ***Static voltage stability*** is defined as an ability of the system to maintain the steady voltage equilibrium when exposed to small disturbances, such as instantaneous system load variation. The short duration of the disturbance would demand response time of a few seconds.
- ***Dynamic voltage stability*** is defined as an ability of the system to maintain the steady voltages when subjected to large disturbances, such as disconnection or loss of synchronism with the system. The examination study during dynamic voltage events would require periods of seconds and sometimes several minutes to achieve the stability.

5.6.1 Voltage Stability Analysis of the System under Consideration

As discussed in chapter-2, the strength of an AC grid at a specific point relies on the SCR level. The SCR value is the ratio between short circuit power (S_{sc}) and the rated source power (P_s) at the point of common coupling (PCC). If the grid is assumed to be modelled as an equivalent Thevenin circuit, then Z_{th} will be the Thevenin impedance at the PCC and the SCR can be expressed as:

$$SCR = \frac{S_{sc}}{P_s} = \frac{V_{PCC}{}^2}{Z_{th} P_s} \tag{5.30}$$

Where S_{SC} is the short circuit power and P_S is the wind turbine power that travels towards the PCC. If the system parameters are rated per unit with the base rating of the wind turbine power, then SCR can be expressed as:

$$SCR = \frac{1}{|Z_{th}|} \tag{5.31}$$

Since $|Z_{th}| = \sqrt{R_{th}^{\,2} + X_{th}^{\,2}}$. If R_{th} is neglected, then SCR can be assumed inversely proportional to the amount of reactance. Which implies that a weak AC grid would possess high reactance magnitude. In a weak AC grid, the incremental change in the power demand by the loads can cause uncontrollable fall in the grid voltage which may lead to complete voltage collapse. To support such situations, reactive power can be injected to improve the power factor and enhance the static voltage stability margins.

From the discussion in chapter-4, the system under consideration does not possess a separate reactive power support system. Therefore, due to limitation of reactive power assistance, the applied technique mostly utilizes the existing active power and redistributes the currents to achieve maximum power transfer by incurring least line losses.

For the analysis, P-V curves are plotted with reference to increased load values for the networks at different SCR values. A comparison is performed between the conventional and the optimal current injection methods. For instance, a simplified distribution system is shown in Fig. 5.11. The system consists of a power source, a distribution line, a connected load and an integrated wind energy conversion system (WECS) as a distributed generation system.

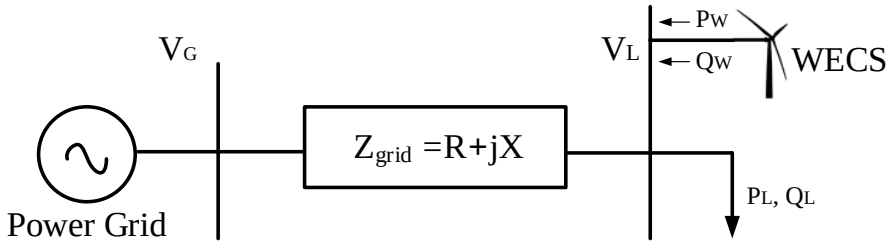

Figure 5.11: Two-node Simplified Distribution System with a WECS

The voltage drop along the line can be expressed as [61]-[62]:

$$\Delta V = V_G - V_L = \frac{R(-P_W + P_L) + X(\pm Q_W + Q_L)}{V_L} \tag{5.32}$$

In an AC grid with low X/R ratio, the load active power demand causes a progressive drop in the grid voltage. However, the system under consideration is a weak grid with high X/R ratio and low SCR. The injection of excessive active power would only be used to meet the load requirement without incurring higher line losses. Since the system provides limited reactive power support, it is considered equal to zero. The drop in the voltage from (5.32) can be modified as:

$$\Delta V = V_G - V_L = \frac{R(-P_W + P_L)}{V_L} \tag{5.33}$$

5.6.2 Case Study of Weak AC Grids at Different SCR Levels

A set of curves are provided to show the relationship between the change in the voltage and the load power. It can be seen that there is a steady drop in the voltage with the increase in active power demand. Furthermore, the voltage variation *ΔV* is depicted for four different SCR levels. The low SCR values have the minimum critical load active power whereas the high SCR values are merely affected and have maximum critical load active power. The change in voltage for low SCR is greater than that of high SCR values.

For comparison and to show the effectiveness of the optimal current injection technique, two cases are discussed below:

Case-1: With Balanced Current Injection Method

In this case, balanced currents are injected and voltage stability trend is shown in terms of gradual drop in the voltage recorded at different SCR values. According to Fig. 5.12, the weak AC grids with lower SCR values have a poor stability limit compared to the ones with higher SCR values.

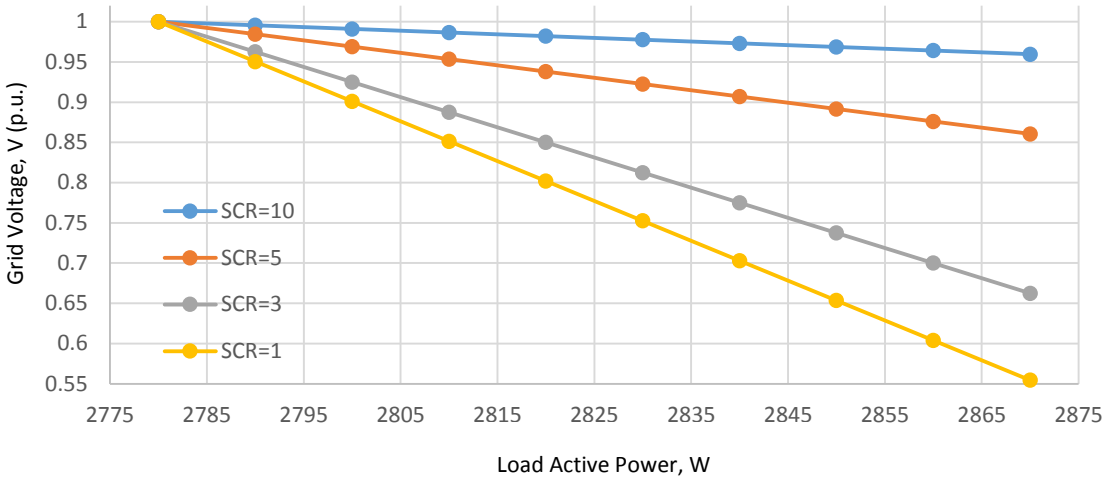

Figure 5.12: P-V curves of AC Grids with different SCR Values during Balanced Currents Injection

Case-2: With Optimal Current Injection Method

Similarly, the voltage drop is shown for the same AC grids mentioned above. However, in this case optimal currents are being injected which increases the resultant active power transfer. From Fig. 5.13, it can be seen that the AC grid with highest SCR level has the highest critical load power and lowest critical voltage.

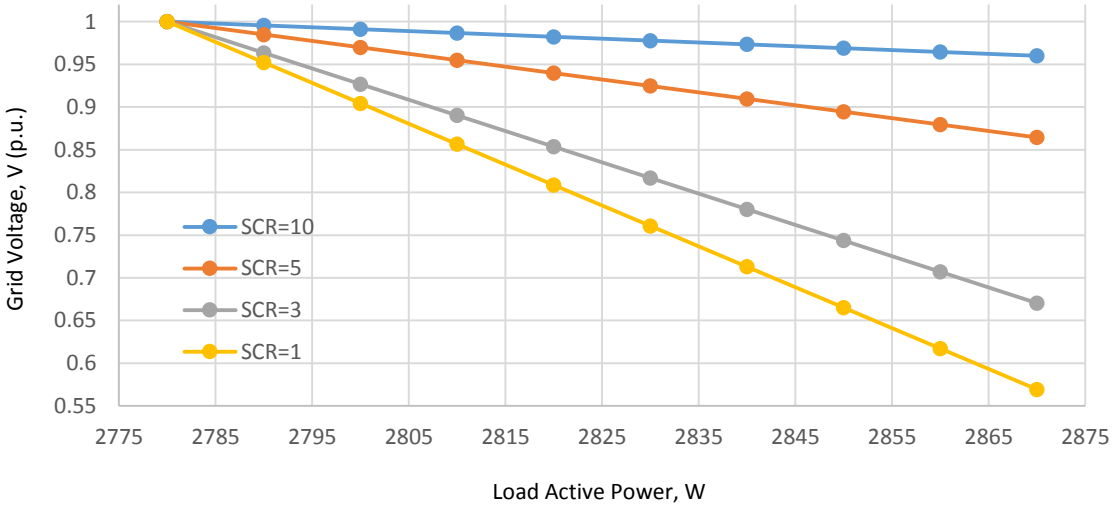

Figure 5.13: P-V curves of AC Grids with different SCR Values during Optimal Currents Injection

The AC grids with low SCR values show higher voltage variation compared to the high SCR values. For instance, from Fig. 5.13 the voltage drop for SCR=10 is only *0.04V* whereas for SCR=1 it is

0.431V. From the comparison between Fig. 5.12 and 5.13, critical load active power with the additional active power injection (case-2) is greater than the normal output (case-1). In other words, the additional active power can increase the voltage stability limit and hence improves the overall voltage stability at the PCC. For example, the AC grid voltage drop for SCR=1 in case-1 is 3.48% more than that of case-2. For case- 2, the percentage voltage variation tends to improve proportionally with the increase in rated source power (P_W). However, at some point reactive power would also be required to support the active power injection.

5.7 Conclusion

This chapter discusses the application of optimal current injection technique during symmetrical grid voltage conditions. The practical implementation of general power theory according to the Thevenin equivalent parameters and reduction of power losses by injection of optimal currents raises important questions to discuss the IEC standards and the grid codes for an unbalanced weak grid. The discussed approach can redefine apparent power and power factor according to varying X/R ratios at the PCC with respect to the Thevenin reference (null) point.

The application of the proposed technique has been tested on a lab-based wind energy system to confirm the optimal distribution of the currents. The discussed technique is elaborated with the help of mathematical equations. Control structure is developed in such a way to provide currents for each phase to achieve minimum power distribution losses as possible. Experimental results are presented and from the comparison, calculated distribution losses are analysed. Furthermore, from Table 5.3-5.4 and Fig. 5.13, it is shown that the set of currents obtained using the optimal current calculation technique provides the most extractable power with least losses and offers enhanced voltage stability for a weak AC grid.

5.8 References

[1] K. Vu et al “Use of Local Measurement to Estimate Voltage-Stability Margins”. *IEEE Trans on Power Systems, Vol.14, No.3, August 1999.*

[2] E. Emanuel “The Need for a Simple and Practical Resolution of the Apparent Power” *European Transactions on Electrical Power 3 (Jan/Feb) (1993)*

[3] M. Depenbrock “Some Remarks to Active and Fictitious Power in Poly-Phase and Single-Phase Systems” *Eur. Trans. Electr. Power Eng. 3 (January) (1992).*

[4] H. Akagi, Y. Kanazawa, A. Nabae "Generalized theory of the Instantaneous Reactive Power in Three-Phase Circuits" *Proc. IEEJ IPEC, Tokyo, Japan, 1983, pp.1375–1386.*

[5] L.S. Czarnecki "On some Misinterpretation of the Instantaneous Reactive Power p–q Theory, *IEEE Trans. Power Electron. 19 (May (3)) (2004) 828–836.*

[6] M. Malengret, T.C Gaunt "General theory of instantaneous power for multi-phase systems with distortion, unbalance and direct current components" *Electric. Power Systems Research, j.epsr.2011.05.016 (Vol. 81, pp 1897-1904)*

[7] M Malengret, T.C Gaunt CT "General theory of average power for multi-phase systems with distortion, unbalance and direct current components. *Electric. Power Systems Research, j.epsr.2011.11.020* (Vol. 84, pp 224-230)

[8] M. Malengret, T.C Gaunt, University of Cape Town, proprietor: Methods and Systems for power injection or extraction in a power network. *UK Patent GB2521414, 27 Jan 2016*.

[9] A. Khan, M.A. Khan, M. Malengret, "Steady State Impedance Estimation of a Weak Grid to Assist Optimal Current Injection for Minimal Power Losses" *IEEE Energy Conversion Congress and Exposition (ECCE), 2016.*

[10] M.Noroozian, "Use of UPFC for optimal power flow control*"IEEE Transactions on Power Delivery,* pp. 1629-1634 1997.

[11] Z. Liang and J. Duncan Glover, "A Zoom Feature for a Dynamic Programming Solution to Economic Dispatch Including Transmission Losses" *IEEE Transactions on Power Systems,* pp 544-550, 1992.

[12] O. Alsac, "Further Developments in LP-based Optimal Power Flow" *IEEE Transactions on Power Systems,* pp 697-711. 1990.

[13] J.Yuryevich and K.P. Wong, "Evolutionary Programming-based Optimal Power Flow Algorithm, *IEEE Transactions on Power Systems*, pp 1245-1250, 1999.

[14] K.Y.Lee, Y.M.Park, J.L.Oritz, "Fuel Cost Minimisation for Both Real and Reactive Power Dispatches*" IEEE Proceeding C-Generation, Transmission and Distribution,* vol.3. 1984.

[15] K.Y.LEE, Y.M.Park, J.L.Oritz, "A united approach to optimal real and reactive power dispatch", *IEEE Transactions on Power Apparatus and Systems,* pp 1147-1154, 1985.

[16] K. Mamandur and R. Chenoweth, "Optimal control of reactive power flow for improvements in voltage profiles and for real power loss minimization", *IEEE Transactions on Power Apparatus and Systems,* pp 3185-3194, 1981.

[17] N.Deeb, S.M. Shahidehpour," Linear reactive power optimization in a large power network using the decomposition approach" *IEEE Transactions on Power Systems,* pp 428-438, May 1990.

[18] S.C. Savulescu " Qualitative Indices for the System Voltage and Reactive Power Control" *IEEE Transactions of Power Apparatus and Systems,* pp 1413-1421, July 1976.

[19] S. Narita, A. Hammam, "A Computational Algorithm for Real-Time Control of System Voltage and Reactive Power Part I-Problem Foundation", *IEEE Transactions on Power Apparatus and Systems*, pp 2495-2501, Nov, 1971.

[20] M. Geidl, and G. Andersson, "Optimal power flow of multiple energy carriers", *IEEE Transactions on Power Systems,* pp 145-155, Feb 2007.

[21] Leonard L. Grigsby, "Power System Stability and Control", *CRC Press Inc,* May 2007.

[22] Y. Riffonneau, S. Bacha, F. Barruel and S. Ploix, "Optimal Power Flow Management for Grid Connected PV Systems with Batteries" IEEE Transactions on Sustainable Energy, pp 309-320, July 2011.

[23] M.E. Baran, F.F. Wu, "Network Reconfiguration in Distribution Systems for Loss Reduction and Load Balancing" *IEEE Transactions on Power Delivery,* pp 1401-1407, Apr 1989.

[24] H. Akagi, Y. Kanazawa, and A. Nabae, "Instantaneous Reactive Power Compensators Comprising Switching Devices without Energy Storage Components" *IEEE Transactions on Industry Applications,* pp 625-630, 1984.

[25] S.W.Amin, B.F. Wollenberg, “Toward a Smart Grid, Power Delivery for the 21st Century” *IEEE Power and Energy Magazine*, pp 34-41, Oct 2005.

[26] J.A. Momoh “Smart grid design for efficient and flexible power networks operation and control” *IEEE/PES Power Systems Conference and Exposition,* March 2009.

[27] P.K. Dash, B.K. Panigrahi, and G. Panda, “ Power Quality Analysis using S-transform” *IEEE Transactions on Power Delivery,* pp 406-411, April 2003.

[28] Z. Pan, F.Z. Peng, K.A. Corzine, V.R. Stefanovic, J.M. Leuthen and S. Gataric, “Voltage balancing control of diode-clamped multilevel rectifier/inverter systems. Industry Applications” *IEEE Transactions on Industry Applications,* pp 1698-1706, Dec 2005.

[29] W. da Rosa, C. Gerez and E. Belati, "Optimal Distributed Generation Allocating Using Particle Swarm Optimization and Linearized AC Load Flow," in *IEEE Latin America Transactions*, vol. 16, no. 10, pp. 2665-2670, October 2018.

[30] W.F. Tinney, and C.E. Hart *,”Power Flow Solutions by Newton’s Method” IEEE Transactions on Power Apparatus and Systems,* pp 1449-1460, Nov 1967.

[31] D.I. Sun, B. Ashley, B. Brewer, A. Hughes and W. F. Tinney, “Optimal Power Flow by Newton Approach” *IEEE Transactions on Power Apparatus and Systems,* pp 2864-2880, Oct 1984.

[32] H.W. Dommel and W.F. Tinney, “Optimal Power Flow Solutions” *IEEE Transactions on Power Apparatus and Systems,* pp 1866-1876, Oct 1968.

[33] P. Wang, S. Zou and Z. Ma, "A Partial Augmented Lagrangian Method for Decentralized Electric Vehicle Charging in Capacity-Constrained Distribution Networks," in IEEE Access, vol. 7, pp. 118229-118238, 2019.

[34] Y. Sun, Z. Li, W. Tian and M. Shahidehpour, "A Lagrangian Decomposition Approach to Energy Storage Transportation Scheduling in Power Systems," in IEEE Transactions on Power Systems, vol. 31, no. 6, pp. 4348-4356, Nov. 2016.

[35] J. Umenberger and I. R. Manchester, "Specialized Interior-Point Algorithm for Stable Nonlinear System Identification," in IEEE Transactions on Automatic Control, vol. 64, no. 6, pp. 2442-2456, June 2019.

[36] R. Ramos de Souza, A. Roberto Balbo, L. Nepomuceno, E. Cassia Baptista, E. Martins Soler and R. Bento Nogueira Pinheiro, "A primal-dual interior/exterior point method, with combined directions and quadratic test in reactive optimal power flow problems," in IEEE Latin America Transactions, vol. 15, no. 8, pp. 1413-1421, 2017.

[37] W. Lu, M. Liu, S. Lin and L. Li, "Fully Decentralized Optimal Power Flow of Multi-Area Interconnected Power Systems Based on Distributed Interior Point Method," in IEEE Transactions on Power Systems, vol. 33, no. 1, pp. 901-910, Jan. 2018.

[38] N. Singh and K. David, “Optimal location of FACTS devices for congestion management” *Elsevier, Electric Power Systems Research*, pp 71-79, 2001.

[39] M.A. Abido, “Optimal Design of Power-System Stabilizers using Particle Swarm Optimization” *IEEE Transactions on Energy Conversion*, pp 406-413, Nov 2002.

[40] S. E. De León-Aldaco, H. Calleja and J. Aguayo Alquicira, "Metaheuristic Optimization Methods Applied to Power Converters: A Review," in IEEE Transactions on Power Electronics, vol. 30, no. 12, pp. 6791-6803, Dec. 2015.

[41] R. B. A. Koad, A. F. Zobaa and A. El-Shahat, "A Novel MPPT Algorithm Based on Particle Swarm Optimization for Photovoltaic Systems," in IEEE Transactions on Sustainable Energy, vol. 8, no. 2, pp. 468-476, April 2017.

[42] M. Masera, E. F. Bompard, F. Profumo and N. Hadjsaid, "Smart (Electricity) Grids for Smart Cities: Assessing Roles and Societal Impacts," in Proceedings of the IEEE, vol. 106, no. 4, pp. 613-625, April 2018.

[43] A. K. Singh, R. Singh and B. C. Pal, "Stability Analysis of Networked Control in Smart Grids," in IEEE Transactions on Smart Grid, vol. 6, no. 1, pp. 381-390, Jan. 2015.

[44] A. Ferrero and G.S. Furga, “On the Meaning of the Park Power Components in Three Phase Systems under non Sinusoidal Conditions” *IEEE Transactions on Instrumentation and Measurement*, pp 568-577, June 1991.

[45] P. Filipski, "Apparent Power - a Misleading Quantity in the Non-Sinusoidal Power Theory: Are all Non-Sinusoidal Power Theories Doomed to Fail?" *European Transactions on Electrical Power*, pp 21-26, Sep 2007.

[46] L.S. Czarnecki, "On Some Misinterpretations of the Instantaneous Reactive Power P-Q Theory" *IEEE Transactions on Power Electronics*, pp 828-836, May 2004.

[47] S.J. Jeon, "Definitions of Apparent Power and Power Factor in a Power System having Transmission Lines with Unequal Resistances" *IEEE Transactions on Power Delivery*, pp 1806-1811, July 2005.

[48] A.E. Emanual," Apparent and reactive powers in three-phase systems: In search of a physical meaning and a better resolution" *International Transactions on Electrical Energy Systems*, John Willey & Sons, 2007..

[49] M. Depenbrock, "Some Remarks to Active and Fictitious Power in Polyphase and Single Phase Systems" *International Transactions on Electrical Energy Systems,* John Willey & Sons, 2005.

[50] A.E. Emanual, "Powers in Nonsinusoidal Situations a Review of Definitions and Physical Meaning" *IEEE Transactions on Power Delivery*, pp 1377-1389, Jul 1990.

[51] L.S. Czarnecki, "Minimisation of Reactive Power under Non-sinusoidal Conditions" *IEEE Transactions on Instrumentation and Measurement*, pp 18-22, March 1987.

[52] L.S. Czarnecki, "What is Wrong with the Budeanu Concept of Reactive and Distortion Power and Why it Should be Abondoned" *IEEE Transactions on Instrumentation and Measurements*, pp 834-837, Sep 1987.

[53] *M. Depenbrock, D.A. Marshal and J.D. Van Wyk, "*Formulating requirements for a universally applicable power theory as control algorithm in power compensators" *International Transactions on Electrical Energy Systems,* John Willey & Sons, 2007.

[54] J.L. Willems and J. Ghijselen "The Relation between the Generalized Apparent Power and the Voltage Reference*" L'Energia Elettrica*, Volume 81 (2004) Ricerche.

[55] S.J. Jeon, "Considerations on a Reactive Power Concept in a Multiline System" *IEEE Transactions on Power Delievery*, pp 551-559, April 2006.

[56] W.G. Morsi, M.E. El-Hawary, "Defining Power Components in Non-Sinusoidal Unbalanced Polyphase Systems: The Issues" I*EEE Transactions on Power Delivery*, pp 2428-2438, Oct 2007.

[57] C. V. Suresh, S. Sivanagaraju, R. Meda, and K. Srikumar, ―Power flow analysis in the presence of Power Injection Model of IPFC, in 1st International Conference on Automation, Control, Energy and Systems - 2014, ACES 2014, 2014.

[58] H. Anton, Elementary Linear Algebra, 8th Edition, Wiley, Hoboken, NJ, 2000.

[59] H. Su and T. Liu, "Robust Thevenin Equivalent Parameter Estimation for Voltage Stability Assessment," in IEEE Transactions on Power Systems, vol. 33, no. 4, pp. 4637-4639, July 2018.

[60] S. M. Burchett et al., "An Optimal Thévenin Equivalent Estimation Method and its Application to the Voltage Stability Analysis of a Wind Hub," in IEEE Transactions on Power Systems, vol. 33, no. 4, pp. 3644-3652, July 2018.

[61] F. Viawan, "Steady state operation and control of power distribution systems in the presence of distributed generation," Chlamers University of Technology, 2006.

[62] E. Mogos and X. Guillaud, "A voltage regulation system for distributed generation," in *IEEE PES Power Systems Conference and Exposition,* pp. 30–37, 2004.

Chapter 6
Coordinated Current Injection during Unbalanced/Asymmetrical Grid Voltages

6.1 Introduction

A considerable amount of research has already been done on the performance of wind farms connected to healthy grids during different kinds of faults. Multiple contingency solutions have also been provided to deal with these grid faults. However, asymmetrical faults are not studied exclusively when it comes to weak grid conditions. This is presumably due to its less severity and less impact on the power system instability. Nevertheless, from the recent research stats it is found out that asymmetrical faults do occur frequently. It is indicated that, symmetrical faults only appear 5% compared to asymmetrical faults; i.e in the form of single line to ground fault 70%, line-to-line fault 15% and double line to ground fault 10% [1].

Since asymmetrical faults occur quite frequently, the WECS are designed to prevent disconnection from the grid and at the same time recover from the fault condition. With respect to grid code compliance under fault conditions; e.g. German VDN and ENSTO-E both grid codes have discussed fault ride through (FRT) requirements. According to German VDN, 1pu reactive current needs to be injected when the grid voltage drops below 50% during a symmetrical fault. Similarly, in ENSTO-E the reactive current injection during symmetrical faults requires the WPP or a single WT to provide 2/3 of additional reactive current for the time period specified by the transmission system operator (TSO). In relation with the asymmetrical faults, not much explanation is provided in VDN on how to calculate the required reactive current. However, 40% of the maximum rated current is allowed to be injected. In ENSTO-E the amount of required reactive current is decided between the TSO and the supplier [2]-[3].

To deal with the abovementioned scenario, a case study is done in this chapter by implementing asymmetrical faults on a type-4 WECS integrated into a weak AC grid. A Thevenin equivalent model of the grid is considered from Fig. 4.7 and its estimated dynamic parameters (X, R) are utilised from Table 4.1 for the calculation and injection of the coordinated currents.

The proposed coordinated current calculation technique defines the active/reactive current transfer limits, which assist in calculating the limited active/reactive powers needed to be transferred to the grid. By limiting the power transfer, the amount of incoming active power from the WPP can also be restricted, which eventually enables the system to implement low voltage ride through (LVRT) without the aid of any additional hardware. This is considered as one of the major contributions of the thesis as mentioned in section 1.8.

Validation of the analysis is done on the hardware from section 5.5.5. With reference to the discussion in chapter-3, the grid side converter (GSC) performs two important functions. Firstly, it generates small active/reactive power perturbations to apply impedance estimation. Once the impedance is known, this information is used to calculate the coordinated currents to be injected with respect to the defined current transfer limits. On the other hand, the machine side converter (MSC) regulates the DC-link voltage and limits the active power coming from the generator to implement LVRT.

6.2 Problems during Asymmetrical Faults

Any unbalance in the system which occurs for a steady state, stays for a longer period of time and could impose detrimental effects on the components. An asymmetrical fault exists for a short period of time but with high order of intensity. During an asymmetrical fault, the wind turbines are supposed to stay connected and assist the positive sequence voltage by injecting positive sequence reactive current [4]. From power system analysis [5], phase over-voltage occurs on the non-faulty phases. The neutral grounding of the power systems is usually designed to utilize the zero sequence impedance to avoid high phase over-voltages and fault currents during asymmetrical faults. For example, a bus is considered to be properly grounded if the ratio between zero and positive sequences impedances is kept between *1* and *3*. The conventional

methods employed during a grid fault condition only inject positive sequence reactive current to boost the positive sequence voltage. However, in case of modern WPP when a positive sequence current is injected during an asymmetrical fault by keeping the negative sequence current as zero, all three phases get boosted. This is because the WPP will act as an open circuit when the negative sequence is kept as zero. Consequently, the negative voltage component does not get attenuated and propagates in the system. This additional boost in the voltages occur due to the coupling between positive, negative and zero sequence components. Therefore, higher phase over-voltages appear at the PCC which need to be mitigated as much as possible.

6.2.1 Coupling during Asymmetrical Faults

According to power systems analysis, all sequence impedances are interconnected through a fault impedance at the fault point [5]-[6]. Consequently, all sequence voltages are coupled and get affected if any of the phases goes faulty. The amount of boost in negative and zero sequence voltages depends on the type of fault and the fault impedance while the magnitude of the voltage is regulated by the WPP. For weak grids with high impedance, the WPP can regulate the voltage more easily compared to a strong grid [7].

Coupling can be explained more by comparing the sequence voltages at the point of fault. Two cases could be considered, with or without the injection of reactive current by the WPP during a fault. For instance an equivalent circuit of a single line to ground (SLG) fault is illustrated in Fig. 6.1 to show the effect of coupling [5][6][8].

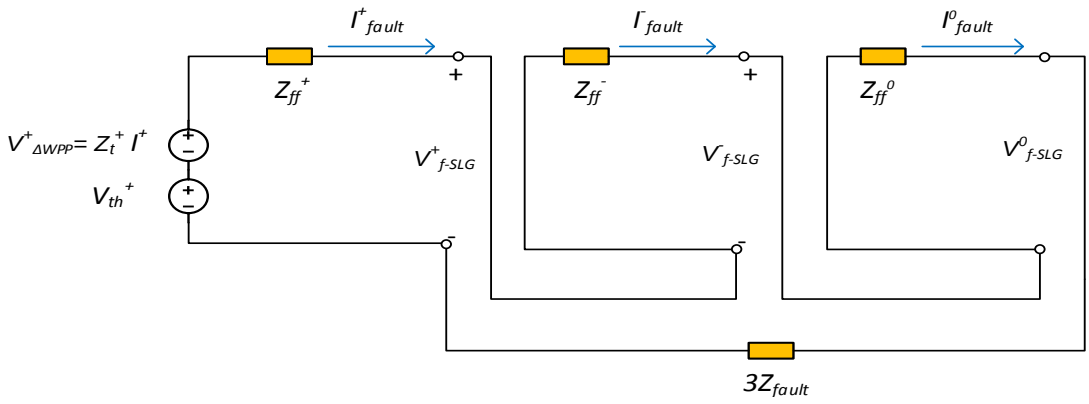

Figure 6.1: Equivalent Circuit Representing SLG Fault [4]

The resulting impact of the positive sequence current injection by the WPP on the negative and zero sequence voltages can be calculated using voltage division rule. The pre-fault voltage at the point of fault is the Thevenin voltage V_{th}^{+}, which relies on the power flow. During a fault condition, the injection of positive sequence current from the WPP can also boost the phase voltages and the boosted positive sequence voltage $V_{\Delta WPP}^{+}$ is calculated as:

$$V_{\Delta WPP}{}^{+} = Z_t{}^{+} I^{+} \tag{6.1}$$

Where, Z_t^{+} is the positive sequence transfer impedance and I^{+} is the current phasor moving from the WPP to the faulted point [7]. From Fig. 6.1, positive, negative and zero sequence voltages are given in equations (6.2)-(6.4).

$$V_{SLG}{}^{+} = (V_{th}{}^{+} + Z_t{}^{+} I^{+}) \left(\frac{Z^{-} + Z^{0} + 3Z_{fault}}{Z^{+} + Z^{-} + Z^{0} + 3Z_{fault}} \right) = (V_{th}{}^{+} + V_{\Delta WPP}{}^{+}) \left(\frac{Z^{-} + Z^{0} + 3Z_{fault}}{Z^{+} + Z^{-} + Z^{0} + 3Z_{fault}} \right) \tag{6.2}$$

$$V_{SLG}{}^{-} = (V_{th}{}^{+} + Z_t{}^{+} I^{+}) \left(\frac{Z^{-}}{Z^{+} + Z^{-} + Z^{0} + 3Z_{fault}} \right) = (V_{th}{}^{+} + V_{\Delta WPP}{}^{+}) \left(\frac{Z^{-}}{Z^{+} + Z^{-} + Z^{0} + 3Z_{fault}} \right) \tag{6.3}$$

$$V_{SLG}{}^{0} = (V_{th}{}^{+} + Z_t{}^{+} I^{+}) \left(\frac{Z^{0}}{Z^{+} + Z^{-} + Z^{0} + 3Z_{fault}} \right) = (V_{th}{}^{+} + V_{\Delta WPP}{}^{+}) \left(\frac{Z^{0}}{Z^{+} + Z^{-} + Z^{0} + 3Z_{fault}} \right) \tag{6.4}$$

Based on the above expressions, the coupling factor could be calculated among the sequences. This idea is implemented in the final experimental algorithm to perform decoupled injection of the currents in all three phases and is also illustrated in Appendix-B.

Similarly for double line to ground (DLG) fault, the equivalent circuit is shown in Fig. 6.2 and the coupling effect on positive, negative and zero sequence voltages is expressed in equations (6.5)-(6.7).

$$V_{DLG}{}^{+} = (V_{th}{}^{+} + I^{+} Z_t{}^{+}) \left(\frac{Z^{-} // (Z^{0} + 3Z_{fault})}{Z^{+} + Z^{-} // (Z^{0} + 3Z_{fault})} \right) = (V_{th}{}^{+} + V_{\Delta WPP}{}^{+}) \left(\frac{Z^{0} + 3Z_{fault}}{Z^{-} + 2Z^{0} + 6Z_{fault}} \right) \tag{6.5}$$

$$V_{DLG}{}^{-} = (V_{th}{}^{+} + I^{+} Z_t{}^{+}) \left(\frac{Z^{-} // (Z^{0} + 3Z_{fault})}{Z^{+} + Z^{-} // (Z^{0} + 3Z_{fault})} \right) = (V_{th}{}^{+} + V_{\Delta WPP}{}^{+}) \left(\frac{Z^{0} + 3Z_{fault}}{Z^{-} + 2Z^{0} + 6Z_{fault}} \right) \tag{6.6}$$

$$V_{DLG}{}^{0} = V_{DLG}{}^{+}\left(\frac{Z^{0}}{Z^{0}+3Z_{fault}}\right) = (V_{th}{}^{+} + V_{\Delta WPP}{}^{+})\left(\frac{Z^{0}}{Z^{-}+2Z^{0}+6Z_{fault}}\right) \cong V_{DLG}{}^{+} \quad (6.7)$$

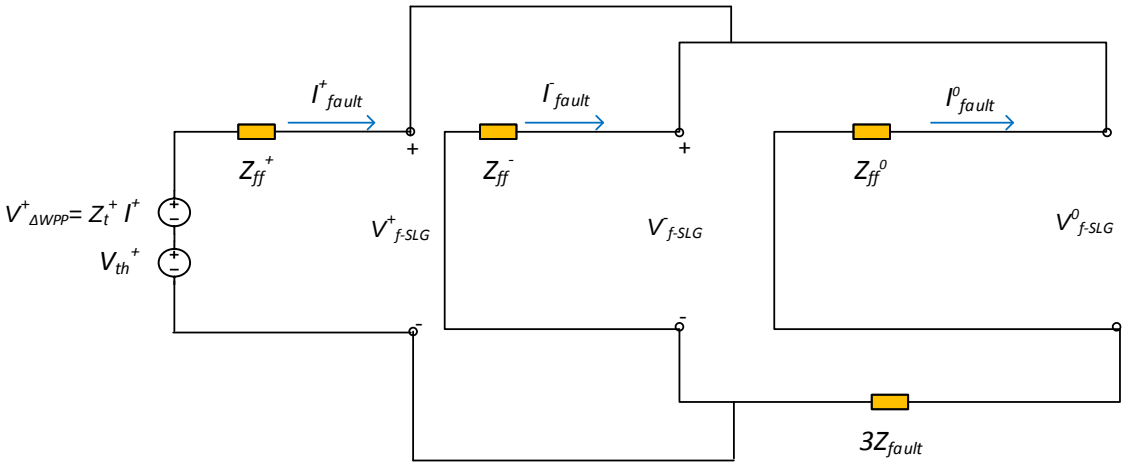

Figure 6.2: Equivalent Circuit Representing DLG Fault [4]

From Fig. 6.2, it can be deduced that the positive and negative sequence voltages at a fault point are equal. When the fault impedance (which is smaller than the positive sequence impedance) is neglected in the analysis, zero sequence voltage is boosted by the same amount as positive sequence voltage. Similarly, the negative sequence voltage also gets boosted by the same amount due to coupling. For instance, from equation (6.5) if the transfer impedance is Z_t =0.2pu, then 1pu reactive current injection would boost the positive sequence voltage by 0.1pu. This is going to be equal to the boost in negative and zero sequence voltages.

The coupling discussed above has not been explored much in the previous wind power studies during asymmetrical faults. This is due to the reason that in the previous studies, asymmetrical fault was not created realistically as a short circuit between phases or ground; instead it was implemented by changing the grid side voltage sources. Consequently, the sequence components did not have any coupling in between and whenever positive sequence currents were injected, it never had any effect on the negative and zero sequence voltages. However, in real asymmetrical faults study, it is important to understand the interconnection between the sequences.

6.3 Active and Reactive Current Flow

This section focuses on the calculation and injection of active and reactive currents by the WPP into the grid. Firstly, the current angle characteristics are studied and then transfer limits are derived based on the line impedance.

6.3.1 Current Angle Characteristics

As mentioned in the section 2.6, the converters are programmed to perform coordinated power injection. This is based on the coordination of active and reactive powers so that the current magnitude I_{mag} remains within the maximum rated limits. For a weak AC grid with low X/R ratio, more of active current I_d is injected to support the active power, whereas for high X/R ratio reactive current I_q is prioritised to keep the coordination. The maximum coordinated current magnitude can be expressed as:

$$I_{\mathrm{mag}} = \sqrt{I_d^2 + I_q^2} \leq I_{rated} \tag{6.8}$$

From the discussion in section 3.4, the current-angle characteristics can be expressed below as:

$$I_d = \frac{P}{V_1} = \frac{V_2 X}{Z^2}\sin\theta_v + \frac{V_1 R}{Z^2} - \frac{V_2 R\cos\theta_v}{Z^2} \tag{6.9}$$

$$I_q = \frac{Q}{V_1} = \frac{V_1 X}{Z^2} - \frac{V_2 X\cos\theta_v}{Z^2} - \frac{V_2 R\sin\theta_v}{Z^2} \tag{6.10}$$

From the discussion in section 4.5.1, the control is employed for each phase depending on its dynamic impedance and the source voltage magnitude. The modified technique detects if the steady state has been reached by the system to confirm decoupled current injections without generating any transients.

With reference to Fig. 6.3 below, if a very deep voltage sag appears on the grid, then V_2 will approach close to zero. To achieve maximum stability at this point, equations (6.9) and (6.10) can be utilised to work out the ratio between active and reactive currents as:

$$V_2 = 0 \Rightarrow I_d = \frac{V_1 R}{Z^2} \text{ and } I_q = \frac{V_1 X}{Z^2} \Rightarrow \frac{I_d}{I_q} = \frac{R}{X} \quad (6.11)$$

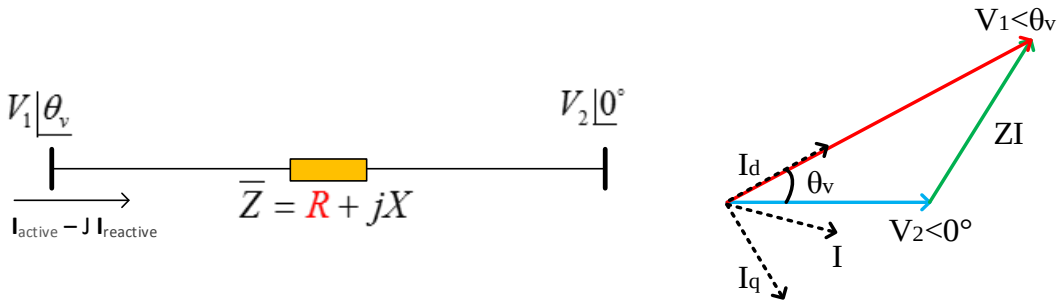

Figure 6.3: Single Line Current Flow and Phasor Diagram

6.3.2 Active and Reactive Current Transfer Limit

In order to derive the current transfer limit during asymmetrical faults, it should be considered that a WT injects controlled active and reactive currents as a function of voltage magnitude and the line impedance. To understand it better, Fig. 6.3 above is considered which represents the source and the receiving end voltages. Another vector diagram is shown in Fig. 6.4, which represents the magnitude of V_2. Since active and reactive currents are injected with reference to V_1, V_2 can be traced as a voltage phasor with an angle of *ZI* with respect to V_1. For analysis, V_2 will remain constant and V_1 will vary while locating the *ZI*. For every limit of the current magnitude, the θ_I will be from *0°* to *360°*. However, the θ_Z will always be less than *90°* due to the existing resistive component in the line impedance.

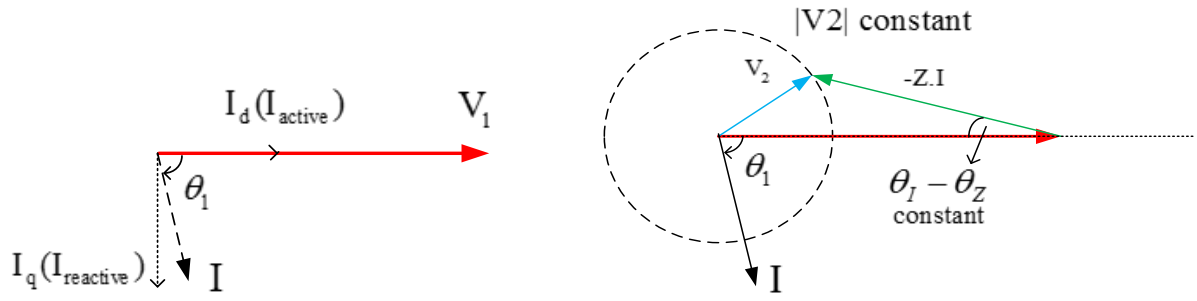

Figure 6.4: Current Phasors for Limit Derivation

To understand the concept of current injection limits, a lumped three phase impedance is considered with X/R=*4.2*. A Thevenin equivalent model of a weak grid which is being considered is illustrated in Fig. 6.5.

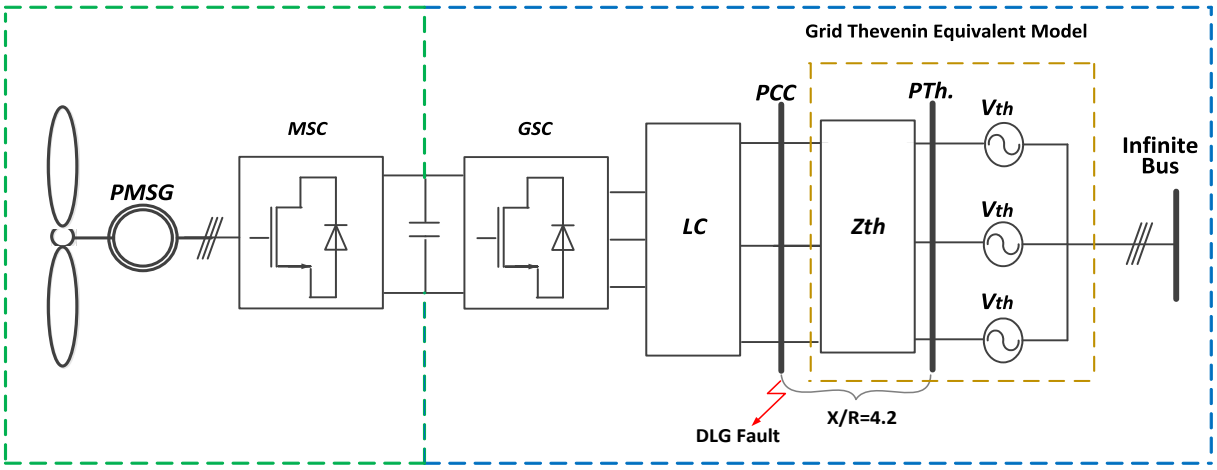

Figure 6.5: System Block Diagram

In case of a SLG or a DLG fault, unbalanced grid voltages would be seen at the PCC. The degree of unbalance in each phase will be calculated with respect to the voltages at the output of the GSC. In the case of asymmetrical grid faults, four conditions could be considered for the limited current injection [10]:

a) Pure reactive current injection: θ_I =90°
b) Pure active current injection: θ_I =0°
c) Active and reactive current injection: 90°> θ_I > θ_Z , θ_Z > θ_I > 0°
d) Active and reactive current injection: θ_I = θ_Z

6.3.2.1 Current Magnitude Limit for θ_I =90° (Pure Reactive)

For pure reactive current injection, the θ_I is going to be orthogonal with respect to θ_Z .Since the magnitude of V_2 is set to remain constant after the fault has been occurred. The low operating point of V_1 is shown in Fig. 6.6(a) for the initial value of the current magnitude. To show the maximum limit of the current, its magnitude will be increased in a way so that the angle difference between V_1 and V_2 becomes *90*° as illustrated in Fig 6.6(b). To give the maximum magnitude of V_1 and to obey the maximum current transfer limit, the tip of *ZI* phasor needs to

touch the boundary of the circle. If the current magnitude is increased further, the magnitude of *ZI* phasor will also increase and will eventually intersect the V_2 circle which implies that larger V_2 is required.

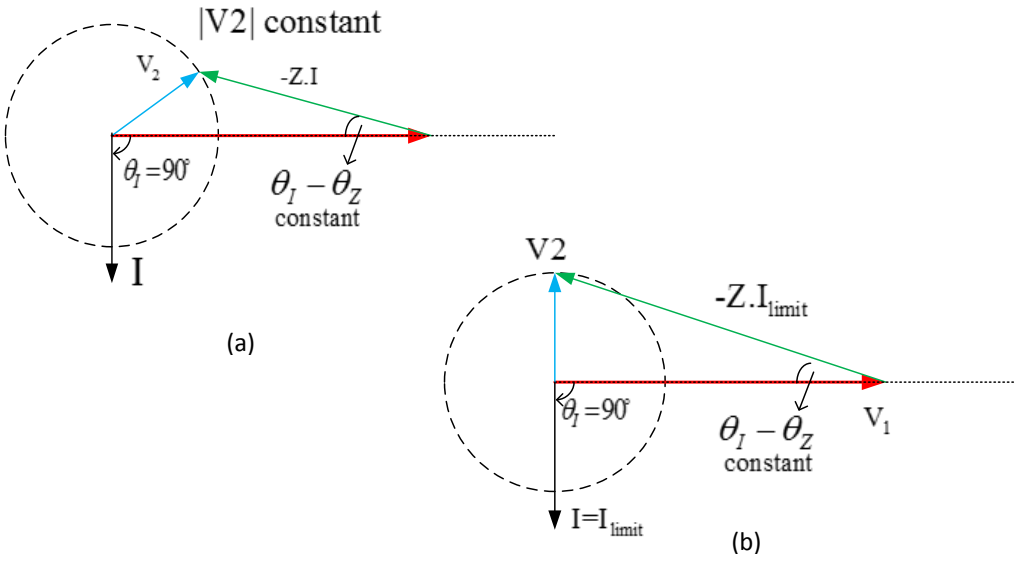

Figure 6.6: Current Transfer Limit for θ_I=90°

Hence the current transfer limit for pure reactive current injection can be expressed as:

$$\theta_I = 90° \Rightarrow V_2 = ZI_{limit}\sin(\theta_I - \theta_Z) \Rightarrow I_{limit} = \frac{V_2}{Z\cos(\theta_Z)} = \frac{V_2}{R} \tag{6.12}$$

From Fig. 6.6 it can be stated that, when the current magnitude is increased beyond the limit for a very low receiving end voltage V_2, the operating point cannot be found. This means that unlimited pure reactive current cannot be injected with zero active current. The limit could be set to infinity if *R* was equal to zero. However, it is practically not possible and hence pure reactive current needs to be injected according to the defined limit.

6.3.2.2 Current Magnitude Limit for θ_I=0° (Pure Active)

For pure active current injection without reactive current, the magnitude of the current is increased with an angle θ_I=0° until the phase difference between V_1 and V_2 approaches *90*°. At this point, the current magnitude will be maximum with a possible operating point. From Fig. 6.7

it can be observed that by applying the abovementioned conditions, V_1 will reduce almost to zero. The current transfer limit can be expressed as:

$$\theta_I = 0° \Rightarrow V_2 = ZI_{limit}\sin(\theta_Z - \theta_I) \Rightarrow I_{limit} = \frac{V_2}{Z\sin(\theta_Z)} = \frac{V_2}{X} \tag{6.13}$$

From the above expression, it can be deduced that pure unlimited active power cannot be injected without reactive current component. When the receiving end voltage drops close to zero, the reactive component eventually increases and reduce the limit of the pure active current. In case of weak AC grids, this is a very widely discussed point when it comes to limiting active power injection.

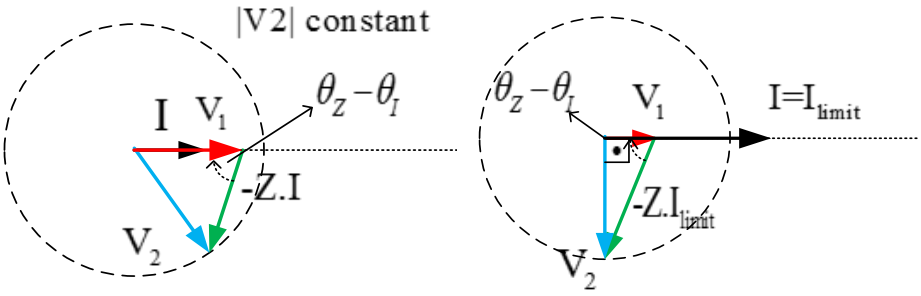

Figure 6.7: Current Transfer Limit for θ_I=0°

6.3.2.3 Current Magnitude Limit for 90°>θI >θZ , θZ >θI >0° (Active and Reactive)

For both active and reactive current injection transfer limits, the magnitude of the current will be continuously increased while keeping the θ_I constant. At this point, both active and reactive powers will get consumed as the angle difference between V_1 and V_2 approaches *90*°.

By following the same technique as discussed in previous cases, for *90*° >θ_I> θ_Z, the current transfer limit is expressed in (6.14) with the aid from Fig. 6.8 below.

$$90° > \theta_I > \theta_Z \Rightarrow V_2 = ZI_{limit}\sin(\theta_I - \theta_Z) \Rightarrow I_{limit} = \frac{V_2}{Z\sin(\theta_I - \theta_Z)} \tag{6.14}$$

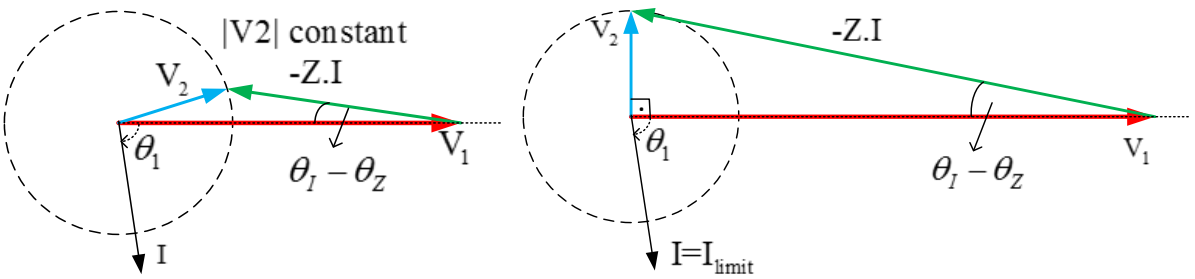

Figure 6.8: Current Transfer Limit for 90°> $\theta_I > \theta_Z$

Unlike the previous cases, for $\theta_Z > \theta_I > 0°$ the magnitude of V_1 decreases with the increase in current magnitude due to highly active current injection. From Fig. 6.9 below, the current transfer limit can be expressed as:

$$\theta_Z > \theta_I > 0° \Rightarrow V_2 = ZI_{limit}\sin(\theta_Z - \theta_I) \Rightarrow I_{limit} = \frac{V_2}{Z\sin(\theta_Z - \theta_I)} \tag{6.15}$$

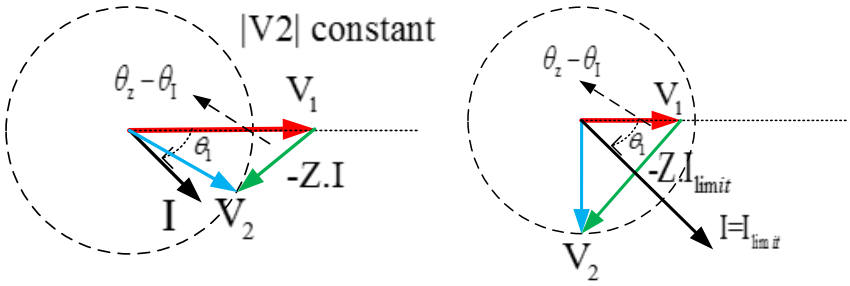

Figure 6.9: Current Transfer Limit for $\theta_Z > \theta_I > 0°$

Similarly, for the case when $90°+\theta_Z > \theta_I > 270°+\theta_Z$, this situation hardly happens with wind turbines during low voltage condition. However, from Fig. 6.10 it can be seen that V_1 drops down to zero for the maximum current and the transfer limit can be expressed as:

$$270° + \theta_Z > \theta_I > 270° + \theta_Z \Rightarrow V_2 = ZI_{limit} \Rightarrow I_{limit} = \frac{V_2}{Z} \tag{6.16}$$

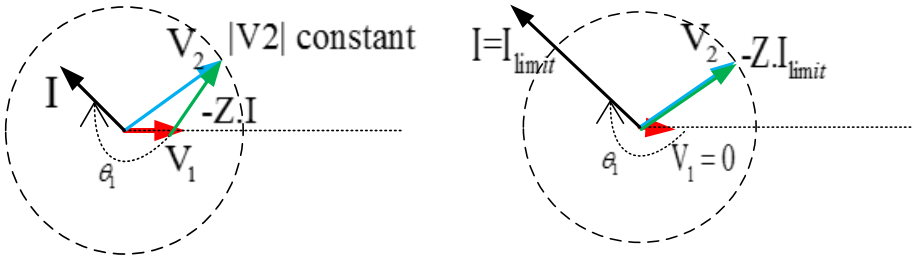

Figure 6.10: Current Transfer Limit for $270°+\theta_Z > \theta_I > 90°+\theta_Z$

6.3.2.4 Current Magnitude Limit for $\theta_I = \theta_Z$

When $\theta_I = \theta_Z$, there will always be an operating point with no limit on the current transfer limit as shown in Fig. 6.11. This is considered to be an ideal case, as it is difficult for the current injection angle to be exactly equal to the impedance angle ($\theta_Z = \tan^{-1}X/R$). For a weak grid, the dynamic parameters are always changing and recursive impedance measurements are needed to be taken for the best estimation.

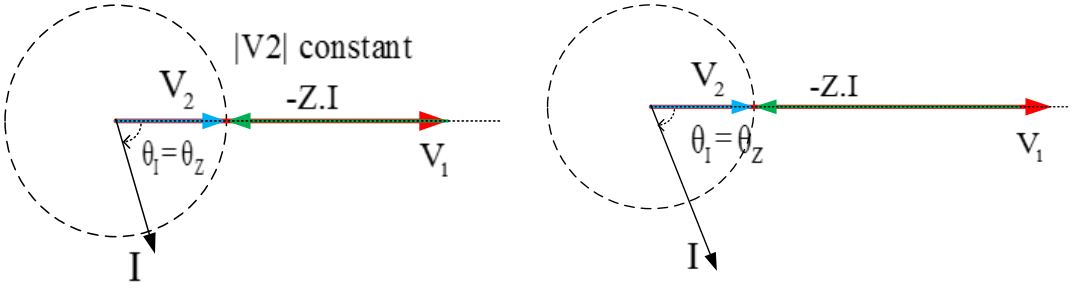

Figure 6.11: Current Transfer Limit for $\theta_I = \theta_Z$

Considering there is no limit to the transfer of currents, the magnitude of V_1 will increase with the increase of current magnitude. However, at some point it will reach the rated magnitude, which means that there is limit to the current injection based on limitation of sending end voltage V_1.

The above mentioned discussion is summarized in Table 6.1. The summary shows that the current transfer limits are based on the receiving end voltage V_2 and the impedance characteristics $R+jX$.

Table 6.1. Current Transfer Limits Depending upon the Angle of Current Injection

Angle of Current Injection	Current Transfer Limit
$\theta_I = 90°$	$I_{limit} \leq V_2/R$
$\theta_I = 0°$	$I_{limit} \leq V_2/X$
$90° > \theta_I > \theta_Z$ $\theta_Z > \theta_I > 0°$	$I_{limit} \leq V_2/Z\text{Sin}(\theta_I - \theta_Z)$ $I_{limit} \leq V_2/Z\text{Sin}(\theta_Z - \theta_I)$
$\theta_I = \theta_Z$	$I_{limit} = \infty$

6.4 Current Transfer Limit for a Grid Integrated Wind Turbine

A single line diagram of a wind turbine integrated into an AC grid is shown in Fig. 6.12 below.

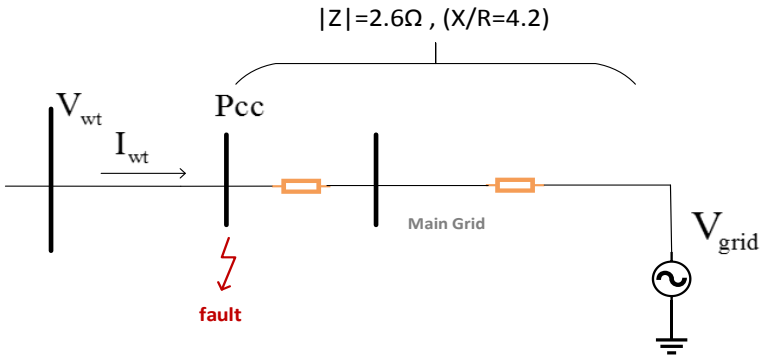

Figure 6.12: WPP Connected to Thevenin Equivalent Model of Grid

If a fault occurs at the PCC, then the flow of currents from the wind turbine (WT) to the fault point can be represented by another single line diagram in Fig. 6.13. Where, Z represents the line impedance and V_f is the voltage at the fault point.

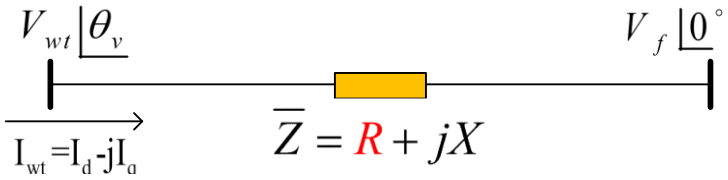

Figure 6.13: Flow of Current from WT to the Fault Point

From the experimental setup shown in chapter-4, a three phase lumped impedance (*Z= 0.60+j2.53* with *X/R=4.2*) is connected between the GSC and the grid emulator. Since the three wire network is emulated with the help of a three-phase programmable power supply, voltage dips could be performed on any of the phases independently. From the abovementioned current transfer limit theory, V_f will remain constant during the fault. It is also defined that the lower the voltage at the fault point is, the narrower the limit of the current transfer will be. At this point, the angle of the current injection ($\tan^{-1} I_q/I_d$) should be close to the angle of impedance; i.e $\tan^{-1}X/R= 76.6°$. The rated current magnitude coming from the wind turbine is *4.41*A. From the discussion in chapter-3, the active power coming from the generator is already being limited by the MSC. The maximum reactive current I_q that could be injected, should be within the transfer limits explained above. However, I_{limit} should also be less than or equal to I_{rated} of the GSC; i.e $I_{\lim it} = \sqrt{I_d^2 + I_q^2} \leq I_{rated}$.

From the current transfer theory, it can be derived that any current with magnitude less than V_f/Z, is always within the safe transfer limits and can be expressed as:

$$I_{WT} < \frac{V_f}{Z} \quad \} \quad for \quad 0° < \theta_I < 360° \tag{6.17}$$

In other words, the current injected according to the abovementioned condition would definitely be inside the transfer limits. However, the current injection would be very small. For example, current injected by a WT within the transfer limit for a fault with remaining voltage less than 10% and impedance 0.20pu, would be 0.10/0.20=0.5pu. This limited injection of current is used as a reference for the evaluation of a scheme discussed in the section 6.5.

From the discussion above, it can be summarized that similar to active/reactive power transfer limits, current transfer limits also exist for a grid connected system. For a grid connected WT, it is shown that for a very low voltage at the fault point, the current injection should also be reduced according to the transfer limit theory. This consideration is very important when it comes to integrating WT in weak AC grids. However, it is usually overlooked when the grid codes are designed.

6.5 X/R based Current Injection

From the discussion above, it is noticed that current transfer limit is based on the remaining voltage at the receiving end and the impedance between the GSC and the fault point. Hence a simple solution is provided to calculate the active and reactive current references for the wind turbine to stay within the transfer limits. From section *6.3.2.4*, it can be seen that when a current is injected with the same angle as that of the impedance, the operating point will always be within the current transfer limits. This means that the ratio between reactive and active currents should be equal to the X/R ratio.

Most of the grid codes are designed for maximum reactive current injection and the amount of active current is decided between the TSO and the supplier. However, to calculate and inject the amount of reactive current within the current transfer limits, an algorithm based on X/R ratio is illustrated in Fig. 6.14.

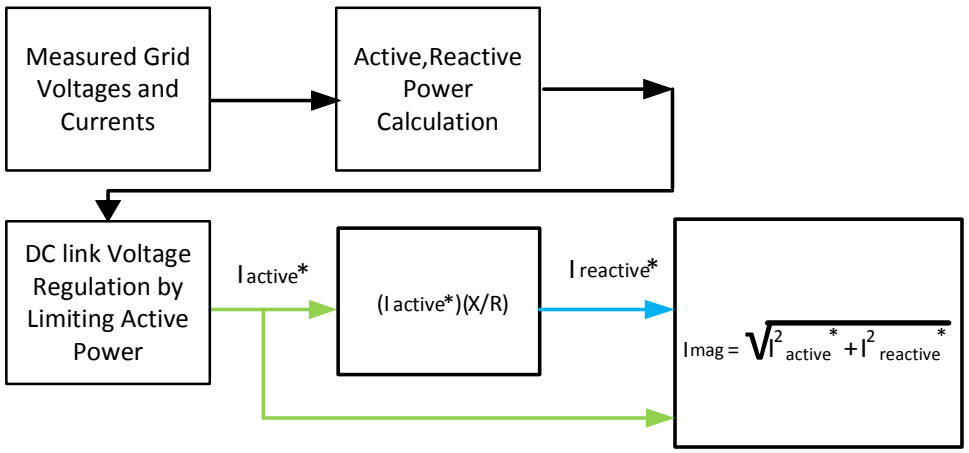

Figure 6.14: Reactive Current Calculation based on X/R

From the example given in the previous section, if the estimated impedance is *Z= 0.60+j2.53* with *X/R=4.2*. The angle of impedance will be $\tan^{-1}X/R$= *76.6°*. Hence, a high reactive current should be injected with the same angle as that of the angle of impedance i.e $\tan^{-1} I_q/I_d \approx 76.6°$. For instance, if I_d=*1.1A*, then, I_q can be calculated as:

$$\frac{I_q}{I_d} = \frac{X}{R} \Rightarrow I_q = \frac{X}{R}.I_d = 4.62A \tag{6.18}$$

The reactive current calculated above must also stay within the rated current limit when injected with a small amount of active current which is being adjusted by the MSC and later on by the GSC. Hence the injection of reactive current depends on the amount of active current being transferred and is depicted in Fig. 6.15.

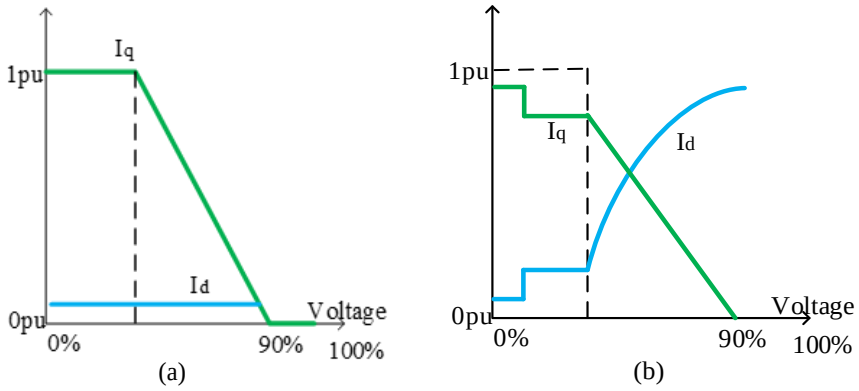

Figure 6.15: X/R based Current Injection, (a) without and (b) with algorithm

It can be seen from Fig. 6.15 (b) that the I_q decreases in accordance with the I_d, just to make sure that I_{mag} must not exceed the rated limit. By adopting the proposed technique, there are two major advantages. Firstly, the power factor during the fault would always be greater than zero. Secondly, by having a non-zero active current, there is always real power available and eventually more apparent power will be available to be absorbed by the load. For instance, if the power factor drops to *0.3* for a *3*kW system, then *10kVA* of apparent power will be required to be transferred to the load.

6.5.1 X/R Parameter Uncertainty and Bandwidth Limit

From the discussion in section 6.3.2, it is found out that the band of the current transfer limit gets narrower as the fault voltage (V_f) goes minimum or when the magnitude of impedance (Z) increases. The method proposed above, would always have a small degree of uncertainty when estimating the X/R parameters. If the parameters are not estimated correctly, then the I_q calculation from the equation (6.17) will also give erroneous results. Furthermore, the angle of impedance would also be incorrect, which means that the condition illustrated in Fig. 6.11 cannot be fulfilled.

In order to study the impedance angle precision, Fig. 6.16 is considered to calculate the allowed uncertainty and is based on the current transfer limit theory. The magnitude of the current will stay constant and the point will be located where the current reference deviates from the angle of impedance. The allowed angle deviation can be expressed as [10]:

$$\left|I_{WT}\right| = \frac{\left|\frac{V_f}{Z}\right|}{\left|ZSin\left(\theta_I - \theta_Z\right)\right|} \tag{6.19}$$

If the I_{WT} is 1pu, then

$$\left|Sin\left(\theta_I - \theta_Z\right)\right| = \left|I_{WT}\right|\left|\frac{V_f}{Z}\right|$$

$$\left|\left(\theta_I - \theta_Z\right)\right| \approx \left|I_{WT}\right|\left|\frac{V_f}{Z}\right| \quad \Rightarrow \quad \theta_I = \theta_Z \pm \left|I_{WT}\right|\left|\frac{V_f}{Z}\right| \text{ (in radians)} \tag{6.20}$$

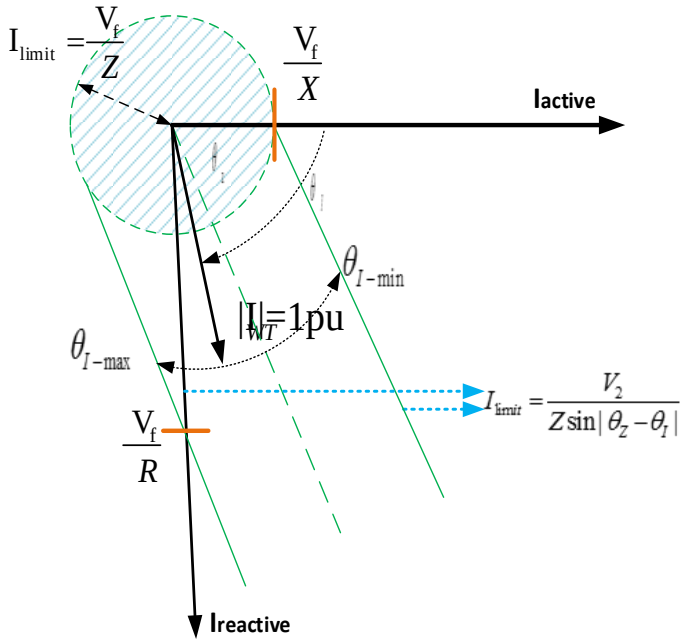

Figure 6.16: Allowed Current Angle Bandwidth

With reference to the Fig. 6.16 if the current magnitude is fixed at 1pu, with 20% (0.20pu) remaining voltage at the fault point and with 0.5pu of impedance, then the deviation between the current angle and angle of impedance should not be more than *23.57*° to stay within the limit. A general expression representing the angle estimation error, and at the same time satisfying the current transfer limit can be written as:

$$\theta_{Z-err} \leq |I_{WT}| \left| \frac{V_f}{Z} \right| \quad \textit{(in radians)} \tag{6.21}$$

The above expression assures that if a current is injected with an angle of $\pm\,\theta_{Z\text{-}err}$, then the current would certainly stay within the limit. Furthermore, if the remaining voltage at the fault point is reduced further than 10% (0.1pu) then the allowed angle deviation reduces to *11.53*°. This shows that, by lowering the remaining voltage at the fault point, the angle bandwidth will also become narrower. Due to this uncertainty, *X/R* method is applicable for specific values of the remaining voltages at the fault point. In this thesis, 20% of the remaining voltage is considered for the experimental results.

6.6 Dual Sequence Current Injection

From the discussion in section 6.2, coupling between positive, negative and zero sequences has been seen during asymmetrical faults. To mitigate or balance out the oscillations occurred due to the coupling, multiple control techniques related to WTs have been studied in the literature [11]-[18]. However, these techniques only deal with the issues on the WT side by reducing the negative sequence component and not considering the grid side impact onto the WT power generation. Especially when an asymmetrical fault occurs on the grid side and the WT continues to generate the active power without knowledge of the impact of extra active power being transferred to the grid. In the section 6.2, it has been studied that by using conventional methods, injection of pure positive sequence reactive current can cause negative sequence over-voltages and phase unbalance. To mitigate this coupling effect, dual sequence current injection has been performed in this chapter. By following this method, the faulty phases will be supported by injecting limited positive and negative sequence currents in accordance with the current transfer limit theory.

From the discussion in section 3.4, the voltage expressions for positive and negative sequences can be given as:

$$V_{dq,conv}{}^{+} = R_T I_{dq}^{+} + L_T \frac{dI_{dq}^{+}}{dt} + j\omega L_T I_{dq}^{+} + V_{dq,grid}^{+} \tag{6.22}$$

$$V_{dq,conv}{}^{-} = R_T I_{dq}^{-} + L_T \frac{dI_{dq}^{-}}{dt} - j\omega L_T I_{dq}^{-} + V_{dq,grid}^{-} \tag{6.23}$$

Where R_T and L_T are the resistance and inductance of the grid side filter and the line impedance. $V_{dq,conv}$ is the voltage at the GSC output, $V_{dq,grid}$ is the voltage at the PCC and I_{dq} is the current represented in synchronous reference frame. The indexes (+,-) indicate the positive and negative sequence components and ω is the angular frequency of the grid voltage. The apparent power (S) to be absorbed by the load during unbalanced condition can be expressed as:

$$S = (e^{j\omega t} V_{dq,grid}^{+} + e^{-j\omega t} V_{dq,grid}^{-})(e^{j\omega t} I_{dq}^{+} + e^{-j\omega t} I_{dq}^{-}) \tag{6.24}$$

By expanding the above expression, active (*P*) and reactive (*Q*) powers can be represented as:

$$P(t) = P_o + P_c \cos(2\omega t) + P_s \sin(2\omega t) \tag{6.25}$$

$$Q(t) = Q_o + Q_c \cos(2\omega t) + Q_s \sin(2\omega t) \tag{6.26}$$

It is to be noted that during asymmetrical faults, dual current controller for positive and negative sequences is used to reduce the DC link over-voltages and the second order components. As a result, the two components P_c and P_s are set to be zero for the final analysis. Hence, *P(t)* will be equal to P_o and is expressed below:

$$P(t) = \frac{3}{2}(V^+_{d,grid} I^+_d + V^+_{q,grid} I^+_q + V^-_{d,grid} I^-_d + V^-_{q,grid} I^-_q) \tag{6.27}$$

And similarly,

$$Q(t) = \frac{3}{2}(V^+_{q,grid} I^+_d - V^+_{d,grid} I^+_q + V^-_{q,grid} I^-_d - V^-_{d,grid} I^-_q) \tag{6.28}$$

For the computation of positive and negative sequence currents, required to implement a dual vector control can be expressed as [19]-[20]:

$$\begin{bmatrix} P(t) \\ Q(t) \\ 0 \\ 0 \end{bmatrix} = \frac{3}{2} \begin{bmatrix} V^+_{d,grid} & V^+_{q,grid} & V^-_{d,grid} & V^-_{q,grid} \\ V^+_{q,grid} & -V^+_{d,grid} & V^-_{q,grid} & -V^-_{d,grid} \\ V^-_{q,grid} & V^-_{d,grid} & -V^+_{q,grid} & V^+_{d,grid} \\ V^-_{d,grid} & V^-_{q,grid} & V^+_{d,grid} & V^+_{q,grid} \end{bmatrix} \begin{bmatrix} I^+_d \\ I^+_q \\ I^-_d \\ I^-_q \end{bmatrix} \tag{6.29}$$

If, $V^+_{dq,\,grid} = V^+_{dq}$ and $V^-_{dq,\,grid} = V^-_{dq}$, then;

$$\begin{bmatrix} I^+_d \\ I^+_q \\ I^-_d \\ I^-_q \end{bmatrix} = \frac{2}{3} \begin{bmatrix} V^+_d & V^+_q & V^-_d & V^-_q \\ V^+_q & -V^+_d & V^-_q & -V^-_d \\ V^-_q & V^-_d & -V^+_q & V^+_d \\ V^-_d & V^-_q & V^+_d & V^+_q \end{bmatrix}^{-1} \begin{bmatrix} P(t) \\ Q(t) \\ 0 \\ 0 \end{bmatrix} \tag{6.30}$$

Where, *Q(t)* will be set according to the current transfer limit explained in section 6.3 and *P(t)* is the maximum active power reference equal to P_{grid} obtained from equation (3.34), in chapter-3.

$$P(t) = P_{grid} = P_{gen} - P_{conv} - P_{filter} = 2980W \tag{6.31}$$

6.6.1 Active and Reactive Current Calculation for Limited Power Transfer during FRT

The power calculated in equation (6.31) is the maximum power that could be extracted from the wind turbine at the PCC. During an asymmetrical fault the PMSG does not sense the fault and continues to generate active power which eventually ends up creating DC link over-voltages. To regulate the DC link voltage during asymmetrical fault, a control structure is developed and discussed in chapter-3 for the MSC. The GSC on the other hand, will control the generated power and inject the active and reactive currents according to the current transfer limit theory discussed in section 6.3. However, to determine the values of positive and negative current components to be injected for limited power transfer, an analysis is performed below.

Firstly, it is assumed that the current in each phase will be less than I_{max}. Secondly, from the equation (6.30) positive and negative sequence components of the voltage at the PCC and GSC currents are separated and expressed for limited active power transfer. The expressions below are derived after solving the matrix presented in equation (6.30). Due to space limitation, the beginning part of the calculations is not shown here. Hence, the expressions for positive and negative sequence currents are given below as:

$$I_d^+ = \frac{2[(|V_{dq}^+|^2 + |V_{dq}^-|^2)P_{\lim}V_d^+ + (|V_{dq}^+|^2 - |V_{dq}^-|^2)Q(t)V_q^+]}{3(|V_{dq}^+|^2 - |V_{dq}^-|^2)(|V_{dq}^+|^2 + |V_{dq}^-|^2)} \tag{6.32}$$

$$I_q^+ = \frac{2[(|V_{dq}^+|^2 + |V_{dq}^-|^2)P_{\lim}V_q^+ - (|V_{dq}^+|^2 - |V_{dq}^-|^2)Q(t)V_d^+]}{3(|V_{dq}^+|^2 - |V_{dq}^-|^2)(|V_{dq}^+|^2 + |V_{dq}^-|^2)} \tag{6.33}$$

$$I_d^- = \frac{2[-(|V_{dq}^+|^2 + |V_{dq}^-|^2)P_{\lim}V_q^- + (|V_{dq}^+|^2 - |V_{dq}^-|^2)Q(t)V_d^-]}{3(|V_{dq}^+|^2 - |V_{dq}^-|^2)(|V_{dq}^+|^2 + |V_{dq}^-|^2)} \tag{6.34}$$

$$I_q^- = \frac{2[-(|V_{dq}^+|^2 + |V_{dq}^-|^2)P_{\lim}V_d^- - (|V_{dq}^+|^2 - |V_{dq}^-|^2)Q(t)V_q^-]}{3(|V_{dq}^+|^2 - |V_{dq}^-|^2)(|V_{dq}^+|^2 + |V_{dq}^-|^2)} \tag{6.35}$$

The sum of positive and negative *dq*-axis currents should be less than I_{max}, so the current limitation of the GSC currents can be expressed as:

$$\mathrm{I}_{\max} \geq |\,\mathrm{I}_{dq}^{+}\,| + |\,\mathrm{I}_{dq}^{-}\,| \tag{6.36}$$

Where, $|\,\mathrm{I}_{dq}^{+}\,| = \sqrt{|\,\mathrm{I}_{d}^{+}\,|^{2} + |\,\mathrm{I}_{q}^{+}\,|^{2}}$ and $|\,\mathrm{I}_{dq}^{-}\,| = \sqrt{|\,\mathrm{I}_{d}^{-}\,|^{2} + |\,\mathrm{I}_{q}^{-}\,|^{2}}$.

If the negative sequence currents are used to reduce the second order component fluctuations. Then the ratio of negative to positive sequence should be equal to the unbalance factor, and expressed as:

$$u = |\,\mathrm{I}_{dq}^{-}\,| / |\,\mathrm{I}_{dq}^{+}\,| = |\,V_{dq}^{-}\,| / |\,V_{dq}^{+}\,| \tag{6.37}$$

By combining equations (6.36) and (6.37), the maximum positive sequence current which can be produced by the GSC is expressed as:

$$|\,\mathrm{I}_{dq-\max}^{+}\,| = \frac{|\,\mathrm{I}_{dq}^{+}\,| + |\,\mathrm{I}_{dq}^{-}\,|}{[1 + (|\,\mathrm{I}_{dq}^{-}\,| / |\,\mathrm{I}_{dq}^{+}\,|)]} = \frac{\mathrm{I}_{\max}}{1+u} \tag{6.38}$$

The reactive power *Q(t)* required at the PCC can be given as:

$$Q(t) = \frac{3}{2}\sqrt{|\,V_{dq}^{+}\,|^{2} + |\,V_{dq}^{-}\,|^{2}}\, I_{q}^{+-}$$

$$Q(t) = \frac{3}{2}\left[\sqrt{[V_{d}^{+2} + V_{q}^{+2}] + [V_{d}^{-2} + V_{q}^{-2}]}\right] I_{q}^{+-} \tag{6.39}$$

Where, $I_{q}^{+-} = |\,I_{q}^{+}\,| + |\,I_{q}^{-}\,|$. If the negative sequence component is utilised to reduce the second order components in the voltage. Then the positive sequence component will be required to calculate the magnitude of reactive current needed according to the current transfer limit. Hence I_{q}^{+} can be formulated as:

$$I_{q}^{+} = \alpha\sqrt{I_{\max}}\ ,\ \text{where}\ \{\alpha = \frac{X}{R}\} \tag{6.40}$$

Hence, *Q(t)* can be redefined in equation (6.41) below. It is to be noted that the reactive power *Q(t)* can be calculated according to varying X/R ratios by just replacing the value of *α*.

$$Q(t) = \frac{3}{2}\left[\sqrt{[V_d^{+2} + V_q^{+2}] + [V_d^{-2} + V_q^{-2}]}\right]\alpha\sqrt{I_{\max}} \tag{6.41}$$

Similarly by squaring the equation (6.36), it can be expressed in terms of positive sequence as:

$$I_{\max}^2 = |\,I_{dq}^{+}\,|^2\,(1+u)^2 \tag{6.42}$$

By inserting equations (6.32)-(6.35) in (6.42), the limited active power required during an asymmetrical fault can be given as:

$$P_{\lim} = \frac{3}{2} I_{\max}\,|\,V_{dq}^{+}\,|\,(1-u^2) \tag{6.43}$$

$$P_{\lim} = \frac{3}{2} I_{\max}\,|\,V_{dq}^{+}\,|\left[1 - \frac{|\,V_{dq}^{-}\,|^2}{|\,V_{dq}^{+}\,|^2}\right] \tag{6.44}$$

$$P_{\lim} = \frac{3}{2} I_{\max}\left(\sqrt{|\,V_d^{+}\,|^2 + |\,V_q^{+}\,|^2}\right)\left[1 - \frac{|\,V_d^{-}\,|^2 + |\,V_q^{-}\,|^2}{|\,V_d^{+}\,|^2 + |\,V_q^{+}\,|^2}\right] \tag{6.45}$$

As mentioned in the beginning of this chapter that the limited current injection technique mainly focuses on asymmetrical faults where the grid voltage (V_{PCC}) drops lower than *50*% of the nominal value or the unbalance factor (u) goes higher than *0.5*. Therefore, this study is undertaken for deep voltage sags because it has not been discussed explicitly in the published research literature. With asymmetrical faults on single or double lines, the V_{PCC} goes below *50*% only when a short circuit occurs in one or two lines. This was not simple to be achieved in the lab environment. However, it was accomplished by implementing two-phase 80% dip with the help of a grid emulator. By implementing the two-phase *80*% dip, V_{PCC} was made to drop below *50*%. An example is demonstrated in section 6.7.1.

In case where V_{PCC} does not drop below *50*%, another example is given in section 6.7.2 to show the validity of the proposed technique. A single phase *80*% dip is applied with the unbalance factor equal to *0.32*. To implement the limited current technique, an unbalance reference factor *'k'* is introduced for V_{PCC}*>50*%. Hence, the equation (6.41) can be improved as:

$$Q(t) = \frac{3}{2}\left[\sqrt{[V_d^{+2} + V_q^{+2}] + [V_d^{-2} + V_q^{-2}]}\right]\alpha\sqrt{I_{\max}}.k \tag{6.46}$$

Where,

$$k = \begin{cases} 1 \ldots\ldots\ldots\ldots\ldots\ldots\ldots (u \geq 0.5) \\ 1 + \dfrac{\sqrt{1+u^2}}{(1+u)\alpha} \ldots\ldots\ldots (u \leq 0.5) \end{cases}$$

After defining *Q(t)*, it is made sure that the solution for P_{lim} also exists for all the conditions. Hence, equation (6.45) is improved as:

$$P_{\lim} = \frac{3}{2} I_{\max} \left(\sqrt{|V_d^+|^2 + |V_q^+|^2} \right) \left[1 - \frac{|V_d^-|^2 + |V_q^-|^2}{|V_d^+|^2 + |V_q^+|^2} \right] \cdot \left[(1+u^2) - \frac{\sqrt{k}}{(1+u)^2} \right] \qquad (6.47)$$

From equation (6.47), it can be seen that the P_{lim} depends on the maximum rated current value, positive and negative sequence voltages, *X/R* ratio and the unbalance factor. After calculation of *Q(t)* and P_{lim} , these values can be used in expressions (6.32)-(6.35) to calculate the positive and negative sequence currents required to limit the power transfer. It is worth noting that by limiting the active power with the GSC, the generated active power by the PMSG could also be limited hence eliminating the need of an additional device (e.g crowbar) for the dissipation of excessive wind power. Also, the GSC will be able to inject reactive currents according to different grid codes or in the case of this thesis, it will inject reactive currents according to varying X/R ratios and the unbalance factor.

6.7 Experimental Setup and Results

To validate the effectiveness of the analysis performed in sections 6.5 and 6.6, numerical examples are given and supplemented with experimental results to demonstrate the active/reactive power limitation during an asymmetrical fault condition. The physical experimental setup of the block diagram shown in Fig. 6.5 is illustrated below in Fig 6.17.

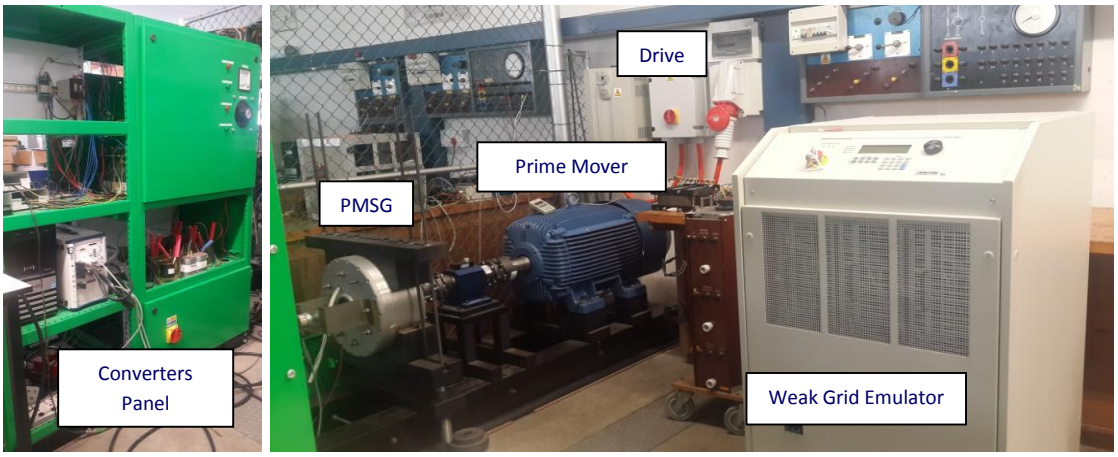

Figure 6.17: Laboratory Test Bench

6.7.1 Two Phase Unbalanced Voltage Dip

A scenario is assumed where a DLG fault / two phase voltage dip (*80%* on *phases B* and *C*) is implemented with the following PCC measurements:

V_d^+=105V, V_q^+=*-22*V, V_d^-=*-68*V, V_q^-=15V and *X/R*=4.2. The rated current of the PMSG is *4.41A* (RMS). From equation (6.41), the reactive power reference is calculated as Q*(t)=1341VAr*. The limited active power from equation (6.45) can be computed as P_{lim} *=432W*. By substituting these powers and the maximum rated current in expressions (6.32)-(6.35), the positive and negative sequence currents can be calculated as: I_d^+*=3.3A*, I_q^+*=-6.6A*, I_d^-*=-4.32A* and I_q^-=2A.

According to the scenario described above, Fig. 6.18 (a) on the next page illustrates a two-phase dip at the PCC with 20% remaining voltages on phases *B* and *C*. The converted positive sequence *dq* voltage components are shown in Fig. 6.18 (b) and their separate zoomed-in waveforms are shown in Fig. 6.18 (c) and (d). Similarly, the converted negative sequence *dq* voltage components are shown in Fig. 6.19 (a) and their zoomed-in waveforms are illustrated in Fig. 6.19 (b).

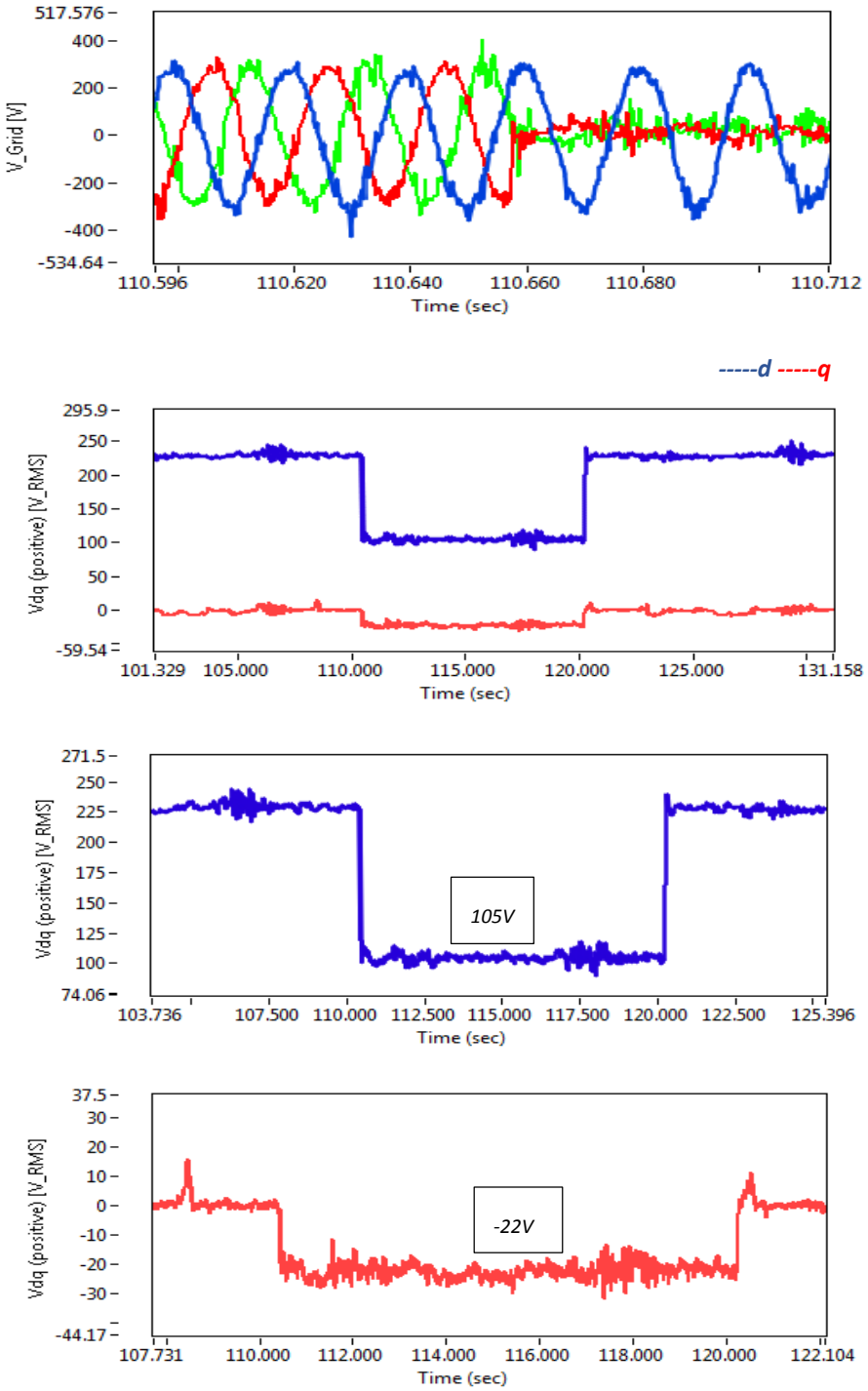

Figure 6.18: (a) PCC Voltage, (b) d-q axis Positive Sequence Voltages, (c) Zoomed-in d-axis Positive Sequence Voltage, (d) Zoomed-in q-axis Positive Sequence Voltage

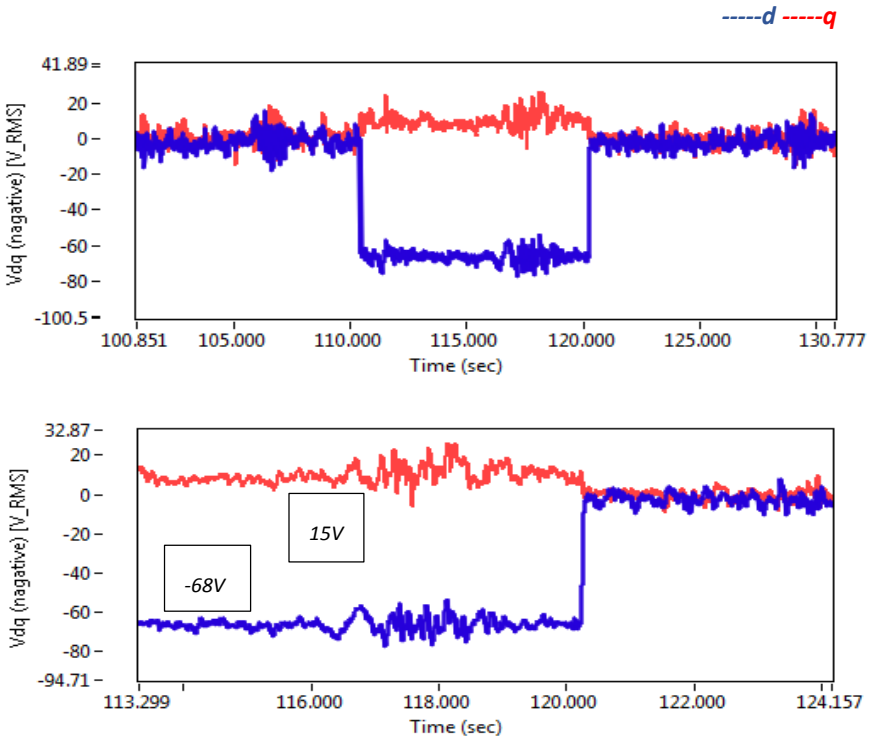

Figure 6.19: (a) d-q axis Negative Sequence Voltages, (b) Zoomed-in d-q axis Negative Sequence Voltages

Fig. 6.20 (b) shows the zoomed-in limited active power and the required reactive power according to the currents illustrated in Fig. 6.21. It should be noticed from the equation (6.41), that the reactive power requirement increases with the increase of *X/R* ratio. The DC link voltage is also illustrated in Fig. 6.20 (c). It is regulated within the safety limit with the help of MSC and without using any external hardware. Low-scaled second order harmonics can also be seen in the DC link voltage. These harmonics could be reduced by implementing a dual vector control on the machine side. However, due to the size of the code and FPGA space limitation, dual vector control has only been applied to implement the grid side control. To stabilise the DC link voltage, pitch control is implemented and increased speed of the generator can also be observed during the fault in Fig. 6.20 (d).

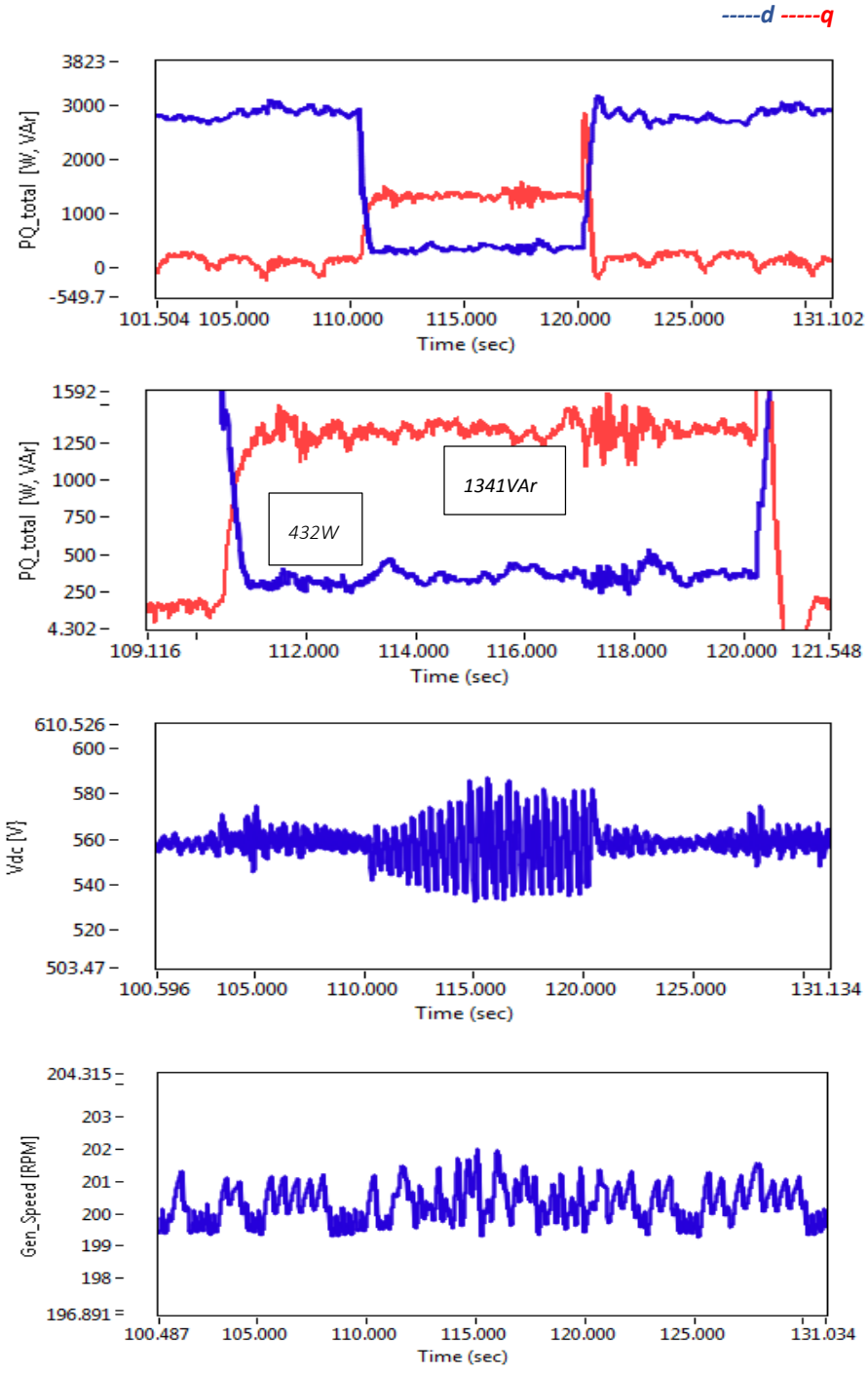

Figure 6.20: (a) Applied Active and Reactive Powers, (b) Zoomed-in Active and Reactive Powers, (c) DC link Voltage, (d) Generator Speed

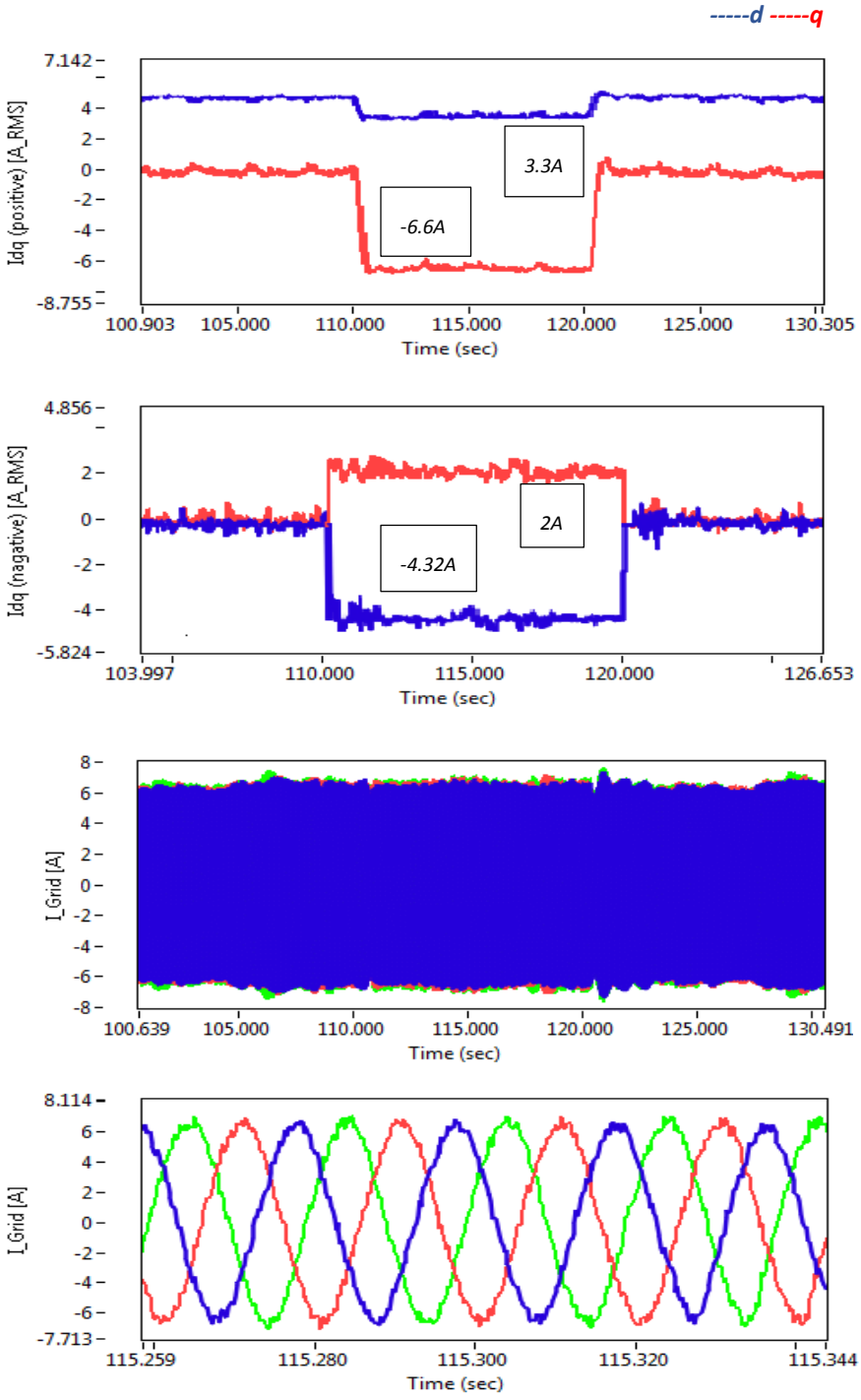

Figure 6.21: (a) d-q axis Positive Sequence Currents, (b) d-q axis Negative Sequence Currents, (c) Grid Side Currents, (d) Zoomed-in Grid Side Currents during Fault

In Fig. 6.21, grid side currents are shown. **This is the main contribution of this chapter**. From Fig. 6.21 (a) positive sequence currents can be seen which are obtained from equations (6.32)-(6.33). Similarly the negative sequence components obtained from the equations (6.34)-(6.35) are illustrated in Fig. 6.21 (b). With reference to Fig. 6.18 (a), due to deep voltage dip (20% remaining voltage), higher magnitude of negative sequence component is injected. By implementing the derived limits, the peak magnitude of the three phase currents is also kept within the rated current limit as shown in Fig. 6.21 (c) and (d). It is worth noting that $|I_d|$ is reduced but not set equal to zero and subsequently $|I_q|$is also injected within the defined limit. Furthermore, their calculated ratio from the results '*4.6*' is approximately equal to the *X/R* ratio '*4.2'*. The *X/R* based current injection, can also assist in avoiding other unbalance conditions such as loss of synchronism (LOS) between the system and grid's frequency during deep voltage sags [10].

6.7.2 Single Phase Unbalanced Voltage Dip

Another scenario is assumed where a SLG fault / single phase voltage dip (*80% phase-C*) is implemented with the following PCC measurements:

V_d^+=170V, V_q^+=*-5*V, V_d^-=*-22*V, V_q^-=*50V*, *X/R*=4.2 and the rated current of the PMSG is *4.41A* (RMS). The section described above for the current transfer limit, is for deep voltage sag situations where V_{PCC} <50% of the nominal value. However, for the case where V_{PCC} >50%, the expressions (6.32)-(6.35) could give over-currents if reactive and active powers are not updated. To prevent this situation, the improved reactive and active power equations (6.46)-(6.47) will be applied. With the V_{PCC} >50% and unbalance factor less than 0.*5*, reduced reactive power is required. This means there is less chance of instability and the current injection does not strictly have to follow the angle of impedance because of its less impact on the stability of the system. Hence I_q/I_d does not have to be equal to the *X/R* ratio. The limited current injection method shows the optimal active power limitation along with the reactive power supply. The purpose here is to demonstrate the relevance of the proposed technique under different conditions.

According to the scenario described above, Fig. 6.22 (a) illustrates a single-phase (*Phase-C*) dip at the PCC with *20*% remaining voltage on that phase. The converted positive and negative sequence *dq*-axis voltage components are shown in Fig. 6.22 (b) and (c).

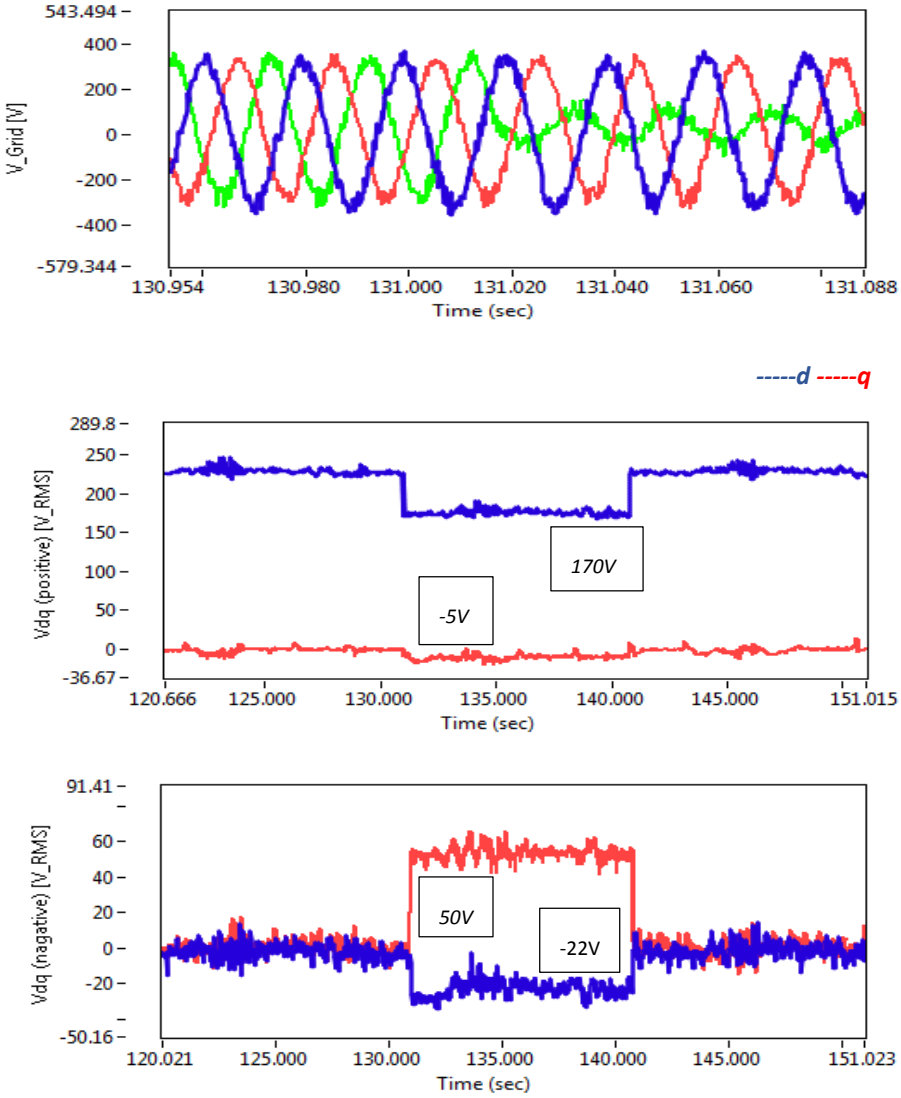

Figure 6.22: (a) PCC Voltage, (b) d-q axis Positive Sequence Voltages, (c) d-q axis Negative Sequence Voltages

Fig. 6.23 (a) shows the limited active power and the required reactive power according to the calculated currents illustrated in Fig. 6.24. The reactive power reference was calculated to be Q*(t)=900VAr* and the limited active power was computed as P_{lim} *=1190W*. By substituting these powers and the maximum rated current in expressions (6.32)-(6.35), the positive and negative sequence currents can be calculated as: I_d^+*=5A*, I_q^+*=-3.3A*, I_d^-*=-1.92A* and I_q^-*=-0.25*A. The DC link voltage regulation is illustrated in Fig. 6.23 (b) and the generator speed profile during the fault can also be seen in Fig. 6.23 (c).

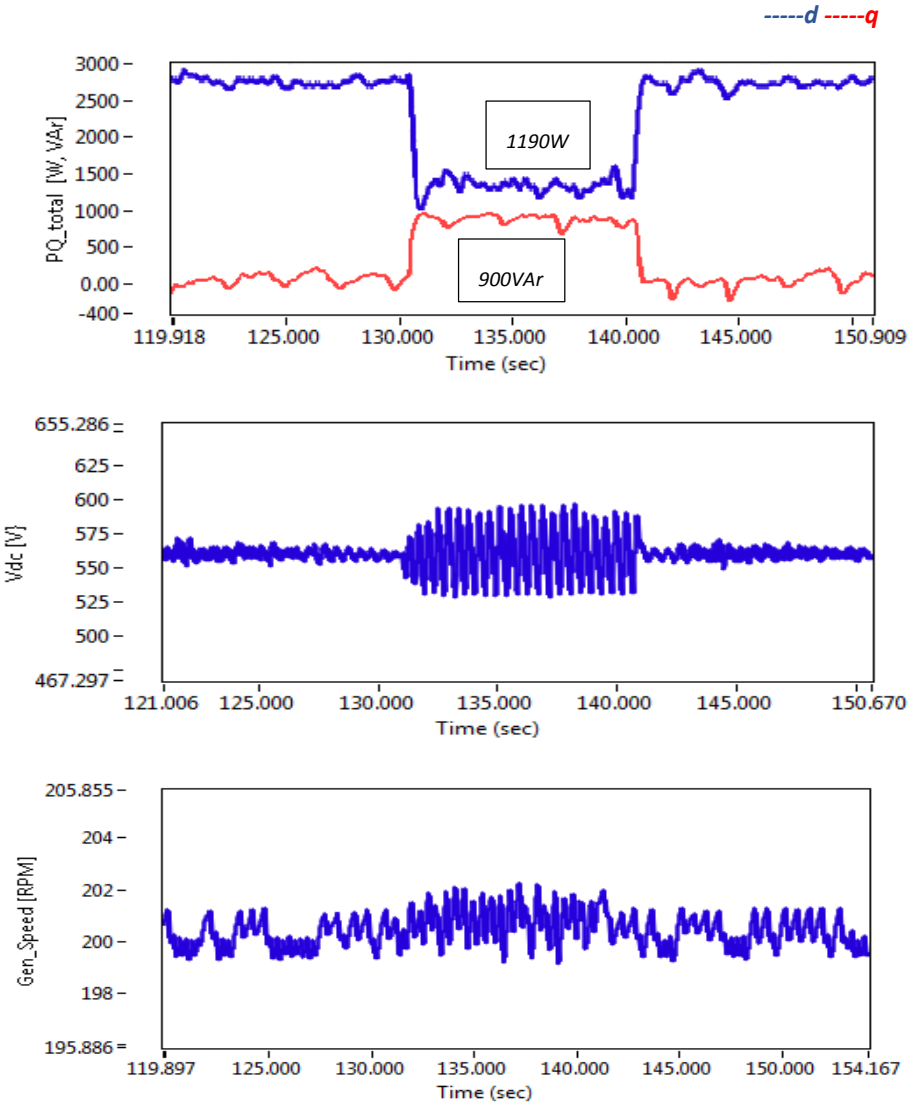

Figure 6.23: (a) Applied Active and Reactive Powers, (b) DC link Voltage, (c) Generator Speed

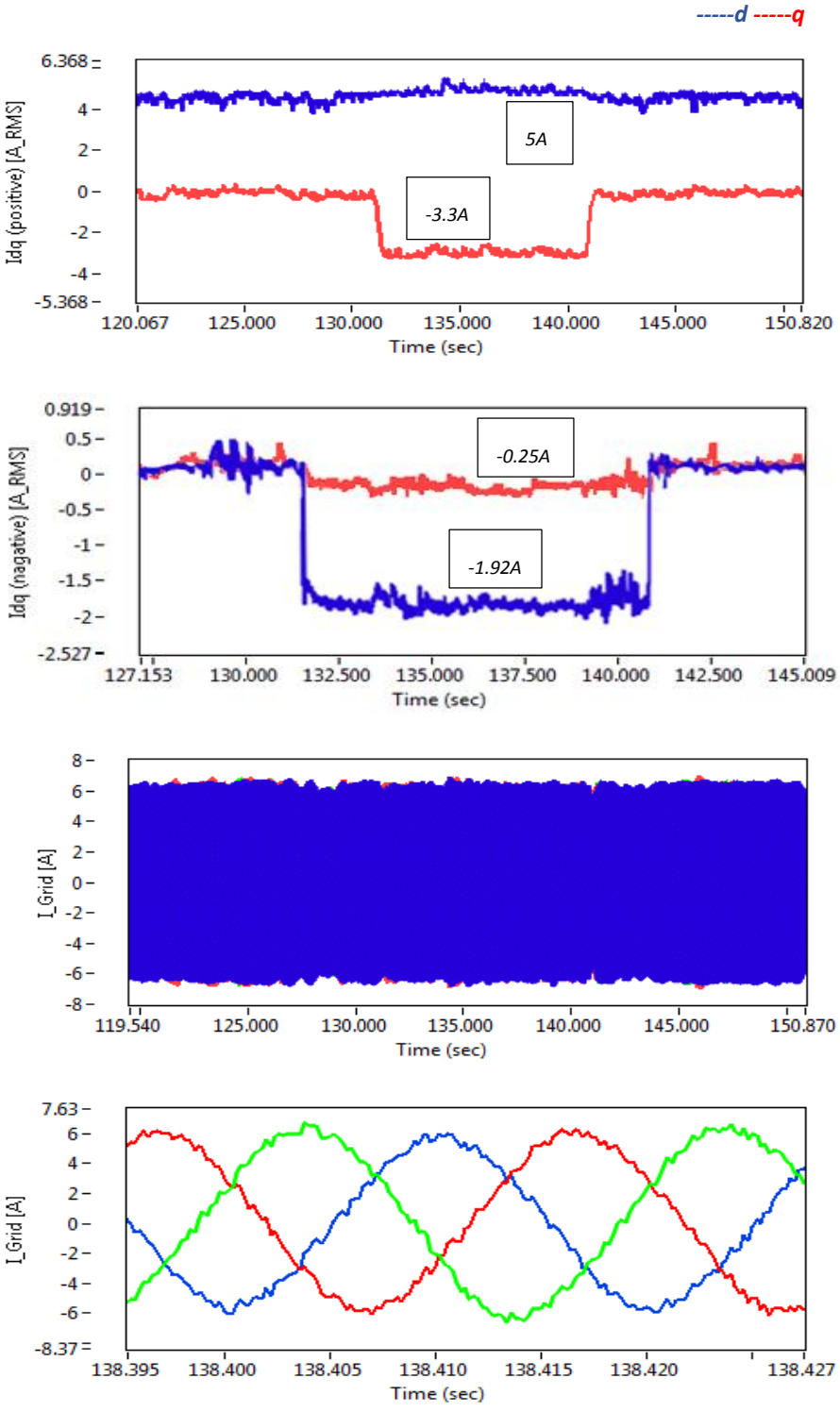

Figure 6.24: (a) d-q axis Positive Sequence Currents, (b) d-q axis Negative Sequence Currents, (c) Grid Side Currents, (d) Zoomed-in Grid Side Currents during Fault

In Fig. 6.24 (a) and (b), positive and negative sequence currents can be seen which are injected to obtain the active and reactive powers calculated from equations (6.46)-(6.47). Since the V_{PCC} is greater than 50% of the nominal value, less amount of negative sequence component is injected. Furthermore, by implementing the derived limits, the peak magnitude of the three phase currents is also kept within the rated current limit as shown in Fig. 6.24 (c) and (d).

6.8 Conclusion

This chapter discusses the impact of asymmetrical faults on a grid connected wind energy system. Two cases of DLG and SLG faults (double- and single-phase dips) are highlighted where coupling problems are presented between the symmetrical components. To mitigate that, current injection technique is proposed with limited injection of active and reactive components. The derived limits are dependent on the varying X/R ratios and based on that, active and reactive current components are injected in order to maintain stable DC link voltage and limited GSC peak currents.

The practical implementation of the abovementioned study suggests modification in the international grid codes for integration of WECS into weak AC grids during asymmetrical faults. From the results, it is shown that the proposed technique eliminates the need of an external hardware for DC link overvoltage suppression and implements FRT. Furthermore, the peak currents are also kept within the defined limits with the aid of positive and negative sequence currents injection. The overall power factor has also been kept greater than zero because the active current component is not forced down to zero when the V_{PCC} drops below *50*%.

6.9 References

[1] J. Mohammadi, S. Afsharnia, S. Vaez-Zadeh and S. Farhangi, "Improved fault ride through strategy for doubly fed induction generator based wind turbines under both symmetrical and asymmetrical grid faults," in *IET Renewable Power Generation*, vol. 10, no. 8, pp. 1114-1122, 9 2016.

[2] Transmission Code 2007. Networks and System Rules of the German Transmission System operators, VDN-e.v. beim VDEW, www.vdn-berlin.de, August 2007.

[3] V. O. Zambrano, E. B. Makram, and R. G. Harley, "Transient response of synchronous and asynchronous machines to asymmetrical faults in an unbalanced network," *Electric Power Systems Research*, vol. 14, no. 2, pp. 155-166, 1988.

[4] Ö. Göksu, R. Teodorescu, C. L. Bak, F. Iov and P. C. Kjær, "Impact of wind power plant reactive current injection during asymmetrical grid faults," in *IET Renewable Power Generation*, vol. 7, no. 5, pp. 484-492, Sept. 2013.

[5] N. Jelani and M. Molinas, "Asymmetrical Fault Ride Through as Ancillary Service by Constant Power Loads in Grid-Connected Wind Farm," in *IEEE Transactions on Power Electronics*, vol. 30, no. 3, pp. 1704-1713, March 2015.

[6] M. KHAN, Y. XIAOMING and H. SUN, "Coupled Behavior of Voltage and Phase Angle during Transients in Modern Power System," *International Conference on Power System Technology* (POWERCON), Guangzhou, pp. 480-487, 2018.

[7] C. Kjaer, P. Florin, C.L. Bak, R. Teodorescu and O. Gosku "Impact of Wind Power Plant Reactive Current Injection during Asymmetrical Faults," *IET Renewable Power Generation,* 2013.

[8] R. Li, H. Geng and G. Yang, "Fault ride-through of renewable energy conversion systems during voltage recovery," *in Journal of Modern Power Systems and Clean Energy*, vol. 4, no. 1, pp. 28-39, January 2016.

[9] I. Erlich, F. Shewarega, S. Engelhardt, J. Kretschmann, J. Fortmann, and F. Koch, "Effect of Wind Turbine Output Current during Faults on Grid Voltage and the Transient Stability of Wind Parks," *IEEE Power & Energy Society General Meeting,* pp.1-8, 26-30 July 2009.

[10] O. Goksu, R. Teodorescu, C.L. Bak, F. Iov and P.C. Kjaer " Instability of Wind Turbine Converters During Current Injection to Low Voltage Grid Faults and PLL Frequency Based Stability Solution" *IEEE Transactions on Power Systems*, vol.29, no.4, July 2014.

[11] L. Wang, W. He, J. Hu and N. Wang, "Coordinated strategy between positive- and negative-sequence currents of wind farms for transient stability enhancement of synchronous generators under asymmetrical grid faults," *International Conference on Renewable Power Generation (RPG 2015*), Beijing, pp. 1-6, 2015.

[12] D. I. Brandao, F. E. G. Mendes, R. V. Ferreira, S. M. Silva and I. A. Pires, "Active and Reactive Power Injection Strategies for Three-Phase Four-Wire Inverters During Symmetrical/Asymmetrical Voltage Sags," in *IEEE Transactions on Industry Applications*, vol. 55, no. 3, pp. 2347-2355, May-June 2019.

[13] M. B. Shamseh, R. Inzunza, I. Fukasawa, T. Tanaka and T. Ambo, "Grid Support During Asymmetrical Faults using Negative Sequence Current Injection," 2019 *IEEE 4th International Future Energy Electronics Conference (IFEEC)*, Singapore, Singapore, pp. 1-6, 2019.

[14] D. Roiu, R. I. Bojoi, L. R. Limongi, A. Tenconi, "New Stationary Frame Control Scheme for Three-Phase PWM Rectifiers Under Unbalanced Voltage Dips Conditions," *IEEE Transactions on Industry Applications,* vol.46, no.1, pp.268-277, Jan.-Feb. 2010.

[15] A. Junyent-Ferre, O. Gomis-Bellmunt, T. C. Green, D. E. Soto-Sanchez, "Current Control Reference Calculation Issues for the Operation of Renewable Source Grid Interface VSCs Under Unbalanced Voltage Sags," *IEEE Transactions on Power Electronics,* vol.26, no.12, pp.3744-3753, Dec. 2011.

[16] J. Mohammadi, S. Afsharnia, S. Vaez-Zadeh and S. Farhangi, "Improved fault ride through strategy for doubly fed induction generator based wind turbines under both symmetrical and asymmetrical grid faults," in *IET Renewable Power Generation*, vol. 10, no. 8, pp. 1114-1122, 9 2016.

[17] M. M. Shabestary and Y. A. I. Mohamed, "Asymmetrical Ride-Through and Grid Support in Converter-Interfaced DG Units Under Unbalanced Conditions," in *IEEE Transactions on Industrial Electronics*, vol. 66, no. 2, pp. 1130-1141, Feb. 2019.

[18] A. Camacho, M. Castilla, J. Miret, J. Vasquez, E. Alarcon-Gallo, "Flexible Voltage Support Control for Three Phase Distributed Generation Inverters Under Grid Fault," *IEEE Transactions on Industrial Electronics*, vol.60, no.4, pp.1429,1441,April 2013.

[19] M. Diaz, R. Cardenas, "Analysis of Synchronous and Stationary Reference Frame Control Strategies to Fulfil LVRT Requirements in Wind Energy Conversion Systems, *9th International Conference on Ecological Vehicles and Renewable Energies (EVER),* 2014.

[20] Hu, Y., Zhu, Z.Q. and Odavic, M. "Instantaneous Power Control for Suppressing the Second Harmonic DC Bus Voltage under Generic Unbalanced Operating Conditions". *IEEE Transactions on Power Electronics*. p. 1. ISSN 0885-8993, 2016.

Chapter 7
Conclusions and Recommendations

The findings from the thesis present valuable insight about the current injection techniques adopted to optimize the power transfer of a grid connected wind energy system. The contributions made are disseminated in each chapter of the thesis. Special attention is given to the derivation of the current injection techniques which are achieved by conducting a detailed analysis of weak AC grids. To supplement the analysis, experimentation is performed and algorithms are tailored to accommodate the desired functions of the techniques.

7.1 Conclusions

In this work, two modified current injection techniques were proposed to optimise the power transfer during symmetrical and asymmetrical grid voltage conditions. The implementation of the techniques was based on the information collected from the dynamic parameters of a weak AC grid. Currents were injected during both voltage conditions and the results were compared with the conventional current injection methods to validate the effectiveness of the proposed techniques.

Based on the performed analysis and results, the conclusions drawn from the thesis are mentioned below:

- In chapter-2, integration of wind energy systems with weak AC grids and the design considerations were highlighted based on the grid strength. Basic components of the wind generator and the control parameters were discussed. Grid code requirement during fault conditions and fault ride through techniques were examined. Different fault conditions were considered for wind power plants and methods were discussed to rectify the unbalance with the aid of power converters.

- In chapter-3, basic concepts of the wind turbine parameters and conversion of wind power into electrical power were reviewed. The associated power profiles were studied by deriving the primary wind energy expressions such as power coefficient, tip speed ratio and MPPT. Control models were investigated for both machine and grid side converters. The machine side converter was operated under two control loops, where the inner loop controlled the direct current magnitude and the outer loop managed the quadrature current for DC link voltage regulation. The grid side converter performed as a STATCOM and independently injected active/reactive currents according to the given conditions. Dual sequence vector control was discussed for the asymmetrical voltage faults. An analysis was also performed to predict the transferred power from the turbine to the PCC by considering system's actual parameters.

- In chapter-4, grid impedance was estimated to assist formulation of the current injection techniques. Multiple grid impedance estimation methods were reviewed. The PQ variation technique was chosen and modified in order to be applied per phase. Single phase transformed model of a three phase system was presented in *dq* rotating reference frame. Experimental investigation was performed on a set of known impedances to validate the scheme and the designed control. To determine the percentage calculation error of the proposed technique, a comparison was also shown between actual and estimated values of the impedances.

- In chapter-5, application of optimal current injection technique was discussed for symmetrical grid voltage conditions. The proposed technique was tested on a lab-based wind energy system to confirm the optimal distribution of the currents. The technique was elaborated with the help of mathematical equations and the control structure was developed in order to allow minimum power distribution losses with enhanced voltage stability. A comparison based on the experimental analysis was also presented to confirm the validity of the technique.

- In chapter-6, asymmetrical faults were discussed. To mitigate the faults, coordinated current injection technique was proposed and implemented which offered limited injection of active and reactive powers. The derived limits were dependent on varying X/R ratios and based on that, active and reactive current components were injected to maintain the stable DC link voltage and limited grid side peak currents. Numerical analysis along with the experimental results validated the proposed technique. It was shown that the proposed technique eliminated the need of an external hardware for DC link overvoltage suppression and implemented FRT.

7.2 Research Contributions

In this thesis, per phase control model of the PQ variation technique is proposed for the grid impedance measurement. Based on that, two modified current calculation techniques are implemented to optimize the power transfer of a WECS integrated into a weak AC grid, during symmetrical and asymmetrical voltage conditions. Asymmetrical faults in weak AC grids, which were not studied before explicitly, are also part of the discussion. Furthermore, active and reactive current transfer limits are defined, which could be a useful contribution in modifying the modern grid codes.

With respect to research contributions, a research paper has been published in a peer-reviewed IEEE conference. It was based on calculation and injection of optimal currents during symmetrical voltage conditions. The title is:

- *"Steady State Impedance Estimation of a Weak Grid to Assist Optimal Current Injection for Minimal Power Losses" in IEEE Energy Conversion Congress & Exposition, USA, Sep 2016.*

Extension of the above mentioned paper is published at IET Journal of Electric Power Applications 2019 (Oct). The title is:

- *“Optimal Current Calculation for a PMSG based Wind Energy system Integrated into an Unbalanced Weak Grid”*

One more paper reviewing the wind turbine generator topologies is published at International Transactions on Electrical Energy Systems 2019 (Dec). The Title is:

- *"Deployment of Onshore Wind Turbine Generator Topologies - Opportunities and Challenges"*

Another paper describing the limited injection of coordinated currents during asymmetrical faults is under review at IEEE Transactions on Industrial Electronics 2020 (May). The title is:

- *"Limited Current Calculation to Support LVRT for a PMSG-based WECS Operating under Asymmetrical Weak Grid Conditions"*

7.3 Limitations

In summary, the energy capture over available wind speed and the power transfer was enhanced by efficiently utilising the back-to-back converters topology. Since a type-4 wind turbine configuration was under consideration, full scale converters were employed on both machine and grid sides.

On the grid side, even though the converter had the capability of independent injection of active and reactive currents, there were still certain limitations which were to be set through the current limitation model in the converter control frame. For a two-level full scale converter, the overload capacity was 10% above the rated conditions. That means, if the maximum current is 1.1 p.u with 1 p.u active current then according to $I_{max} = \sqrt{I^2{}_{real} + I^2{}_{imaginary}} \leq I_{rated}$, there is only 0.45 p.u capacity left for the reactive current to compensate. Therefore, to allow maximum reactive current, the magnitude of the active current had to be reduced carefully according to the limits defined in the coordinated current calculation technique for asymmetrical faults.

For the optimal current injection technique during symmetrical voltages, the grid was considered as a Thevenin equivalent model of a distributed network where each line would have an independent source and likely to have unequal connected loads. Therefore, for unequal loads, the technique proposed unequal and sometimes higher currents. Since there was no support

from any shunt ancillary device and the information of the impedance at the point of design was also unknown, the back-to-back converters were decided to be chosen slightly higher than the generator rating, i.e approximately $1.5*P_{gen}$.

The increase in the power rating of the converters did not really affect the cost to a large extent. Considering this as a limitation, it can be overcome by connecting a shunt converter to support the fault conditions. However, that would increase the overall control complexity and cost of the system, as well as undermine the objective of the research.

To estimate the line impedance, PQ power variation method was employed because of its simple implementation and relevance with the theme of the research conducted in this thesis. Other methods such as inter-harmonics or current transient injection could also be applied but on the cost of increased computational intensity and DSP/FPGA space consumption. Furthermore, for online implementation of these methods, a separate shunt connected device was also required.

Moreover, the grid under consideration was inductive in nature with high X/R, it was more sensitive to reactive power variations which lead to grid voltage variations. The equipment used to calculate the ΔV_d was not sophisticated enough to detect minor shifts as shown in Figures 4.10 (e), 4.11 (e) and 4.12 (e). So, from equations (4.13) and (4.14) when I_q was perturbed, ΔV_d was in the range of detectable magnitude which aided the controller towards better estimation of L_{th}. However, in comparison when I_d was perturbed for R_{th} calculation, ΔV_d resulted in lower magnitude and had a higher percentage of error.

7.3 Recommendations for Future Work

In chapter-4, the experimental procedure for estimating the grid impedance was based on steady state conditions. Since the theme of the thesis is power optimization, PQ variation method was adopted for the impedance estimation. Even though the procedure was self-automated but due to multiple number of functions to be performed by the grid-side converter, the impedance estimation was performed separately each time before the current injection techniques were applied. It is therefore recommended that a separate hardware can be used to execute the functions in parallel.

The presented concepts were verified on an aggregated wind generator which provided analysis at a fundamental level. More work can be done by taking into account the dynamics of multiple machines comprising a wind power plant.

The study conducted in this thesis highlights the integration of a wind generator with a weak AC grid during symmetrical and asymmetrical voltage conditions. The experimental investigation is done by considering a SCR value of 3. This was the minimum value that could be selected due to hardware constraints in the laboratory. For future research, the operation of the system can be analysed at SCR=1 by considering different set of connected line impedances.

The case-study can be extended in future by incorporating variable wind conditions so as to check the system's dynamic response. Multilevel converters can also be used to achieve higher voltage levels. Small signal and frequency stability analysis can also be considered to support the analysis.

7.4 Concluding Remarks

According to modern international grid codes, it is an important requirement for grid connected WECS' that the power converters must be able to regulate ±0.5% of the controlled voltage by supplying reactive power to supplement the grid voltage without requesting support from any external device. However, in case of weak grids which are usually located in remote areas, the grid faults occur quite frequently and sometimes the shunt connected support is also not available. Due to such limitations, type-4 wind turbine configuration is commonly employed in these areas at MV level. Considering such a system with no external hardware support, the available power converters must be utilised in such a way to support the grid by optimally injecting the currents during fault conditions. Thus, by employing the current injection techniques discussed in this thesis, the aforementioned concerns can be served effectively.

Appendix-A

Transfer Functions of Generator, DC-link and Grid side Controllers

Table A.1. System Parameters

Generator Type	*PMSG, 3.3kW,200rpm,380V*
No. of Pole Pairs, p	*15*
Stator resistance, R_s	*0.76Ω*
d-axis stator inductance, L_d	*6.5mH*
q-axis stator inductance, L_q	*6.5mH*
Switching Frequency, f_{SW}	*5kHz*
Filter Capacitance, C_f	*5μF*
Filter Inductance, L	*4.7mH*
Damping Resistance, r	*1.4Ω*
DC-link Capacitance, C_s	*4700μF*

a) Generator Side Current Control

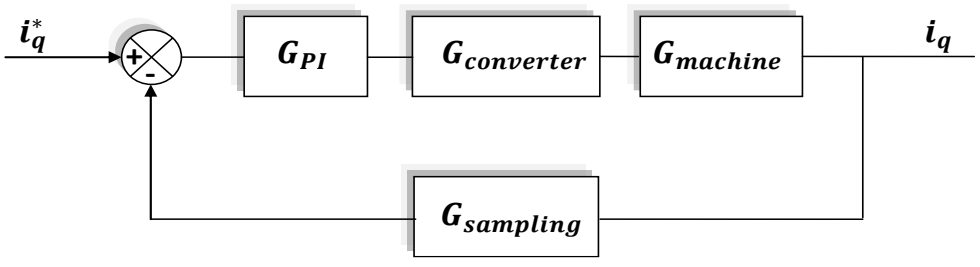

Figure A.1: PMSG Current Control Loop

Table A.2. Transfer Functions of PMSG Current Control Loop

$G_{PI} = \frac{K_p(T_i s + 1)}{T_i s}$
$G_{Converter} = \frac{1}{T_{switching} s + 1}$
$G_{machine} = \frac{K_E}{T_E s + 1}$
$K_E = \frac{1}{R_s}$, $T_E = \frac{L_s}{R_s}$
$G_{Sampling} = \frac{1}{T_{sampling} s + 1}$
$G_{characteristic} = 1 + \frac{T_E}{K_E K_p} s + \frac{T_E T_c}{K_E K_p} s^2$
$K_p = \frac{T_E}{2 K_E T_c}$
$T_i = T_E$
$K_i = \frac{K_p}{T_i}$
Calculated:
$K_p = 10.8333$
$K_i = 1259$
Modified Using MATLAB Sisotool:
$K_p = 1.63$
$K_i = 0.95$

b) Generator Speed Control

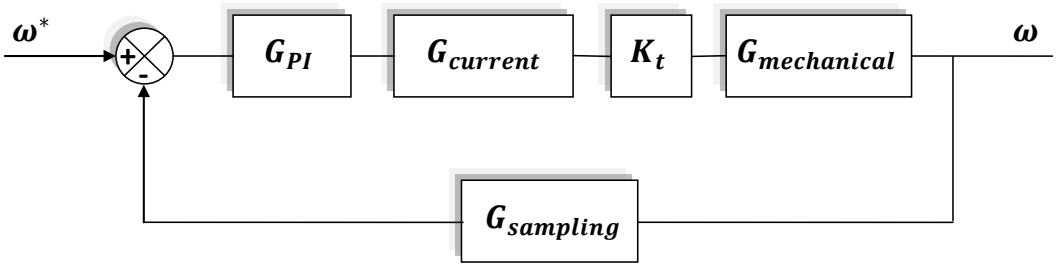

Figure A.2: PMSG Speed Control Loop

Table A.3. Transfer Functions of Speed Control Loop

$G_{PI} = \frac{K_p(T_i s + 1)}{T_i s}$
$G_{current} = \frac{1}{T_{current} s + 1}$
$K_t = \frac{3}{2} p^2 \lambda_{af}$
$G_{mechanical} = \frac{K_m}{T_m s + 1}$
$K_m = \frac{1}{B_s}$, $T_E = \frac{J_s}{B_s}$
$G_{OL} = \frac{K_p(T_i s + 1)}{T_i s} \frac{1}{T_{current} s + 1} \frac{1}{T_{sampling} s + 1} K_t \frac{K_m}{T_m s + 1}$
$G_{OL} = \frac{K_\Sigma (T_i s + 1)}{s^2 (T_s s + 1)}$
$K_\Sigma = \frac{K_p K_t K_m}{T_i T_m}$
$G_{characteristic} = s^3 + \frac{1}{T_s} s^2 + \frac{K_\Sigma T_i + 1}{T_s} s + \frac{K_\Sigma}{T_s}$
$K_p = \frac{K_\Sigma T_i T_m}{K_t K_m}$
Calculated:
$K_p = 2.68$
$K_i = 319$
Modified Using MATLAB Sisotool:
$K_p = 0.2$
$K_i = 1.25$

c) DC link Voltage Control

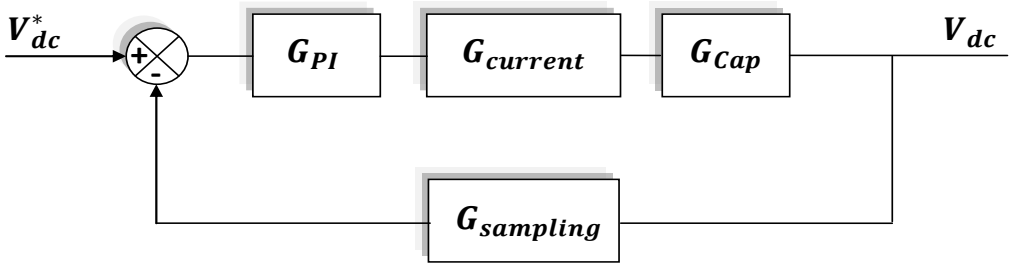

Figure A.3: DC Link Voltage Control Loop

Table A.4. Transfer Functions of DC link Voltage Control Loop

$G_{PI} = \frac{K_p(T_i s + 1)}{T_i s}$
$G_{current} = \frac{1}{T_{current} s + 1}$
$G_{cap} = \frac{1}{Cs}$
$G_{OL} = \frac{K_p(T_i s + 1)}{T_i s} \frac{1}{T_{current} s + 1} \frac{1}{T_{sampling} s + 1} \frac{1}{Cs}$
$G_{OL} = \frac{K_\Sigma(T_i s + 1)}{s^2(T_s s + 1)}$
$K_\Sigma = \frac{K_p}{T_i C}$
$G_{characteristic} = s^3 + \frac{1}{T_s} s^2 + \frac{K_\Sigma T_i + 1}{T_s} s + \frac{K_\Sigma}{T_s}$
$\sigma = \frac{1}{(\alpha + 2) T_s}$
$K_\Sigma = T_s \left(1 + \frac{1 - \zeta^2}{\zeta^2}\right) \sigma^3$
$T_i = \frac{\left(2\alpha + 1 + \frac{1 - \zeta^2}{\zeta^2}\right) \sigma^2 T_s}{K_\Sigma}$
$K_p = K_\Sigma T_i C$
Calculated:
$K_p = 3.36$
$K_i = 533$
Modified Using MATLAB Sisotool:
$K_p = 13.46$
$K_i = 0.78$

d) Grid Side *d-axis* Current Controller

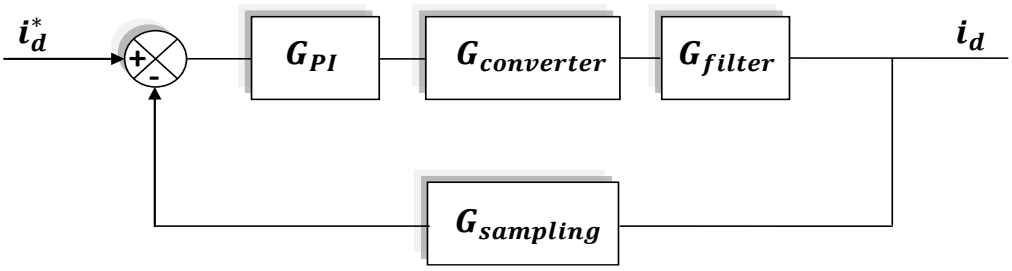

Figure A.4: *d-axis* Grid Side Current Control Loop

Table A.5. Transfer Functions of d-axis Grid Current Control Loop

$G_{PI} = \frac{K_p(T_i s + 1)}{T_i s}$
$G_{Converter} = \frac{1}{T_{switching} s + 1}$
$G_{Filter} = \frac{K_E}{T_E s + 1}$
$T_E = \frac{L_I + L_g}{R}$, $K_E = \frac{1}{R}$
$G_{Sampling} = \frac{1}{T_{sampling} s + 1}$
$G_{characteristic} = 1 + \frac{T_E}{K_E K_p} s + \frac{T_E T_c}{K_E K_p} s^2$
$K_p = \frac{T_E}{2 K_E T_c}$
$T_i = T_E$
$K_i = \frac{K_p}{T_i}$
Calculated:
$K_p = 21.14$
$K_i = 2936$
Modified Using MATLAB Sisotool:
$K_p = 2.25$
$K_i = 1.25$

Appendix-B

LabView Codes

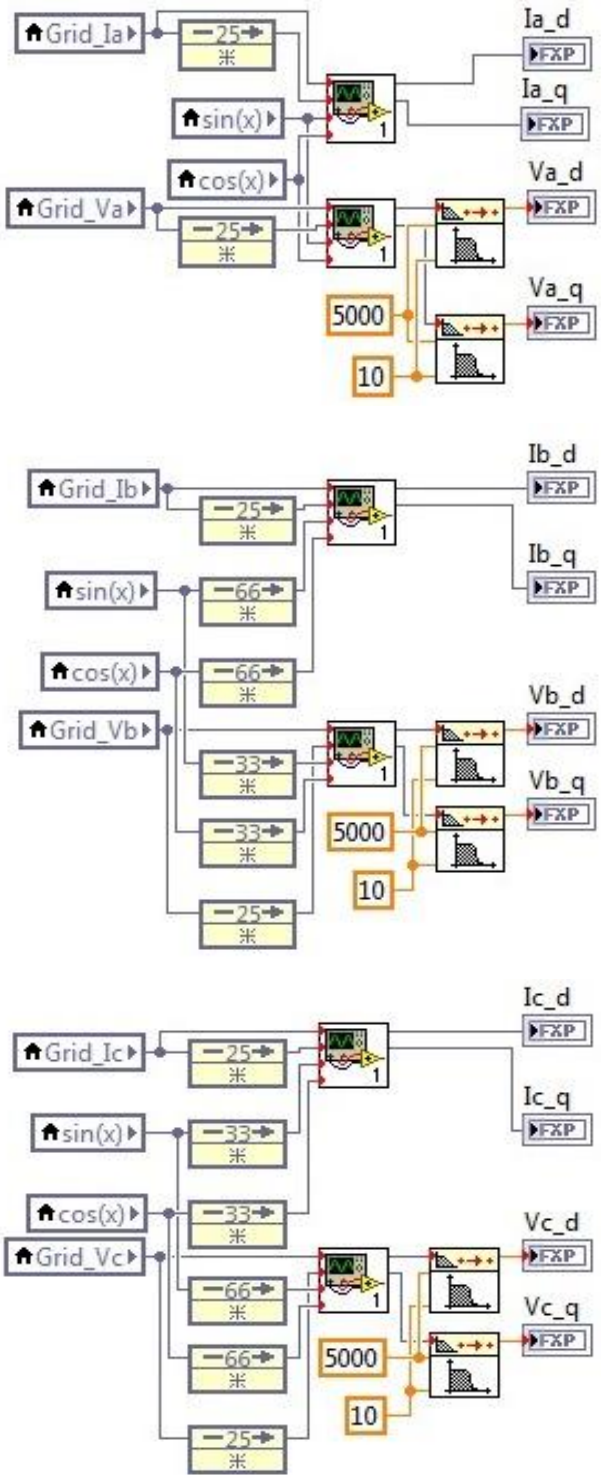

Figure B.1: Generation of Quarter Cycle Delay on Single Phase Quantities to Create Orthogonal Signals for Park's Transformation

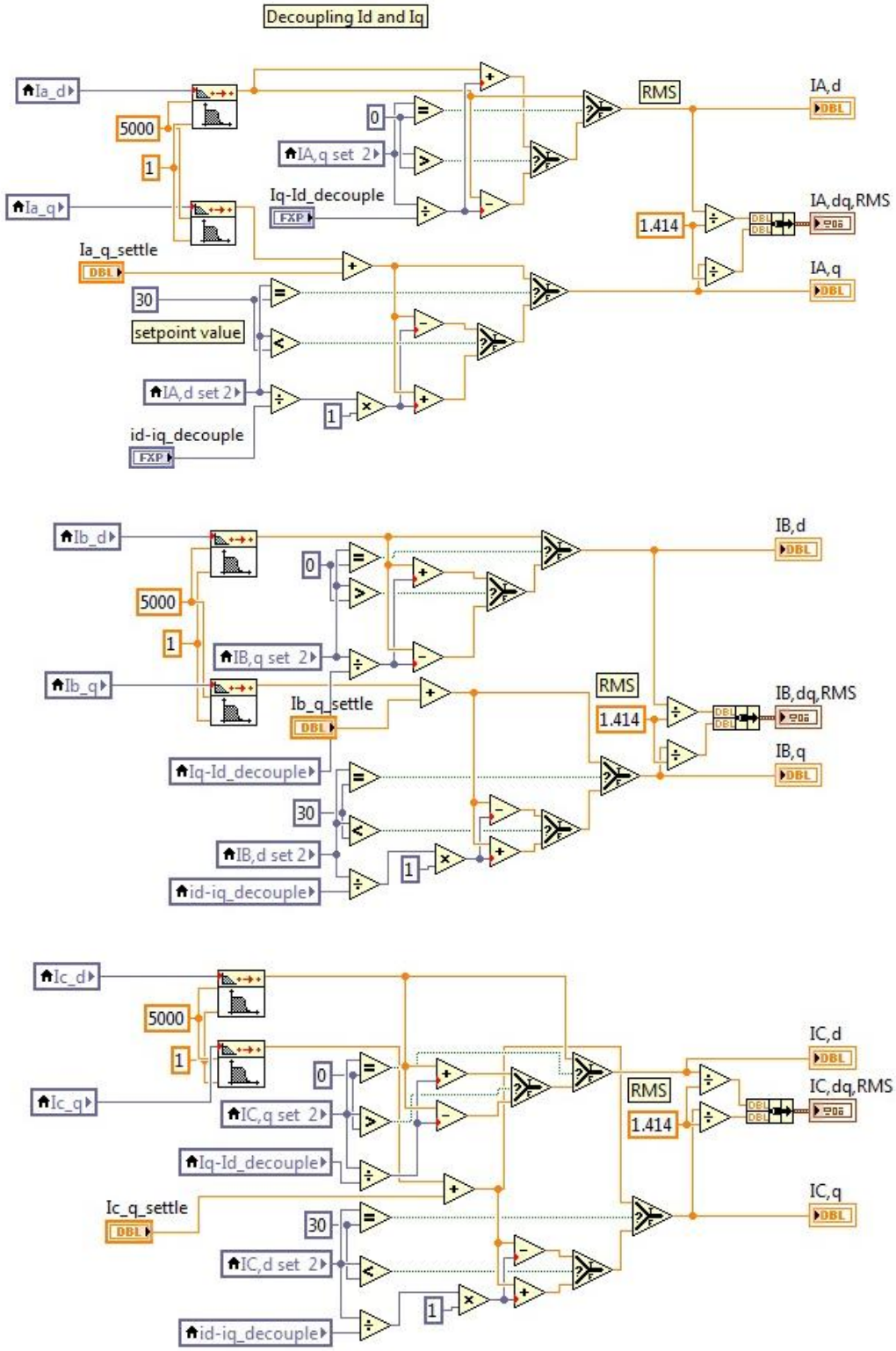

Figure B.2: Decoupling of *dq-axis* Current Components during Unbalanced Grid Voltages

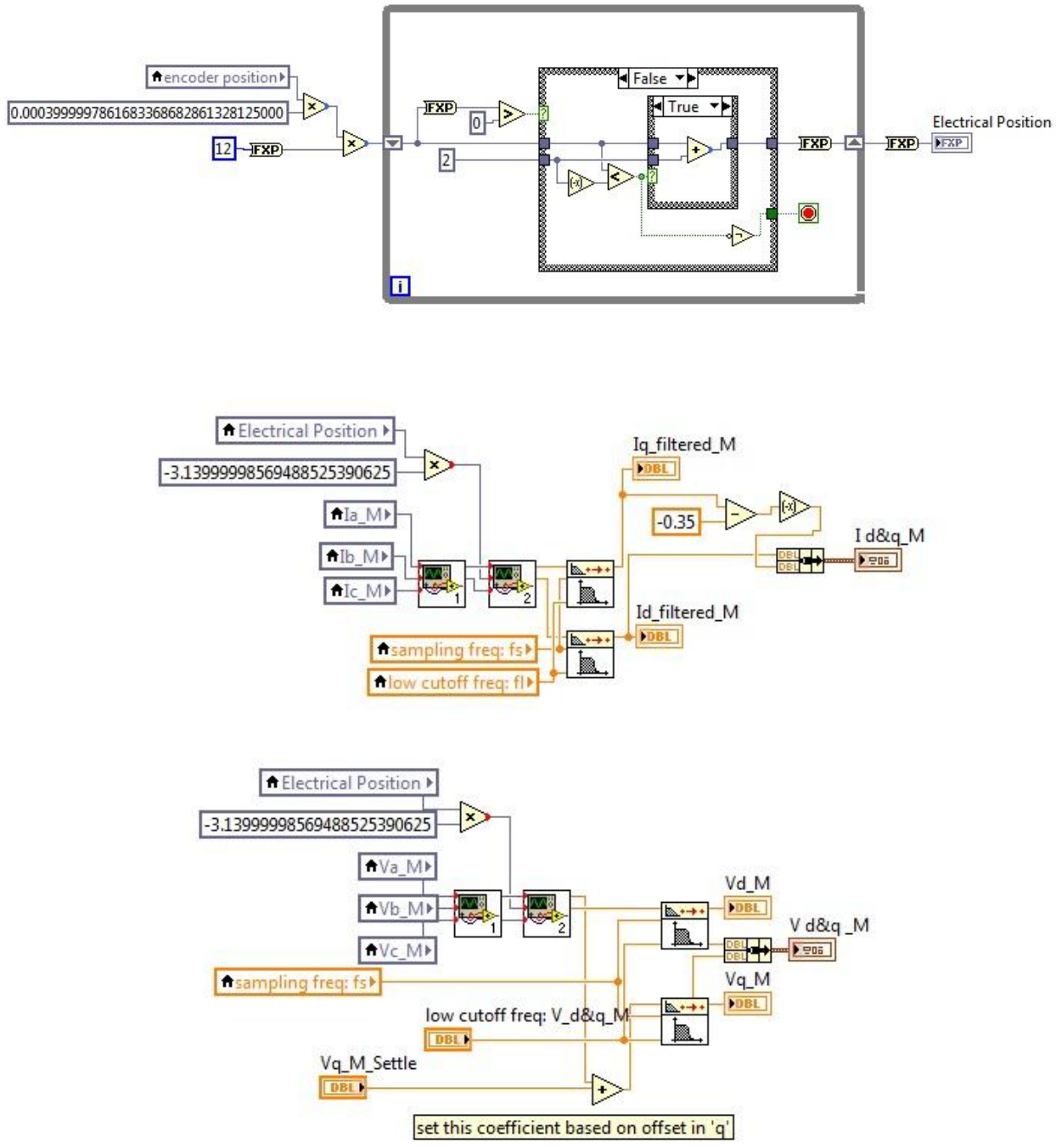

Figure B.3: Generator Current and Voltage Components Acquisition for Control Feedback

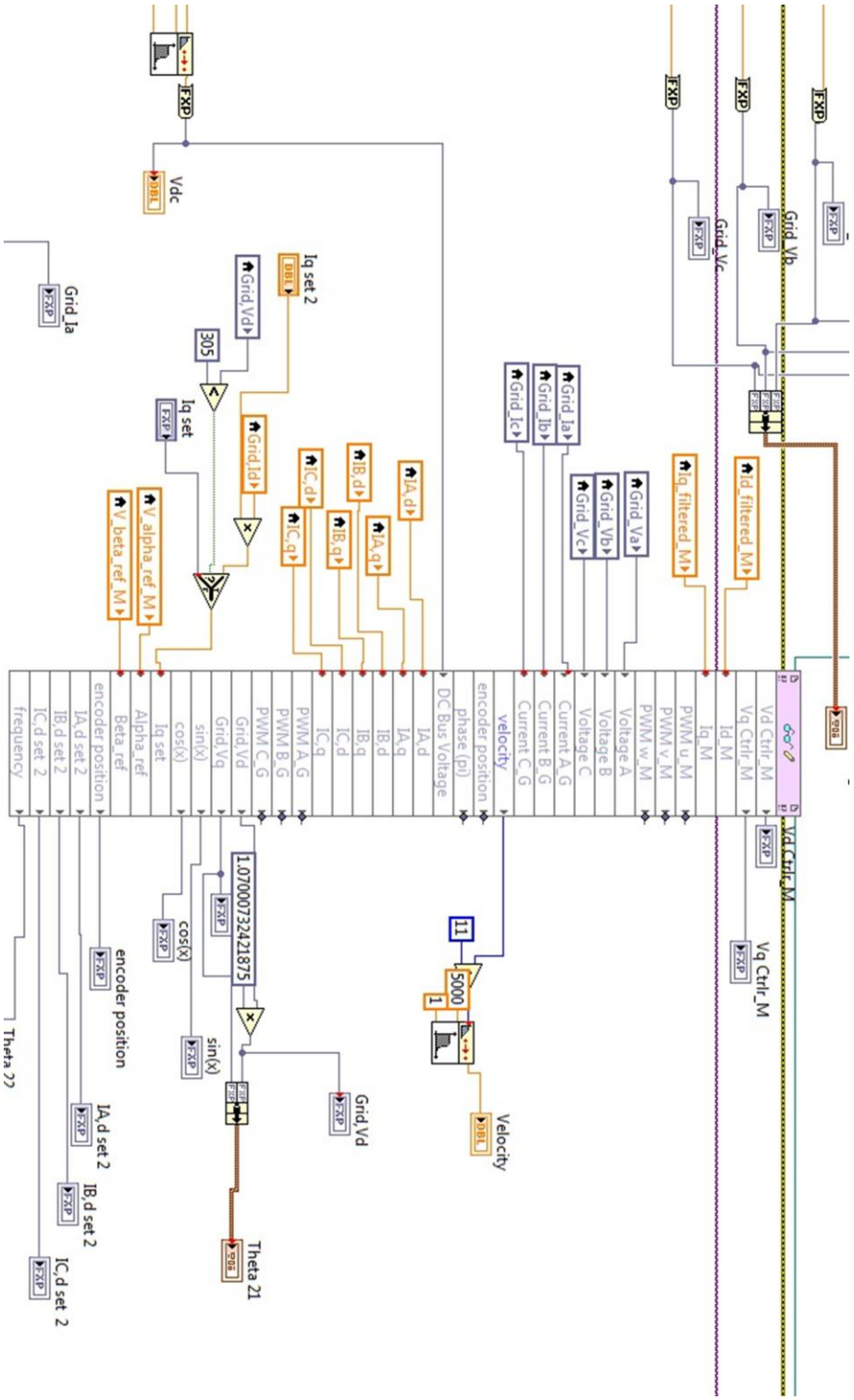

Figure B.4: Transfer of ADC Signals to FPGA

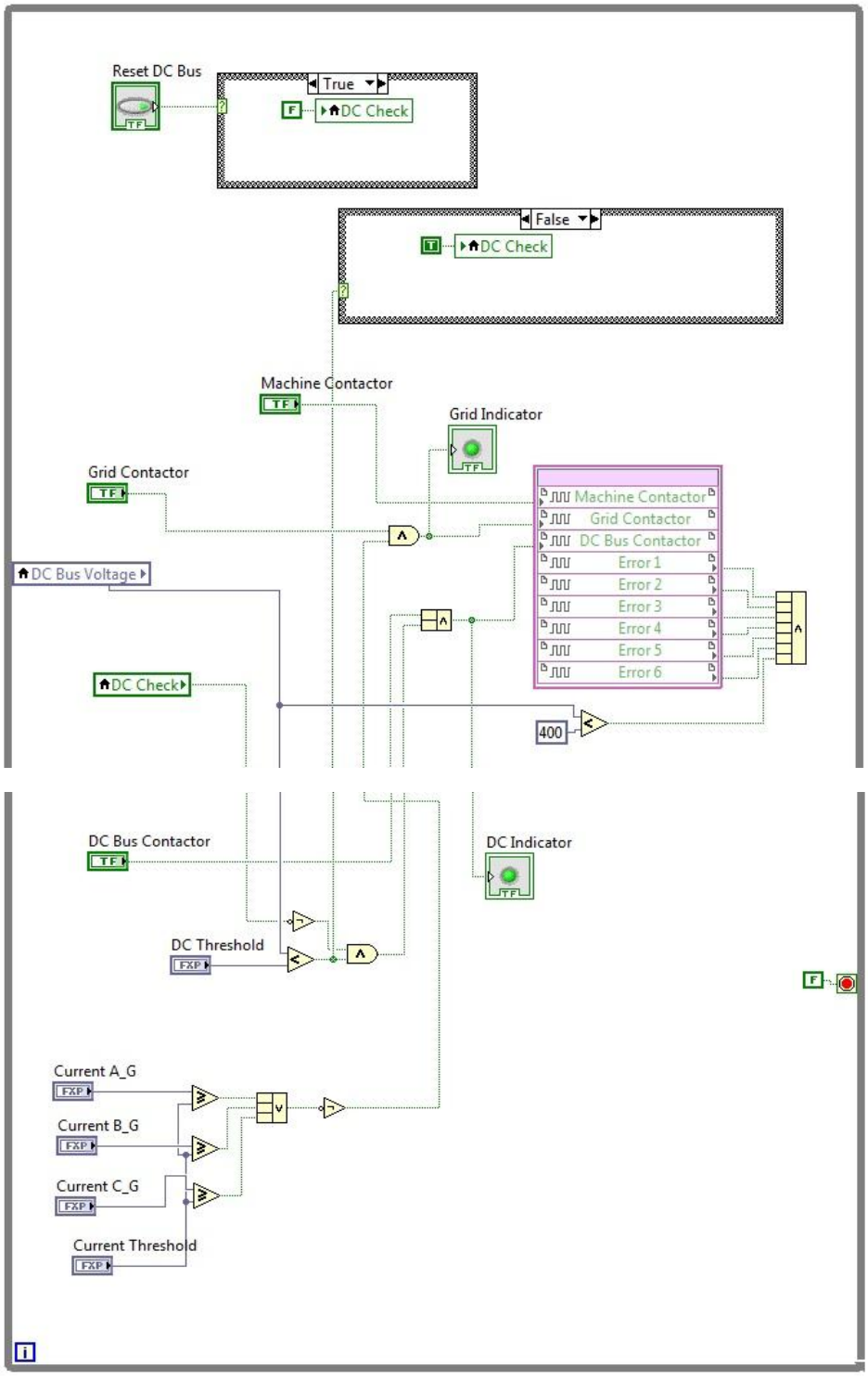

Figure B.5: Error Triggering Functions for Protection

Appendix C

Video Link of the Hardware Lab Setup:

- https://youtu.be/RxwUl2lfJkY

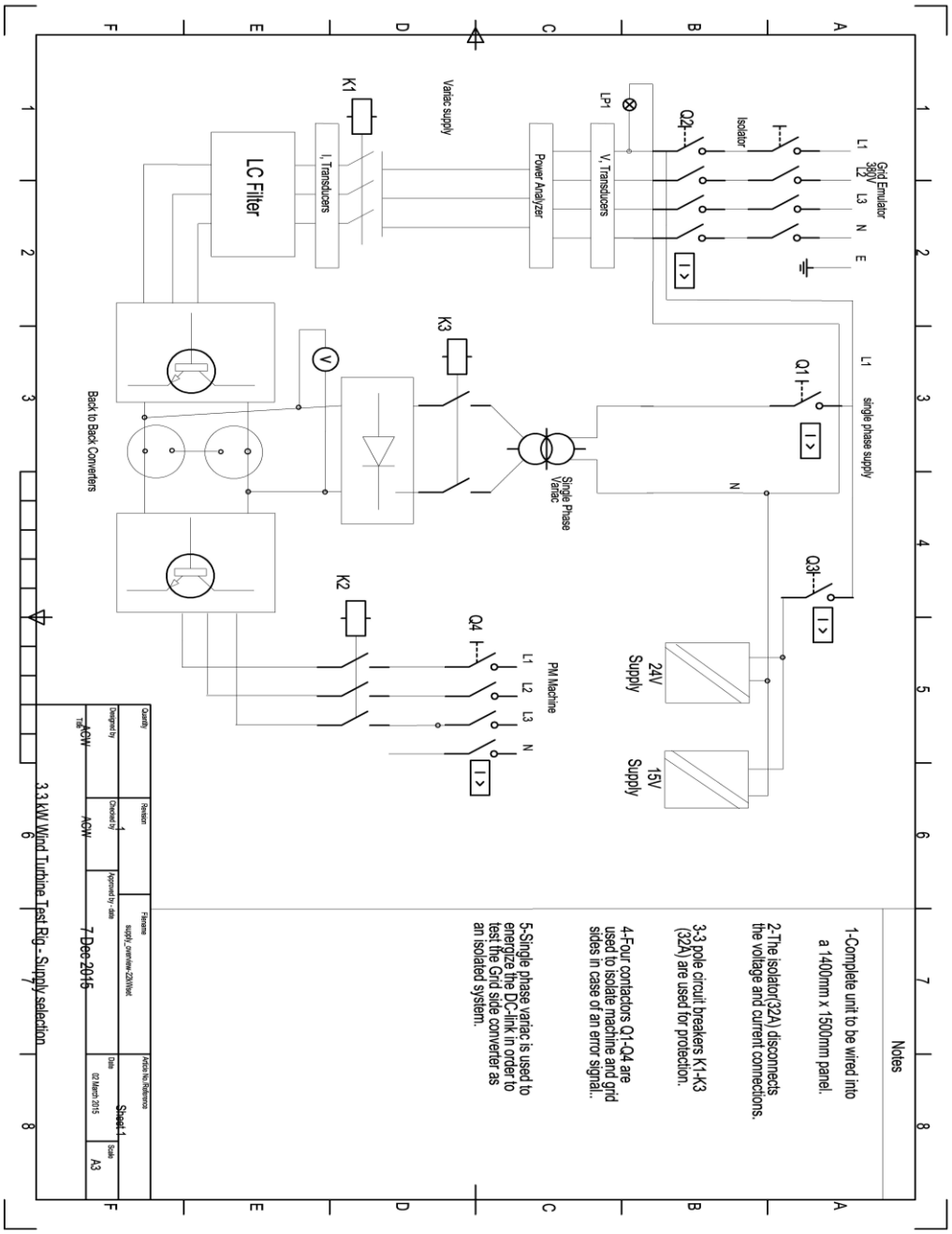

Figure C.1: Hardware Panel Layout

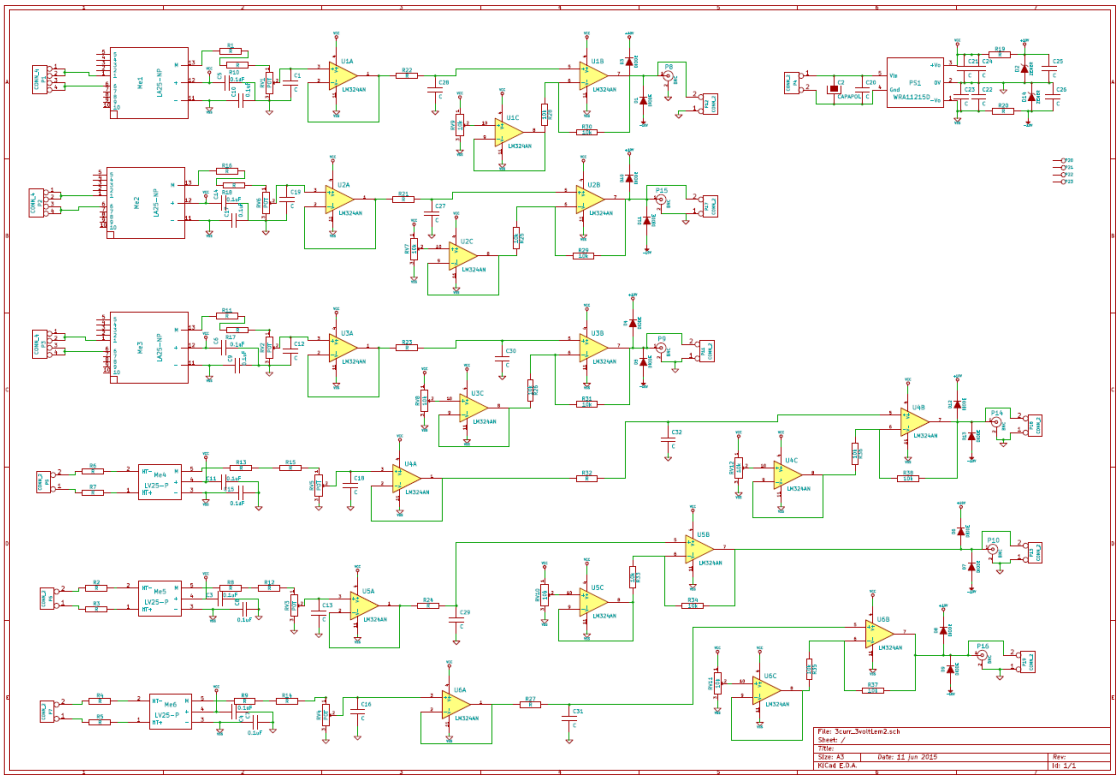

Figure C.2: Schematic diagram for V and I Transducers' ICs

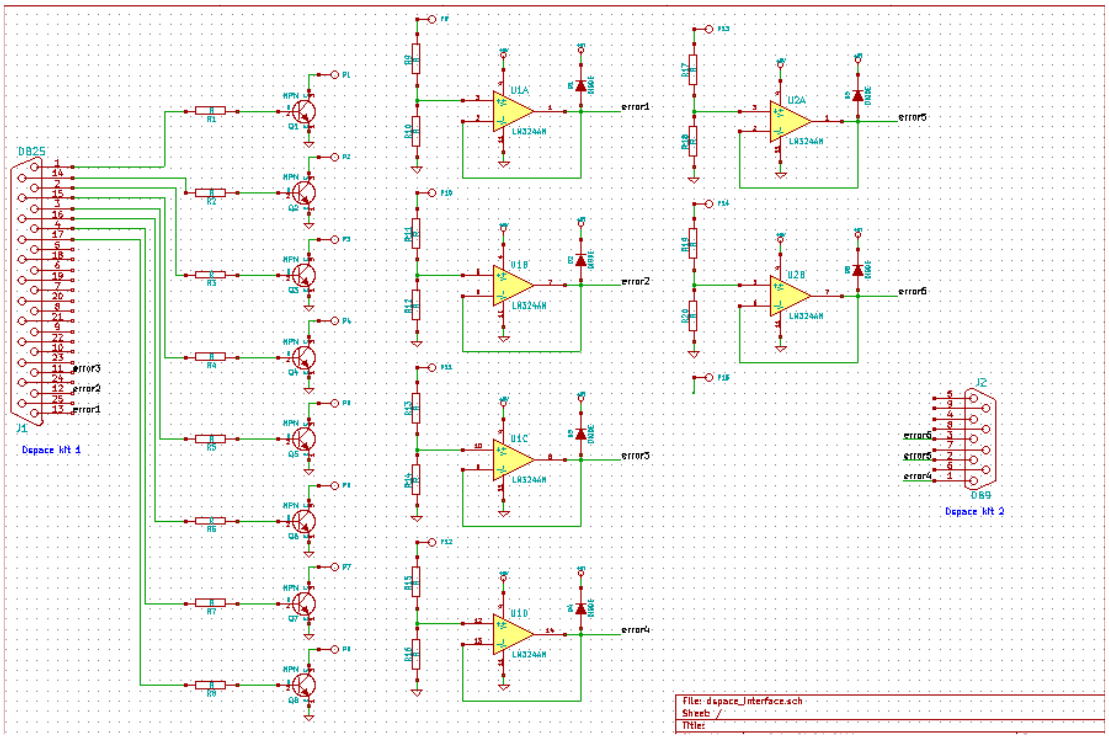

Figure C.3: Relay and Error Signal Circuit Board

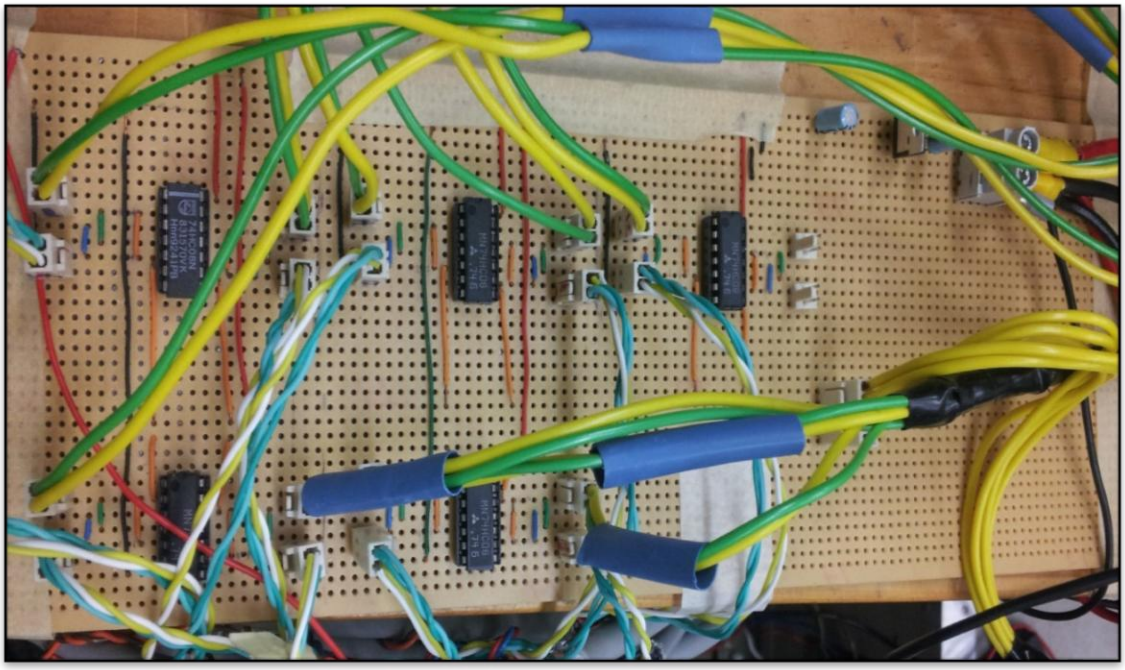

Figure C.4: Voltage Shifter board for FPGA Signal Regulation

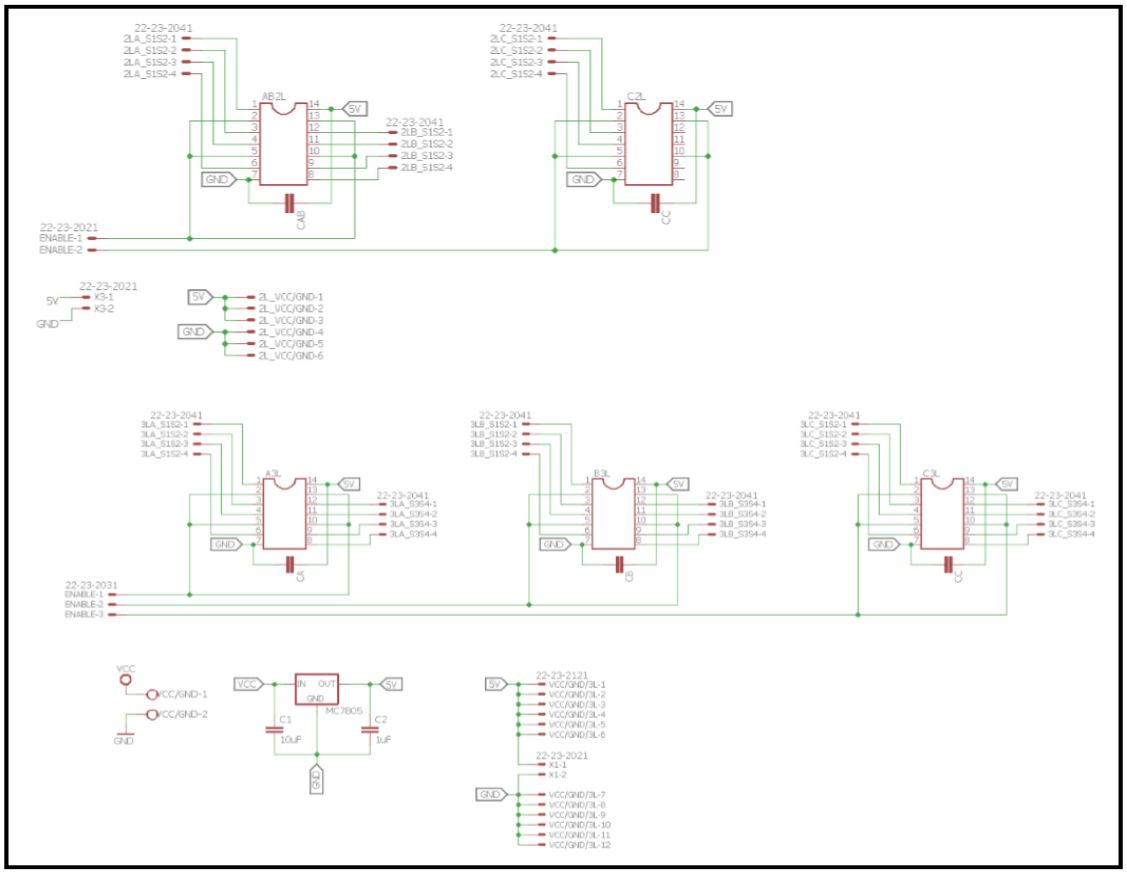

Figure C.5: Schematic diagram for FPGA level shifter

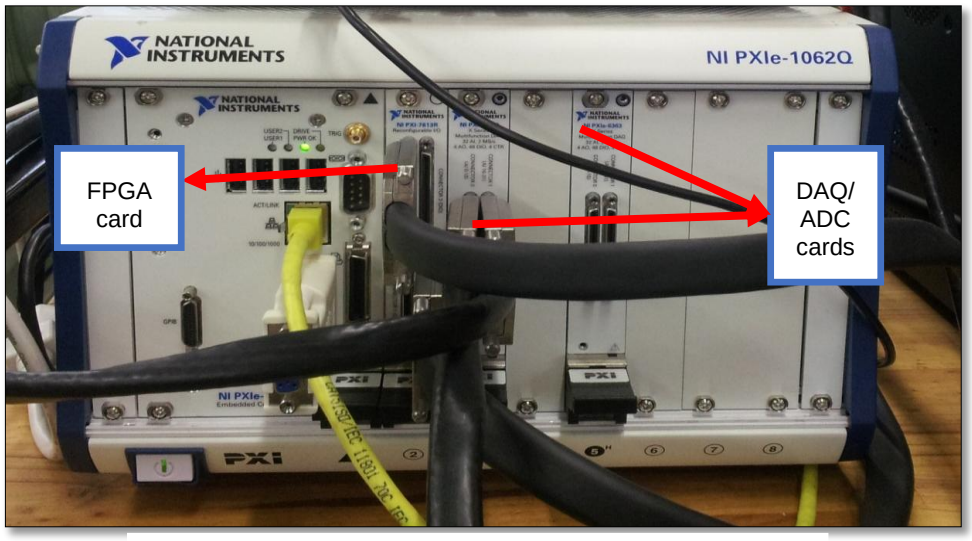

Figure C.6: PXI Chassis Mounted with FPGA and DAQ Cards

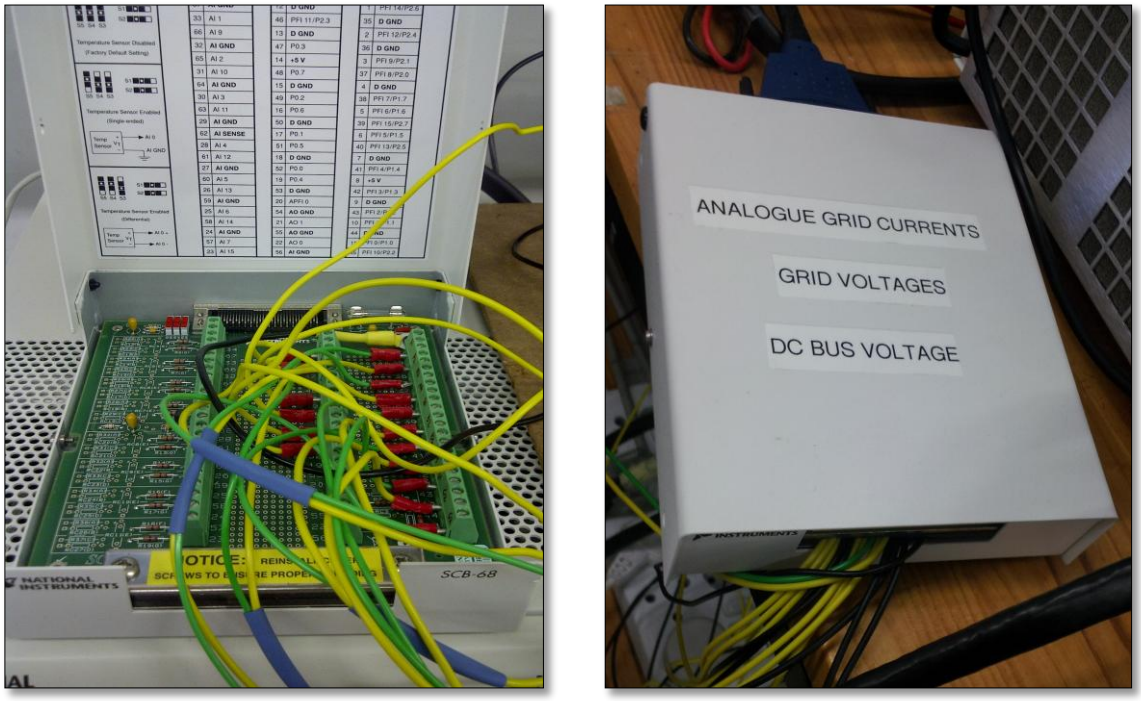

Figure C.7: SCB Connector Boards

- **PXIe-6363:** http://www.ni.com/datasheet/pdf/en/ds-151
- **PXI-7813R:** http://www.ni.com/datasheet/pdf/en/ds-98
- **SCB-68:** http://www.ni.com/pdf/manuals/371745c.pdf

- **Grid Emulator Details:** https://www.powerandtest.com/power/ac-power-sources/mx-series